

1

2 **A Novel Multidimensional Search for**
3 **Diboson Resonances in the Boosted Dijet Final State**

4 **and**

5 **Encoding Jet Substructure with a Deep Neural Network**

7 Dissertation

8 zur
9 Erlangung der naturwissenschaftlichen Doktorwürde
10 (Dr. sc. nat.)

11 vorgelegt der
12 Mathematisch-naturwissenschaftlichen Fakultät
13 der
14 Universität Zürich

15 von

16 Thea Klaeboe Arrestad
17 aus
18 Norwegen

19 Promotionskommission:

20 Prof. Dr. Ben Kilminster (Vorsitz)
21 Prof. Dr. Florencia Canelli
22 Prof. Dr. Jesse Thaler
23 Dr. Andreas Hinzmann

24 Zürich 2019

Abstract

In this doctoral thesis I will present three different searches for new heavy resonances decaying to pairs of vector bosons in the all-hadronic final state. The analyzed data were collected by the CMS experiment at the LHC during the first three years of data-taking at a collision center-of-mass energy of 13 TeV, corresponding to an integrated luminosity of 2.7 (2015), 35.9 (2016) and 77.3 (2016+2017) fb^{-1} , and the searches were the first of their kind to ever be performed at such a high collision energy. The diboson final states under consideration are challenging to resolve due to the bosons being highly energetic (“boosted”), resulting in the two quarks from the decay being collimated and merging into a single jet. This leads to a dijet final state topology where each jet displays some energy substructure. The first search I will present, was one of the two first CMS searches in boosted final states with 13 TeV data to become published, and the first to take advantage of jet substructure at the trigger level. It was a high profile analysis due to a previously observed $3.4\ (1.3)\ \sigma$ excess around 2 TeV in the 8 TeV dataset, as analyzed by ATLAS (CMS), and I brought the search to a published result within six months after 13 TeV data taking began (and within ten months after embarking on my PhD). Following this, in my second analysis I optimized, validated and commissioned the novel PUPPI softdrop jet grooming algorithm for vector-boson tagging and, in addition, developed dedicated mass corrections for the softdrop jet mass. The algorithm and corresponding mass corrections are now the default for vector boson tagging in CMS and used by several analyses. It was the first published result taking advantage of PUPPI softdrop jet grooming. The third and final search I will present introduces a novel multidimensional search framework, which can be used to search for resonances peaking anywhere in the 3D spectrum of the dijet and groomed jet mass spectra. Validated through a search with hadronically decaying vector bosons in the final state, which I will present here, the framework can be used to incorporate all resonance searches with hadronically decaying vector boson or hadronically decaying Higgs boson final states, as well as for generic searches for any boosted object peaking in jet mass. In the context of this search, a simultaneous fit to the $W(q\bar{q})$ and $Z(q\bar{q})$ jet mass peaks from the Standard Model (SM) $V(\bar{q}q)+\text{jets}$ process has been performed, for the first time allowing to constrain the groomed jet mass scale and resolution from this SM process. Finally, I will present a deep neural network for vector-boson tagging, which encodes jet clustering- and substructure-like variables into the neural network layers themselves. This algorithm significantly improves the analysis sensitivity, and can also be used as a stepping stone in the development of a generic anti-QCD tagger. The latter will be of great importance when attempting to use the multidimensional framework for model-independent searches.

Zusammenfassung

In dieser Doktorarbeit werde ich drei verschiedene Analysen über neue schwere Resonanzen vorstellen, die in Paare von Vektorbosonen zerfallen und welche wiederum in Quarks zerfallen (hadronic). Die analysierten Daten wurden vom CMS-Experiment am LHC während der ersten drei Jahre der Datenaufnahme bei einer Kollisionsschwerpunktsenergie von 13 TeV gesammelt, was einer integrierten Luminosität von 2.7 (2015), 35.9 (2016) und 77.3 (2016 + 2017) fb^{-1} entspricht. Diese Analysen waren die ersten ihrer Art, die jemals bei einer so hohen Kollisionsenergie durchgeführt wurden. Die Endzustände des Dibosons sind schwierig zu lösen, da die Bosonen hochenergetisch (“boosted”) sind, was dazu führt, dass die beiden Quarks aus dem Zerfall kollimiert werden und zu einem einzigen Jet verschmelzen. Dies führt zu einer Dijet-Endzustands-Topologie, bei der jeder Jet eine Energieunterstruktur aufweist. Die erste Analyse, die ich vorstellen werde, war eine der ersten veröffentlichten CMS-Analysen in “boosted” Endzuständen mit 13 TeV-Daten, und die erste, welche die Jet-Substruktur auf Trigger-Ebene nutzte. Es war eine hoch gehandelte Analyse aufgrund eines zuvor beobachteten $3,4\ (1,3)\ \sigma$ -Überschusses um 2 TeV im 8 TeV-Datensatz, der von ATLAS (CMS) analysiert wurde. Ich habe die Analyse innerhalb von sechs Monaten nachdem die 13 TeV-Datenaufnahme begonnen hatte zu einem veröffentlichten Ergebnis gebracht. Im Anschluss daran habe ich in meiner zweiten Analyse den neuartigen PUPPI-Softdrop-Algorithmus für das Vektor-Boson-Tagging optimiert, validiert und in Betrieb genommen und zusätzlich spezielle Massenkorrekturen für die Softdrop-Jet-Masse entwickelt. Der Algorithmus und die entsprechenden Massenkorrekturen sind jetzt der Standard für das Vektor-Boson-Tagging in CMS und werden von mehreren Analysen verwendet. Es war das erste veröffentlichte Ergebnis, bei dem PUPPI-Softdrop genutzt wurde. Die dritte und letzte Analyse führt ein neuartiges multidimensionales Analyse-Framework ein, mit dem nach Resonanzen irgendwo im 3D-Spektrum der Dijet- und Groomed Jet-Massenspektren gesucht werden kann. Validiert durch die VV-All-Hadronic Analyse, kann dieses Framework für alle Resonanzanalysen über “hadronic” zerfallende Vektorbosonen oder “hadronic” zerfallende Higgs-Boson-Endzustände sowie generische Analysen über geboostete Objekt, die in der Jet-Masse ihren Höhepunkt erreichen, verwendet werden. Schließlich werde ich ein Deep Neural Network für das Vektor-Boson-Tagging vorstellen, welches Jet-Clustering- und substrukturähnliche Variablen in die neuronalen Netzwerkschichten encodiert. Dieser Algorithmus verbessert die Analyseempfindlichkeit erheblich und kann auch als Grundlage für die Entwicklung eines generischen Anti-QCD-Taggers verwendet werden. Letzteres ist von großer Bedeutung, wenn versucht wird, dieses mehrdimensionale Framework für modellunabhängige Analysen zu verwenden.

Contents

⁹⁷	I Theoretical background	15
⁹⁸	1 The Standard Model	17
⁹⁹	1.1 Fundamental particles: quarks and leptons	17
¹⁰⁰	1.2 The Standard Model Lagrangian	19
¹⁰¹	1.2.1 The quantum chromodynamics sector	21
¹⁰²	1.2.2 The electroweak sector	23
¹⁰³	1.2.3 The Higgs sector	26
¹⁰⁴	2 Beyond Standard Model Physics	31
¹⁰⁵	2.1 Shortcomings of the Standard Model	31
¹⁰⁶	2.2 Compositeness	33
¹⁰⁷	2.2.1 Heavy Vector Triplet formalism	33
¹⁰⁸	2.3 Warped extra dimensions	36
¹⁰⁹	II Experimental setup	39
¹¹⁰	3 The Large Hadron Collider	41
¹¹¹	4 The CMS detector	45
¹¹²	4.1 Coordinate system	46
¹¹³	4.2 Tracking detectors	47
¹¹⁴	4.3 Electromagnetic calorimeter	48
¹¹⁵	4.4 Hadronic calorimeter	51
¹¹⁶	4.5 Muon chambers	54

¹¹⁷	5 The CMS trigger system	57
¹¹⁸	6 Event reconstruction	59
¹¹⁹	6.1 Track and primary vertex reconstruction	59
¹²⁰	6.2 The Particle Flow Algorithm	61
¹²¹	6.2.1 Reconstruction of the Particle Flow inputs	62
¹²²	6.2.2 Particle Flow identification	64
¹²³	6.3 Pile-up removal	68
¹²⁴	6.3.1 Charged Hadron Subtraction	68
¹²⁵	6.3.2 Pile up per particle identification (PUPPI)	68
¹²⁶	6.4 Jet reconstruction	70
¹²⁷	6.4.1 Jet clustering	70
¹²⁸	6.4.2 PF jets in CMS	72
¹²⁹	6.4.3 Jet energy corrections	73
¹³⁰	6.5 Jet substructure reconstruction	75
¹³¹	6.5.1 Grooming	76
¹³²	6.5.2 N-subjettiness	80
¹³³	6.5.3 Vector boson tagging	82
¹³⁴	6.6 Monte Carlo Event Generators	85
¹³⁵	III Diboson resonance searches in CMS	87
¹³⁶	7 Search I: First search for diboson resonances at 13 TeV	89
¹³⁷	7.1 A small bump	91
¹³⁸	7.2 Analysis strategy	92
¹³⁹	7.3 Data and simulated samples	94
¹⁴⁰	7.4 Event selection	95
¹⁴¹	7.4.1 Triggering	95
¹⁴²	7.4.2 Preselection	97
¹⁴³	7.4.3 Vector boson tagging	99
¹⁴⁴	7.4.4 Analysis categorization	106
¹⁴⁵	7.5 Background modeling	111
¹⁴⁶	7.6 Signal modeling	114
¹⁴⁷	7.7 V-tagging scale factors	115
¹⁴⁸	7.7.1 Event selection	115

149	7.7.2	Fitting procedure	119
150	7.7.3	Systematic uncertainties	122
151	7.7.4	Fit results	124
152	7.7.5	Impact on search variables	125
153	7.8	Systematic uncertainties	126
154	7.9	Results	127
155	7.10	Limits	127
156	7.10.1	All-hadronic analysis only	127
157	7.10.2	Semi-leptonic and all-hadronic combination	128
158	8	Search II: A new pileup resistant and perturbative safe tagger	135
159	8.1	Towards robust boosted jet tagging	137
160	8.2	Analysis strategy	138
161	8.3	Data and simulated samples	139
162	8.4	Event selection	139
163	8.4.1	Triggering	140
164	8.4.2	Preselection	140
165	8.5	Developing a new W-tagger	144
166	8.5.1	Dedicated PUPPI softdrop jet mass corrections	145
167	8.5.2	W-tagging performance	149
168	8.5.3	Efficiency scale factors, jet mass scale and resolution	151
169	8.5.4	W-tagging mistag rate measurement	154
170	8.6	Mass and purity categorization	157
171	8.7	Background modeling	158
172	8.8	Signal modeling	160
173	8.9	Systematic uncertainties	161
174	8.10	Results	162
175	8.10.1	Early analysis	162
176	8.10.2	Full 2016 dataset	162
177	9	Search III: A novel framework for multi-dimensional searches	173
178	9.1	Small bumps and tri-bosons	175
179	9.2	Analysis strategy	177
180	9.3	Data and simulated samples	178
181	9.4	Event selection	178
182	9.5	Triggering	180

183	9.5.1 Trigger turn-on modeling	181
184	9.6 A mass- and p_T -decorrelated tagger	184
185	9.6.1 Data to simulation scale factors	189
186	9.6.2 p_T -dependence	192
187	9.7 The multidimensional fit	195
188	9.7.1 Modeling of the signal	196
189	9.7.2 Modeling of the non-resonant background	199
190	9.7.3 Modeling of the resonant background	203
191	9.8 Systematic uncertainties	208
192	9.9 Background model validation	211
193	9.9.1 Variations of QCD multijet predictions	211
194	9.9.2 Fit to data control region	211
195	9.9.3 Bias test in pseudodata	212
196	9.10 Results	224
197	9.10.1 Limits	227
198	9.10.2 Pulls of nuisance parameters	231
199	10 Summary	235
200	IV Encoding jet substructure in a deep neural network	239
201	11 A Lorentz invariance based Deep Neural Network for W-tagging	243
202	11.1 LoLa	243
203	11.1.1 Architecture	244
204	11.1.2 Input	244
205	11.1.3 The Combination Layer	247
206	11.1.4 The Lorentz Layer	249
207	11.2 Performance	251
208	11.3 Dependence on jet mass and p_T	252
209	11.3.1 p_T -decorrelation	253
210	11.3.2 Mass sculpting	255
211	11.4 Validation	257
212	12 Summary	261

213	V Final conclusions and outlook	263
214	A V-tagging	269
215	A.1 mMDT and underlying event	270
216	A.2 N-subjettiness on groomed jets	271
217	B Search I: Limits per mass category	275
218	B.1 Limits per mass category	276
219	C Search II	285
220	C.1 W-tagging scale factor: Additional plots	286
221	C.2 Efficiency scale factors for 2.5 fb^{-1}	288
222	C.3 Background fit checks	290
223	C.3.1 Background fit checks in data sideband	291
224	C.3.2 Background fit checks in QCD MC	298
225	C.4 F-test in signal region	302
226	D Search III	307
227	D.1 Signal fits	308
228	D.2 2016 kernels	309
229	D.3 Resonant background	309

Introduction

230

231 The Standard Model of particle physics (SM) is one of the greatest accomplishments of fundamen-
232 tal science. The degree to which it can accurately predict observed phenomena is unprecedented,
233 and it has allowed us to incorporate all of particle physics into one single equation that explains
234 what we can see in the world around us. However, it has some shortcomings. One major problem
235 is that the Standard Model and gravity are incompatible at very high energies and that any
236 incorporation of gravity into a quantum field theory framework results in a non-renormalizable
237 theory. The SM also fails to explain why gravity is so much weaker than the electromagnetic
238 and nuclear forces. This, together with a few other problems, has lead scientists to search for
239 extensions to the Standard Model, commonly referred to as *Beyond Standard Model physics*
240 (BSM). These models are usually accompanied by predicted observables not included in the
241 Standard Model, where the observation of these, or the lack thereof, is a way of falsifying or
242 supporting the model.

243

244 In this thesis, I look for such observables by searching for new massive particles predicted
245 by SM extensions. These particles have the property that they can decay into vector bosons, W^\pm
246 and Z^0 , and usually have a very small interaction probability. The vector bosons are heavy and
247 unstable and will quickly decay into leptons or quarks. In order to counterbalance the small
248 interaction probability associated with generating such a new heavy particle, a final state with
249 two vector bosons decaying hadronically is required since the branching ratio for a vector boson
250 decaying to hadrons is significantly higher than that into leptons. This final state is complicated
251 by the presence of an overwhelming QCD multijet background and the fact that, due to the high
252 mass of the resonance, the vector bosons are highly energetic and their quark decay products get
253 merged into a single jet due to the small angular opening between them. The latter offers an
254 opportunity to distinguish between vector boson jets and jets coming from a quark or a gluon due
255 to the expected differences in jets mass and geometrical substructure within the jet. Algorithms
256 designed to improve the jet mass resolution and resolve jet substructure are commonly referred to

257 as *jet substructure methods*. These will be a recurring topic of this thesis due to my own personal
258 contributions to the field.

259

260 Three searches for heavy resonances decaying to dibosons in the all-hadronic final state will
261 be presented. The first analysis to be discussed was the first of its kind to be performed at a
262 center-of-mass energy of $\sqrt{s} = 13 \text{ TeV}$ and the first published result to take advantage of jet
263 substructure at trigger level. The second led to the development of a novel pileup robust and
264 perturbative safe vector boson tagging algorithm, which afterwards became the default tagging
265 algorithm in CMS. Finally, the third search introduces a completely new way of doing diboson
266 searches in a multi-dimensional space, allowing for the incorporation of all VV, VH and HH
267 searches (where V = W,Z and H = Higgs boson) into one common framework, as well as any
268 generic search for resonances peaking in jet mass and dijet invariant mass.

269

270 In addition to the tree searches, I will present a deep neural network for vector boson tag-
271 ging intended to improve the analysis sensitivity for future searches. In this algorithm, jet
272 clustering and substructure-like variables are embedded into the neural network layers themselves.
273 That makes it a good starting point in the development of a generic anti-QCD tagger capable
274 of distinguishing between the QCD background and any signal with some geometrical substruc-
275 ture peaking in the jet groomed mass spectrum. Such a tagger would, in combination with the
276 multidimensional fit framework, lead to a completely new way of doing model independent searches.

277

278 This thesis is organized in five parts. Part I provides the theoretical background and moti-
279 vation for the searches presented here. First, the Standard Model is introduced together with a
280 discussion of its known shortcomings, followed by a chapter presenting two possible extensions to
281 the Standard Model, both of which are probed in this thesis. Part II consists of a description of
282 the experimental setup used to collect the data which is analyzed here, as well as the different
283 algorithms used in order to reconstruct each event. Part I and Part II mainly consist of work
284 done by others which has been vital for the completion of this work. The remaining three parts
285 are dedicated to my own personal contributions. In Part III, the three searches described above
286 are presented in chronological order, each with a personal introduction motivating the analysis in
287 question. Following this, in Part IV, the deep neural network based vector boson tagger for future
288 analyses will be presented. Both parts end with their own concluding summary and outlook, in
289 Section 10 and Section 12. In Part V, a final summary of the obtained results and a discussion of
290 the future for the analysis is given.

291

Part I

292

Theoretical background

293

CHAPTER 1

294

The Standard Model

295 Everything this thesis is built on has its roots in the Standard Model (SM). The Standard Model
296 of particle physics addresses the question *What is matter made of?* on the smallest possible scale.
297 It links the fundamental constituents of the universe together along with the forces that bind
298 them, in order to describe and predict the laws of nature. The Standard Model is formulated as a
299 quantum field theory, where the fundamental particles are spin-1/2 fermions which interact with
300 one another through the exchange of spin-1 gauge bosons. These interactions come in three forms,
301 mediated by three different types of gauge bosons: The electromagnetic force, mediated through
302 photons; the weak force, mediated through W and Z bosons; and the strong force, mediated by
303 gluons. How the fundamental particles interact also defines which properties they exhibit. In
304 addition, the Standard Model includes a field very different from the others, the Higgs field. The
305 Higgs field interacts with both fermions and bosons and is what gives all particles their mass.
306 One thing the Standard Model fails to incorporate is the force of gravity. This shortcoming is one
307 of the main motivations for looking for alternative models beyond the Standard Model (BSM),
308 which is the main topic of this thesis.

309 **1.1 Fundamental particles: quarks and leptons**

310 It appears that all matter in the universe can be described by a very small collection of fundamental
311 particles, six leptons and six quarks. These are collectively called fermions and are, as far as
312 we can tell, truly elementary (not composed of any other particles). Leptons are particles with
313 integer or zero electric charge, defined in units of electron charge. They come in three flavors, or
314 generations, and their mass increases with generation. Each generation of leptons consists of two
315 particles: one charged lepton and one neutrally charged particle denoted as *neutrino* (ν). The

³¹⁶ three generations can be arranged in a doublet structure, and are as follows.

$$\begin{pmatrix} \nu_e \\ e \end{pmatrix} \quad \begin{pmatrix} \nu_\mu \\ \mu \end{pmatrix} \quad \begin{pmatrix} \nu_\tau \\ \tau \end{pmatrix} \quad (1.1)$$

³¹⁷ The charged leptons can be positively or negatively charged, defined in units of electron charge ³¹⁸ e . By convention the leptons of matter are negatively charged, e^- , μ^- , and τ^- , whereas the ³¹⁹ positively charged leptons, e^+ , μ^+ , and τ^+ are considered their anti-particles. A summary of the lepton properties is listed in Table 1.1. Leptons interact with one another through the

Lepton	Mass	Charge
e^-	0.51 MeV	e
μ^-	105.7 MeV	e
τ^-	1776.9 MeV	e
$\nu_i, i = e, \mu, \tau$	$\sum_i m_i < 0.170$ eV	0

Table 1.1: Lepton Properties [1, 2].

³²⁰

³²¹ *electromagnetic and weak forces*, which will be explained in more detail in Section 1.2.2. ³²² The other six fundamental particles of matter are the *quarks*. They are distinguished from the ³²³ leptons in that they, in addition to interacting through the weak and electromagnetic forces, ³²⁴ interact with one another through the *strong force*, described in Section 1.2.1. This force binds ³²⁵ the quarks together to form baryons (like protons and neutrons) or mesons (like pions), and in ³²⁶ addition, keeps the quarks from being observed as free particles such that they are only visible ³²⁷ through their baryon or meson bound states (commonly referred to as *hadrons*). Also organized ³²⁸ in three generations, the six quarks are called *up*, *down*, *charm*, *strange*, *top* and *bottom*, and are ³²⁹ organized in flavor doublets as follow

$$\begin{pmatrix} u \\ d \end{pmatrix} \quad \begin{pmatrix} c \\ s \end{pmatrix} \quad \begin{pmatrix} t \\ b \end{pmatrix} \quad (1.2)$$

³³⁰ Each quark comes with a fractional charge of $\frac{2}{3}$ (u, c and t) and $-\frac{1}{3}$ (d, s and b) of one electron ³³¹ charge. As with the leptons, there are also distinct particles of opposite charge, anti-quarks. ³³² Some of the quark properties are listed in Table 1.2.

³³³ These 12 fermions, together with their corresponding anti-particles, represent the fundamental ³³⁴ particles of the universe and constitute all matter around us. There are four fundamental forces ³³⁵ that we know of: gravity, electromagnetism, the weak force and the strong force. Gravity is ³³⁶ extremely weak compared to the other forces and we currently lack a quantum field theory of

Quark	Mass	Charge
u	1 – 5 MeV	$\frac{2}{3}e$
d	3 – 9 MeV	$-\frac{1}{3}e$
c	1.15 – 1.35 GeV	$\frac{2}{3}e$
s	75 – 170 MeV	$-\frac{1}{3}e$
t	172.4 ± 0.1 GeV	$\frac{2}{3}e$
b	4.0 – 4.4 GeV	$-\frac{1}{3}e$

Table 1.2: Quark Properties

its interaction, therefore it is typically ignored in high energy physics experiments. All particles that are electrically charged, the charged leptons (e , μ and τ) and all of the quarks, interact through the electromagnetic force. These interactions are governed by the laws of Quantum Electrodynamics (QED), and are mediated through the massless and electrically neutral spin-1 photon. All of the fermions, including the electrically neutral neutrinos, feel the weak force and undergo weak interactions. The weak force is mediated through the vector bosons W^+ , W^- and Z^0 , which are heavy charged particles with a spin of 1. Finally, there is the strong force, mediated by the massless and electrically neutral spin-1 gluon. Only quarks interact via the strong force, and it is that interaction that makes the quarks so fundamentally different from leptons and neutrinos. Their interaction is governed by the laws of Quantum Chromodynamics (QCD). All of these interactions can be represented in one common gauge theory, the Standard Model.

1.2 The Standard Model Lagrangian

The Standard Model is a quantum gauge field theory in which each particle is described as a dynamical field with a value at each space-time coordinate. These fields are governed by a Lagrangian density function, the Standard Model. For instance, the Lagrangian density of a free fermion, one not interacting with any other fields, is

$$\mathcal{L} = \bar{\Psi}(x^\mu)(i\lambda^\mu \partial_\mu - m)\Psi(x^\mu) \quad (1.3)$$

where $\Psi(x^\mu)$ represents any spin-1/2 fermion field, also called *Dirac field*, as a function of space-time; $\bar{\Psi} = \Psi^\dagger \gamma_0$, where γ^0 is one of the gamma matrices γ^μ and is included in order to make $\bar{\Psi}\Psi$ invariant under Lorentz transformation; and m is the mass of the fermion in question. Any interaction between the fundamental particles due to the fundamental forces, can be described as variations in the Lagrangian of quantum fields and are represented as additional terms in the

³⁵⁸ equation above.

³⁵⁹ Being a gauge theory, the Standard Model has the property of gauge invariance, meaning
³⁶⁰ that measurable quantities stay the same despite the fields themselves changing. If observables
³⁶¹ stay the same after a field transformation, there is a symmetry in the system. The symmetries
³⁶² of the Standard Model arise due to the fact that fermions of a given type are indistinguishable
³⁶³ from one another. These symmetries result in the presence of *force mediators*, which arise
³⁶⁴ as a representation of infinitesimal generators of some symmetry group. The fermion fields
³⁶⁵ can be arranged as particle multiplets where one transforms into the other under a symmetry
³⁶⁶ transformation. A symmetry transformation produce rotations between the particles of a given
³⁶⁷ multiplet, but never to a field outside of that group. The symmetry group of the Standard Model
³⁶⁸ is the direct product

$$SU(3)_C \otimes SU(2)_L \otimes U(1)_Y. \quad (1.4)$$

$SU(3)_C$ is the color (C) symmetry allowing the rotation of quarks, arranged in color multiplets, into one another, corresponding to interactions produced by the strong force. The colors are denoted as red, green and blue. $SU(2)_L \otimes U(1)_Y$ represent the electroweak force with weak left-handed isospin L and weak hypercharge Y symmetries, acting on L and Y multiplets, respectively. The particle multiplets of the Standard Model can then be written as $\mathcal{G}_{SM} \ni x = (C, L)_{(Y)}$ and are (for illustrations only for the the 1st generation):

$$Q = (3, 2)_{(1/3)} = \begin{pmatrix} u_r & u_g & u_b \\ d_r & d_g & d_b \end{pmatrix} \sim \text{quark multiplet} \quad (1.5)$$

$$L = (1, 2)_{(-1)} = \begin{pmatrix} \nu_e & e \end{pmatrix} \sim \text{leptonic doublet} \quad (1.6)$$

$$u^c = (\bar{3}, 1)_{(-4/3)} = \begin{pmatrix} u_r^c & u_g^c & u_b^c \end{pmatrix} \sim \text{anti-up quarks} \quad (1.7)$$

$$d^c = (\bar{3}, 1)_{(2/3)} = \begin{pmatrix} d_r^c & d_g^c & d_b^c \end{pmatrix} \sim \text{anti-down quarks} \quad (1.8)$$

$$e^c = (1, 1)_{(2)} \sim \text{positron} \quad (1.9)$$

$$(1.10)$$

³⁶⁹ The right-handed neutrino (which in needed to generate a Dirac mass for the neutrinos) is not
³⁷⁰ included here because it is a SM *singlet* and does not transform under the SM group \mathcal{G}_{SM} , but
³⁷¹ it could be written as $\nu^c = (1, 1)_{(0)}$. The positron e^c , on the other hand, is included as its
³⁷² hypercharge is non-zero and it therefore undergoes $U(1)_Y$ interactions. These five multiplets exist
³⁷³ for each of the three generations.

³⁷⁴ The numbers representing each multiplet correspond to which representation it belongs to. For

375 instance, we see that the quark multiplet transforms as a triplet under $SU(3)_C$, a doublet under
 376 $SU(2)_L$ and has a non-zero hypercharge, corresponding to a non-trivial representation under
 377 $U(1)_Y$. That corresponds to saying that quarks interact through all of the three fundamental
 378 interactions. From that notation, it is also clear that leptons do not carry color charge, and will
 379 only interact via the electroweak interactions.

380 From the multiplets above, we see that u^c and d^c transform as singlets under $SU(2)_L$, meaning
 381 they do not interact. This, however, does not mean they do not feel the electroweak force. The
 382 electroweak gauge bosons W and Z are not directly part of $SU(2)_L$, rather, they are a linear
 383 combination of $SU(2)_L$ and $U(1)_Y$ and anything with a non-zero weak hypercharge Y will interact
 384 with them. This is also true for the photon, which also is a linear combination of $SU(2)_L$ and
 385 $U(1)_Y$. These interactions; the strong, weak and electromagnetic, will be explained in more detail
 386 in the following sections.

387 1.2.1 The quantum chromodynamics sector

388 The group $SU(3)_C$ describes the strong interaction mediated by gluons, and is described by
 389 the quantum gauge theory Quantum Chromodynamics (QCD). The group is generated by
 390 8 linearly independent matrices $T^a = \frac{\lambda^a}{2}$, where λ^a are the Gell-Mann matrices [3]. The
 391 generator matrices do not commute with one another, but rather satisfy the commutation relation
 392 $[\lambda^i/2, \lambda^j/2] = if^{ijk}\lambda_k/2$. This property makes the $SU(3)_C$ group *non-Abelian*, which consequently
 393 results in the gluons themselves being charged and displaying self-interactions. Gluons are charged
 394 with one unit of color and one unit of anti-color. Quarks, the only fundamental particles interacting
 395 with the strong force, are arranged in the simplest representation of $SU(3)$ and come with one
 396 unit of color or anti-color.

397 The generators are collectively referred to as the *group representation* of $SU(3)_C$. Any
 398 group element can be written as $e^{-i\theta^a g_a}$, where a runs from 1 to 8, θ^a are real numbers
 399 and g_a represent one of the eight linearly independent $\lambda/2$ matrices (generators). Given one
 400 representation, one can always find another one through any local gauge transformation that
 401 leaves the commutator unchanged. In this case, the group elements are the quark fields, and a
 402 local gauge transformation of fields becomes

$$\Psi(x^\mu) \rightarrow e^{-ig_s\theta^a(x^\mu)T^a} \Psi(x^\mu), \quad (1.11)$$

403 where g_s is the strong coupling, $\theta^a(x^\mu)$ some arbitrary function and a runs over the eight
 404 generators of the group. In order to keep the Lagrangian in Equation 1.3 invariant under such a
 405 transformation, an additional term must be added, replacing the partial derivative ∂_μ with the

406 covariant derivative

$$D_\mu = \partial_\mu + ig_s A_\mu^a T^a, \quad (1.12)$$

407 introducing a tensor A_μ^a that represents the 8 gluon fields. The QCD Lagrangian then becomes

$$\mathcal{L}_{QCD} = -\frac{1}{4} F_a^{\mu\nu} F_{\mu\nu}^a + \bar{\Psi}(x^\mu)(i\lambda^\mu D_\mu - m)\Psi(x^\mu), \quad (1.13)$$

408 where $F_{\mu\nu}^a$ is the gauge field of the group, the gluon field tensor

$$F_{\mu\nu}^a = \partial_\mu A_\nu^a - \partial_\nu A_\mu^a + g_s f^{abc} A_\mu^b A_\nu^c. \quad (1.14)$$

409 The first term in Equation 1.13 represents the quark-gluon interaction, leading to vertices like
 410 the one on the left in Figure 1.1. The second, the gluon field kinetic term, picks up the *structure*
 411 *constant* f^{abc} due to the commutation relation of the λ matrices. This term creates self-interactions
 between the gluon fields, like the two shown on the right in Figure 1.1. These self-interactions

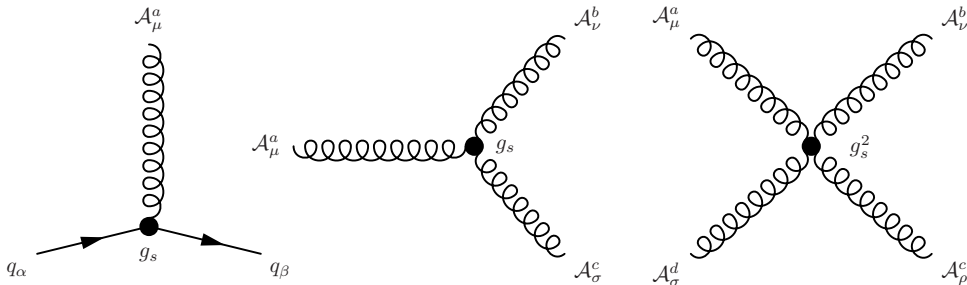


Figure 1.1: The QCD interaction vertices: quark interaction with the gluon field (left), and three-gluon (middle) and four-gluon (right) self-interaction vertices.

412
 413 have severe consequences: any bare color charge, like a quark, will be surrounded by a sea of
 414 virtual gluons and quarks that share the same color. When probing the quark color at higher
 415 and higher energies, corresponding to shorter and shorter distances, the color charge decreases
 416 until only the bare charge is visible. There, the quarks are essentially free and can be observed as
 417 distinguishable particles. This property is referred to as *asymptotic freedom*. For the same reasons,
 418 when going further and further away from a bare color charge, the sea of charges surrounding
 419 it makes the observed charge increase. That results in a strong attractive force between color
 420 charges at large distances, where the potential energy between the two grows linearly with the
 421 distance between them as

$$V(r) = -\frac{4\alpha_s}{3r} + kr, \quad (1.15)$$

422 where r is the distance between the quarks and α_s is the coupling strength of QCD. When the

423 distance between the quarks grows very large, this potential energy is enough to create real
 424 quark-antiquark pairs from the vacuum in order to reduce the potential energy, a process called
 425 *fragmentation*. Whenever one tries to separate quarks from one another they will fragment,
 426 which consequently means that quarks are never observed on their own. Rather, they form
 427 colorless (uncharged under the color charge) bound states of mesons or baryons (collectively
 428 called hadrons), a property called *color confinement*. The energy for which the confinement into
 429 hadrons occurs, also called *hadronization*, is defined through experimental measurement and
 430 found to be $\Lambda_{QCD} = 100 - 500$ MeV (around the mass of the lightest hadrons). The effective
 431 charge between the quarks, α_S , changes as a function of energy as

$$\alpha_S(Q) = -\frac{6\pi}{33 - 2n_f} \ln(Q/\Lambda_{QCD}) \quad (1.16)$$

432 where Q is the energy of the probe used to measure the charge and n_f is the number of quark
 433 flavors (u, d, c, s, b, t) at that energy. The value α_S is around 0.1 for energies between 100-1000
 434 GeV.

435 1.2.2 The electroweak sector

436 The electromagnetic and weak interactions arise from the breaking of $SU(2)_L \otimes U(1)_Y$ symmetry.
 437 While the unification of the electromagnetic and weak force is obtained under the $SU(2)_L \otimes U(1)_Y$
 438 group, the predicted gauge bosons of such a group are not observed in nature: three charged
 439 massless vector bosons and one neutral massless boson. Rather, the W^\pm , Z^0 and the photon arise
 440 from the spontaneous symmetry breaking of $SU(2)_L \otimes U(1)_Y$ to $U(1)_{EM}$. This happens due to
 441 the *Higgs mechanism*, and exactly how this occurs will be the topic of Section 1.2.3.

442 The symmetry under $SU(2)_L$ is called weak left-handed isospin L , and the symmetry under
 443 $U(1)_Y$ is the weak hypercharge Y . The name “left-handed” arise from the fact that *parity* is
 444 violated in the electroweak interactions. All the fundamental fermions have a *chirality*, defined
 445 as the projection of the particles spin along its direction of motion. Charged weak interactions
 446 are only observed for fermions of left-handed chirality (vector minus axial coupling, V-A). While
 447 the left-handed fermion fields are in the simplest doublet representation of $SU(2)$ with weak
 448 isospin $I = 1/2$, the fermions of right-handed chirality are therefore in the singlet representation
 449 with weak isospin $I = 0$, meaning they do not interact with the gauge bosons of $SU(2)_L$. The
 450 chirality of any fermion Ψ can be defined through the operator γ^5 , the product of the four Dirac
 451 matrices [4] $\gamma^5 = i\gamma^1\gamma^2\gamma^3\gamma^4$. Any fermion field can be projected into its chiral components Ψ_L or

⁴⁵² Ψ_R through the projection operation

$$\Psi_L = \frac{1 - \gamma^5}{2} \quad \text{and} \quad \Psi_R = \frac{1 + \gamma^5}{2}. \quad (1.17)$$

The gauge field tensor of the group of $SU(2)_L$ symmetry is $W_{\mu\nu}^a$, where a runs over the 3 generators of the group. The conserved charge associated with the group is the *third* component of weak isospin I_3 , and all weak interactions must preserve I_3 . The generators of the group are defined as $T_i = \frac{\sigma_i}{2}$, where σ_i are the Pauli matrices [5]. As for $SU(3)_C$, the group is non-abelian and the generators follow the commutation relation $[\sigma_i/2, \sigma_j/2] = i\epsilon_{ijk}\sigma_k/2$, where ϵ_{ijk} is the Levi-Civita permutation symbol [6]. This in turn implies self-interactions between the gauge bosons of the group. The latter group, $U(1)_Y$ of weak hypercharge Y , is abelian and hence displays no self-interaction. The gauge field tensor $B_{\mu\nu}^a$ interacts with both left- and right-handed fermion fields. Similar to the case for QCD, a local gauge transformation of $SU(2)_L \otimes U(1)_Y$ requires the addition of additional terms in the derivative in order to keep the Lagrangian invariant. The partial derivative ∂_μ is replaced by the covariant derivatives

$$D_\mu \Psi_L = (\partial_\mu + ig_2 T_a W_\mu^a + ig_1 \frac{Y}{2} B_\mu^a) \Psi_L \quad (1.18)$$

$$D_\mu \Psi_R = (\partial_\mu + ig_1 \frac{Y}{2} B_\mu^a) \Psi_R. \quad (1.19)$$

⁴⁵³ After the substitution, the electroweak Lagrangian can be written as a sum of four terms:

$$\mathcal{L}_{EW} = \mathcal{L}_{gauge} + \mathcal{L}_f + \mathcal{L}_{Yukawa} + \mathcal{L}_\phi. \quad (1.20)$$

⁴⁵⁴ The first term, \mathcal{L}_{gauge} , represent the kinetic field tensor and is

$$\mathcal{L}_{gauge} = -\frac{1}{4} W_a^{\mu\nu} W_{\mu\nu}^a - \frac{1}{4} \mathcal{B}^{\mu\nu} \mathcal{B}_{\mu\nu} \quad (1.21)$$

where the gauge field tensors are

$$W_{\mu\nu}^a = \partial_\mu W_\nu^a - \partial_\nu W_\mu^a - g_2 \epsilon^{ijk} W_\mu^j W_\nu^k, \quad \text{with } i = 1 - 3 \text{ and} \quad (1.22)$$

$$B_{\mu\nu} = \partial_\mu B_\nu - \partial_\nu B_\mu. \quad (1.23)$$

⁴⁵⁵ The non-abelian nature of $SU(2)_L$ leads to trilinear and quadrilinear couplings between the photon and vector bosons as illustrated in Figure 1.2.

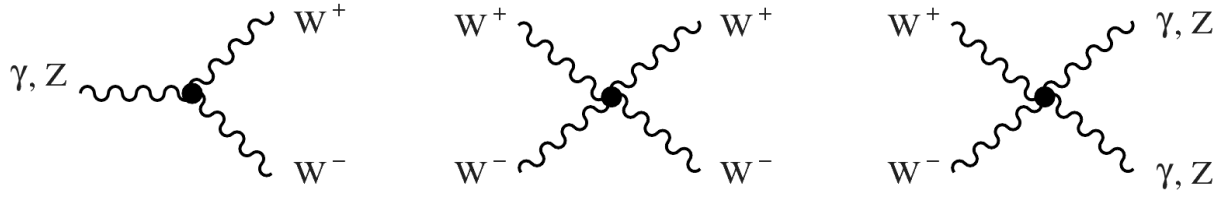


Figure 1.2: The electroweak self-interaction vertices: trilinear (left), and quadri-linear (middle and right) vertices.

457

The second term describe the boson fields coupling to fermions and is

$$\mathcal{L}_f = \bar{Q}_i i\lambda^\mu D_\mu Q_i + \bar{u}_i^c i\lambda^\mu D_\mu u_i^c + \bar{d}_i^c i\lambda^\mu D_\mu d_i^c + \bar{L}_i i\lambda^\mu D_\mu L_i + \bar{e}_i^c i\lambda^\mu D_\mu e_i^c, \quad (1.24)$$

458 where we have expressed each term using the particle multiplets in Equation 1.5 and the subscript
 459 i runs over the three fermion generations. They all interact differently under $SU(2)_L \times U(1)_Y$
 460 due to their different charges.

461 Up until now we have considered the Lagrangian before spontaneous symmetry breaking, where
 462 we have three charged massless bosons and one massless neutral boson, a constellation we know to
 463 be wrong from observations. When I have referred to interaction vertices, I have loosely referred
 464 to W , Z and γ vertices without explicitly defining them. We will show in Section 1.2.3 that,
 465 due to spontaneous symmetry breaking, the charged gauge boson fields W^\pm in reality are linear
 466 combinations of W_μ^1 and W_μ^2 given as

$$W^\pm = \frac{1}{\sqrt{2}}(W_\mu^1 \mp iW_\mu^2). \quad (1.25)$$

467 These are responsible for *charged-current interactions*, which turn up-type fermions into their
 468 corresponding down-type fermions within the same generation, and vice-versa. The electrically
 469 neutral Z boson and the photon fields are expressed in terms of W_μ^3 and B_μ through the weak
 470 mixing angle [7] as

$$\begin{pmatrix} \gamma \\ Z^0 \end{pmatrix} = \begin{pmatrix} \cos \theta_W & \sin \theta_W \\ -\sin \theta_W & \cos \theta_W \end{pmatrix} \begin{pmatrix} B \\ W^3 \end{pmatrix} \quad (1.26)$$

471 where θ_W can be expressed through the $SU(2)_L$ and $U(1)_Y$ couplings g_1 and g_2 as

$$\cos \theta_W = \frac{g_1}{\sqrt{g_1^2 + g_2^2}} \quad \text{and} \quad \sin \theta_W = \frac{g_2}{\sqrt{g_1^2 + g_2^2}}. \quad (1.27)$$

⁴⁷² The electric charge is defined through weak isospin and hypercharge, and is

$$Q = I_3 + \frac{Y}{2}. \quad (1.28)$$

⁴⁷³ A few of the fermion-boson vertices are shown in Figure 1.3.

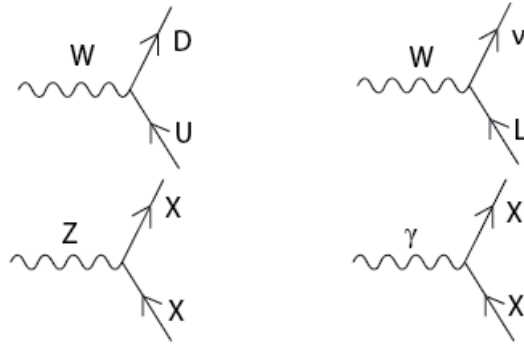


Figure 1.3: The electroweak fermion interaction vertices. Top: charged-current interaction vertex connecting a charged vector boson W^\pm to quarks (left) and leptons (right). Bottom: neutral-current interactions between the neutral Z^0 boson and any fermion (left), and between a γ and electrically charged fermions.

⁴⁷⁴ The last two terms, \mathcal{L}_{Yukawa} and \mathcal{L}_ϕ , are related to the Higgs boson and represent couplings
⁴⁷⁵ to the Higgs field: the Yukawa interaction term which generates masses for the fermions due to
⁴⁷⁶ the non-zero Higgs vacuum expectation value, and the Higgs bosons interactions with itself and
⁴⁷⁷ with the gauge bosons. Introduced as an extension to the original Standard Model, the Higgs
⁴⁷⁸ sector is one of the greatest accomplishments of particle physics in the 20th century and one of
⁴⁷⁹ the reasons why the LHC was built. How it arises is what we will turn to next.

⁴⁸⁰ 1.2.3 The Higgs sector

⁴⁸¹ The problem of having massless gauge bosons under $SU(2)_L \times U(1)_Y$, while observing massive W
⁴⁸² and Z bosons, was independently solved by three different groups and has become known as the
⁴⁸³ Englert–Brout–Higgs–Guralnik–Hagen–Kibble mechanism of spontaneous symmetry breaking [8–
⁴⁸⁴ 10], an accomplishment for which Peter Higgs and Francois Englert shared the 2013 Nobel Prize.
⁴⁸⁵ It began with the realization that the breaking of a local gauge symmetry could give rise to a final
⁴⁸⁶ mass for the gauge boson involved. This was first discovered in association with superconductivity,
⁴⁸⁷ where it was found that when a normal metal becomes superconducting the photon field inside
⁴⁸⁸ the superconductor would acquire a finite mass [11].

⁴⁸⁹ Spontaneous breaking of a global gauge symmetry

⁴⁹⁰ In order to achieve spontaneous symmetry breaking, Jeffrey Goldstone [12] suggested introducing
⁴⁹¹ a massive complex scalar field ϕ with quantum numbers of the vacuum and then giving the field
⁴⁹² a vacuum expectation value. The field

$$\phi = \frac{1}{\sqrt{2}}(\phi_1 + i\phi_2) \quad (1.29)$$

⁴⁹³ would have a Lagrangian of the form

$$\mathcal{L} = \partial^\mu \bar{\phi} \partial_\mu \phi - \mu_0^2 \bar{\phi} \phi - \frac{\lambda_0}{6} (\bar{\phi} \phi)^2, \quad (1.30)$$

⁴⁹⁴ where λ_0 is the coupling constant and μ_0 is the mass. The Lagrangian is invariant under $U(1)$,
⁴⁹⁵ though in this case under a global symmetry and not a local one. If one takes μ_0^2 to be negative,
⁴⁹⁶ the potential will get a minima along a circle of radius v such that

$$\phi_1^2 + \phi_2^2 = v^2 \quad \text{and} \quad v^2 = \frac{\mu_0^2}{\lambda_0}, \quad (1.31)$$

and take the form of a “Mexican Hat” as shown in Figure 1.4. The variable v is referred to as the

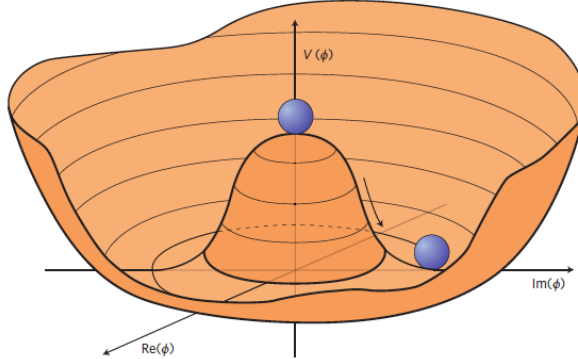


Figure 1.4: The potential $V(\phi)$ for a complex scalar field with $\mu_0^2 < 0$ [13].

⁴⁹⁷

⁴⁹⁸ vacuum expectation value (VEV). The lowest value of the Hamiltonian is now at $\phi = v$ rather
⁴⁹⁹ than at $\phi = 0$. Goldstone then translated the field to a minimum energy position $\phi' = \phi + v$ and
⁵⁰⁰ gave the field a vacuum expectation value, effectively breaking the symmetry between the two
⁵⁰¹ field components, but keeping the Lagrangian invariant. This complex field can be expanded
⁵⁰² around the ground state in terms of two real fields η and ϵ that represent deviations from the

503 minimum:

$$\phi(x) = \frac{1}{\sqrt{2}} * (v + \eta(x) + i\epsilon(x)) \quad (1.32)$$

504 The Lagrangian then becomes

$$\mathcal{L} = \frac{1}{2}(\partial_\mu\epsilon)^2 + \frac{1}{2}(\partial_\mu\eta)^2 + \mu_0^2\eta^2 + \text{additional terms.} \quad (1.33)$$

505 The third term has the form of a mass term for the scalar η field. However, the ϵ field has no mass
 506 term, meaning that the theory contains a massless scalar, referred to as a *Goldstone boson*. This
 507 is expressed through *Goldstone's theorem*, which states that whenever a continuous symmetry of
 508 a physical system is spontaneously broken, massless scalars will occur. Rather than providing a
 509 mass term for the vector bosons, the theory acquired one massive scalar and one massless scalar
 510 not observed in nature, requiring the gauge theory of weak interactions to look for solutions
 511 elsewhere.

512 The Higgs mechanism

513 The solution to the problem came a few years later, in 1964, when spontaneous symmetry breaking
 514 of a *local* gauge symmetry was studied rather than a global. For a $U(1)$ symmetry, this requires
 515 the Lagrangian to be invariant under $\phi \rightarrow e^{i\theta(x)}\phi$, with the derivative replacement

$$D_\mu = \partial_\mu - ieA_\mu. \quad (1.34)$$

516 After translating the field ϕ to its true ground state and writing out the Lagrangian,

$$\mathcal{L} = \frac{1}{2}(\partial_\mu\epsilon)^2 + \frac{1}{2}(\partial_\mu\eta)^2 - v^2\lambda\eta^2 + \frac{1}{2}v^2e^2A_\mu A^\mu - ev, A_\mu\partial^\mu\epsilon - \frac{1}{4}F_a^{\mu\nu}F_{\mu\nu}^a \quad (1.35)$$

517 we see that the particle spectrum now contains a massless Goldstone boson ϵ , a massive scalar
 518 η and, finally, a massive vector A_μ with $m_A = ev$. Despite the success of having dynamically
 519 created the mass for the gauge field, one had to tackle the problem of the massless scalar. The
 520 solution was found through the realization that one of the fields was unphysical; by giving mass
 521 to the vector A_μ , the polarization degrees of freedom had increased from 2 to 3 through adding
 522 a longitudinal polarization. However, this should not be possible when simply translating field
 523 variables. It was found that through a simple gauge transformation with a different set of fields

$$A_\mu \rightarrow A_\mu + \frac{1}{ev}\partial_\mu\theta, \quad (1.36)$$

524 the Goldstone boson would disappear and turn into the longitudinal polarization of the massive
 525 gauge boson and that the theory was left with one massive vector gauge boson, A_μ , and another
 526 massive scalar, h . This is what is referred to as the *Higgs mechanism*.

527 **The Weinberg-Salam Model**

The final step is to formulate the Higgs mechanism such that the vector bosons W^\pm and Z^0 become massive, while the photon remains massless. To do so Sheldon Glashow, Abdus Salam, and Steven Weinberg (all awarded the 1979 Nobel Prize for electroweak unification), added a gauge-invariant term to the electroweak Lagrangian of the following form:

$$\mathcal{L}_{Higgs} = \left| (i\partial_\mu - g_2 T_a W_\mu^a - v g_1 \frac{Y}{2} B_\mu^a) \phi \right|^2 - V(\phi). \quad (1.37)$$

528 The ϕ_i has to belong to $SU(2) \times U(1)$ multiplets, and the simplest configuration corresponds to
 529 four fields in an isospin doublet of weak hypercharge $Y = 1$:

$$\phi = \begin{pmatrix} \phi^+ \\ \phi^0 \end{pmatrix} = \begin{pmatrix} \frac{\phi_1 + i\phi_2}{\sqrt{2}} \\ \frac{\phi_3 + i\phi_4}{\sqrt{2}} \end{pmatrix}. \quad (1.38)$$

530 To generate the necessary masses, the Higgs potential from the previous section is used, with a
 531 vacuum expectation value of

$$\phi_0 = \frac{1}{\sqrt{2}} \begin{pmatrix} 0 \\ v \end{pmatrix}. \quad (1.39)$$

532 This specific choice of charges, VEV and fields insure that the $U(1)_{em}$ symmetry with $Q = T^3 + \frac{Y}{2}$
 533 remains unbroken, keeping the photon massless. The three others break the symmetry and
 534 become massive gauge bosons: the W^+ , W^- and Z^0 . The mass terms for the gauge bosons finally
 535 become

$$M_W = \frac{1}{2} v g_1 \quad \text{and} \quad M_Z = \frac{1}{2} v \sqrt{g_1^2 + g_2^2}, \quad (1.40)$$

536 with the Weinberg angle θ_W defined as

$$\text{with } \frac{M_W}{M_Z} = \cos \theta_W. \quad (1.41)$$

537 As mentioned in Section 1.2.2, the fermions also get their masses through interacting with the
 538 Higgs field, corresponding to the \mathcal{L}_{Yukawa} term in the electroweak Lagrangian in Equation 1.20.
 539 This is done in the same way as for the bosons: an additional $SU(2) \times U(1)$ invariant term for

⁵⁴⁰ each generation is added, for instance for the electron:

$$-G_e \left[\begin{pmatrix} \bar{\nu}_e & \bar{e} \end{pmatrix}_L \begin{pmatrix} \phi^+ \\ \phi^0 \end{pmatrix} e^R + \bar{e}_R \begin{pmatrix} \phi^- & \bar{\phi}^0 \end{pmatrix} \begin{pmatrix} \nu_e \\ e \end{pmatrix}_L \right], \quad (1.42)$$

⁵⁴¹ where G_E is the electron coupling. We then spontaneously break the symmetry with

$$\phi = \frac{1}{\sqrt{2}} \begin{pmatrix} 0 \\ v + h(x) \end{pmatrix}, \quad (1.43)$$

⁵⁴² where the neutral Higgs field $h(x)$ is the only remnant of the Higgs doublet after spontaneous
⁵⁴³ symmetry breaking. After substitution, the final Lagrangian for the electron mass becomes

$$\mathcal{L}_{Yukawa}^e = -\frac{G_e}{\sqrt{2}} v (\bar{e}_L e_R + \bar{e}_R e_L) \left(1 + \frac{h}{v}\right). \quad (1.44)$$

⁵⁴⁴ We can choose G_e such that

$$m_e = -\frac{G_e v}{\sqrt{2}}, \quad (1.45)$$

⁵⁴⁵ and generate the electron mass as

$$\mathcal{L}_{Yukawa}^e = -m_e \bar{e} e - \frac{m_e}{v} \bar{e} e h. \quad (1.46)$$

⁵⁴⁶ In summary, all the fermion masses are generated through the interaction of the fermion fields
⁵⁴⁷ with the Higgs field. From the equation above, we see that the fermion masses are not predicted
⁵⁴⁸ from the theory as the coupling G is arbitrary. The Standard Model therefore cannot provide an
⁵⁴⁹ explanation for the difference in hierarchy between the couplings. We also see that the Lagrangian
⁵⁵⁰ contains an interaction term coupling the Higgs scalar to the fermions and that this term depends
⁵⁵¹ on the mass of the fermion. The Higgs boson therefore couples more strongly to heavy fermions
⁵⁵² than to lighter ones.

553

CHAPTER 2

554

Beyond Standard Model Physics

555 2.1 Shortcomings of the Standard Model

556 Despite being an extremely successful and predictive theory, the Standard Model has its short-
557 comings. The most obvious one is its failure to successfully unite with the gravitational force
558 at very high energies (or, correspondingly, short distances). Gravity is beautifully described in
559 General Relativity (GR) as a classical theory: a force caused by the curvature of space-time in
560 the presence of matter and energy. The theory does not utilize quantum fields and energy is not
561 quantized. The scales between the Standard Model, a quantum field theory (QFT), and General
562 Relativity are completely different: space-time is curved on astronomical scales, where the force of
563 gravity is measurable, while quantum field theories deal with things on the smallest possible scales,
564 where variations in space-time are essentially invisible. Hence, to the Standard Model, space-time
565 is approximately flat and gravity does not exist. In order to have an elegant unified theory
566 of all the forces, attempts have been made to have a quantum field theory of the gravitational
567 force by extending the Standard Model particle family to incorporate a particle to mediate the
568 gravitational force called the *graviton*, a massless gauge boson of spin-2. The problem is that
569 gravity is universally attractive, meaning nothing “cancels” it. That leads to loop divergences
570 that cannot be reabsorbed through renormalization and every effort of integrating gravity in the
571 SM in a renormalizable way has thus far failed. However, it has been shown that the Standard
572 Model and General Relativity are fully compatible in the low-curvature and low-energy regime,
573 and that GR is an inevitable consequence of the quantum mechanics of interacting gravitons.
574 The full non-linear structure of GR can be derived through QFT, yielding graviton couplings to
575 the SM which are uniquely determined. This has led to several proposals for extending the SM in
576 order to incorporate the force mediating gravitons.

577 In addition to the difficulties of incorporating gravity into a quantum field theory framework,
 578 problems occur at small distances at which quantum gravitational effects would become apparent,
 579 the Planck scale. This can be represented by the Planck mass, the mass of the smallest possible
 580 black hole. When comparing the Planck mass to the masses of the electroweak bosons W and Z,
 581 we find that the Planck mass is 10^{16} times heavier than the electroweak bosons, such that there
 582 is a *hierarchy* between the mass scales of gravity and the electroweak forces. The reason why
 583 this observed hierarchy occurs has to do with the Higgs vacuum expectation value (VEV): the
 584 Higgs field has a measured vacuum expectation value of 246 GeV and this is, as discussed in the
 585 section above, what gives the W and Z bosons their mass. However, when actually calculating
 586 the Higgs VEV and taking all loop corrections into account, it would receive corrections on the
 587 order of the Planck energy, yielding a Higgs boson mass 10^{16} times larger than observed. This is
 588 called the *hierarchy problem*. Quantum loop corrections of this magnitude only happen for scalar
 589 particles such as the Higgs boson. Fermions are protected from such divergences through their
 590 chiral structure, and gauge bosons are protected through gauge invariance. The question is then
 591 why the Higgs VEV, and consequently the Higgs, W and Z boson masses are so much smaller
 592 than the natural mass scale.

593 Of course, it is possible that the Higgs boson mass just happens to be 125 GeV due to some
 594 fine-tuned, large cancellations that keeps the mass from approaching the Planck mass, as is
 595 currently held by the Standard Model. However, this is neither very elegant nor very probable
 596 without a well-motivated reason why such a cancellation should occur. Rather, in order to resolve
 597 the problem of scales, theories Beyond the Standard Model (BSM) have been introduced. The
 598 theories that I will probe in this thesis are amongst those.

599 Two Beyond Standard Model theories will be considered in this thesis: Compositeness and
 600 extra dimensional theories. Compositeness attacks the hierarchy problem by assuming that the
 601 Standard Model breaks down at an energy between the weak and Planck scales and that, around
 602 the TeV scale, the Higgs boson no longer appears to be a single scalar particle but a composite
 603 state of two fermions. In the following, I will present the study of composite models in the context
 604 of the *Heavy Vector Triplet formalism*, described in Section 2.2.1. Warped extra dimensional
 605 theories on the other hand, attempt to solve the hierarchy problem by forcing gravity to be
 606 concentrated on another “brane” and letting its strength fall off exponentially through an extra
 607 dimension.

608 2.2 Compositeness

609 In composite Higgs models, the Higgs boson is assumed to be a bound state of fundamental
 610 constituents held together by some new strong force [14, 15]. This removes the hierarchy problem
 611 since we no longer have an elementary scalar in the Standard Model, hence no loop corrections
 612 going to infinity. The compositeness of the Higgs boson becomes apparent at the energy scale Λ ,
 613 where Λ has to be at least 10 TeV, since anything below that is ruled out by electroweak precision
 614 measurements. The Higgs boson is assumed to be a pseudo-Goldstone boson of some approximate
 615 symmetry, where pseudo-Goldstone bosons are bosons with a tiny mass that approach zero in
 616 the limit of the symmetry becoming exact. The approximate symmetry is broken at the scale
 617 f , where $\Lambda = 4\pi f$. Being a pseudo-Goldstone boson, the Higgs boson mass is protected from
 618 divergent quantum loop corrections up to the scale of compositeness and, above that scale,
 619 is no longer an elementary scalar. The theory is based on the breaking of two parallel global
 620 symmetries $[SU(2)_1 \times U(1)_1] \times [SU(2)_2 \times U(1)_2]$, with Goldstone bosons becoming the longitudinal
 621 components of the three predicted gauge bosons of the symmetry group W'^{\pm} and Z' . These have
 622 masses of the order of the compositeness scale

$$M(W'^{\pm}) \simeq M(Z') = \frac{g}{\sin 2\theta} f, \quad (2.1)$$

623 where $\tan \theta = g_1/g_2$, the ratio of couplings of the $SU(2)$ groups. The predicted decay widths are
 624 roughly the same for Z' and W' and are as follows:

$$\begin{aligned} \Gamma(W'^{\pm} \rightarrow \ell\nu, Z' \rightarrow \ell\ell) &= \frac{g^2 \cot^2 \theta}{96\pi} M \\ \Gamma(W'^{\pm} \rightarrow q\bar{q}', Z' \rightarrow q\bar{q}) &= \frac{g^2 \cot^2 \theta}{32\pi} M \\ \Gamma(W'^{\pm} \rightarrow WZ, Z' \rightarrow WW) &= \frac{g^2 \cot^2 2\theta}{192\pi} M. \end{aligned} \quad (2.2)$$

625 Decays into fermions therefore dominate at $\cot \theta \geq 1/2$, whereas decays into bosons are enhanced
 626 for very low $\cot \theta$. These generic composite models can be studied with the Heavy Vector Triplet
 627 formalism.

628 2.2.1 Heavy Vector Triplet formalism

629 There are many BSM theories that predict the presence of spin-1 particles with masses at the
 630 TeV scale, each with their own list of model parameters. In most cases, however, when looking for
 631 such new particles, experiments are not sensitive to the specifics of the model but only the masses

and couplings of the resonances. We can therefore start from a *simplified model* that describes the dynamics of the new spin-1 vector through a simple phenomenological Lagrangian that only retains couplings and mass. In the Heavy Vector Triplet formalism [16], a real vector V_μ^a , where r runs from 1 to 3, is introduced in the adjoint representation of $SU(2)L$ and represents one charged and one neutral heavy spin-one particle with charge eigenstates

$$V_\mu^\pm = \frac{V_\mu^1 \mp i V_\mu^2}{\sqrt{2}} \quad \text{and} \quad V_\mu^0 = V_\mu^3. \quad (2.3)$$

The simplified Lagrangian governing the dynamics is given as

$$\begin{aligned} \mathcal{L}_V = & -\frac{1}{4} \mathcal{D}_{[\mu} V_{\nu]}^a \mathcal{D}^{[\mu} V^{\nu]a} + \frac{m_V^2}{2} V_\mu^a V^{\mu a} \\ & + ig_V c_H V_\mu^a H^\dagger \tau^a \overleftrightarrow{\mathcal{D}}^\mu H + \frac{g^2}{g_V} c_F V_\mu^a J_F^{\mu a} \\ & + \text{additional terms.} \end{aligned} \quad (2.4)$$

The first line describes the kinematic and mass terms of the vector V , and the second line, which is of most interest to us, describes the coupling to the Higgs boson current and the left-handed fermionic currents. In the coupling to the Higgs current, the coefficient c_H leads to vertices involving the Higgs field and the Goldstone bosons, representing the longitudinally polarized SM vector bosons, W and Z. This term therefore governs the decay modes of the vector V into electroweak bosons, the decay mode of interest for this thesis. The second coupling term describes the interaction with leptons and quarks and is governed by the parameter c_F . A formalism is adopted where the interactions are weighted with a coupling g_V and g^2/g_V , where g is the gauge coupling of the group and g_V represents the “typical strength” of the vector interactions. Another interesting feature of the theory is that, after electroweak symmetry breaking provides the heavy vector with its mass, the charged and neutral vectors are found to be mass degenerate and expected to have similar production and decay rates.

After having defined the generic framework, explicit models with fixed values of c_H and c_f can be studied, where only the resonance mass m_V and coupling g_V are left as free parameters. In this thesis, we probe two benchmark models called HVT model A and HVT model B, as introduced in [16]. The reason why these two models are interesting is that the first probes rather weakly coupled extensions of the SM, and the latter, strongly coupled scenarios. That implies very different sizes of g_V , where values of $g_V = 1$ for model A and $g_V = 3$ for model B are used in [16]. For these values of g_V , model A predicts a comparable branching fraction for decays into bosons and fermions, the decay into fermions only enhanced by a factor of 2, while for model B, the

dominant branching fraction is to dibosons with decays into fermions severely suppressed. The branching fraction for the different decay modes of HVT model A and B, are shown in Figure 2.1. For obvious reasons, model B is of most interest for the searches presented here.

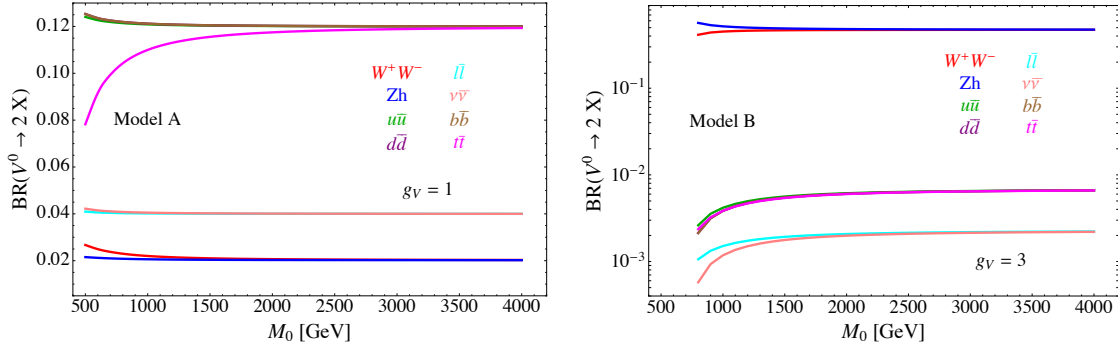


Figure 2.1: Predicted branching fractions of a Z' for two explicit HVT models: Model $A_{g_V=1}$ (left) and model $B_{g_V=3}$ (right) [16].

661 2.3 Warped extra dimensions

662 Extra dimensional theories also offer solutions to the hierarchy problem. This thesis focuses on
 663 Randall-Sundrum (RS) warped extra dimensional scenarios [17]. In RS models, a new curved
 664 spatial dimension y is proposed, leading to a 5-dimensional space-time bounded by two (3+1)-
 665 dimensional planes, or *branes*: the UV/Planck and the IR/TeV brane. The new metric now
 666 depends on the radius r and the curvature factor k of the new extra dimension, with

$$ds^2 = e^{-2ky} \eta_{\mu\nu} dx^\mu dx^\nu + dy^2; 0 < y < \pi R. \quad (2.5)$$

667 Gravity is concentrated and relatively strong at the Planck brane at $y = 0$, which is separated
 668 from us by the fifth dimension. Our observed four-dimensional reality and the Standard Model
 669 particles reside at the TeV brane, at $y = \pi R$. Only gravity, transmitted through gravitons, is
 670 allowed to propagate through the warped 5D space-time (the “bulk”) and is not confined to
 either brane. Figure 2.2 illustrates how the branes and the bulk are connected. Due to the

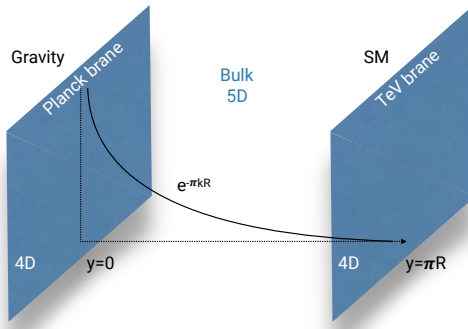


Figure 2.2: The RS model predicts an extra dimension where a 5D space-time stretches between two 4D branes: the Planck brane where gravity is concentrated, and the TeV brane where the SM particles are confined.

671 warping, the Planck mass on the Planck brane gets reduced by a factor of $e^{-\pi k R}$ at the TeV
 672 brane, thereby solving the hierarchy problem. The Planck mass on the TeV brane, which depends
 673 on the geometry of the extra dimension, becomes
 674

$$\bar{M}_{Pl}^2 = V_1 M_*^3, \quad (2.6)$$

where V_1 is the volume of the 1 dimensional added warped dimension and M_*^3 is the 5D Planck mass. One distinct prediction of the model, and a way in which we can test its validity, is the prediction of a tower of TeV-scale excitations with spin-2, so called Kaluza-Klein states, that could be observed in high energy experiments.

In this thesis, we are more interested in an alternative to the original RS model called the “bulk” scenario [18, 19]. In this case, the Standard Model particles, besides the Higgs boson, are also allowed to propagate in the bulk. The light 1st and 2nd generation fermions are localized near the Planck brane, yielding small couplings to the Higgs boson that still resides at the TeV brane, explaining their small masses. Similarly, the top quark is now located near the TeV brane, resulting in a stronger Yukawa coupling to the Higgs boson. In addition, with the gravitons located near the TeV brane and the fermions now residing near the Planck brane, the graviton coupling to fermions is strongly suppressed. SM gluons have a flat distribution throughout the bulk, making gluon-gluon production the dominant production channel of gravitons. Due to the weak vector bosons absorbing the Higgs degree of freedom in spontaneous symmetry breaking, their wave-functions fall off steeply near the TeV brane, resulting in a coupling to the gravitons similar to that of the Higgs and the top. The only free parameters of the theory is the mass of the lightest KK graviton and the ratio $\tilde{k} = \frac{k}{M_{Pl}}$, which controls the widths of the new resonances.

The branching ratios of the Bulk Graviton is shown in Figure 2.3.

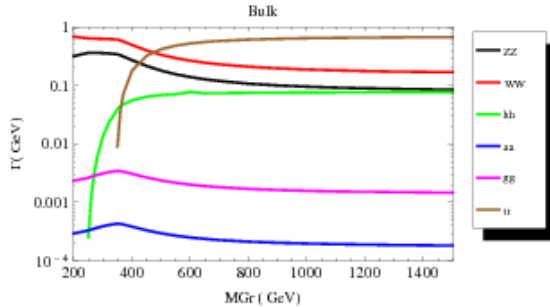


Figure 2.3: Predicted branching fractions for a Bulk Graviton as a function of its mass.

Part II

693

Experimental setup

694

695

CHAPTER 3

696

The Large Hadron Collider

697 In March 1984, the European Organization for Nuclear Research CERN) and the European
698 Committee for Future Accelerators (ECFA) held a workshop in Lausanne entitled “Large Hadron
699 Collider in the LEP Tunnel”. This is history’s first written mention of the Large Hadron Collider
700 (LHC) and the topic under discussion was exactly how to build a new type of high-energy collider,
701 capable of bringing hadrons to collide rather than leptons. The LHC would be housed in a tunnel
702 which, at the time, was under excavation to host the Large Electron-Positron Collider (LEP)
703 designed to collide leptons with center-of-mass-energies up to around 200 GeV. LEP was a circular
704 collider with a circumference of 27 km and the tunnel hosting it was located roughly 100 meters
705 underground beneath France and Switzerland, at the outskirts of Geneva. The justification for
706 building a machine like the LHC was that, once LEP got to its maximum center-of-mass energy,
707 a new and more powerful collider would be needed in its place in order to probe higher energies.
708 While collisions of electrons with positrons provide exceptionally clean and precise measurements
709 due to their being point particles, their lightness prevent them from being accelerated to higher
710 energies in circular colliders due to synchrotron radiation. Collisions of hadrons, however, would
711 allow for center-of-mass energies two orders of magnitude higher than that of LEP. Therefore,
712 after obtaining sufficient statistics when running at a center-of-mass-energy of twice the W boson
713 mass (160 GeV) and reaching a maximum center-of-mass energy of 209 GeV, in a search for the
714 Higgs boson, LEP was dismantled in 2000 in order to make room for the LHC.

715 The Large Hadron Collider first circulated protons in September 2008 and, while having
716 the same 27-kilometer radius as the LEP collider, is capable of accelerating protons up to a
717 center-of-mass energy of around 14 TeV, 70 times that of LEP. The accelerator consists of two
718 oppositely circulating proton beams, isolated from each other and under ultrahigh vacuum. The
719 protons are accelerated up to speeds close to the speed of light through radio frequency (RF)
720 cavities, before being focused to collide at four different interaction points along the ring. These

four collision points correspond to the location of the four LHC particle detectors; ATLAS, CMS, LHCb and ALICE. While ATLAS and CMS are general-purpose detectors, built in order to study a large range of different physics processes, LHCb and ALICE are built for dedicated purposes; LHCb for b-physics processes and ALICE for heavy ion collisions. The journey of a proton from a gas to one of the LHC collision points is as follows. First, hydrogen nuclei are extracted from a small tank of compressed hydrogen gas and stripped of their electrons. The remaining protons are then injected into the LINAC2, a linear accelerator responsible for increasing the proton energy to about 50 MeV through RF cavities that push charged particles forward by switching between positive and negative electric fields. The LINAC2 additionally divides the constant stream of particles into equally spaced “bunches” by careful tuning of the frequency of the field switch. The accelerated protons are then injected into the Proton Synchrotron Booster (PSB), where their energy is increased by thirty fold, to an energy of roughly 1.4 GeV. The two final acceleration stages before the protons reach the LHC ring are the Proton Synchrotron and Super Proton Synchrotron, eventually producing protons with a total energy of 450 GeV. The protons are now ready for the final stage of their travel and are injected into the two beam pipes of the LHC in opposite directions. They are injected in trains of 144 bunches each (on order of 10^{11} protons per bunch), where each bunch is roughly 7.5 meters apart (or 25 ns). There are some larger beam gaps present in each beam in order to give special magnets sufficient time to switch on in order to inject or dump the beam. The largest beam abort gap is roughly 3 ms or 900 m long. The ring is filled with proton bunches until these are equally distributed throughout the two rings, a process taking roughly 4 minutes. This is called a “fill”. Here, the protons are accelerated to their current maximum energy of 6.5 TeV, a process taking roughly 20 minutes, through eight RF cavities. These RF cavities are also responsible for keeping the proton bunches tightly bunched. A complete sketch of the CERN accelerator complex is shown in Figure 3.1. After the beams have reached their maximum energy and are stably circulating in the LHC ring, the bunches are brought to collide. The goal of such a collision, which occurs every 25 nanoseconds, is that some of the protons in each bunch will inelastically collide, allowing the quark and gluon constituents of each proton to interact with one another and produce new and interesting particles. The number of times such an interaction will take place inside a detector per area and time is quantified through the instantaneous luminosity \mathcal{L} , which is the proportionality factor between the number of observable events per second and the cross section σ of the process you are interested in,

$$\frac{dN_{events}}{dt} = \mathcal{L}\sigma. \quad (3.1)$$

The cross section is the probability that an event (like one which would produce new and interesting

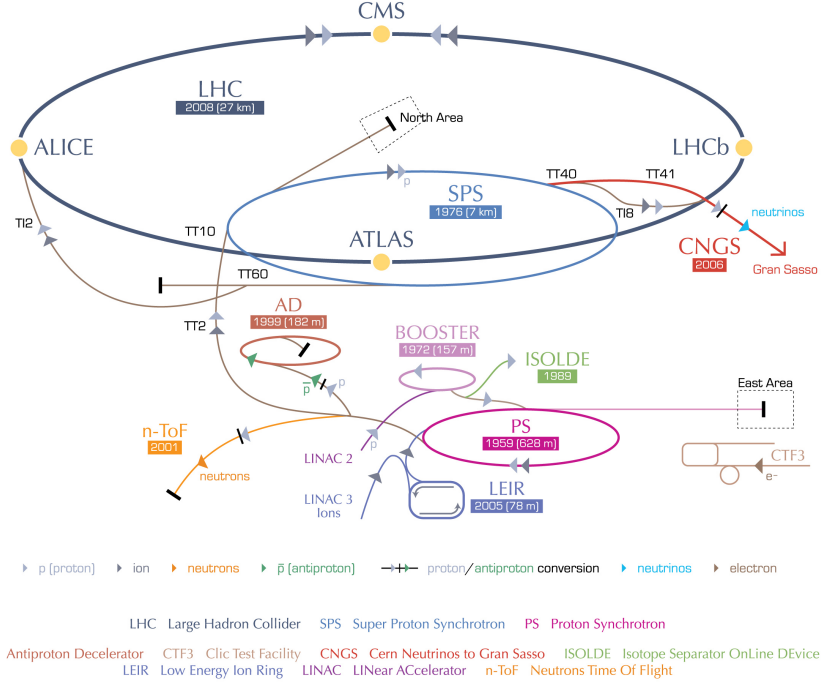


Figure 3.1: The Large Hadron Collider accelerator complex. The four collision points along the ring correspond to the location of the LHC particle detectors CMS, LHCb, ATLAS and ALICE [20].

753 particles) will occur and is measured in barns, where $1 \text{ barn} = 10^{-28} \text{ m}^2$. This luminosity should
754 therefore be as high as possible. It depends only on parameters of the accelerator beams and can,
755 in the case of the LHC, be defined through accelerator quantities as

$$\mathcal{L} = \frac{N_b^2 n_b f_{rev} \gamma_r}{4\pi \epsilon_n \beta_*} F, \quad (3.2)$$

756 where N_b is the number of particles per bunch, n_b is the number of bunches, f_{rev} is their revolution
757 frequency, γ_r is the relativistic gamma factor, ϵ_n is the normalized transverse beam emittance
758 (how confined the particles are in space and momentum), β_* is the beta function at the collision
759 point (how narrow, or “squeezed”, the beam is) and F is a reduction factor to account for
760 the case where the beams do not collide head-on but at slight crossing angles. From this, it
761 becomes clear that the main goal of the LHC is to maximize the number of particles (N_b, n_b),

Parameter	Units	Nominal	2015	2016	2017
Energy	[TeV]	7.0	6.5	6.5	6.5
Bunch spacing	[ns]	25	25	25	25
Bunch intensity	$\times 10^{11}$ [protons/bunch]	1.15	1.15	1.15	1.2-1.45
Bunches per train		144	144	96	144
Total number of bunches		2808	2244	2220	2556
β^*	[cm]	55	80	40	27/25
Peak luminosity	$\times 10^{34}$ [cm $^{-2}$ s $^{-1}$]	1.0	0.5	1.4	2.0
Integrated luminosity			4.2	39.7	50.2

Table 3.1: Some key LHC detector parameters achieved during the first years of data taking with a center-of-mass energy of 13 TeV.

their frequency (f_{rev}) and their energy (γ_r), while at the same time ensuring the protons are packed together as tightly as possible (lower ϵ_n and β^*). Using the nominal values for the LHC, the peak instantaneous luminosity is roughly $\mathcal{L} \sim 10^{34} \text{ cm}^{-2} \text{ s}^{-1}$.

The peak luminosity of the LHC by the end of Run 2 in 2018 was about $2.0 \cdot 10^{34} \text{ cm}^{-2} \text{ s}^{-1}$, corresponding to 2 times the nominal design instantaneous luminosity.

To quantify the size and statistical power of a given LHC dataset, the integrated luminosity is used. This is the integral of the instantaneous luminosity over time and is defined as

$$\mathcal{L}_{int} = \int \mathcal{L} dt. \quad (3.3)$$

It is usually defined in units of inverse cross section, b^{-1} .

Despite the LHC starting up in 2008, there would be another year before data taking began due to technical difficulties with the magnets. In March 2010, the LHC saw its first collision with a center-of-mass energy of 7 TeV, and continued running at this energy, collecting around 5 inverse femtobarns of data by the end of 2011. In 2012, the energy was increased to 8 TeV and the LHC continued running until a planned long shutdown scheduled to begin in February 2013, collecting a total of $\sim 20 \text{ fb}^{-1}$, which allowed the Higgs boson to be discovered. This marked the end of Run 1 and the beginning of a two-year maintenance project intended to prepare the LHC for running at a center-of-mass energy of 13 TeV, a period referred to as Run 2.

Run 2 started in June 2015, and provides the dataset used in thesis. With the accelerator now running at 90% of its nominal energy, and with a peak luminosity between 1-2 times the design luminosity, the LHC managed to collect an impressive $\sim 160 \text{ fb}^{-1}$ with center-of-mass energy of 13 TeV up until its planned shutdown at the end of 2018. Some key LHC accelerator parameters that were in use for the datasets analyzed in this thesis are quoted in Table 3.1.

783

CHAPTER 4

784

The CMS detector

785 The Compact Muon Solenoid (CMS) detector is true to its name. With a diameter of 15
786 meters and a weight of 14000 tons, it is 60% smaller but twice as heavy as its counterpart, the
787 ATLAS detector. Its large weight is due to its solenoid: a superconducting niobium titanium
788 coil circulating 18500 Amps and capable of generating a magnetic field of 3.8 Tesla, the largest
789 superconducting magnet ever built. Together with its corresponding iron return yoke, responsible
790 for returning the escaping magnetic flux, it accounts for 90% of the total detector weight. The
791 CMS detector is cylindrically symmetric and organized such that the inner tracking system begins
792 at a radius of around 3 cm from the beam pipe. It consists of an inner silicon pixel detector and an
793 outer silicon strip tracker, stretching out to a radius of roughly 1.2 meters. Following the tracker
794 are two calorimeter layers: the electromagnetic calorimeter (ECAL) consisting of lead tungstate
795 scintillating crystals and responsible for measuring the energy of electromagnetically interacting
796 particles, followed by the hadronic calorimeter (HCAL) that measures the energy of hadrons.
797 Contrary to “standard” configurations for general purpose detectors, the CMS calorimeters are
798 located inside the superconducting solenoid. This allows the detector to be rather compact, by
799 reducing the necessary radii of the calorimeters, and results in a strong magnetic field due to
800 the large coil radius. The muon detectors are alternated with three layers of steel return yoke,
801 responsible for containing and returning the magnetic field. Only muons and weakly interacting
802 particles are expected to transverse the full detector volume without being stopped. Since the
803 muons bend in the magnetic field of the return yoke, an additional momentum measurement can
804 be made. A schematic overview of the CMS detector is shown in Figure 4.1. In the following, the
805 different sub-detectors will be described in detail.

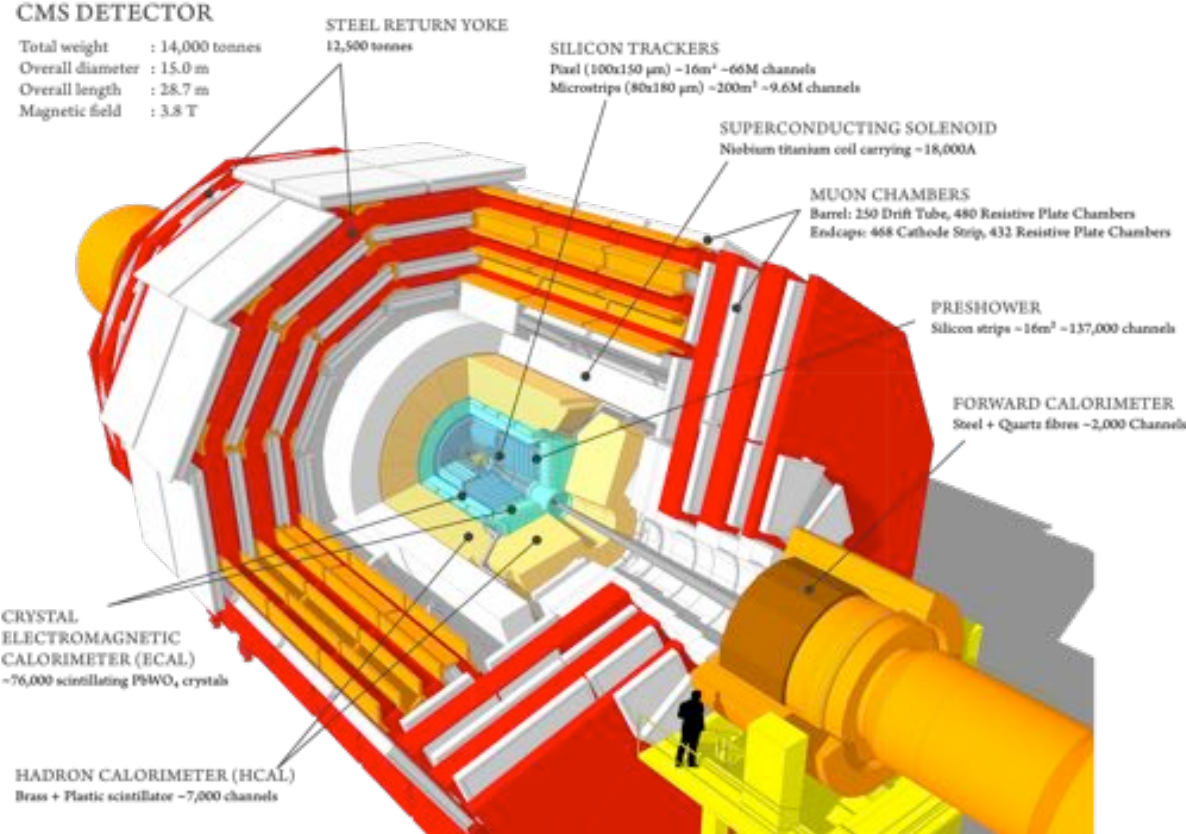


Figure 4.1: The CMS detector and its subsystems: the silicon tracker, electromagnetic and hadron calorimeters, superconducting solenoid and the muon chambers inter-layered with the steel return yoke [21].

4.1 Coordinate system

To describe locations within the CMS detector, a Euclidian space coordinate system is used. Here, the positive z axis points along the beam pipe towards the west, the positive x axis points towards the center of the LHC ring, and the positive y axis up towards the surface of the earth. Due to the cylindrical symmetry of the detector, polar coordinates are more convenient and most frequently encountered. In this scheme, the azimuthal angle ϕ is measured in the xy-plane, where $\phi = 0$ correspond to the positive x axis and $\phi = \pi/2$ correspond to the positive y axis. The polar angle θ is measured with respect to the z axis, $\theta = 0$ aligning with the positive and $\theta = \pi$ with the negative z axis. To define a particles' angle with respect to the beam line, the pseudorapidity $\eta = -\ln \tan(\theta/2)$ is preferred over θ . This is due to the fact that particle production is approximately constant as a function of pseudorapidity and, more importantly,

because differences in pseudorapidity are Lorentz invariant under boosts along the z-axis when assuming massless particles. To measure angular difference between particles in the detector, the variable $\Delta R = \sqrt{\Delta\eta^2 + \Delta\phi^2}$ is used, which is also Lorentz invariant under longitudinal boosts. A summary of the CMS coordinate system together with some example values are shown in Figure 4.2.

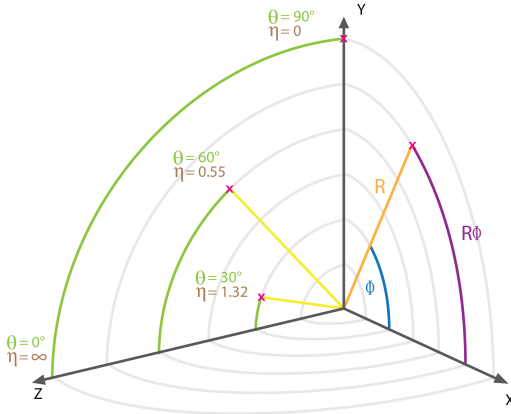


Figure 4.2: The CMS coordinate system [22], shown with some values of θ and η .

821

822 4.2 Tracking detectors

823 The CMS tracker is responsible for accurately reconstructing the momentum of charged particles
 824 and consists of two sub-detectors. Closest to the interaction point, and where the particle intensity
 825 is the highest, the silicon pixel detector is located. Upgraded in 2017, from the so-called Phase-0
 826 to the Phase-1 detector, it is structured with four cylindrical barrel layers at radii 2.9, 6.8, 10.9
 827 and 16.0 cm (the barrel pixel detector) and three disks in each of the forward regions placed
 828 at a distance from the nominal interaction point of 29.1, 39.6 and 51.6 cm (the forward pixel
 829 detector). A sketch of the current Phase-1 pixel detector compared to the Phase-0 detector is
 830 shown in Figure 4.3. The sensors located closest to the beam pipe are subject to hit intensities
 831 of $\mathcal{O}(\text{MHz}/\text{mm}^2)$ such that strict constraints on the sensor pixel size are required in order to
 832 minimize occupancy in the detector. The sensor pixels are $100 \mu\text{m} \times 150 \mu\text{m}$ with a thickness
 833 of $285 \mu\text{m}$, and when counting both barrel and forward pixel detectors, sum up to a total of
 834 124 million channels. The sensors are mounted on detector modules each with 16 read-out chips,
 835 where the type of readout chip depends on how close the module is to the beam pipe. The
 836 inner layer uses readout chips with a rate capability of $600 \text{ MHz}/\text{cm}^2$, while for the outer layers,

readout chips with a rate capability of up to $200 \text{ MHz}/\text{cm}^2$ are sufficient. Since the hit intensity

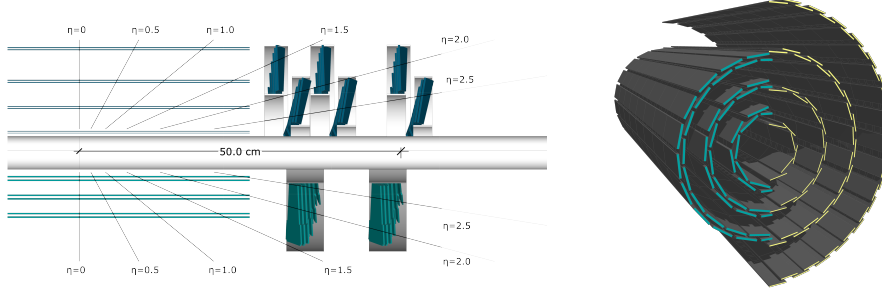


Figure 4.3: Left: The pixel detector layout before (bottom) and after (top) the Phase-1 upgrade. Right: The barrel pixel detector before (left) and after (right) the Phase-1 upgrade [23].

837
838 reduces as you go further away from the beam pipe, the pixel sensors are replaced by silicon
839 strip sensors of larger size, making up the second of the two tracker sub-systems, the silicon strip
840 tracker. There are ten strip layers in total, stretching out to a radius of roughly 130 cm. These
841 are divided into four sections: The inner barrel (TIB) with four strip layers, the two inner endcaps
842 (TID) consisting of three disks each, the outer barrel (TOB) consisting of 6 cylindrical layers,
843 and the two endcaps (TEC) with 9 strip layers each. A schematic overview of the strip tracker
844 layout is shown in Figure 4.4. The strips in the TIB and TID are 10 cm long, with a width of 80
845 μm and a thickness of 320 μm . The TOB and TEC sections consist of slightly larger strips of 25
846 cm \times 180 μm and a thickness of 500 μm . The strip tracker has a total of 10 million detector
847 strips and covers an area of $\sim 200 \text{ m}^2$. To prolong the silicon detector lifetime, the entire tracker
848 (pixel and strip) is kept at a temperature of -20°C with a dedicated cooling system. The tracker
849 has a coverage of up to $|\eta| < 2.6$ and a resolution of roughly $\sigma/p_T \approx 1.5 \times 10^{-5} p_T + 0.005$.

850 4.3 Electromagnetic calorimeter

851 Surrounding the tracking detectors is the electromagnetic crystal calorimeter (ECAL). Consisting
852 of 75 848 laterally segmented scintillating lead tungstate (PbWO_4) crystals, it was designed to
853 have the best possible photon energy and position resolution in order to resolve a Higgs boson
854 decaying into two photons, one of the cleanest discovery channels of the Higgs boson. With a
855 design energy resolution of 0.5% above 100 GeV for photons and electrons, the choice of detector
856 material for the ECAL has been its most crucial design feature. In order to withstand the high
857 doses of radiation and the high magnetic field present within the detector, while at the same time
858 generating well-defined signal responses within the 25 nanoseconds between particle collisions,

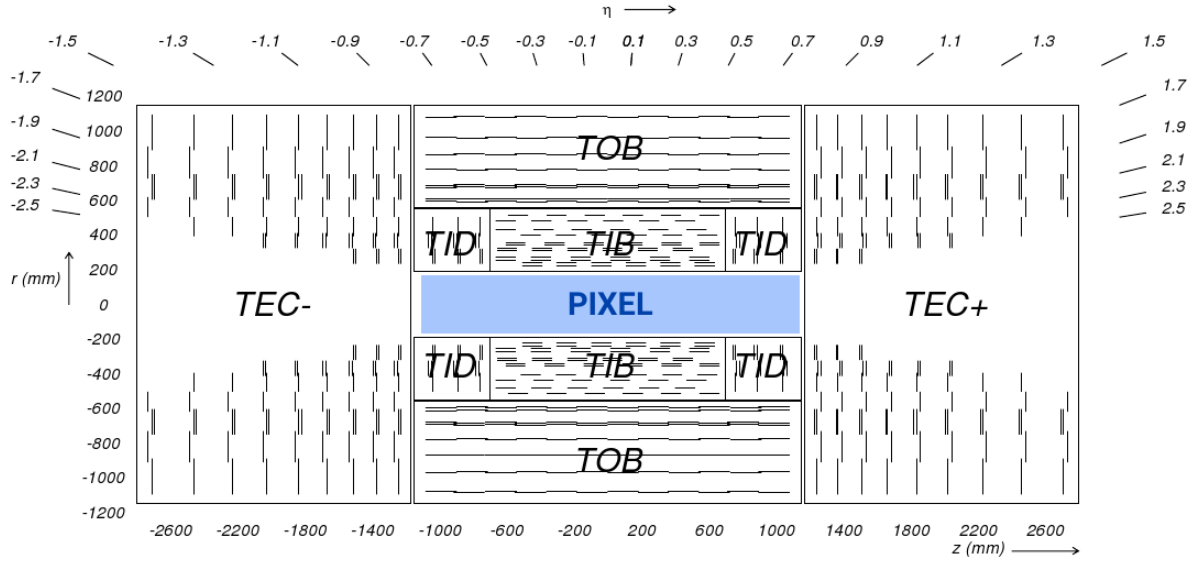


Figure 4.4: Schematic of the CMS silicon strip tracker and its four subsections: the inner barrel (TIB), inner endcaps (TID), the outer barrel (TOB), and the two endcaps (TEC) [24].

an extremely dense and transparent material capable of producing fast and clean photon bursts when hit, is required. Metal-heavy lead tungstate crystals, each taking roughly two days to artificially grow (and a total of about ten years to grow all of them), were chosen. With a density of $\delta = 8.28 \text{ g/cm}^3$ (slightly higher than for stainless steel), the crystals are compact enough to yield excellent performance without taking up too much volume, allowing the ECAL to fit within the CMS superconducting solenoid. The homogeneous medium allows for a better energy resolution as it minimizes the effects from sampling fluctuations, and it additionally contains enough oxygen in crystalline form to make it highly transparent to the entire scintillation emission spectrum. With an extremely short radiation length and small Molière radius ($X_0 = 0.85 \text{ cm}$, $R_M = 2.19 \text{ cm}$), the required homogeneity, granularity, and compactness is obtained, while at the same time emitting 80% of generated light within the 25 ns timeframe required. The largest drawbacks with a lead tungstate detector are the low light yield (100 γ per MeV), requiring dedicated avalanche photodiodes to increase the gain, and the light yield, which strongly depends on the temperature. The detector response to an incident electron changes by $3.8 \pm 0.4 \%$ per degree Celsius which requires the ECAL temperature to be kept stable at 18.0 ± 0.5 degree Celsius, which is obtained through an intricate water cooling system. The ECAL is completely hermetic and sorted into a barrel part (EB), covering pseudorapidities up to $|\eta| < 1.48$, and two endcap parts (EE) extending the total coverage to $|\eta| < 3.0$, in order to match the tracker coverage of $|\eta| < 2.5$. In order to improve the separation power between the γ and π_0 , a pre-shower detector

(ES) using lead absorbers and silicon sensors covers the forward region between $1.65 < |\eta| < 2.6$. The crystals in the barrel are organized into supermodules, each consisting of about 1700 crystals, while the endcap is divided into two half disks consisting of 3662 crystals each (so-called “Dees”). Each PbWO₄ crystal weighs around 1.5 kg and has a slightly tapered shape with a front face of $2.2 \times 2.2 \text{ cm}^2$ in the barrel and $2.86 \times 2.86 \text{ cm}^2$ in the endcaps. The crystals are 23 and 22 cm long in the barrel and endcaps, respectively. The total volume of the calorimeter including barrel and endcaps is 11 m^2 and it weighs a total of 92 tonnes. The ECAL detector layout is illustrated in Figure 4.5.

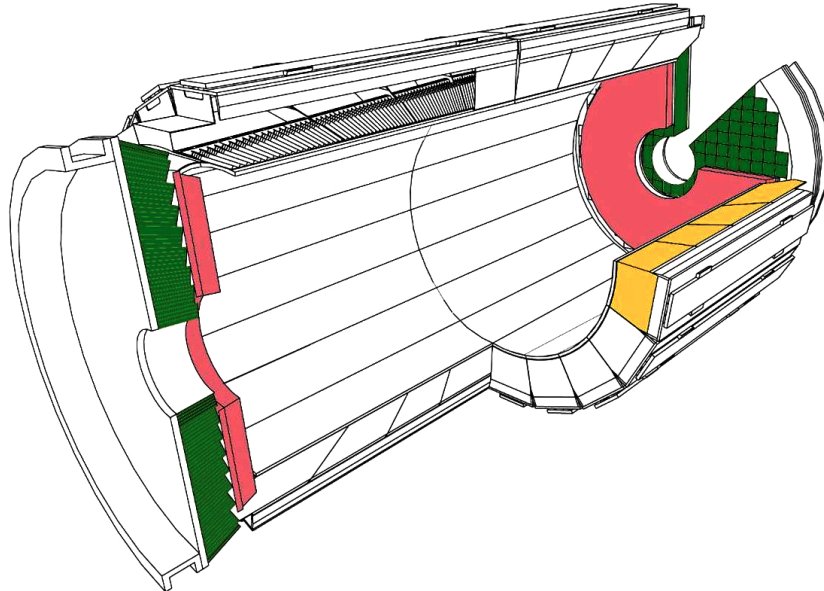


Figure 4.5: A schematic of the CMS electromagnetic calorimeter showing the barrel supermodules (yellow), the individual barrel crystals (black, top left), the endcap modules (green), and the pre-shower detectors (pink) [24].

Having no longitudinal segmentation, the ECAL relies on an accurate reconstruction of the event primary vertex, provided by the tracker, in order to reconstruct the photon angle correctly. The obtained energy resolution of the ECAL can be parametrized in three parts: a stochastic, a noise, and a constant term [25]. It is given as

$$\frac{\sigma_E}{E} = \frac{2.8\%}{\sqrt{E}} \oplus \frac{12\%}{E} \oplus 0.3\%,$$

in which the constant values were estimated using an electron test beam. The constant term of 0.3% is dominated by the non-uniformity in longitudinal light collection [26], and one of the

892 main goals of the detector design was to get this term below 1%. The energy resolution as a function of electron energy is shown in Figure 4.6.

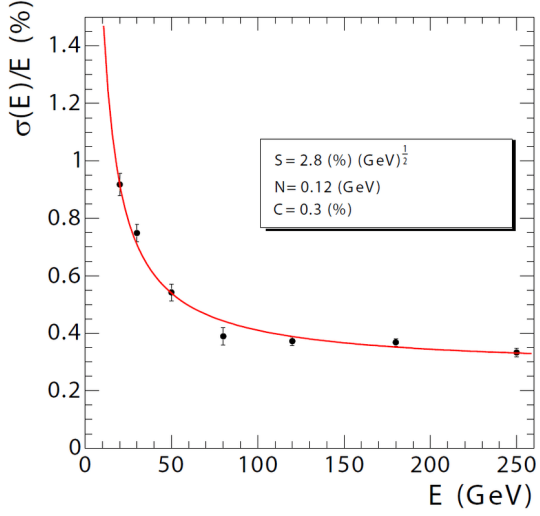


Figure 4.6: The ECAL energy resolution as a function of electron energy as measured in an electron test beam. [25]

893

894 4.4 Hadronic calorimeter

Outside the electromagnetic calorimeter is the hadronic calorimeter (HCAL). The HCAL is a sampling calorimeter, meaning it consists of alternating layers of dense brass absorber material and plastic scintillators. When a particle hits an absorber plate, it interacts with the absorber material and generates a shower of secondary particles which themselves generate new particle showers. These particles then generate light in the scintillating material which is proportional to their energy, and summing up the total amount of generated light over consecutive layers within a region, called a “tower”, is representative of the initial particles energy. It is the combined response of the ECAL and the HCAL that are responsible for measuring the energy of quarks, gluons and neutrinos through the reconstruction of particle jet energy and missing transverse energy. The hadron calorimeter is split into four regions: the inner (HB) and outer (HO) barrel, the endcap (HE) and the forward region (HF). A schematic of the CMS HCAL is shown in Figure 4.7. The inner barrel lies within the superconducting solenoid volume and covers the pseudorapidity range $|\eta| < 1.3$. It consists of 36 identical wedges, each of which weigh 26 tonnes, split into two half barrels (HB+ and HB-). A photograph of the wedges taken during installation is shown in Figure 4.8. The wedges are made up of flat brass absorber plates oriented parallel



Figure 4.7: The four regions of the CMS hadron calorimeter: the inner (HB) and outer (HO) barrel, the endcap (HE) and the forward region (HF) [24]

to the beam axis. These plates consist of a 4-cm thick front steel plate followed by eight 5-cm thick brass plates, six 5.6-cm thick brass plates and ending with a 7.5-cm thick steel back plate. The absorber plates alternate with 4-mm thick plastic scintillator tiles, which are the active medium of the detector, and which are read out using wavelength-shifting plastic fibers. The effective thickness of the barrel hadron calorimeter in terms of interaction lengths increases with the polar angle θ , starting out at about $5.8 \lambda_I$ at an angle of 90 degrees, and increasing to $10.6 \lambda_I$ at $|\eta| < 1.3$. As the energy resolution of the calorimeter depends on how much of the particles shower can be absorbed by the calorimeter, the quality of the energy measurement depends on its thickness. Due to the CMS design, the HB is confined to the volume between the ECAL (ending at a radius of 1.77 m) and the magnetic coil (starting at a radius of 2.95 m). In the central η region, the combined ECAL and HCAL interaction length is too small to sufficiently contain hadron showers. In order to ensure adequate sampling, especially of late starting showers, an additional layer of scintillator has therefore been added outside of the solenoid coil. This is the outer barrel (HO). It uses the coil itself as an absorbing material, increasing the total barrel calorimeter interaction length to $11.8 \lambda_I$. The hadron calorimeter endcaps (HE) are located in the forward region close to the beam pipe and cover the pseudorapidity range $1.3 < |\eta| < 3.0$, a region containing about 35% of the particles produced in collisions. Due to its close proximity to the beam pipe, the endcaps need to handle extremely high rates as well as have a high radiation tolerance. As the resolution in the endcap region is degraded due to pile-up and magnetic field effects, the hadron calorimeter endcaps were designed to minimize the cracks between HB and HE, rather than having the best single-particle resolution (as is the case for the barrel). The absorber plates in the endcaps are mounted in a staggered geometry rather than on top of each other as is



Figure 4.8: The installation of the barrel HCAL wedges, consisting of alternating layers of brass absorber plates and plastic scintillator, each weighing roughly 26 tonnes [27].

done in the barrel, in order to contain no dead material and provide a hermetic self-supporting construction. The HCAL is read out in individual towers with a size $\Delta\eta \times \Delta\phi = 0.087 \times 0.087$ in the barrel, and 0.17×0.17 at larger pseudorapidities. In order to obtain a completely hermetic calorimeter, an additional hadron forward calorimeter (HF) is added in the very forward region. Stretching out to a pseudorapidity of $|\eta| = 5.2$, this detector is located so close to the beam pipe that the particle rate exceeds 10^{11} per cm^2 , receiving roughly 760 GeV per proton-proton collision compared to an average of 100 GeV for the rest of the detector. It consists of two cylindrical steel structures, each with an outer radius of 130 cm and an inner radius of 12.5 cm, located 11.2 meters on either side of the interaction point. Also a sampling calorimeter, it consists of grooved 5-mm thick steel absorber plates, where the quartz fiber active medium is inserted into these grooves. The energy resolution of the CMS ECAL and HCAL detectors for pions is measured in a test beam as a function of energy and is shown in Figure 4.9. The typical electronics noise of the HCAL is measured to be 200 MeV per tower. The inclusion of the HO improves the resolution by 10% for a pion energy of 300 GeV. The final energy resolution parametrization when using ECAL+HB+HO is given by a stochastic and a constant term, as was the case for the ECAL detector, and is

$$\frac{\sigma_E}{E} = \frac{84.7\%}{\sqrt{E}} \oplus 7.4\%.$$

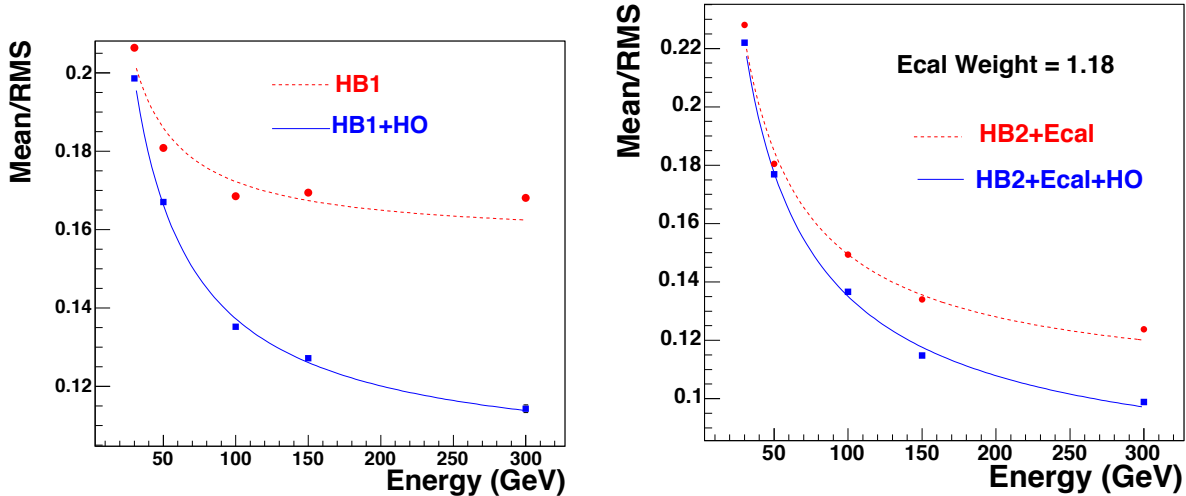


Figure 4.9: The calorimeter energy resolution as a function of pion energy using the HB only or HB+HO (left), and when adding ECAL and HCAL measurements (right) [28].

895 4.5 Muon chambers

The outer part of the CMS detector is dedicated to performing muon identification, momentum measurements, and triggering. The muon system is made up of three types of gaseous particle detectors: drift tube (DT) chambers, cathode strip chambers (CSCs), and resistive plate chambers (RPCs), all integrated into the magnetic return yoke structure. In the barrel region, where particle rates are low and the magnetic field uniform, DT chambers are used and cover the pseudorapidity region $|\eta| < 1.2$. In the endcap regions, however, the muon rates and background levels are considerably higher and the magnetic field itself is large and non-uniform. Therefore, CSCs with finer segmentation, higher radiation resistance, and faster signal collection are used, and cover the region $0.9 < |\eta| < 2.4$. To ensure accurate muon triggering, RPCs are used as a complimentary dedicated muon triggering system, which has been added both in the barrel and in the endcaps. These provide an excellent time resolution and cover the region $|\eta| < 1.6$. These chambers also assist in resolving ambiguities if multiple hits are present within a CSC or DT chamber. A schematic overview of the muon system is shown in Figure 4.10.

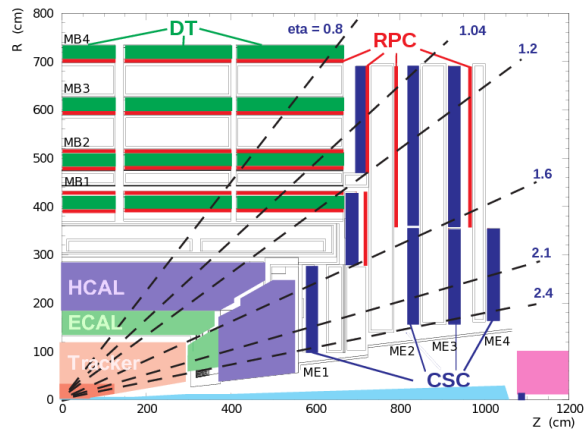


Figure 4.10: A schematic overview of the muon chambers: the DT chambers in the barrel, the CSCs in the endcaps, and the redundant RPC system stretching out to $|\eta| < 1.6$, which are used for triggering purposes [29].

909

CHAPTER 5

910

The CMS trigger system

911 With bunches in CMS colliding at a rate of 40 MHz, there are only 25 nanoseconds between
912 collisions available to process event data. For typical instantaneous luminosities, one billion
913 collisions take place every second, and with an event size of roughly 1 MB, it is impossible for
914 all of these events to be read out and stored to disk. The CMS triggering system is therefore
915 designed to make ultra fast high-quality decisions about which events are interesting and which
916 events are not. The first stage of triggering, called Level 1 (L1), is designed to reduce the event
917 rate to a maximum of 100 kHz through custom-designed hardware. It uses coarse data from
918 the muons system and calorimeters in order to make a decision on whether the event should be
919 recorded or not, a decision that needs to happen within $3.2\mu s$. During this time, the full event
920 data from each sub-detector is stored in detector front-end electronics, awaiting the L1 decision.
921 The information used by L1 is gathered in three steps. First, trigger primitives are created. For
922 the muon system, these consist of track segments from each of the three types of muon detectors.
923 For the calorimeter, trigger primitives are generated by calculating the transverse energy in a
924 trigger tower ($\Delta\eta - \Delta\phi$ of 0.087×0.087) and assigning it to the correct bunch crossing. Trigger
925 primitives from the calorimeter are then passed on to a regional trigger, which defines electrons,
926 muons and jet candidates. Some of this information is passed to the regional muon trigger in
927 order to provide information about whether the particle is minimum ionizing. The global muon
928 trigger then combines track information with calorimeter information and selects a maximum of
929 four muon candidates and calculates their momentum, position, charge and quality. The output
930 from the regional calorimeter trigger is also passed to a global calorimeter trigger which provides
931 information about the jets, total transverse energy and missing energy in the event. Combining
932 the information from the global muon trigger and the global calorimeter trigger, the L1 trigger
933 decides whether to keep the event or not by combining several decisions by simple logic operations
934 (AND/OR/NOT), forming up to 128 algorithms.

935 If the event is accepted, the full event information is read out at a rate of 100 kHz and
936 passed to the High Level Trigger (HLT), a farm of commercially available computers. Here, the
937 full precision of the detector data is used in order to make decisions based on offline-quality
938 reconstruction algorithms. The goal of the HLT is to eventually reduce the event rate to an
939 average of 400 Hz, which will be stored on tape.

940

CHAPTER 6

941

Event reconstruction

942

6.1 Track and primary vertex reconstruction

943 The CMS tracker gets traversed by $\mathcal{O}(1000)$ charged particles at each bunch crossing, produced by
 944 several proton-proton interactions happening simultaneously. This makes track reconstructions
 945 extremely challenging, and is the reason why a high granularity of the tracker is vital. The average
 946 number of vertices per event for the whole Run 2 data taking period is shown in Figure 6.1, with
 an average of 34 interactions per bunch crossing. Track reconstruction encompasses the process of

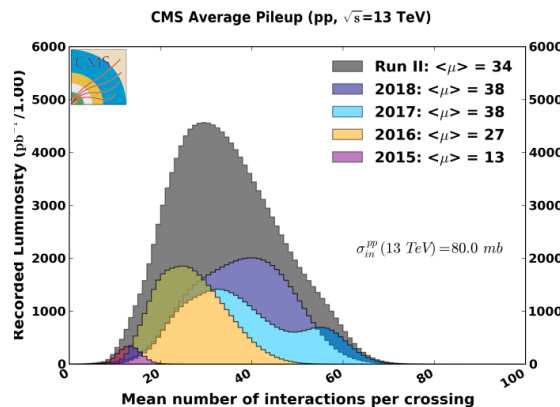


Figure 6.1: The average number of vertices per event in CMS for the whole Run 2 data taking period [30].

947

948 taking hits from the pixel and strip detectors, combining them into particle trajectories, and then
 949 estimating the momentum and flight direction of the charged particle responsible for producing the
 950 hits. It is a computationally heavy process and at CMS it is based on what is called a combinatorial

951 Kalman filter [31]. A Kalman filter is an algorithm that uses time-dependent observations in order
 952 to estimate unknown variables, by proceeding progressively from one measurement to the next,
 953 improving the knowledge of the trajectory with each new measurement. The track reconstruction
 954 software in CMS (called the Combinatorial Track Finder (CTF)) constructs its collection of tracks
 955 by iteratively looping over the hits and reconstructing tracks, then removing those hits which are
 956 already used as inputs for a previous track. It starts from a seed in the innermost tracker layers,
 957 usually two or three hits, and then extrapolates the seed trajectories searching for additional hits
 958 to associate to that candidate. It then disregards tracks that fail certain criteria based on a χ^2
 959 calculation, taking both hit and trajectory uncertainties into account, as well as the number of
 960 missing hits. The track reconstruction algorithm is effective over the full range of the tracker
 961 coverage, up to $|\eta| < 2.5$, and can reconstruct particles with momenta as low as 0.1 GeV and
 962 particles which are produced up to 60 cm from the beam line. In the central region, particles with
 963 a momentum of 100 GeV have a p_T -resolution of roughly 2.8 %, a transverse impact parameter
 964 resolution of 10 μm and a longitudinal impact parameter of 30 μm .

965 In order to define the location and uncertainty of every proton-proton interaction in an
 966 event, primary-vertex reconstruction is performed. Primary vertices lie within a radius of a few
 967 millimeters from the beam axis and are defined as the common origin of groups of tracks. The
 968 reconstruction algorithm takes as input the reconstructed tracks from the previous step which
 969 pass certain selection criteria, clusters the tracks that share a common origin, and then fit for the
 970 position of each vertex. Each track must have at least 2 hits in the pixel layers and no less than 5
 971 hits in the pixel plus strip layers, as well as a $\chi^2 < 20$ from a fit to the particle trajectory, to be
 972 considered as input for the vertex finder. The primary vertex resolution is around 12 μm in x
 973 and 10 μm in z for vertices with at least 50 tracks.

974 Offline, all events are required to have at least one primary vertex reconstructed within a 24
 975 cm window along the beam axis, with a transverse distance from the nominal interaction region
 976 of less than 2 cm. The reconstructed vertex with the largest value of p_T^2 of the summed particles
 977 is selected as the primary interaction vertex where the hard scattering process occurred.

978 6.2 The Particle Flow Algorithm

979 After track reconstruction, what remains is an incoherent collection of tracks, calorimeter clusters
 980 and hits in the muon chambers. In order to connect these, CMS uses an algorithm called Particle
 981 Flow (PF) [32] to combine the information obtained from all sub-detectors in order to infer which
 982 particles were actually produced in the event. The reconstructed physics objects in the order of
 983 which they are reconstructed are

- 984 • muons, through hits in the tracker and in the muon chambers;
- 985 • charged hadrons, through hits in the tracker and energy deposits in the calorimeters;
- 986 • neutral hadrons, through energy deposits in the calorimeters but no hits in the tracker;
- 987 • photons, through energy deposits in the ECAL but not in the HCAL, and no hits in the
 988 tracker; and
- 989 • electrons, through hits in the tracker and energy deposits in the ECAL.

How these different particles propagate through the CMS detector is illustrated in Figure 6.2.

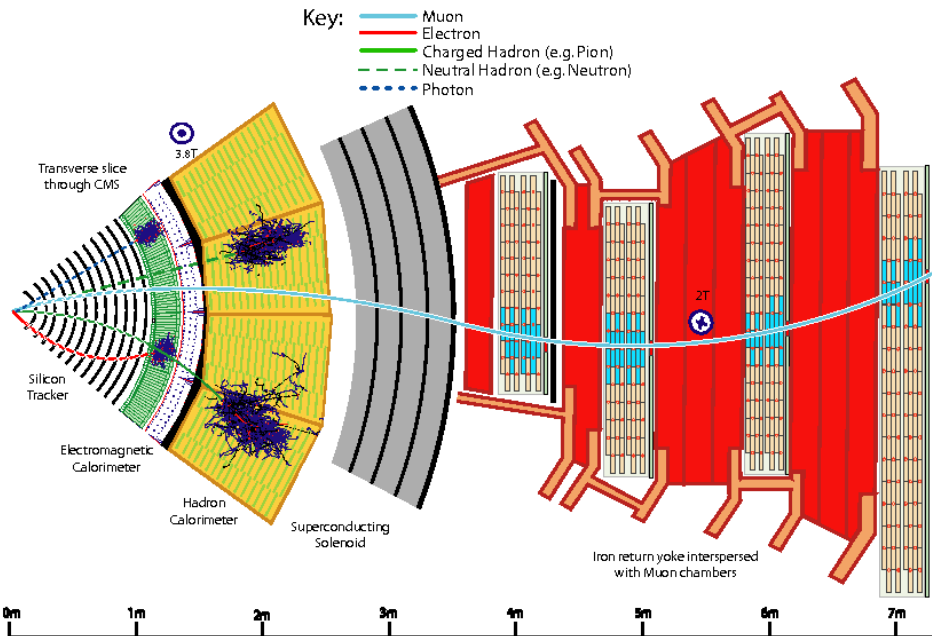


Figure 6.2: Particle interactions in the different subdetectors for a transverse slice through the CMS detector [32].

6.2.1 Reconstruction of the Particle Flow inputs

Electron tracking

Electron seeding is done in two different ways: ECAL-based or tracker-based. In the ECAL-based method, electrons are seeded from ECAL clusters with $E_T > 4 \text{ GeV}$, where the position of the cluster is used to infer which hits in the inner tracker belongs to a given electron or positron. As a large fraction of the electron/positron energy is emitted through bremsstrahlung before even reaching the ECAL, the ECAL superclusters covering a small window in η and a larger window in ϕ are defined in order to fully contain the electron as well as its bremsstrahlung photons. As these superclusters are prone to contamination, tight isolation requirements need to be applied, leading to reconstruction inefficiencies. Therefore, an additional tracker-based seeding approach has been developed. All tracks with $p_T > 2 \text{ GeV}$ are used as potential electron seeds. These tracks are then extrapolated to the ECAL and matched to the closest ECAL cluster. The ratio of the cluster energy to the track momentum is required to be ~ 1 . The electron candidates are then fit with a Gaussian-sum filter (GSF) [33] and required to pass certain criteria based on the score of a boosted-decision-tree (BDT), which combines the number of tracker hits, the χ^2 of the GSF track, the energy loss along the track, and the distance between the extrapolated track to the closest ECAL cluster.

Muon tracking

Muon tracking consists of two parts: the muon spectrometer allows muons to be identified with high efficiency over the full pseudorapidity range, while maintaining a low background due to the absorbing calorimeter layers upstream. The inner tracker on the other hand, provides an accurate measurement of the muon momentum. Three muon quality flags are defined:

- standalone muon: Muon tracks based on hits in the DT or CSC only;
- global muon: A standalone muon track matched to a track in the tracker if the track parameters of the two are compatible; and
- tracker muon: An inner track with $p_T > 0.5 \text{ GeV}$, a total momentum greater than 2.5 GeV , and at least one muon segment matching the extrapolated inner track.

Around 99% of muons produced within $|\eta| < 2.4$ are reconstructed as a global muon or a tracker muon, and very often as both. If the global and tracker muon share the same inner tracker segment, the two are combined.

1021 Calorimeter clusters

1022 The calorimeter clustering is performed separately for each calorimeter subdetector (ECAL barrel
 1023 and endcaps, HCAL barrel and endcaps and the preshower layers). The first step is to define
 1024 cluster seeds from cells with an energy exceeding some predefined threshold and larger than the
 1025 energy in its neighboring cells. Topological clusters are then formed by adding cells to the seed
 1026 which has at least one corner in common with a cell already in the cluster, and that has an energy
 1027 which is at least twice the noise level of the detector. In Figure 6.3, an example of calorimeter
 1028 clustering for a five-particle jet is shown for the HCAL (left) and ECAL (right). In the HCAL
 1029 (left), two seeds have been identified (gray-filled areas) inside a topological cluster consisting of 9
 1030 cells. These are then defined as two HCAL clusters, with a position as indicated by the red circles.
 1031 The green solid lines correspond to charged tracks reconstructed in the tracker, both pointing to
 1032 the center of the HCAL cluster seeds. The observed deposits left by the same particles are shown
 1033 on the right in Figure 6.3, where the K_L^0 , π^- and the two photons from the decay of a π^0 leave
 distinct clusters in the ECAL. The π^+ leaves no energy deposit in this case.

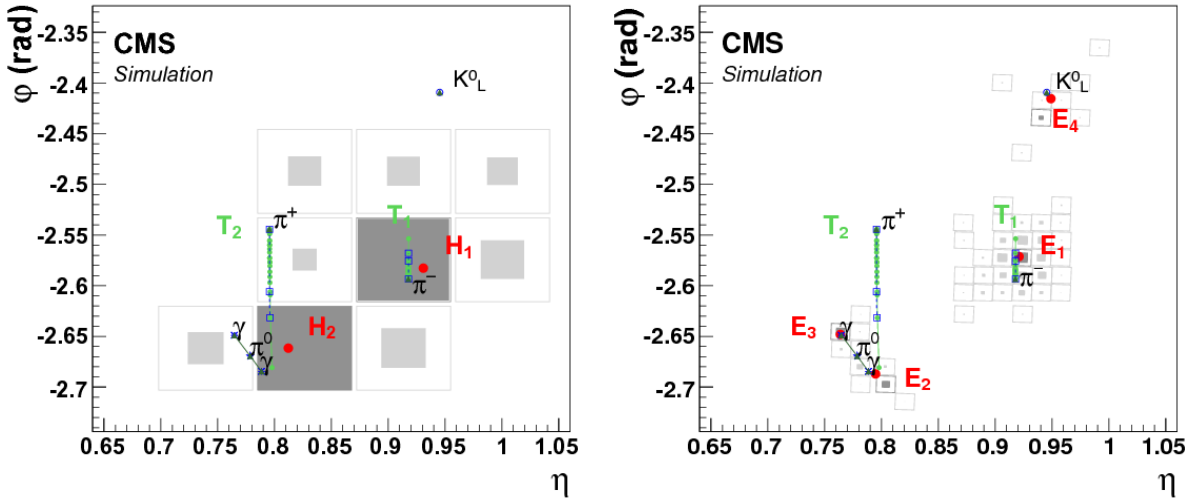


Figure 6.3: The $\eta - \phi$ views of calorimeter clusters generated by a five-particle jet in the HCAL (left) and in the ECAL (right). The squares correspond to calorimeter cells, where the inner area is proportional to the logarithm of the cell energy. Cluster seeds are depicted in dark gray. The dotted blue lines correspond to the simulated particle trajectories, while the green lines correspond to charged tracks reconstructed in the tracker [32].

1035 **6.2.2 Particle Flow identification**

1036 **The link algorithm**

1037 The link algorithm is the algorithm responsible for combining the particle flow elements from
 1038 different subdetectors. It can test any pair of elements in the event based on specific requirements
 1039 depending on the nature of the element, but is restricted to the nearest neighbors in the $\eta - \phi$
 1040 plane. The outputs of the link algorithm are so-called *PF blocks* of linked elements, either directly
 1041 linked or linked through having common elements.

- 1042 • **Inner track - calorimeter cluster link:** The track is interpolated from its last hit,
 1043 through the preshower layers, the ECAL, and ending in the HCAL at a nuclear interaction
 1044 length depth of 1. A link is made if the track is within the cluster areas, where the area
 1045 is enlarged by up to a cell in each direction to account for detector gaps. In case several
 1046 ECAL/HCAL clusters are linked to the same track, only the one with the smallest distance
 1047 in $\eta - \phi$ is kept.

- 1048 • **Calorimeter cluster - cluster link:** A link between ECAL and HCAL clusters, as well
 1049 as between ECAL and preshower clusters, is made when the cluster position of the more
 1050 granular calorimeter is within the cluster envelope of the less granular calorimeter. If there
 1051 are overlapping links, the one with the smallest distance is kept.

- 1052 • **Inner tracker - muon chamber link:** This procedure is described in Section 6.2.1.

1053 For each PF block, the reconstruction proceeds in the following order. First, muons are recon-
 1054 structed and their corresponding PF elements removed from the PF block. This is followed by
 1055 the reconstruction and subsequent removal of electrons and energetic photons. Finally, neutral
 1056 and charged hadrons are reconstructed.

1057 **Muons**

1058 First, isolated global muons are selected by requiring the sum of track p_T and calorimeter energy
 1059 deposits within a cone of $\Delta R = 0.3$ and not belonging to the muon track, to be smaller than
 1060 10 % of the muon p_T . If the muons are non-isolated, they are required to pass the tight muon
 1061 requirement [34] and have at least three matching track segments in the muon detector or have
 1062 matched calorimeter deposits compatible with being a minimum ionizing particle. Muons failing
 1063 both the requirements above are kept if their standalone muon track is of high quality and have a
 1064 lot of hits in the muon detectors, otherwise they are discarded. The muon momentum is defined

from the inner tracker measurement if the muon p_T is less than 200 GeV. Otherwise, it is chosen according to the track fit with the smallest χ^2 probability.

1067

1068 Muons used in this thesis are required to pass an isolation requirement in order to suppress
1069 the background from QCD multijet events where jet constituents are identified as muons. For this,
1070 a cone of radius $\Delta R = 0.3$ is constructed around the muon direction. The isolation parameter is
1071 defined as the scalar sum of the transverse momenta of all additional reconstructed tracks within
1072 the cone, divided by the muon p_T . Muon candidates with an isolation parameter less than 0.1
1073 are considered isolated and are used for further analysis.

1074 Further, the following selection criteria are applied:

- 1075 • the χ^2 of the global muon track fit must be less than 10;
- 1076 • at least one muon-chamber hit is included in the global-muon track fit and the global muon
1077 track fit must include at least one muon chamber hit;
- 1078 • muon segments in at least two of the muon stations must be matched to the muon tracker
1079 track;
- 1080 • the inner tracker track must be no more than 2 millimeters from the primary vertex in the
1081 xy plane and no more than 5 millimeters in the longitudinal direction;
- 1082 • at least one hit in the pixel detector;
- 1083 • at least six layers of the inner tracker must contain hits; and
- 1084 • at least three matching track segments must be found in the muon detectors

1085 **Electrons**

1086 The electrons are seeded from a GSF track, as described in Section 6.2.1. To differentiate electrons
1087 from charged hadrons, the energy deposit in the HCAL within a distance of 0.15 in the $\eta - \phi$
1088 plane of the supercluster is required to be less than 10 % of that of the supercluster. The electron
1089 candidate must further pass a requirement on the output of a dedicated electron-identification
1090 BDT, using inputs such as track-cluster distance, track χ^2 , and number of hits as input. In this
1091 step, isolated photons are also reconstructed, seeded from ECAL superclusters with $|E_T| > 10$ GeV|
1092 and no link to a GSF track. All the tracks and calorimeter deposits used to reconstruct electrons
1093 and isolated photons are further removed from the list of PF blocks.

1094 Only electrons passing certain quality requirements as listed in Table 6.1 are used in this thesis,
1095 with the following variable definitions:

- 1096 • E_T : The supercluster energy ($x \sin(\theta_{track})$), where θ_{track} is the polar angle of the electron
1097 track as measured in the inner tracker layer and extrapolated to the interaction vertex.
- 1098 • η^{sc} : η of the electron supercluster.
- 1100 • **isEcalDriven**: The electron is found through ECAL requirements rather than through
1101 Particle Flow and the tracker.
- 1103 • $\Delta\eta_{in}^{seed}$: difference in η between the track position as measured in the inner layer and extrapolated
1104 to the interaction vertex and then to the calorimeter, and the η of the supercluster.
- 1106 • $\Delta\phi_{in}$: difference in ϕ between the track position as measured in the inner layer and extrapolated
1107 to the interaction vertex and then to the calorimeter, and the ϕ of the supercluster.
- 1109 • **H/E**: Ratio of hadronic energy in the calorimeter towers, within a cone of radius 0.15 centered
1110 at the electron's calorimeter position to the electromagnetic energy of the supercluster.
- 1112 • $\sigma_{in\eta\eta}$: Measure of the energy spread in η in units of crystals of electron energy in a 5×5
1113 block centered on the seed crystal.
- 1115 • **ECAL Isolation**: The transverse electromagnetic energy of all reconstructed hits (with
1116 $E > 0.08$ GeV) in a cone of radius 0.3 centered at the electron's calorimeter position, excluding
1117 those in an inner cone with a radius of 3 crystals and an η strip with a width of 3 crystals.
- 1119 • **Hadronic Depth Isolation**: Defined as the transverse depth of the hadronic energy in
1120 the HCAL inside a cone of 0.3 centered on the electron calorimeter position, excluding
1121 towers in a cone of 0.15 radius.
- 1123 • **Track p_T Isolation**: The sum p_T of the tracks in a ΔR cone of 0.04 to 0.3, excluding an
1124 η region of 0.015.
- 1126 • d_{xy} : Transverse distance between the electron track and the primary vertex.

1129 Hadrons

1130 Finally, after the removal of muons and electrons, the remaining hadrons and non-isolated photons
1131 are identified. HCAL clusters with no track link are defined as neutral hadrons, while ECAL
1132 clusters with no track link are defined as photons (photons are exclusively associated to the ECAL

Variable	Barrel	Endcap
E_T	$> 35 \text{ GeV}$	$> 35 \text{ GeV}$
η range	$ \eta_{sc} < 1.4442$	$1.566 < \eta_{sc} < 2.5$
isEcalDriven	yes	yes
$\Delta\eta_{in}^{seed}$	< 0.004	< 0.006
$\Delta\phi_{in}$	< 0.06	< 0.06
H/E	$< 1/E + 0.05$	$< 5/E + 0.05$
full 5x5 $\sigma_{in in}$	n/a	< 0.03
full 5x5 E^{2x5}/E^{5x5}	$> 0.94 \text{ OR } E^{1x5}/E^{5x5} > 0.83$	n/a
EM+Had. Depth Iso.	$< 2 + 0.03 \times E_T + 0.28 \times \rho$	$E_T < 50 \text{ GeV}: < 2.5 + 0.28 \times \rho$ else: $< 2.5 + 0.03 \times (E_T - 50) + 0.28 \times \rho$
Track p_T iso.	$E_T < 100 \text{ GeV}: < 5 + 1.5 \times \rho$ else: $< 5 + 1.5 \times \rho$	$< 5 + 0.5 \times \rho$
Inner Layer Lost Hits	≤ 1	≤ 1
d_{xy}	< 0.02	< 0.05

Table 6.1: Summary of the electron requirements applied to all electrons used in this analysis.

1133 deposits since neutral hadrons leave only 3 % of their energy in the ECAL). The remaining HCAL
 1134 clusters are then linked to one or more tracks from the inner tracker. In order to determine
 1135 the particle content within a cluster, the sum of track momenta and the calorimeter energy is
 1136 compared. If the calorimeter energy is compatible with the sum of track momenta, a particle
 1137 for each track is inferred, with its corresponding energy taken from the track momentum. If the
 1138 calorimeter energy is larger than the sum of track momenta, a photon or a neutral hadron is
 1139 added, together with one charged hadron for each track within the cluster area.

1140 Missing transverse energy

1141 Neutrinos (and other predicted, non-SM weakly interacting particles) do not interact in the
 1142 detector and are instead inferred from the presence of a momentum imbalance in the detectors
 1143 transverse plane. The missing transverse momentum is defined as the negative p_T vector sum of
 1144 all reconstructed PF candidates in the event,

$$\vec{p}_T^{\text{miss}} = - \sum_i^N \vec{p}_{T,i}, \quad (6.1)$$

1145 and its magnitude, $|\vec{p}_T^{\text{miss}}|$, is referred to as the missing transverse energy E_T^{miss} (which is used as
 1146 a proxy for the neutrino p_T).

1147 6.3 Pile-up removal

1148 Particles originating from proton-proton interactions not associated with the hardest primary
1149 vertex, are denoted as pileup events. These distort observables of interest from the hard scattering
1150 event and must be mitigated through dedicated pileup removal techniques.

1151 6.3.1 Charged Hadron Subtraction

1152 As mentioned previously, primary vertices are reconstructed using tracks from charged hadrons.
1153 If a primary vertex does not correspond to the hard scattering vertex of the event, the charged
1154 hadrons (as reconstructed through Particle Flow) associated to this vertex (called a pileup vertex)
1155 are removed from the event collection of particles and will not participate in any further object
1156 reconstruction. This method is denoted charged hadron subtraction (CHS).

1157 6.3.2 Pile up per particle identification (PUPPI)

1158 CHS was the default pileup removal algorithm in CMS until very recently. In 2014, a new pileup
1159 removal algorithm with improved performance was proposed; the pileup per particle identification
1160 (PUPPI) [35] algorithm. PUPPI uses a combination of local shape information, event pileup
1161 properties, and tracking information to compute a weight describing the degree to which a given
1162 particle is likely to arise from pileup. First, a variable denoted α is computed based on the
1163 difference between soft radiation coming from pileup and the harder collinear QCD pattern. The
1164 shape of α for charged particles is then used as a proxy for all pileup particles and is used on an
1165 event-by-event basis to calculate a weight for each particle. This weight in turn describes the
1166 degree to which particles are pileup-like and are used to rescale the particle four-momenta. The
1167 shape variable for a given particle i is defined as

$$\alpha_i = \log \sum_{\substack{j \in \text{Ch,PV} \\ j \neq i}} \left(\frac{p_{T,j}}{\Delta R_{ij}} \right)^2 \Theta(R_0 - \Delta R_{ij}), \quad (6.2)$$

1168 where Θ is the step function and j refers to the neighboring charged particles from the primary
1169 vertex within a cone of radius $R_0 = 0.4$. Charged particles are defined as coming from the
1170 primary vertex if they are associated to the leading vertex of the event or are within a distance of
1171 $d_z < 0.3$ cm from the leading vertex. In order to determine the probability that a particle comes

from pileup, a χ^2 calculation is performed. The probability is defined as

$$\chi_i^2 = \frac{(\alpha_i - \bar{\alpha}_{PU})^2}{RMS_{PU}^2}, \quad (6.3)$$

where $\bar{\alpha}_{PU}$ is the median value of the α_i distribution for pileup particles in the given event and RMS_{PU} is its RMS. Each particle (neutral and charged) is then assigned a weight $w_i = F_{\chi^2, NDF=1}(\chi_i^2)$, where $F_{\chi^2, NDF=1}$ is the cumulative distribution function of the χ^2 distribution with one degree of freedom. Particles with $w_i < 0.01$ are rejected. In addition, a cut on the weighted p_T of neutral particles of $w_i \cdot p_{T,i} > (A + B \cdot N_{PV})$ GeV is applied, where N_{PV} correspond to the number of reconstructed vertices in the event and A and B are tunable parameters. The performance of the PUPPI algorithm compared to CHS for jet observables is shown in Figure 6.4. The top row shows the absolute mass resolution (left), as well as the mass resolution as a function

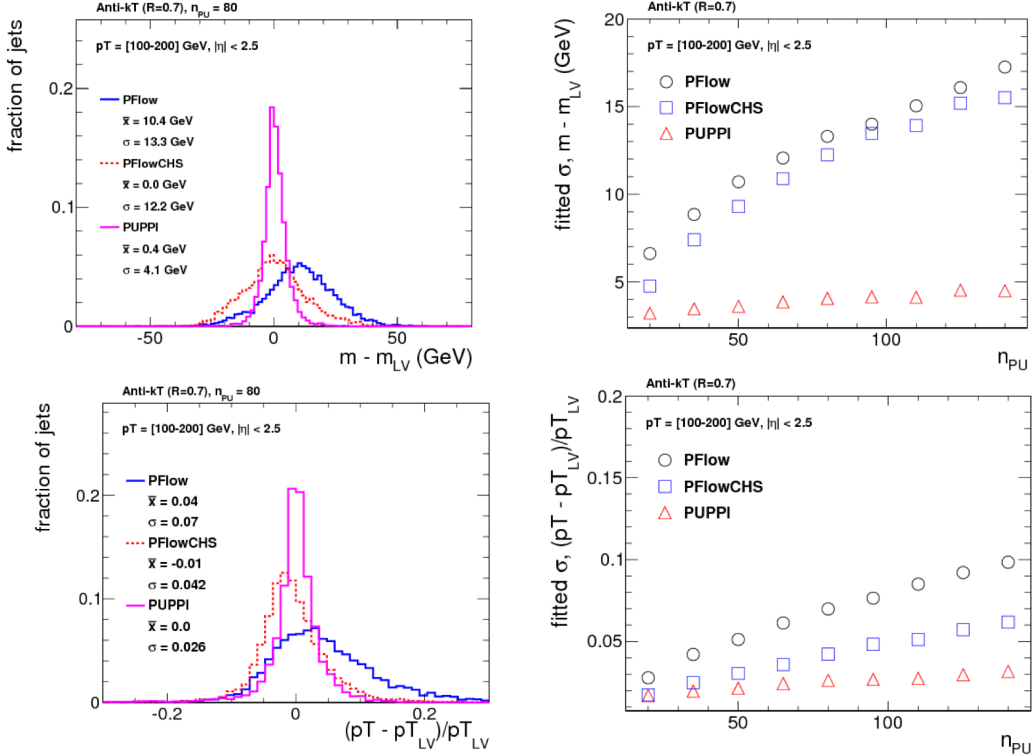


Figure 6.4: The mass (top) and p_T (bottom) resolution comparing PF-only (blue), PF+CHS (red) and PUPPI (pink) jets. The absolute resolution (left) as well as the resolution as a function of the number of reconstructed primary vertices in the event (right) is shown [35].

of N_{PV} for CHS jets (red) and PUPPI (pink) jets. The bottom row shows the corresponding quantities but for jet transverse momentum. A significantly better resolution on jet observables

1183 can be achieved using PUPPI as compared to CHS.

1184 6.4 Jet reconstruction

1185 As explained in Section 1.2.1, quarks and gluons are never themselves visible in a detector. Within
1186 10^{-23} seconds, the timescale of strong interactions, they fragment and hadronize into a collimated
1187 spray of hadrons, a so-called jet. In order to infer the properties of the original parton generating
1188 the jet, the properties of the full particle spray needs to be evaluated. Combining these particles
1189 algorithmically is non-trivial, and several algorithms jet-clustering algorithms exist. These provide
1190 a set of rules for grouping particles together into jets and are usually based on certain distance
1191 requirements between particles as well as rules for how to recombine their momenta. Thanks to
1192 Particle Flow, objects like charged hadrons, neutral hadrons and photons, together with their
1193 estimated energy and direction, are already defined and jet clustering in CMS therefore consists
1194 of associating these particles to one common origin.

1195 6.4.1 Jet clustering

1196 The most common jet clustering algorithms used in hadron colliders are the Cambridge/Aachen
1197 algorithm [36], the k_T algorithm [37] and the anti- k_T algorithm [38]. These are all sequential
1198 recombination algorithms, meaning they systematically go through each particle pair in the event
1199 and recombines them into one particle if the combination satisfies certain criteria. The rules,
1200 shared by all three algorithms, are as follows:

1. For each pair of particles i and j , compute the longitudinally invariant distances

$$d_{ij} = \min(p_{ti}^{2p}, p_{tj}^{2p}) \frac{\Delta R_{ij}^2}{R^2} \quad , \text{with} \quad \Delta R_{ij}^2 = (\eta_i - \eta_j)^2 + (\phi_i - \phi_j)^2, \text{ and} \quad (6.4)$$

$$d_{iB} = p_{ti}^{2p}, \quad (6.5)$$

1201 where d_{ij} is a measure of the relative transverse momenta between the particles, ΔR_{ij}^2 is
1202 the distance between them in the $\eta - \phi$ plane (which can be roughly translated into a
1203 jet radius), ΔR^2 corresponds to a distance parameter which controls the extension of the
1204 jet and d_{iB} is the distance between the particle and the beam. The parameter p is what
1205 separates the three algorithms from one another and controls the relative power of energy
1206 versus geometrical scales. For the anti- k_T algorithm, it is defined as $p = -1$; for the k_T
1207 algorithm, $p = 1$; and in the case of the C/A algorithm, $p = 0$. The consequences of these
1208 choices are explained in detail below.

- 1209 2. Find the minimum distance of d_{ij} and d_{iB} .
 1210 3. If this is d_{ij} , recombine particles i and j and return to step 1.
 1211 4. If it is d_{iB} , the particle i is defined to be a final state jet, and is removed from the list of
 1212 particles. The algorithm proceeds back to step 1.
 1213 5. Repeat until no particles remain.

1214 **Infrared and collinear safety**

1215 There are two requirements that are extremely important when defining jet algorithms: They
 1216 must be 1) *infrared* (IR) and 2) *collinear* (C) safe. *Infrared* safety corresponds to the requirement
 1217 that if the final state particles are modified by the presence of a soft emission, and there are always
 1218 soft emission in QCD events (both perturbative and non-perturbative), then the set of hard jets
 should remain unchanged. This is illustrated by the two left figures in Figure 6.5. Here, the

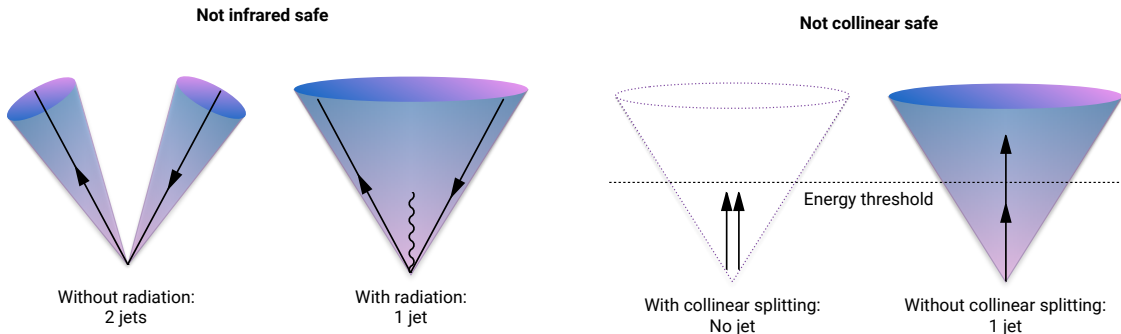


Figure 6.5: An illustration of what would happen for an infrared (left) and collinear (right) unsafe jet algorithm. If an algorithm is infrared unsafe, the presence of a soft emission changes the jet configuration. If an algorithm is collinear unsafe, then if a parton undergoes a collinear splitting this will change the configuration of the jet.

1219
 1220 algorithm is infrared unsafe: the presence of an additional soft gluon changes the jet configuration
 1221 from 2 to 1 jets. If an algorithm is *collinear* unsafe, it means that the jet configuration would
 1222 change if the hard parton undergoes collinear splitting (which a hard parton often does as part of
 1223 the fragmentation process and which are also part of non-perturbative dynamics, like the decay of
 1224 highly energetic hadrons). This is shown in the two left figures of Figure 6.5, where a hard parton
 1225 undergoing collinear splitting fails to be reconstructed due to its daughters being below the energy
 1226 threshold of the algorithm. All sequential recombination algorithms are trivially infrared safe.

1227 **The k_T algorithm**

1228 The k_T algorithm is the oldest of the sequential recombination algorithms and, due to its $p = 1$
1229 definition in Equations 6.4 and 6.5, follows the QCD branching structure in both p_T and in angle
1230 (in reverse). Soft particles are clustered together first, and the final step is the clustering of
1231 the two hardest particles. A consequence of this definition is that there is nothing that keeps
1232 arbitrarily soft particles from being defined as jets, and a minimum cut on the jet p_T should be
1233 introduced. Despite several favorable qualities, the k_T algorithm is not the algorithm of choice in
1234 most hadron collider experiments due to the irregular jets it produces, a consequence of clustering
1235 soft particles first.

1236 **The Cambridge/Aachen algorithm**

1237 The Cambridge/Aachen algorithm, with $p = 0$ in Equations 6.4 and 6.5, follows the QCD
1238 branching structure only in angle as the clustering order is based solely on spatial separation.
1239 The simplest of the algorithms, it recombines all pairs close in ΔR until $\Delta R_{ij} > R$. The benefits
1240 of this is that the clustering history contains information about the presence of any geometrical
1241 substructure within a jet, a feature that will become important in Section 6.5.

1242 **The anti- k_T algorithm**

1243 The default jet clustering algorithm in CMS is the anti- k_T algorithm [38], which follows the
1244 clustering rules in Equations 6.4 and 6.5 with $p = -1$. The algorithm favors the clustering
1245 between high p_T particles, and high and low p_T particles first, disfavoring clustering between soft
1246 particles. That means the algorithm grows around a hard core, yielding jets with a well-defined
1247 cone shaped area. Since the algorithm is infrared- and collinear-safe (IRC safe) and insensitive to
1248 the underlying event (parton remnants not from the hard process) and pileup, , it is chosen as
1249 the main jet algorithm in CMS. A comparison of the resulting jet area in the $\phi - \eta$ plane after
1250 clustering with either k_T , C/A and anti- k_T , is shown in Figure 6.6. The z-axis correspond to the
1251 parton p_T . One can clearly see that when clustering with the anti- k_T algorithm, the produced
1252 jets are circular, with a radius set by R , around the hardest parton.

1253 **6.4.2 PF jets in CMS**

1254 Jet algorithms in CMS mainly use the four-vectors of PF candidates as input and a pileup
1255 removal algorithm is usually applied before clustering occurs. If using CHS (Section 6.3.1),
1256 charged hadrons not associated to the primary vertex are discarded before clustering. If PUPPI

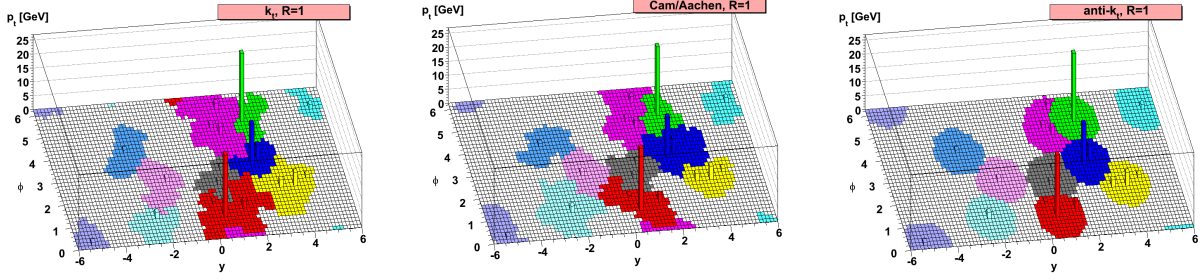


Figure 6.6: A comparison of the resulting jet cone area in the $\phi - \eta - p_T$ plane after clustering the same event with three different jet algorithms: k_T , C/A and $anti-k_T$. [38]

is used (Section 6.3.2), all the PF candidates are reweighted based on how likely they are to have originated from pileup. For the $anti-k_T$ algorithm, CMS by default uses two jet cone sizes: $R=0.4$ and $R=0.8$. Jets with $R=0.4$, called PFAK4, are used for single-prong jets while the larger $R=0.8$ jets, PFAK8, are more often used when looking for jets containing multiple hard quarks/gluons in order to contain all the hadronization products.

These jets are further required to pass certain jet identification requirements provided by the JetMET POG [39], in order to distinguish them from fake jets. All jets used in this analysis are required to pass the *tight ID* requirements which are as follows:

- the jet must contain at least two PF constituents;
- at least one of these constituents must be a charged hadron;
- the fraction of jet energy coming from neutral hadrons must be < 0.90 ;
- the fraction of jet energy coming from neutral electromagnetic energy must be < 0.90 ; and
- the fraction of jet energy coming from charged electromagnetic energy must be < 0.99 .

6.4.3 Jet energy corrections

All jets are further corrected for nonlinearities in p_T and pseudorapidity using standard CMS jet energy corrections (JEC), as described in Ref. [40]. These are intended to bring the measured jet energy closer to the true jet energy by correcting the jet energy scale (JES) and jet energy resolution (JER). The energy corrections are derived in three steps:

- L1: Energy offset corrections intended to remove pileup and electronic noise, both for data and simulation;
- L2L3: A relative (L2) and absolute (L3) correction to particle level jet response for simulation only; and

- 1279 • Residual: A correction for data only meant to correct for residual differences between data
 1280 and simulation.

These are illustrated in Figure 6.7.

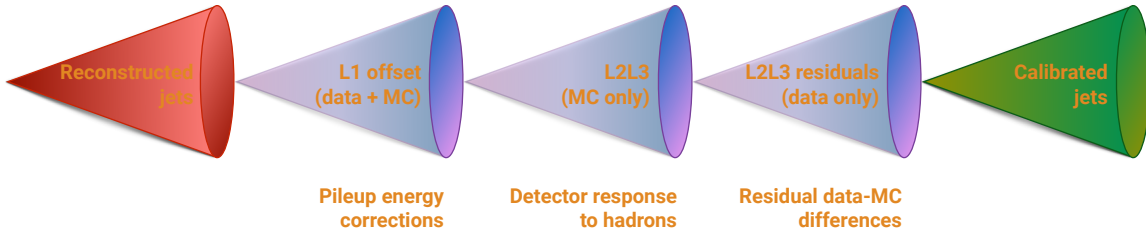


Figure 6.7: The CMS jet energy corrections are derived in three steps: A correction due to offset energy coming from pileup, applied to data and MC, a correction due to the particle-level jet response, also applied to data and MC and finally a correction to account for residual differences between data and MC.

1281

1282 L1 offset correction

1283 The largest correction is the L1 pileup offset correction, which is meant to subtract the additional
 1284 energy in a jet due to pileup. This is done on an event-by-event basis through the *jet area*
 1285 *method* which uses the effective area of the jet multiplied by the average event energy density
 1286 to calculate the size of the offset energy to be subtracted from each jet. An additional p_T - and
 1287 η -dependent term is added in order to account for different pileup densities in different parts
 1288 of the detector and for different jet energies. For data, an additional scalefactor to account for
 1289 data and simulation differences is computed. This is done by constructing a *Random Cone* (*RC*)
 1290 centered at a given η, ϕ and dividing the energy density within that cone in data, evaluated in a
 1291 dataset with no hard interactions (*Zero Bias*), by that of the true energy offset in simulation

1292 L2 relative and L3 absolute corrections

1293 After L1 corrections are applied, corrections to account for the detector response to hadrons are
 1294 derived based on the true detector response in QCD MC. The simulated particle response is
 1295 defined as the ratio

$$R_{\text{particle}} = \frac{p_{T,\text{reco}}}{p_{T,\text{particle}}}. \quad (6.6)$$

1296 These are derived in bins of particle-level p_T and reconstructed η : The L2 relative corrections are
 1297 intended to make the detector response uniform and are derived as a function of η , while the L3

1298 absolute corrections are derived as a function of jet p_T . These corrections are applied both to
1299 data and to MC.

1300 **Residual data corrections**

After L1, L2, and L3 corrections are applied, two additional corrections are derived only for data in order to account for any residual discrepancies between data and MC. This is done by looking at the transverse momentum balance between a jet which is to be calibrated, and some reference object (either another jet, a Z boson, or a photon). If the jet energy scale is not equal to one, a p_T imbalance will be visible. The measurements are performed in a data sample of dijets, where the statistical uncertainty is small but the energy of the reference object poorly measured, as well as in $Z(\mu\mu)$ +jet, $Z(ee)$ +jet and γ +jet samples, where the energy of the Z and γ is very well known but the statistics are small.

The “L2 relative” residual correction is measured in dijet events by comparing the measured p_T of the reference jet, required to be central with $\eta < 1.3$, to that of the calibration jet, with an unconstrained η . This is done as a function of jet η , in bins of average jet p_T . The “L3 relative” residual correction, is instead measured in W/γ + jet events by comparing the measured jet p_T to the p_T of the precisely measured Z/γ , as a function of jet p_T . The response,

$$R_{\text{jet},p_T} = \frac{p_{T,\text{jet}}}{p_{T,\text{ref}}}$$

1301 is then evaluated in data and in simulation. The ratio of the two, $R_{\text{data}}/R_{\text{MC}}$, defines the residual
1302 corrections.

1303

1304 The above description of jet energy corrections in CMS is meant as a rough, instructive summary
1305 only. A full description of the measurement techniques used in CMS can be found in [40].

1306 **6.5 Jet substructure reconstruction**

1307 In analyses looking for highly energetic (“boosted”) vector bosons, the opening angle between the
1308 vector boson quark decay products becomes so small that the highly boosted boson appears as a
1309 single large jet instead of two well-separated smaller jets. The distance between the two quarks,
1310 in the case of a hadronic decay, depends on the mass of the vector boson and its p_T and goes as

$$\Delta R = \frac{2M_V}{p_{T,V}}. \quad (6.7)$$

1311 Above a W boson p_T of 200 GeV, the two quarks are therefore merged into a single large cone jet
 1312 of size $R = 0.8$. A sketch of the two different situation is shown in Figure 6.8. If the W p_T is well
 1313 below 200 GeV, its decay products are two well-defined jets (left). However, once the W boson
 1314 transverse momenta is approximately 200 GeV, both the quarks are completely contained within
 a single jet (right), referred to as a W jet. In order to distinguish jets from hadronically decaying

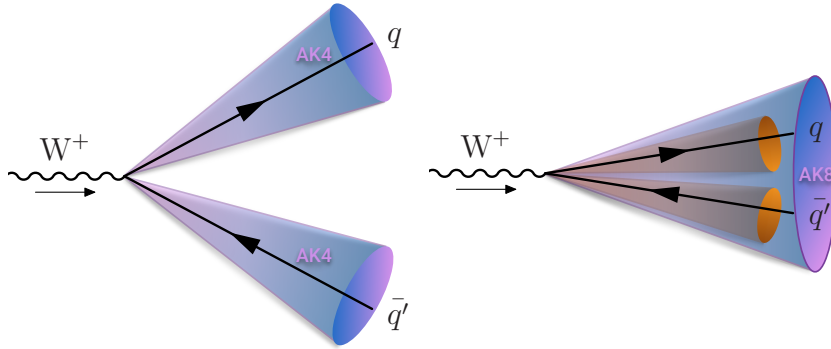


Figure 6.8: If the mass of the resonance is low enough, the quark decay products of each vector boson are well separated and clustered into distinguishable AK4 jets (left). If the transverse momentum of the vector boson is greater than 200 GeV, the vector boson decay products are merged into one single large cone AK8 jet.

1315
 1316 vector bosons, either W or Z bosons, from those of quarks or gluons produced by QCD, the jet
 1317 mass would in principle be a good discriminant since we know the W boson has a mass of around
 1318 80 GeV while the quark or gluon mass is close to zero. At very high transverse momenta, however,
 1319 the width (and therefore the mass) of QCD jets may become equally large. In addition, diffuse
 1320 radiation caused by the underlying event and pileup give rise to a significant number of additional
 1321 particles in the event contributing to the total jet mass. Therefore, being able to accurately and
 1322 efficiently separate highly boosted QCD jets from highly boosted vector bosons requires other
 1323 methods. In order to remove the underlying event and pileup, algorithms like PUPPI and CHS
 1324 can be used. In order to improve the mass resolution further, dedicated grooming algorithms
 1325 must be applied.

1326 6.5.1 Grooming

1327 Grooming was introduced as a tool to improve the mass resolution of large radius jets without
 1328 significantly changing the background and signal event numbers. It consists of removing the
 1329 softest parts of a jet in order to resolve its “true” mass, by means of reclustering and identifying
 1330 soft particles within the jet that can be removed.

1331 **Trimming**

The trimming algorithm [41] is a grooming algorithm mostly used at trigger level in CMS (also where it is used in this thesis). It works in the following way: starting from a large jet clustered with either anti- k_T or C/A (in the case of CMS), it reclusters the jet using the k_T algorithm in order to create subjets of some size R_{sub} . It then proceeds to check whether each subjet has a momentum fraction above a certain threshold,

$$p_{T,i}/p_{T,jet} > p_{T,frac}.$$

1332 If the subjet fails this requirement, it is removed. The remaining subjets are then assembled into
 1333 a new “trimmed” jet. The effect of trimming on real W boson jets and QCD quark or gluon jets
 1334 for different values of r_{sub} and $p_{T,frac}$ is shown in Figure 6.9. The best signal mass resolution is
 1335 obtained with $r_{sub} = 0.2$ and $p_{T,frac} = 0.03$, which is also the parameter setting that provides the
 1336 best signal discrimination from background by pushing the QCD jet mass closer to zero. These
 1337 are the default values of the tuned parameters of the trimming algorithm in CMS ($r_{sub} = 0.2$ and
 $p_{T,frac} = 0.03$).

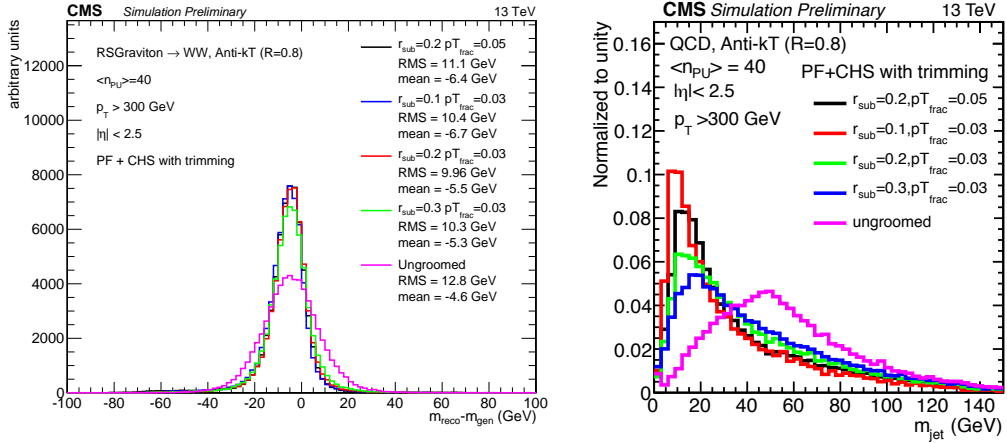


Figure 6.9: The effect of trimming on a signal jet (left) and a background jet (right) for different values of the tuned parameters r_{sub} and $p_{T,frac}$ [42].

1338

1339 **Pruning**

1340 The pruning algorithm, in addition to removing soft particles, has an additional requirement on
 1341 the distance between any recombination that is at wide angle. It proceeds by reclustering the jet

1342 with the C/A algorithm, requiring at each step that

$$\frac{\min(p_{T,i}, p_{T,j})}{p_{T,P}} > z_{cut} \quad \text{and} \quad \Delta R_{i,j} < D_{cut} = \frac{2r_{cut}m_{jet}}{p_T}. \quad (6.8)$$

1343 The first requirement is a requirement on the hardness of the combination. The variables $p_{T,i}$ and
 1344 $p_{T,j}$ correspond to the transverse momenta of each protojet (single particle or group of particles
 1345 already combined in a previous step) and $p_{T,P}$ is the combined p_T of the two. The protojet with
 1346 the lowest transverse momenta is removed if its hardness is below z_{cut} , or if it forms an angle
 1347 wider than D_{cut} relative to the axis of the recombination of the two protojets. In CMS, the tuned
 1348 parameters are set to $r_{cut} = 0.5$ and where $z_{cut} = 0.1$. Figure 6.10 shows the ungroomed as well
 1349 as the pruned jet mass distribution for signal (left) and background (right) jets. The highest
 amount of signal and background separation in CMS, is achieved with $r_{cut} = 0.5$ and $z_{cut} = 0.1$.

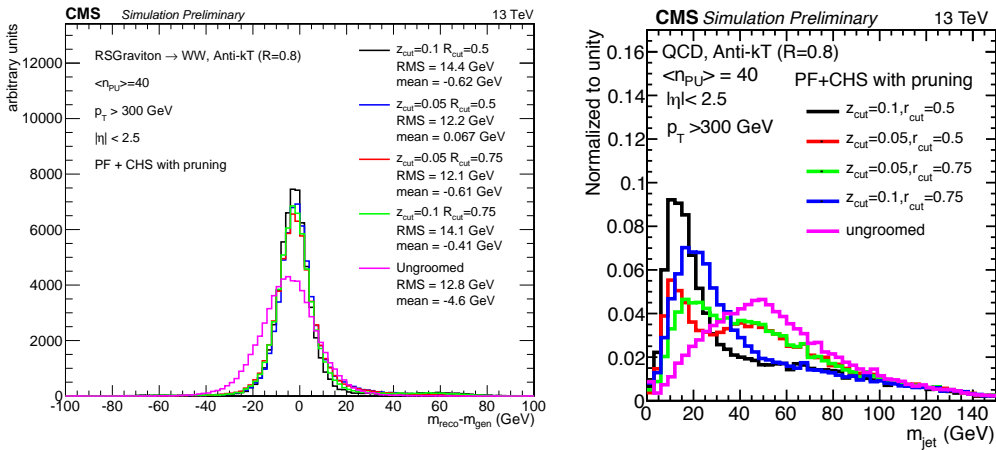


Figure 6.10: The effect of pruning on a signal jet (left) and a background jet (right) for different values of the tuned parameters z_{cut} and r_{cut} [42].

¹³⁵¹ **Modified Mass Drop Tagger and Soft Drop**

¹³⁵² The mass drop tagger (MDT) [43] is based on the idea that a W or Z jet is formed by two quark
¹³⁵³ subjets and that, therefore, the mass of each subjet is much smaller than their combined mass
¹³⁵⁴ (and much smaller than the mass of the boson itself). A QCD jet is, on the other hand, formed
¹³⁵⁵ by continuous soft radiation, meaning that its heaviest subjet should be close to the mass of the
¹³⁵⁶ jet itself. The MDT tagger therefore starts from a jet j clustered with the C/A algorithm and
¹³⁵⁷ then declusters it again, defining subjets s_1 and s_2 , where $m_{s_1} > m_{s_2}$. If a significant mass drop
¹³⁵⁸ occurred during declustering, $m_{s_1} < \mu m_j$, where m_j is the mass of the jet j , and the splitting
¹³⁵⁹ is not too asymmetric, $\min(p_{T,s_1}^2, p_{T,s_2}^2) \Delta R(s_1, s_2) / m_j^2 > y_{cut}$, the jet j is selected as the tagged
¹³⁶⁰ jet. Otherwise j is set equal to s_1 and the procedure starts over. The modified mass drop
¹³⁶¹ tagger (mMDT) [44] is a modification of MDT where the subjet with the largest transverse mass,
¹³⁶² $m^2 + p_T^2$, instead of bare mass, m , is followed. This fixes a flaw in the MDT tagger so that, in
¹³⁶³ cases where the mass drop and asymmetry conditions are not satisfied, the more energetic rather
¹³⁶⁴ than the heavier branch is followed. The recommended default version of mMDT additionally
¹³⁶⁵ does not use the mass drop condition, $m_{s_1} < \mu m_j$, as it was shown to have a negligible impact
¹³⁶⁶ on the jet mass distribution for QCD jets [44]. In addition, the mMDT algorithm by default uses
¹³⁶⁷ a z_{cut} criteria, as for pruning, rather than a y_{cut} criteria. The modified mass drop condition is
¹³⁶⁸ generalized through the soft drop declustering method [45], simply called Soft Drop, which allows
¹³⁶⁹ for different types of angular requirements to enter the condition. The Soft Drop condition is the
¹³⁷⁰ following,

$$\frac{\min(p_{T,1}, p_{T,2})}{p_{T,1} + p_{T,2}} > z_{cut} \frac{\Delta R_{12}^\beta}{R_0}, \quad (6.9)$$

¹³⁷¹ where the asymmetry condition now is defined directly through the transverse momentum fractions
¹³⁷² of the subjets, rather than through a k_T distance to the jet mass. If the splitting is not too
¹³⁷³ asymmetric, the condition is met and the full jet is deemed the softdrop jet. Otherwise only the
¹³⁷⁴ highest- p_T subjet is kept and the declustering continues. If the jet can not be declustered any
¹³⁷⁵ further, it can either be removed from consideration, so-called “tagging”-mode, or deemed the
¹³⁷⁶ final soft-dropped jet, “grooming”-mode. A $\beta = 0$ corresponds to the modified mass drop tagger
¹³⁷⁷ and removes all soft emission wider than the dominant two-prong substructure. For $\beta > 0$, soft
¹³⁷⁸ radiation is removed, but some fraction of soft-collinear radiation is kept. Lastly, with $\beta < 0$,
¹³⁷⁹ Soft Drop can remove soft as well as collinear radiation. The performance of Soft Drop on W jets
¹³⁸⁰ and QCD quark/gluon jets for different values of β is shown in Figure 6.11. The modified mass
¹³⁸¹ drop tagger (Softdrop with $\beta=0$) with $z_{cut} = 0.1$ is the default Soft Drop settings in CMS, due
¹³⁸² to it providing the best signal/background discrimination while maintaining an excellent signal
¹³⁸³ mass resolution.

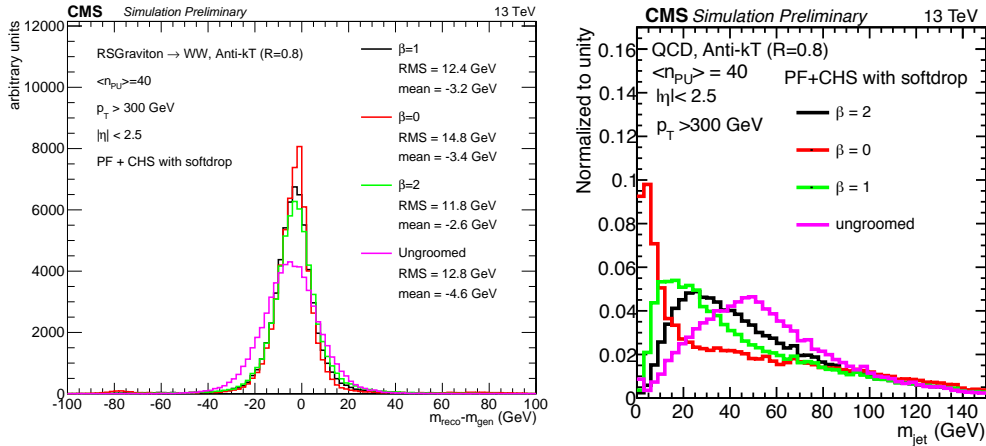


Figure 6.11: The effect of softdrop on a signal jet (left) and a background jet (right) for different values of the tuned parameters β . $\beta = 0$ corresponds to the Modified Mass Drop Tagger, which is the default Softdrop setting in CMS [42].

1384 6.5.2 N-subjettiness

1385 After using the algorithms above, there is still information in the jet structure itself that can
 1386 distinguish W/Z jets from quark/gluon jets. A W or Z jet consists of two well-defined high- p_T
 1387 subjets. A quark/gluon jet instead is made from a single parton, and consists of several large angle,
 1388 asymmetric splittings, as illustrated in Figure 6.12. The N-subjettiness algorithm [46]

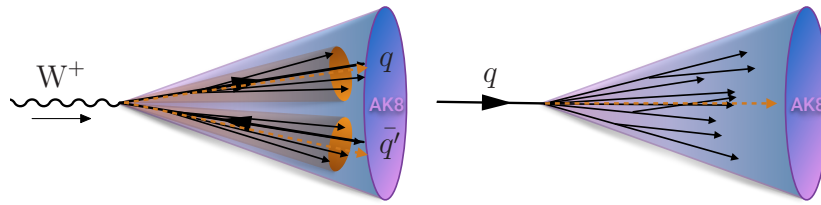


Figure 6.12: A jet stemming from the decay of a W will usually have two well-separated high- p_T subjets, while a jet with a single-prong origin consists of several large angel splittings.

1388
 1389 takes advantage of this fact by attempting to count the number of hard sub-elements within a jet.
 1390 This is quantified through the n-subjettiness variable, τ_N , defined as

$$\tau_N = \frac{1}{d_0} \sum_k p_{T,k} \min(\Delta R_{1,k}, \Delta R_{2,k}, \dots, \Delta R_{N,k}), \quad (6.10)$$

1391 where k runs over all the jet constituents, $p_{T,k}$ is the constituent transverse momentum, and
 1392 $\Delta R_{i,k}$ is the distance between the constituent and candidate subjet axes. These subjet axes are

1393 obtained through a one-pass optimization procedure which minimizes N-subjettiness [47]. The
1394 normalization factor in front is given as

$$d_0 = \sum_k p_{T,k} R_0, \quad (6.11)$$

1395 where R_0 corresponds to the cone size of the initial jet. With this definition, jets with $\tau_N = 0$
1396 have most of their constituents aligned along the subjet axes. However, if $\tau_N \gg 0$, a large
1397 fraction of the energy is radiated away from the subjet directions and the jet is more likely to
1398 have more than N subjets. In CMS, and as recommended by the authors in [46], the ratio τ_2/τ_1
1399 is used to discriminate W jets from QCD jets. The reason for this is that, while signal jets are
1400 expected to have a large τ_1 , quark/gluon can similarly have large τ_1 due to the diffuse radiation
1401 present. However, QCD jets with a large τ_1 tend to have an equally large τ_2 , while signal jets
1402 do not, hence the ratio of the two provides greater separation power. This can be seen from
Figure 6.13. In CMS, the n-subjettiness algorithm is by default applied to ungroomed jets. The

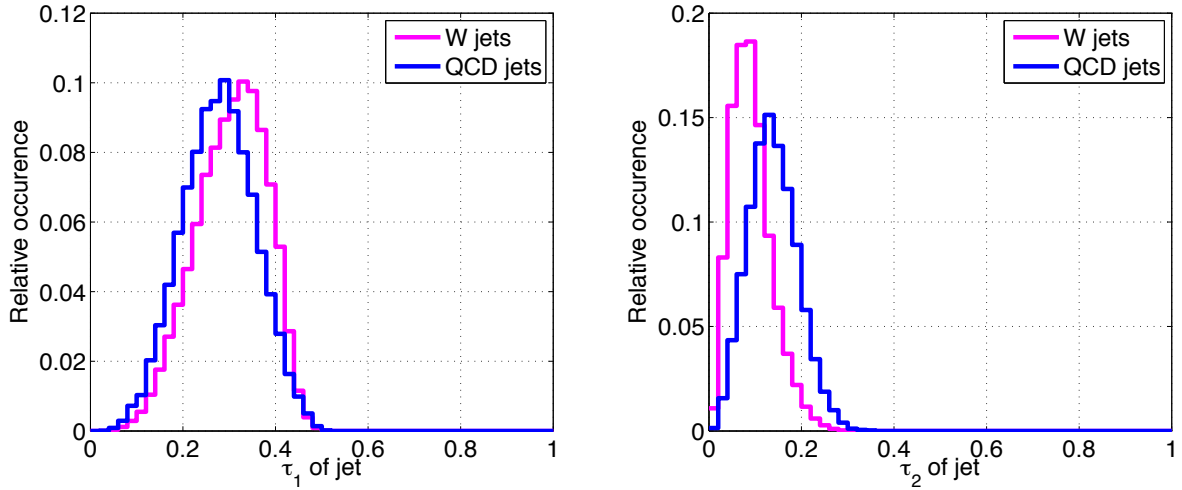


Figure 6.13: The distribution of the n-subjettiness variables τ_1 (left) and τ_2 (right) for signal jets and background jets. On their own, the τ_N variables provide little discriminating power [46].

1403
1404 distribution of τ_{21} for signal and background jets with different pileup subtraction algorithms
1405 applied is shown in Figure 6.14, where τ_{21} in combination with PF+PUPPI (green), yields a
1406 distribution most similar to the generated one (black).

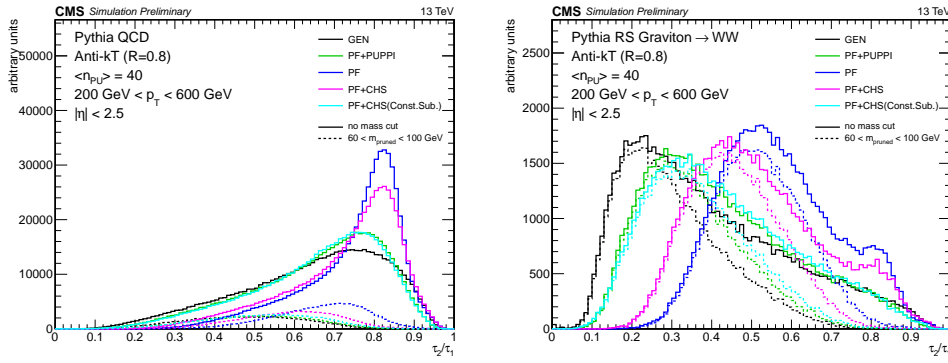


Figure 6.14: The distribution of the n-subjettiness ratio τ_{21} for signal jets (left) and background jets (right) with different combinations of pileup subtraction algorithms applied. The solid lines corresponds to the τ_{21} distribution with no mass cut applied, while the dotted lines are within a mass window of 60–100 GeV [42].

6.5.3 Vector boson tagging

In order to discriminate W and Z bosons from quark/gluon jets a combination of a groomer and shape-tagger (like n-subjettiness) is usually used. Typical values for tagging W jets is a groomed jet mass between 60 and 100 GeV and $\tau_{21} < 0.5$. The exact combination and value of cuts is analysis dependent, and has been optimized for each search presented in this thesis. The details are thoroughly explained in each section.

Polarization effects

The vector boson polarization has a significant effect on the W-tagging efficiency. The helicity angle θ^* , defined as the angle between the outgoing quark daughters of the W boson in its rest frame relative to its direction of motion [48], is very different for longitudinally polarized vector bosons, W_L , and transversely polarized vector bosons W_T [49]. Figure 6.15 shows the $\cos \theta^*$ distribution for the outgoing quarks from $W_L \rightarrow q\bar{q}$ (black) and $W_T \rightarrow q\bar{q}$ (red) decays, and it can be observed that transversely polarized W bosons decay with the quarks emitted closer to the vector boson direction of motion. The consequence of this, is that there is a higher asymmetry in the transverse momenta of the two quarks from a W_T decay. This in turn causes grooming algorithms, designed to remove soft constituents of a jet, tend to reject particles coming from the softer quark, resulting in a lower jet mass and a drop in tagging efficiency. Figure 6.16 shows the W-jet tagging efficiency versus q/g jet mistagging rate for a selection on the jet pruned mass of $60 \text{ GeV} < m_{\text{pruned}} < 100 \text{ GeV}$, scanning τ_{21} cuts (here for CA R=0.8 jets).

The tagging efficiency for transversely polarized W bosons (green) is significantly lower than

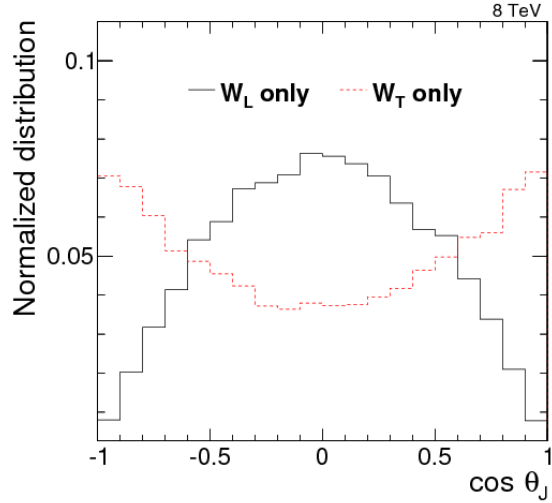


Figure 6.15: The helicity angle for generated quarks from $W_L \rightarrow q\bar{q}$ (black) and $W_T \rightarrow q\bar{q}$ (red) decays [49].

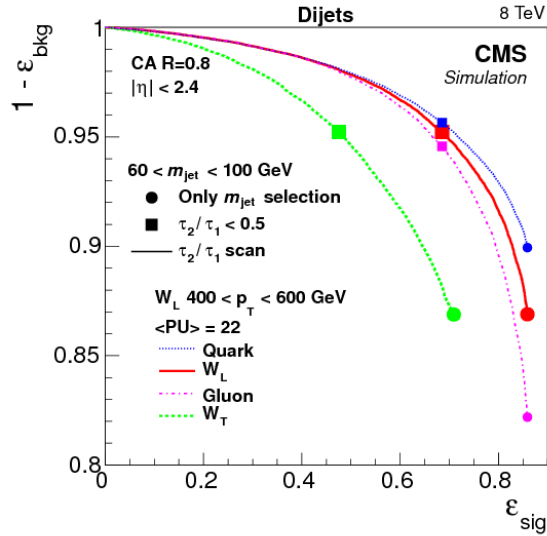


Figure 6.16: The helicity angle for generated quarks from $W_L \rightarrow q\bar{q}$ (black) and $W_T \rightarrow q\bar{q}$ (red) decays [49].

¹⁴²⁷ the tagging efficiency for longitudinally polarized bosons (red). This can be explained by looking
¹⁴²⁸ at the $\cos \theta^*$ distribution on reconstructed level, using the C/A subjets, with a cut on the jet
¹⁴²⁹ pruned mass of $60 \text{ GeV} < m_{\text{pruned}} < 100 \text{ GeV}$, as shown in Figure 6.17. When comparing to

¹⁴³⁰ the distribution at generator level with no groomed mass window applied, Figure 6.15, one can see that the W_T jets with $\cos \theta \sim 1$ are completely removed. This is due to two effects: the

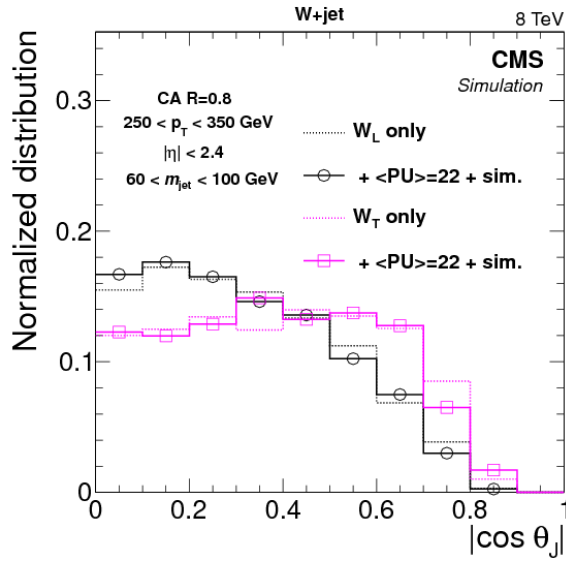


Figure 6.17: The helicity angle for subjets from $W_L \rightarrow q\bar{q}$ (black) and $W_T \rightarrow q\bar{q}$ (pink) decays [49].

¹⁴³¹
¹⁴³² p_T -asymmetry explained above and the fact that the ΔR distribution between the two quarks is
¹⁴³³ much smaller in the case of W_L , making them more likely to be fully contained within a jet cone
¹⁴³⁴ of $R=0.8$.

1435 6.6 Monte Carlo Event Generators

1436 Monte Carlo event generators offer a realistic estimate of high-energy collisions on an event-by-
1437 event basis, allowing us to estimate signal and background processes accurately. Simulated events
1438 are usually produced in three steps, beginning with the hard process through hadronization and
1439 decay. First, a matrix element generator simulates the hard scattering process and subsequent
1440 decays. Secondly, the showering and hadronization of unstable particles is performed and, lastly,
1441 the final-state particles are passed through a full detector simulation in order to reproduce a
1442 range of experimental effects.

1443 General-purpose Monte Carlo (GPMC) generators, like HERWIG ++ [50] and PYTHIA 8 [51],
1444 deal with both perturbative as well as hadronization phenomena, simulating an event all the
1445 way up until detector simulation. In HERWIG ++ and PYTHIA 8, the hardest processes are only
1446 simulated at the lowest order of perturbative expansion, meaning $2 \rightarrow 2$ or $2 \rightarrow 3$ scatterings.
1447 In order to have tree-level matrix elements with an arbitrary final-state multiplicity, they can
1448 be combined with programs used to generate parton-level events at higher accuracy, which are
1449 then processed through showering and hadronization with the GPMC generators. One popular
1450 program for generating matrix elements is MADGRAPH [52]. This, however, still correspond
1451 to a tree-level (leading order) approach. To go to next-to-leading-order (NLO), meaning the
1452 inclusion of virtual corrections, two methods exist: MC@NLO [53, 54] and POWHEG [55]. These
1453 combine the full next-to-leading-order prediction for inclusive processes with the subsequent
1454 parton showers, either by a subtraction method regularizing the real contributions, or by a
1455 matrix-element correction of the parton shower branching probability. After hadronization, all
1456 final state particles are passed through a full simulation of the CMS detector. This is done with
1457 GEANT4 [56], which models the interaction and showering of particles with materials, and outputs
1458 position-dependent energy deposits.

1459 For the work presented in this thesis, simulated samples of the Standard Model background
1460 processes are used to optimize the analysis and in some cases provide flexible background templates.
1461 QCD multijet production is simulated with four generator configurations: 1. PYTHIA standalone,
1462 2. the LO mode of MADGRAPH matched with PYTHIA, 3. POWHEG matched with PYTHIA and 4.
1463 HERWIG++ 2.7.1 with tune CUETHS1 [57]. Top-quark pair production is modeled with POWHEG
1464 and showered with PYTHIA unless otherwise stated. W+jets and Z+jets production are simulated
1465 with the leading-order (LO) mode of MADGRAPH matched with PYTHIA. Signal samples are
1466 generated with standalone PYTHIA. All samples are processed through a GEANT4-based simulation
1467 of the CMS detector. To simulate the effect of additional proton-proton collisions within the
1468 same or adjacent bunch crossings (pileup), additional inelastic events are generated using PYTHIA

¹⁴⁶⁹ and superimposed on the hard-scattering events. The simulated MC events are finally weighted to reproduce the distribution of the number of pileup interactions observed in data.

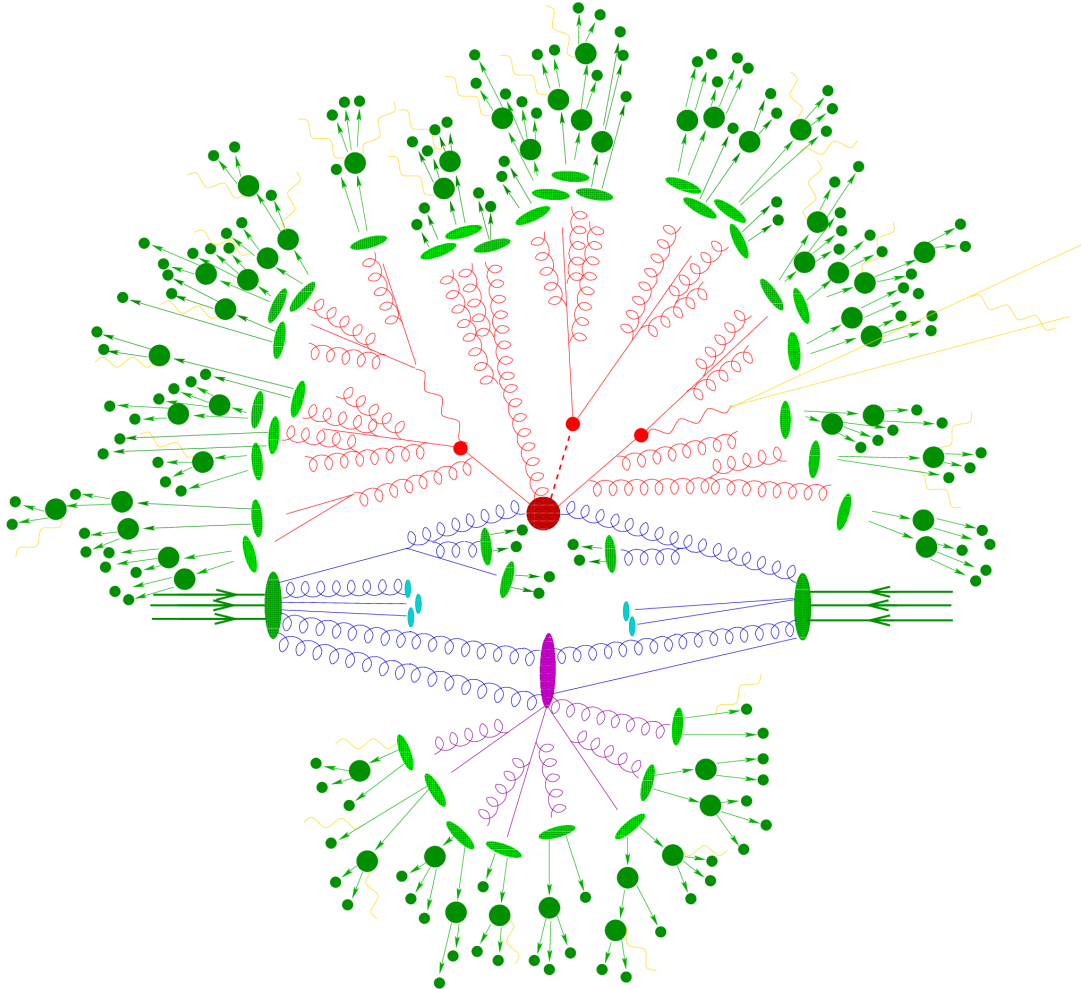


Figure 6.18: An illustration of a hadron-hadron collision as simulated by a MC generator. The hard collision center corresponds to the red circle and the branches represent parton showers. The purple circle is a second hard scattering event. The dark green circles represent the decay of hadrons and the yellow lines illustrate photons.

1471

Part III

1472

Diboson resonance searches in CMS

1473

CHAPTER 7

1474

Search I: First search for diboson resonances at 13 TeV

1475

1476 When the LHC started its Run II data taking period in summer 2015, it would be the first time
1477 ever for a particle collider to produce collisions with center-of-mass energies as high as 13 TeV.
1478 The Higgs boson, for which the LHC was designed to observe, had been discovered at the end of
1479 the previous data taking era, leaving us with a Standard Model that we know is either in need
1480 of extensions or only an effective theory valid in a certain energy domain. The Run II search
1481 program would therefore be oriented around two main efforts: Precision measurements of the
1482 newly discovered Higgs boson and searches for physics beyond the standard model.

1483

1484 I started my PhD four months before the first 13 TeV collisions took place and had to consider
1485 the following: What was the most interesting search that could be done on a short time scale
1486 (to be presented 6 months after first collisions, which would be at the CERN end-of-year
1487 “Jamboree”), whose physics objects could be reconstructed and understood on a relatively short
1488 time scale, and would be robust enough in case there were issues with the never-before-validated
1489 13 TeV Monte Carlo?

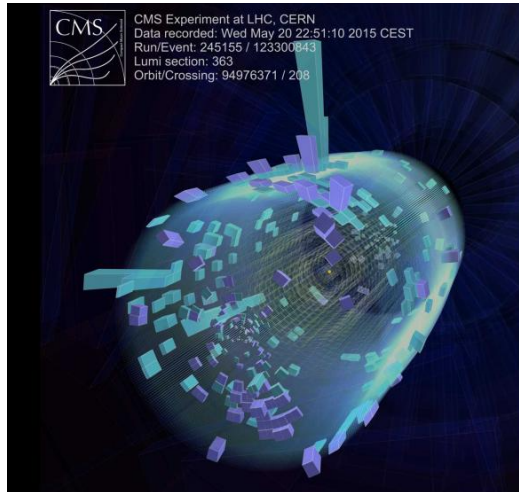
1490

1491 The attention of the high-energy physics community has in the past years been focused on certain
1492 “hot topics”: In 2018 and currently in 2019, the excitement is over leptoquarks, which could
1493 explain anomalies observed by LHCb and b-factories; in 2016 and 2017 it was diphoton resonances,
1494 with $> 3\sigma$ excesses observed at the same mass in both CMS and ATLAS. And in 2015 during the
1495 13 TeV LHC start-up, attention was centered on diboson resonances in the all-hadronic final state.
1496 The choice was therefore clear: My first analysis would be a search for diboson resonances in the
1497 boosted dijet final state. With a background model based on a smooth fit to data in the signal region,

1498 *eliminating the need for accurate QCD MC predictions, this was a simple one-background only*
 1499 *(QCD) analysis, feasible to finalize in one year, given dedication and sufficient effort. Despite its*
 1500 *straightforwardness, due to observed 8 TeV excesses, it was in addition considered a high-profile*
 1501 *analysis.*

1502

1503 *This search became one of the first “boosted” searches published with data collected with a 13*
 1504 *TeV center-of-mass energy, as well as the first search to take advantage of dedicated “grooming”*
triggers. It was published with 2.7 fb^{-1} of 2015 data.



Published in the Journal of High Energy Physics (2017), DOI: [10.1007/JHEP03\(2017\)162](https://doi.org/10.1007/JHEP03(2017)162)

1505

1506 7.1 A small bump

1507 On June 2nd, 2015, the day before CMS recorded its first ever 13 TeV event, a pre-print appeared
 1508 on the arXiv titled, “Search for high-mass diboson resonances with boson-tagged jets in proton-
 1509 proton collisions at $\sqrt{s} = 8$ TeV with the ATLAS detector” [52]. It was an analysis of the full
 1510 ATLAS Run 1 dataset, corresponding to 20.3 fb^{-1} , searching for heavy resonances decaying to
 1511 vector bosons in the all-hadronic state. The analysis documented a 3.4σ excess for a heavy
 1512 resonance decaying to WZ with a mass of around 2 TeV. The corresponding CMS analysis,
 1513 published the previous year, had a 1.3σ excess at roughly the same resonance mass, but was
 1514 mostly compatible compatible with a WW final state hypothesis [58]. Figure 7.1 shows the
 1515 corresponding dijet invariant mass spectrum as seen by ATLAS (left) and the upper limit on the
 1516 production times the cross section for a G_{Bulk} decaying to WW (right) as documented by CMS.

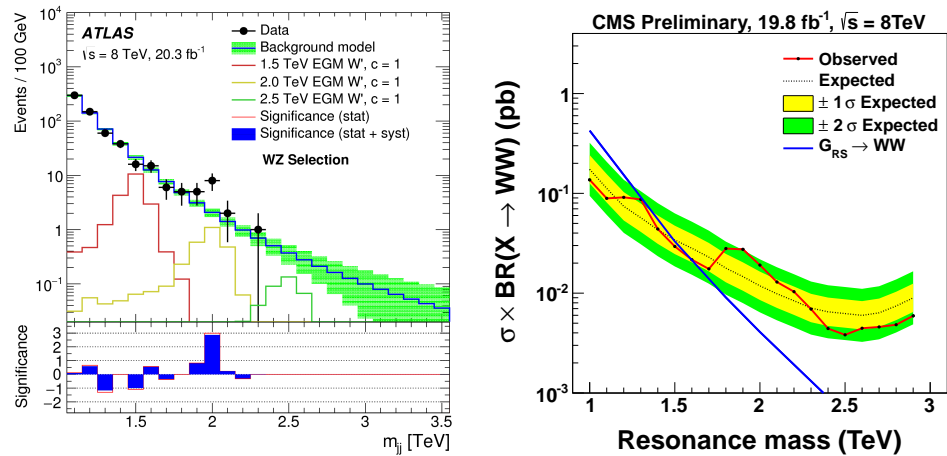


Figure 7.1: A “bump” corresponding to 3.4σ in the dijet invariant mass spectrum around 2 TeV (left) observed by ATLAS when analyzing the full 8 TeV dataset [52], together with a similar excess (1.3σ) observed in the corresponding CMS analysis [58].

1517 The two measurements were found to be compatible, favoring a heavy resonance with a
 1518 production cross section of around 5 femtobarn and a mass between 1.9 and 2.0 TeV decaying to
 1519 either WW, WZ or ZZ [59]. Figure 7.2 shows the obtained p-value from the ATLAS (red) and
 1520 CMS (blue) searches, as well as their combination (black). In addition to the observed excesses
 1521 in the vector boson final states, another 3σ excess for a resonance with a mass of 1.8 TeV had
 1522 been observed in the search for heavy resonances decaying to a W and a Higgs boson [60] at 1.8
 1523 TeV. The combination of the excesses and the timing of the ATLAS paper, naturally led to some
 1524 excitement, and in the coming weeks, the arXiv was flooded with theory papers attempting an

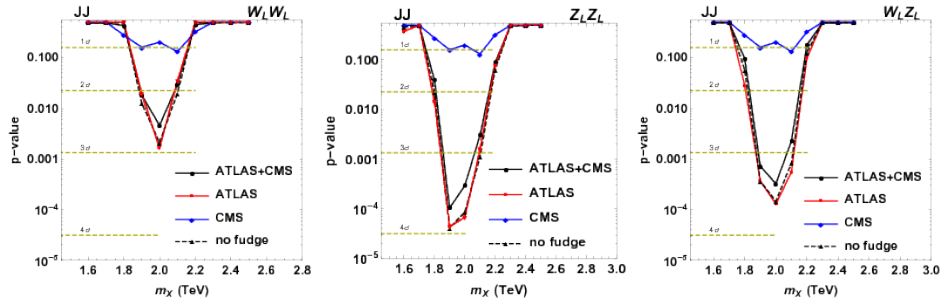


Figure 7.2: p-values as a function of resonance mass obtained with an emulation of the ATLAS (red) and CMS (blue) searches as well as the combination of the two (black). Here for a W_W (left), W_Z (middle) and Z_Z (right) hypothesis [59].

explanation of the deviations.

In addition, one of the main benefits of increasing the LHC center-of-mass energy from 8 to 13 TeV was that the partonic luminosity would increase. One could therefore expect the same number of signal events in the 20 fb^{-1} data set collected with a center-of-mass energy of 8 TeV, for a considerably smaller luminosity with a center-of-mass energy of 13 TeV. Figure 7.3 shows the system mass that can be probed with the expected 2015 integrated luminosity of 3 fb^{-1} collected with a center-of-mass energy of 13 TeV, as a function of the probeable mass with 20 fb^{-1} of 8 TeV data for different partonic channels of qq , qg , and gg . For example, a 2 TeV mass resonance would be observable in both datasets. We therefore expected that the small excess observed in the VV all-hadronic final state would be observable in the 2015 dataset if the signal was genuine.

7.2 Analysis strategy

When a resonance X with a mass above 1 TeV decays into a vector-boson pair, the bosons have a very high energy ($\tilde{p}_T = M_X/2 = 500 \text{ GeV}$, assuming X is produced at rest) is referred to as boosted. The decay products of a hadronically decaying boosted vector boson will therefore not appear as back-to-back in the lab frame but rather be collimated, as described in Section 6.5. This results in a final state with two high-pt, large-radius jets, such that the AK algorithm with an $R=0.8$ is expected to fully contain the two quarks coming from the vector boson decay. This is illustrated in Figure 7.4. The two jets are each expected to have a mass around the W or Z boson mass, and some intrinsic substructure stemming from their two-pronged decay. The invariant mass of the dijet system, m_{jj} , should be roughly equal to the resonance mass M_X . This dijet system is the final state under scrutiny and the dijet invariant mass is the parameter of interest.

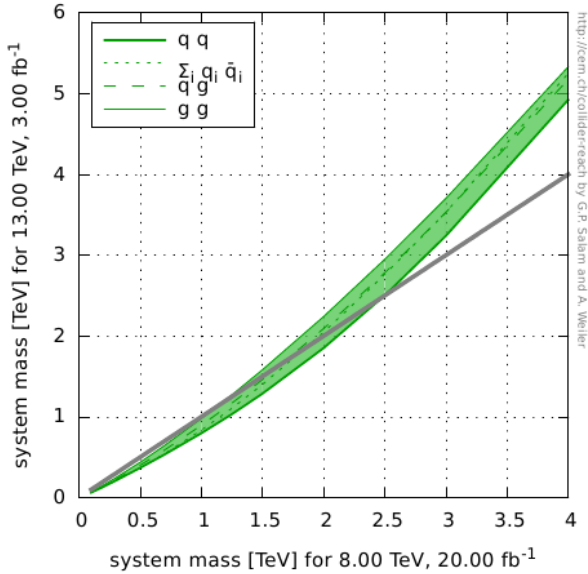


Figure 7.3: The system mass that can be probed with 3 fb^{-1} of 13 TeV data (y-axis) as a function of the probeable system mass with 20 fb^{-1} of 8 TeV data (x-axis) for different partonic channels (generated with [61]).

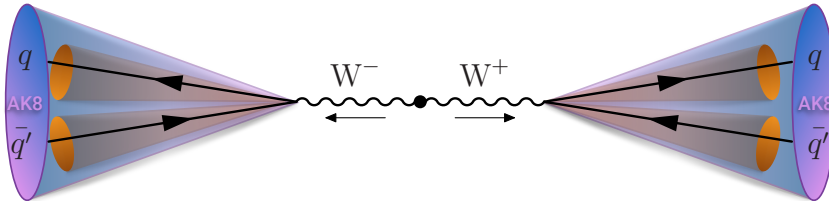


Figure 7.4: If a heavy ($> 1 \text{ TeV}$) resonance decays into vector bosons, the transverse momentum of each boson will be large and its decay products are merged into one single large cone AK8 jet.

1547 The final states of WW, ZZ, and WZ would produce similar final states.

1548 The main background for such an analysis is QCD multijet events. As mentioned in Section 6.5,
 1549 quark/gluon jets can obtain a high mass due to diffuse radiation and QCD processes have such a
 1550 large cross section that the number of QCD jets with a mass compatible with the W mass can be
 1551 large. In order to discriminate between the two, we take advantage of three properties. First, the
 1552 groomed mass of signal and background jets should be very different. Second, signal jets should
 1553 appear two-prong like, as opposed to quark/gluon jets, and third, the dijet invariant mass for the
 1554 signal process should peak around the resonance mass while the QCD spectrum is predicted to
 1555 be smoothly falling. Section 7.5 explains this assumption in more detail. The strategy therefore

1556 consists of performing a smoothness test on m_{jj} of the observed data, a so-called “bump-hunt”,
 1557 by assuming that the signal will appear as a bump on top of a smooth distribution. This is
 illustrated in Figure 7.5. The benefit of such a method is that there is no need for a simulation

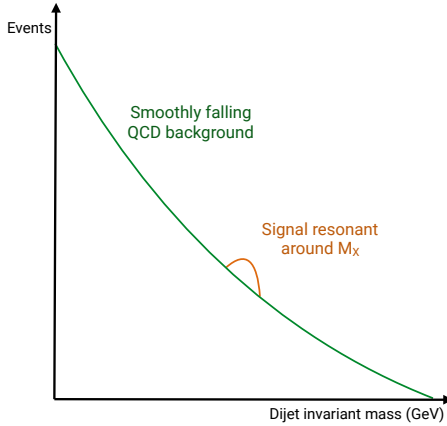


Figure 7.5: The search strategy consists of looking for signal “bumps” in the dijet invariant mass on top of a smoothly falling QCD multijet background.

1558
 1559 of the background and the strategy is simple and robust. The disadvantage is that the analysis
 1560 is intrinsically limited to regions where the dijet invariant mass spectrum is smooth and hence
 1561 regions with discontinuities due to trigger turn-ons or kinematic selections must be avoided.

1562 7.3 Data and simulated samples

1563 The data analyzed in this search correspond to a total integrated luminosity of 2.7 fb^{-1} collected at
 1564 a center-of mass energy of 13 TeV between June and December 2015. The instantaneous luminosity
 1565 of the LHC during this run was around half of the design luminosity ($0.5 \times 10^{34} \text{ cm}^{-2} \text{ s}^{-1}$), with
 1566 an average number of primary vertices per event of $\langle \mu \rangle = 13$.

1567 The bulk graviton model (see Section 2.3) and the HVT model (W' and Z' , see Section 2.2.1)
 1568 are used as benchmark signal processes. In these models, the vector gauge bosons are produced
 1569 with a longitudinal polarization in more than 99% of the cases, which leads to a 24% higher
 1570 acceptance per boson for reasons explained in Section 6.5.3. For the HVT model, a scenario
 1571 (model B) with $g_V = 3$, $c_H = -0.976243$, and $c_F = 1.02433$ is chosen, where the heavy resonance
 1572 predominantly couple to bosons and the coupling to fermions is suppressed. The bulk graviton
 1573 samples were generated with $\tilde{k} = 0.5$. The resonance masses considered lie in the range 1.2 to
 1574 4 TeV and are generated under the assumption of a natural width negligible with respect to

1575 the experimental resolution (narrow-width approximation). All signal samples are generated at
 1576 leading order with MADGRAPH5_AMC@NLO v2.2.2 [62].

1577 Simulated samples of the production of QCD multijet events are generated to leading order
 1578 using PYTHIA version 8.205 [63] with the CUETP8M1 tune [57] and are used to validate the
 1579 analysis procedure.

1580 7.4 Event selection

1581 7.4.1 Triggering

1582 The first selection to be confronted in any analysis is the trigger selection. Due to an overwhelming
 1583 QCD background in all-hadronic final states, the threshold for fully-hadronic triggers is very
 1584 large in order to keep the trigger rate low (preferably around 10-30 Hz). In this analysis, we
 1585 therefore decided to take advantage of triggers that place requirements on the jet’s groomed mass
 1586 in addition to the “standard” jet triggers based on the scalar sum of jet transverse energy H_T .
 1587 These “boosted” triggers were never before tested in data, and this analysis was the first published
 1588 result taking advantage of grooming at the trigger level in CMS. The following H_T -based High
 1589 Level Triggers (HLT), referred to as inclusive triggers in the following, are used:

- 1590 • HLT_PFHT650_WideJetMJJ900DEtaJJ1p5,
- 1591 • HLT_PFHT650_WideJetMJJ950DEtaJJ1p5, and
- 1592 • HLT_PFHT800.

1593 Here, *PFHT650* refers to a total H_T of at least 650 GeV. *WideJet* means jets reconstructed
 1594 with the *wide jet algorithm* [64], an algorithm inspired by jet grooming intended to reduce
 1595 sensitivity to gluon radiation. The two AK R=0.4 jets with the largest p_T in the event are
 1596 used as seeds. Geometrically close jets are then combined into the closest jet seed if they are
 1597 within $\Delta R = \sqrt{(\Delta\eta)^2 + (\Delta\phi)^2}$, and these two jets form a dijet system used for further selections.
 1598 *MJJ900* refers to a wide-jet dijet mass of at least 900 GeV, and *DataJJ1p5* means there is an
 1599 additional cut on the $|\Delta\eta|$ between the two wide jets for reasons that will be explained below. In
 1600 addition, two triggers based on jet grooming are used. These require a trimmed jet mass (see
 1601 Section 3.5.1) of 30 and 50 GeV, yielding the triggers:

- 1602 • HLT_AK8PFJet360_TrimMass30 and
- 1603 • HLT_AK8PFHT700_TrimR0p1PT0p03Mass50.

1604 The tuneable parameters for the trimming algorithm are set to $r_{sub} = 0.2$ and $p_{T,frac} = 0.03$.
 1605 The trigger requiring a trimmed jet mass of at least 30 GeV is seeded by single-object Level 1
 1606 triggers with jet p_T thresholds of 176 or 200 GeV, and the remaining triggers require an online
 1607 H_T of at least 150 or 175 GeV.

In order to avoid any kinks in the dijet invariant mass spectrum due to the presence of a trigger turn-on, we determine the dijet invariant mass at which the analysis triggers are fully efficient ($> 99\%$), and only consider signal events above this value. In order to estimate the trigger efficiency, we use a trigger with a lower H_T threshold of 650 GeV as a reference trigger. This trigger has a prescale of 40, meaning events are only recorded one out of 40 times. It is seeded by L1 H_T triggers with thresholds of 150 or 175 GeV. We then define the efficiency as

$$\text{Efficiency} = \frac{N_{trigger+ref}}{N_{ref}}$$

1608 where $N_{trigger+ref}$ corresponds to the number of events passing the trigger under study as well as
 1609 the reference trigger, and N_{ref} corresponds to the number of events passing the reference trigger.
 1610 Figure 7.6 shows the trigger turn-on curves as a function of dijet invariant mass for jets where
 1611 one of the jets is required to have a pruned mass larger than 65 GeV (in other words, compatible
 1612 with a W jet). A sharp turn-on for the inclusive triggers (top left) is observed, reaching the
 1613 100% efficiency plateau for dijet masses of around 1.0–1.1 TeV. The grooming triggers, however,
 1614 turn on more slowly and are not fully efficient until dijet invariant masses reach around 1.2 TeV
 1615 (top right). The real power of the grooming triggers become clear when considering them in
 1616 addition to the H_T -based triggers. The bottom plot in Figure 7.6 compares the trigger turn-on
 1617 curves as a function of dijet invariant mass for jets passing one of the three inclusive triggers
 1618 only, one of the grooming triggers only, and when combining all of them. Here, one can see that
 1619 the 99% efficiency threshold is lowered by 75 GeV when including the substructure triggers, once
 1620 substructure is required at analysis level. This combination of triggers allowed the analysis to
 1621 consider dijet invariant masses as low as 1 TeV. As a measure of the performance of the grooming
 1622 triggers, we have in addition looked at the trigger efficiencies as a function of the offline groomed
 1623 mass (using the pruned and softdrop algorithms described in Sections 6.5.1 and 6.5.1), for the
 1624 grooming trigger with the lowest mass threshold (30 GeV). This is shown in Figure 7.7, where an
 1625 additional cut on the jet transverse momentum of one of the jets of 600 GeV is required and no
 1626 other mass cut is applied. The trigger plateau is reached for offline groomed-jet masses around
 1627 50 GeV.

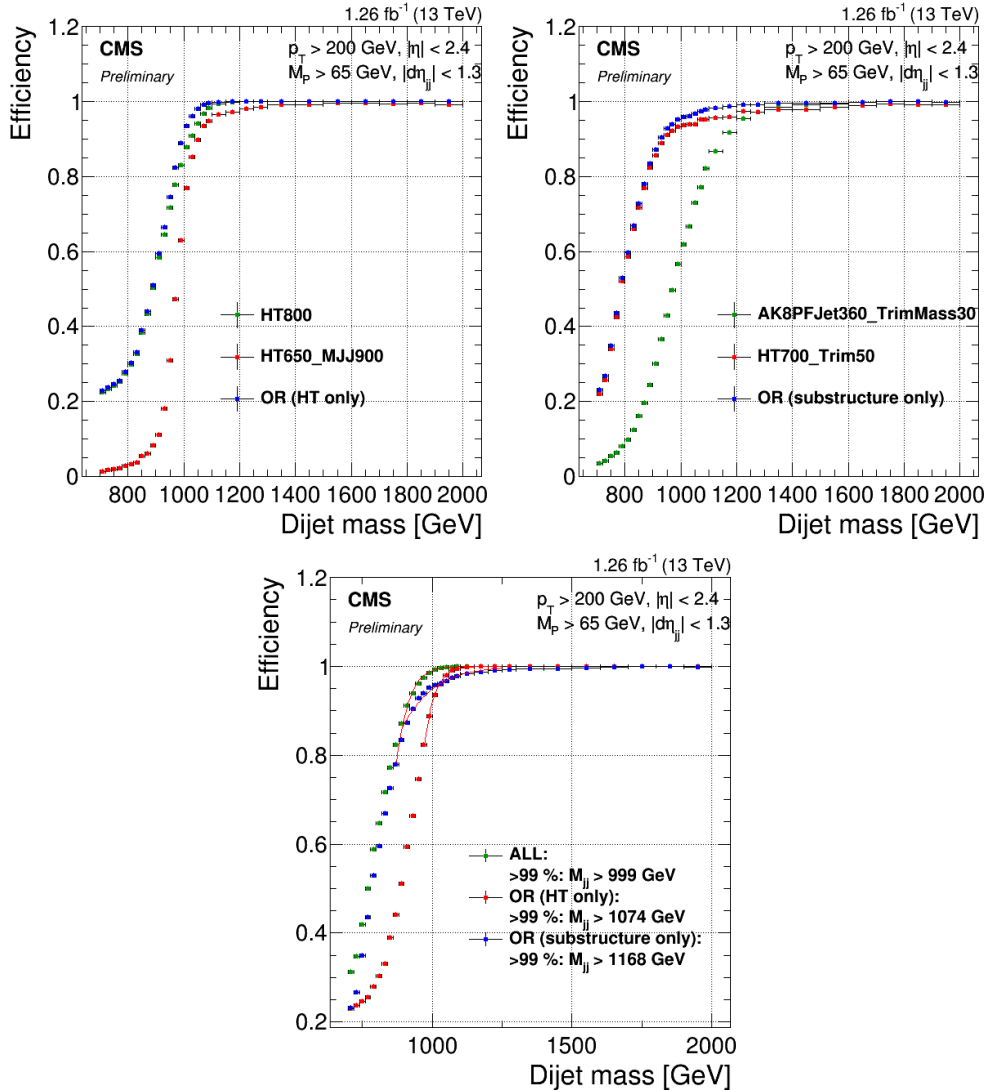


Figure 7.6: Top: Efficiency for the inclusive triggers (top left) and the grooming triggers (top right) as a function of dijet invariant mass for jet pairs where one jet has a pruned mass larger than 65 GeV. Bottom: Comparison of trigger efficiencies for jets passing one of the HT-triggers only (red), for jets passing one of the grooming-triggers only (blue) and for jets passing one of the HT-triggers or one of the grooming triggers (green). Here as a function of dijet invariant mass for all jet pairs passing loose selections and where one jet has a pruned mass larger than 65 GeV. The 99% efficiency threshold is lowered by 75 GeV when including substructure taggers.

7.4.2 Preselection

After trigger selections, and the corresponding requirement of a dijet invariant mass above 1 TeV to ensure a smooth falling background, we begin the process of maximizing the signal significance

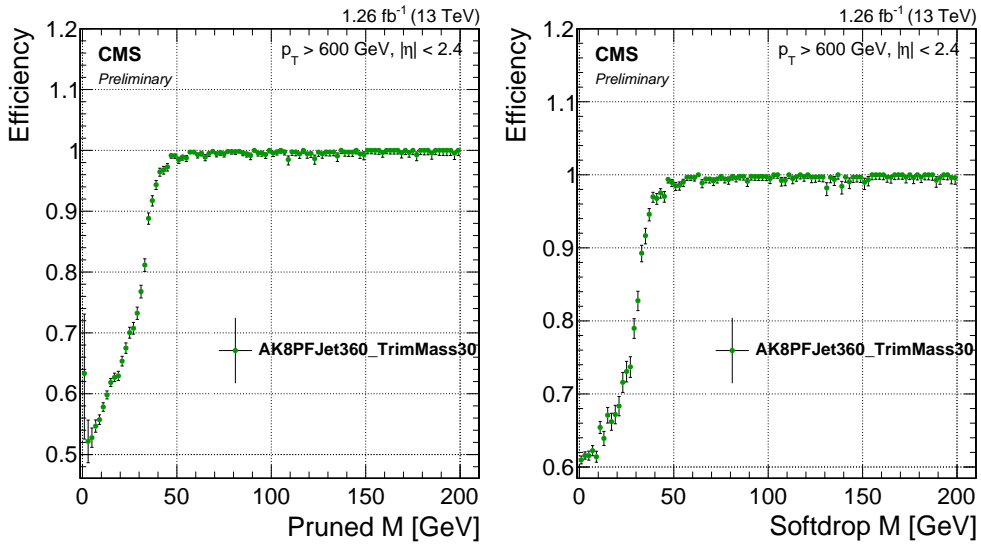


Figure 7.7: Efficiency for the lowest threshold grooming trigger as a function of pruned-jet (left) and softdrop-jet (right) mass for jets with $p_T > 600$ GeV.

1631 while keeping the background low. This is done by optimizing the selection requirements on the
 1632 jets. The jets used in this analysis are clustered with the anti- k_T jet clustering algorithm with a
 1633 clustering parameter of $R = 0.8$ (see Section 6.4) to allow containment of the full vector-boson
 1634 decay products. Since a minimum transverse momentum of 200 GeV is required for the decay
 1635 products of a W/Z to be fully contained within an $R=0.8$ jet, events are further selected by
 1636 requiring at least two jets with $p_T > 200$ GeV. These are in addition required to be central, with
 1637 an $|\eta| < 2.4$. The two highest p_T jets in the event passing these criteria are selected as potential
 1638 vector boson candidates. As our main background is QCD multijet events, we further take
 1639 advantage of the fact that the angular distribution between these, mainly t-channel, processes
 1640 are very different from the s-channel signal processes under study. The crosssection for QCD
 1641 t-channel processes as a function of the opening angle with respect to the beam axis (θ^*), exhibit
 1642 a pole around $\cos \theta^* = 1$, meaning QCD t-channel jets are mostly produced in the forward
 1643 direction, with an opening angle with respect to the beam axis close to zero. The signal jets on
 1644 the other hand, produced through an s-channel process, are concentrated in the barrel region.
 1645 We therefore require the jets to have a separation of $|\Delta\eta| < 1.3$ in order to reduce the QCD
 1646 multijets background. The distribution of $|\Delta\eta|$ between the two highest- p_T jets for QCD, as
 1647 well as for different signal scenarios, is shown in Figure 7.8. A cut of $|\Delta\eta|_{jj} < 1.3$ removes the
 1648 t-channel pole at $\cos \theta^* = 1$ and is in addition found to yield the highest signal sensitivity. In
 1649 addition to these requirements on the jets themselves, a veto on jets overlapping with leptons is

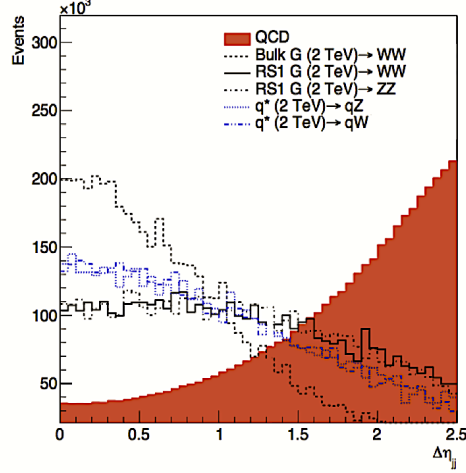


Figure 7.8: $|\Delta\eta|$ between the two highest- p_T jets for QCD jets and jets stemming from different signal scenarios.

1650 applied. Here the overlap $\Delta R(\text{jet}, \text{lepton})$ between the jet candidate and a lepton is required to
 1651 be larger than 0.8. Leptons used for this veto are required to pass the identification requirements
 1652 described in Section 6.2.2 and 6.2.2, have a transverse momentum larger than 35 (30) GeV, and a
 1653 pseudorapidity smaller than 2.5 (2.4) in the case of electrons (muons). The p_T , η , dijet invariant
 1654 mass, and $|\Delta\eta|_{jj}$ distribution for the two leading jets in the event after the above preselections
 1655 have been applied is shown in Figure 9.6.

1656 7.4.3 Vector boson tagging

1657 After preselections, we take advantage of the jet substructure algorithms described in Section 6.5 to
 1658 further separate boosted W/Z jets from the QCD multijet background. In the 8 TeV analysis [58]
 1659 published the previous year, the pruning algorithm was the chosen grooming algorithm of CMS.
 1660 However, recent progress had been made in the development of alternative grooming algorithms
 1661 that had favorable properties from a theoretical point of view (see Sections 6.5.1 and 8.5). We
 1662 therefore studied two different grooming algorithms: pruning and softdrop (with $\beta = 0$ and
 1663 $z_{cut} = 0.1$). A comparison of the jet mass for W, Z, and H jets after either the softdrop (dotted
 1664 lines) or pruning (solid lines) algorithms were applied is shown in Figure 7.10. One of the first
 1665 observations we made comparing the two grooming algorithms was that there appeared to be
 1666 a strong dependence of the softdrop mass on the jet p_T . Figure 7.11 shows the pruned (left)
 1667 and softdrop (right) mass distributions for W jets coming from the decay of a G_{bulk} with a
 1668 resonance mass of $0.8 \text{ TeV} < M_X < 4 \text{ TeV}$. While the pruned jet mass mean appeared stable

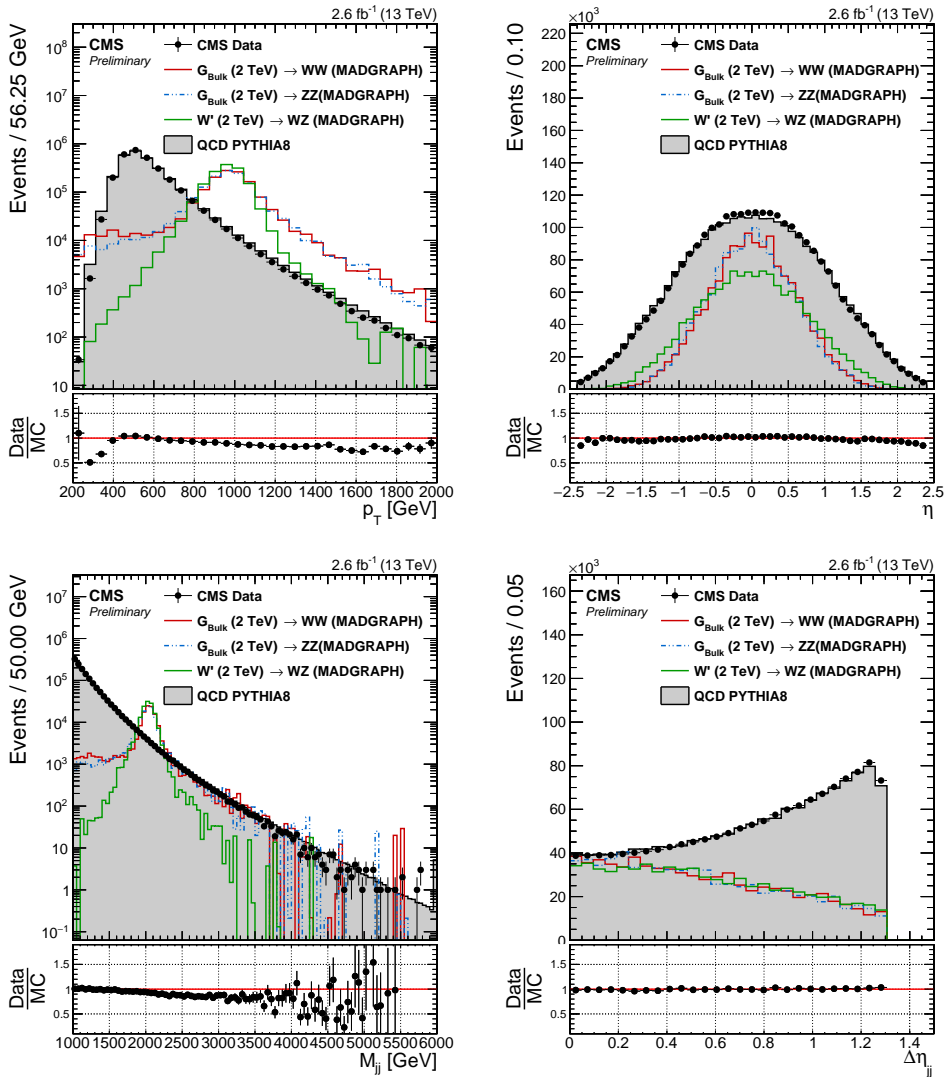


Figure 7.9: Jet p_T (top left), η (top right), dijet invariant mass (bottom left) and $|\Delta\eta|_{jj}$ (bottom right) distribution for the two leading jets in the event after loose preselections are applied. The signal is scaled by an arbitrary number.

as the jet transverse momenta of the jet increased ($p_T \sim M_X/2$), the mean of the softdrop jet mass shifted towards lower values as jet p_T increased. In order to investigate whether this was a reconstruction effect or an algorithmic effect, we additionally looked at the pruned and softdrop mass for generator-level jets (jets clustered with generator-level particles not passed through the detector simulation). Figure 7.12 shows the reconstructed (solid line) and generator-level (dotted line) jet mass distributions after pruning (left) or softdrop (right) have been applied. Again,

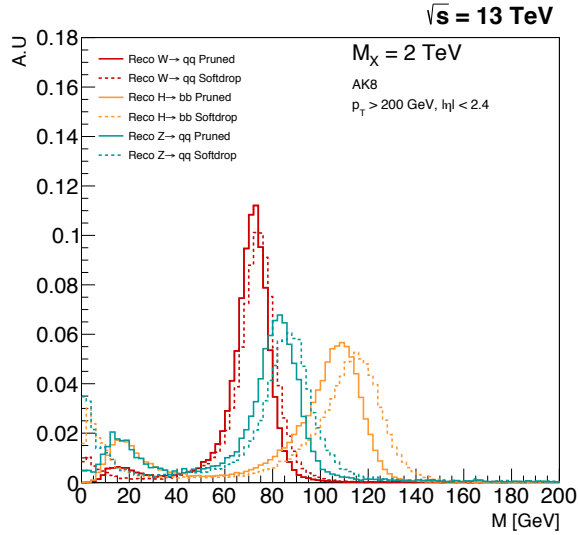


Figure 7.10: The softdrop (dotted lines) and the pruned (solid lines) jet mass for W, Z and H jets.

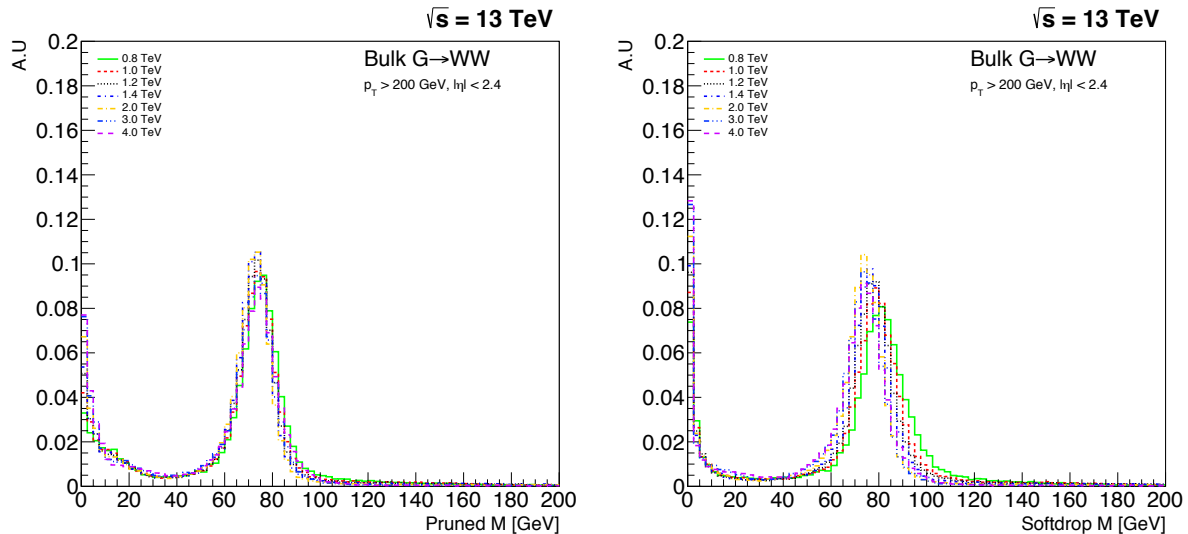


Figure 7.11: The jet mass distribution for W jets coming from a G_{bulk} of masses in the range $0.8 \text{ TeV} < M_X < 4 \text{ TeV}$ decaying to WW, here with pruning applied (left) and softdrop (right). A strong shift in the jet mass mean as a function of p_T ($\sim M_X/2$), is observed for jets groomed with the softdrop algorithm. Charge hadron subtraction is applied to all jets before clustering.

¹⁶⁷⁵ the distributions are compared for jets with very different p_T profiles, here for W jets coming

from a $G_{\text{bulk}} \rightarrow WW$ of mass 0.8 TeV (red) yielding a p_T of about 400 GeV, and a mass of 2.0 TeV, yielding a p_T of about 1 TeV. Interestingly, we observe a p_T -dependent mass shift already for generator level softdrop jets (comparing the dotted lines in the right plot), an effect further enhanced at reconstruction level. This effect is not present for pruned jets, for either generator level or reconstruction level. The observed p_T -dependence of the softdrop mass was problematic

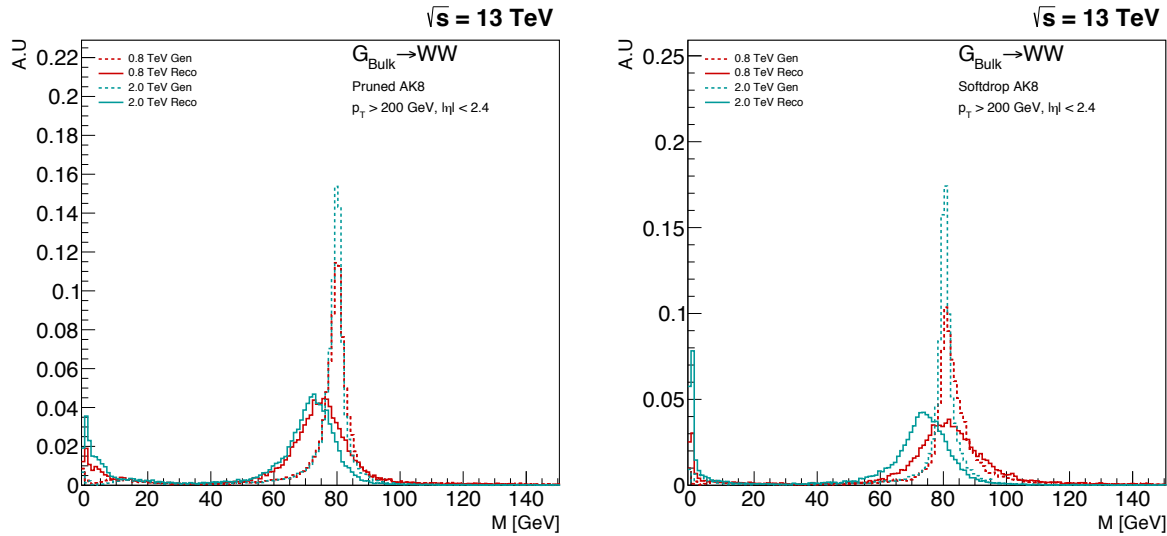


Figure 7.12: The reconstructed (solid line) and generator level (dotted line) jet mass distribution for W jets coming from a $G_{\text{bulk}} \rightarrow WW$ of mass $M_X = 0.8 \text{ TeV}$ (red), roughly $p_T \sim 400 \text{ GeV}$, and $M_X = 2.0 \text{ TeV}$ (blue), $p_T \sim 1 \text{ TeV}$. Here for the pruned (left) and softdrop (right) jet mass.

due to the fact that it would require a p_T -dependent mass window. This would again require several different measurements to produce an efficiency scale factor between simulation and data, for each mass window, or a significantly higher uncertainty on the signal yield. Due to these findings, the grooming algorithm of choice for this analysis is pruning, with the signal selection window defined as $65 \text{ GeV} < m_p < 105 \text{ GeV}$. The above findings will be important for subsequent analyses and are revisited in Section 8.

The variable used to determine the substructure of the V jets is the n-subjettiness ratio τ_{21} , as described in Section 6.5.2. The τ_{21} variable is correlated to the pruned jet mass, however, it still provides additional signal discrimination when applied after the pruned jet mass selection. Figure 7.13 shows the τ_{21} distribution for the QCD background and W jets from a signal decay before (left) and after (right) a pruned mass cut of $65 \text{ GeV} < m_p < 105 \text{ GeV}$ has been applied. We perform a cut optimization on τ_{21} after all analysis selections, including the pruned mass window of $65 \text{ GeV} < m_p < 105 \text{ GeV}$, have been applied. This is done by scanning over thresholds

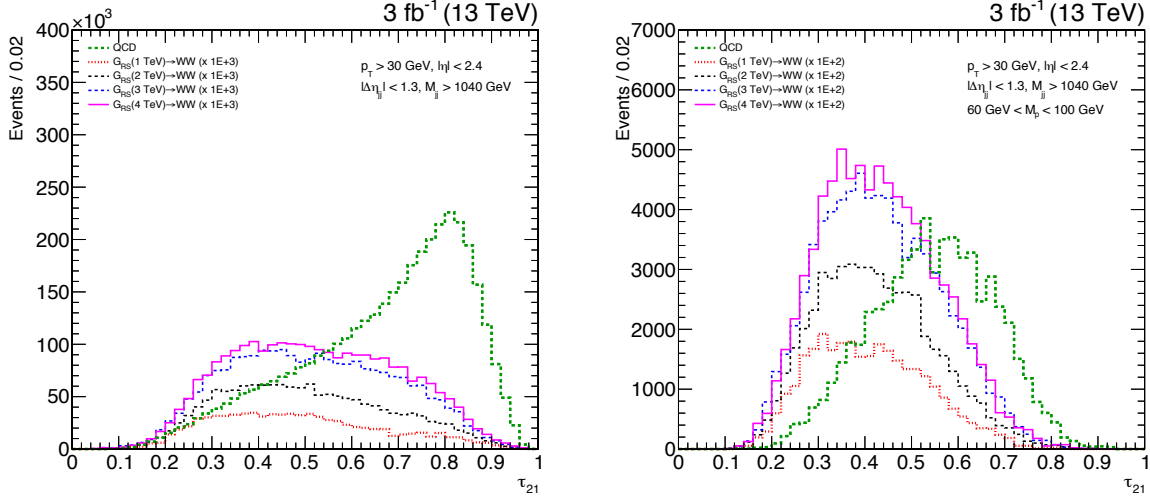


Figure 7.13: The τ_{21} distribution for QCD background and signal jets before (left) and after (right) a pruned mass window is applied. The discriminating power of τ_{21} is strongly reduced after grooming.

for the τ_{21} variable, and for each threshold, computing the Punzi significance [65] defined as

$$S = \frac{\epsilon_S}{1 + \sqrt{B}},$$

where ϵ_S is the signal efficiency and B is the total number of background events. The selection with the highest significance is defined as the optimal value. The signals under consideration are W jets coming from the decay of a G_{bulk} with $1 \text{ TeV} < m_X < 4 \text{ TeV}$, against a background of light-flavored QCD jets. Only jets with a dijet invariant mass in a 20% window around the resonance mass are considered. The Punzi significance as a function of the upper cut value on τ_{21} is shown on the left in Figure 7.14. The optimal cut gets looser as the dijet invariant mass increases, something which can be understood when looking at the QCD dijet invariant mass spectrum in Figure 9.6. The number of QCD jets falls off exponentially with m_{jj} , meaning that the background at 4 TeV is considerably lower than at 1 TeV. This allows for a looser cut on τ_{21} as m_{jj} increases. In order to choose a single cut which works reasonably well for all values of resonance mass, we look at the ratio of a given τ_{21} cut over the significance of the best cut at that mass value. This is shown in the right plot of Figure 7.14. Choosing signal events with a $\tau_{21} < 0.45$ yields the most stable performance out of the investigated τ_{21} selection requirements and also maintains low background rates at low m_{jj} . This selection is therefore used for our main analysis category. In order to account for the fact that background rates are lower for

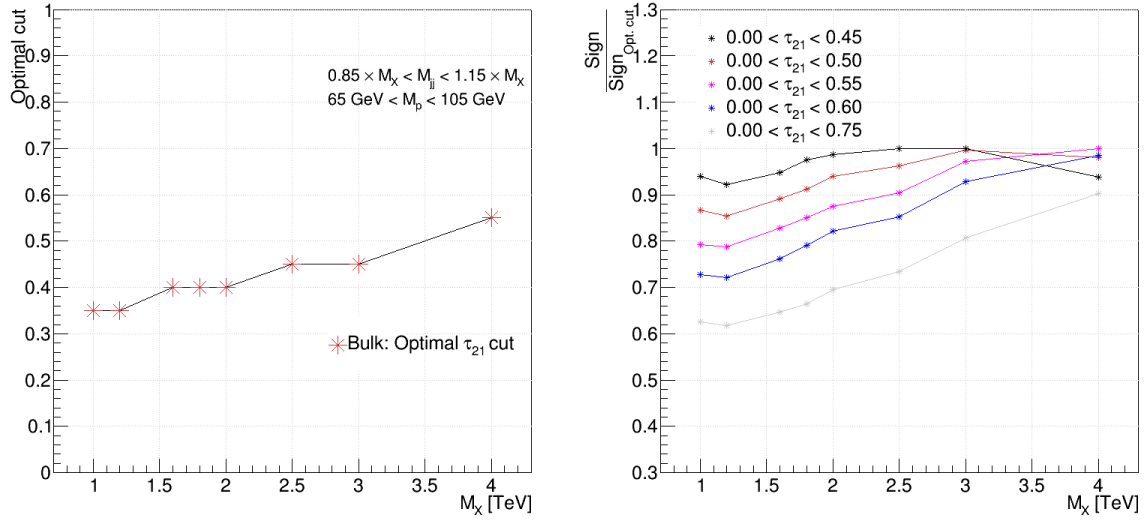


Figure 7.14: Left: Optimal upper value of τ_{21} for selecting the signal as a function of G_{bulk} mass. Right: The ratio of a given τ_{21} cut over the significance of the best cut at that mass value.

higher values of m_{jj} , we add an additional analysis category, $0.45 < \tau_{21} < 0.75$, which contains $> 95\%$ of the signal and enhances the analysis sensitivity in the case when the background is low. These categories are hereafter referred to as the *high-purity* (HP) category, for jets with $0 < \tau_{21} \leq 0.45$, and the *low-purity* (LP) category, for jets with $0.45 < \tau_{21} \leq 0.75$. QCD jets from light-flavor quarks and gluons (u,d,s,g) can be incorrectly identified as W-jets, and these events are referred to as “mistags” of the W-tagger. The W-tagging efficiency and QCD light-flavored jet mistagging rate for a W-tagger consisting of $0 < \tau_{21} \leq 0.45$ and $65 \text{ GeV} < m_p < 105 \text{ GeV}$ is shown in Figure 7.15, both as a function of jet p_T and as a function of number of primary vertices in the event. The signal efficiency when applying only the pruned jet mass selection is around 80% with a mistag rate of $\sim 15\%$. After applying the τ_{21} selection, the signal efficiency drops to around 55% and the mistagging rate to $\sim 2\%$. Another interesting feature is the dependence of τ_{21} on jet p_T and pileup, compared to the resilience of the groomed mass as a function of the same variables. This will be another feature we explore in the second analysis (Section 8). Figure 7.16 shows the pruned jet mass (left) and the τ_{21} distribution (right) for signal and background Monte Carlo, as well as the distributions measured in data.

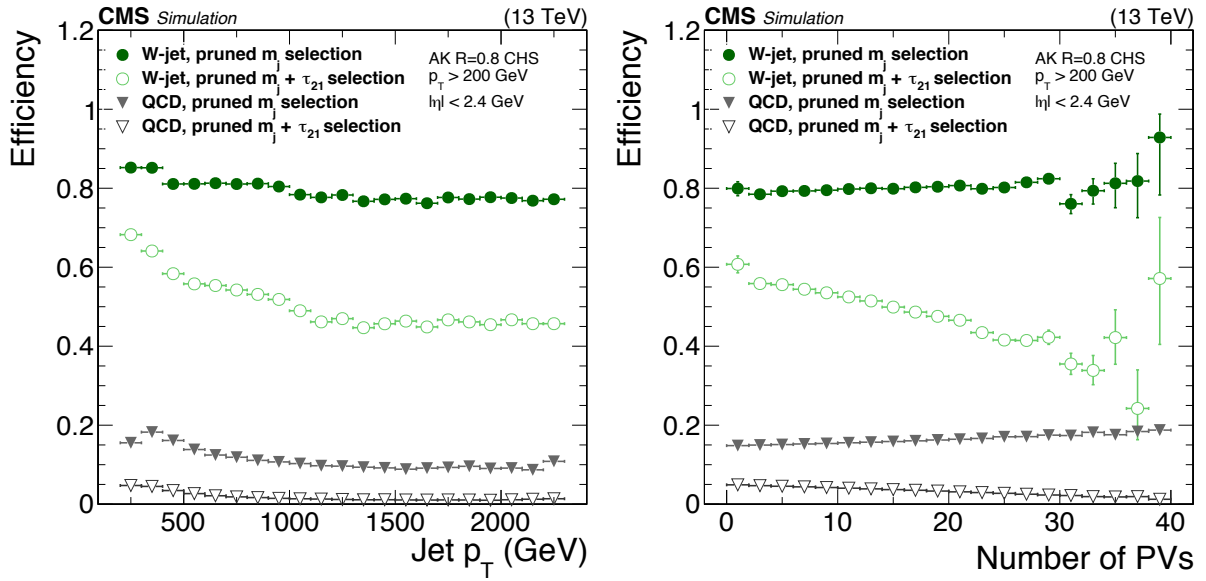


Figure 7.15: The W-tagging efficiency (green) and light jet mistag rate (grey) for a selection based on either the pruned jet mass or the pruned jet mass and τ_{21} as a function of p_T (left) and the number of primary vertices (right).

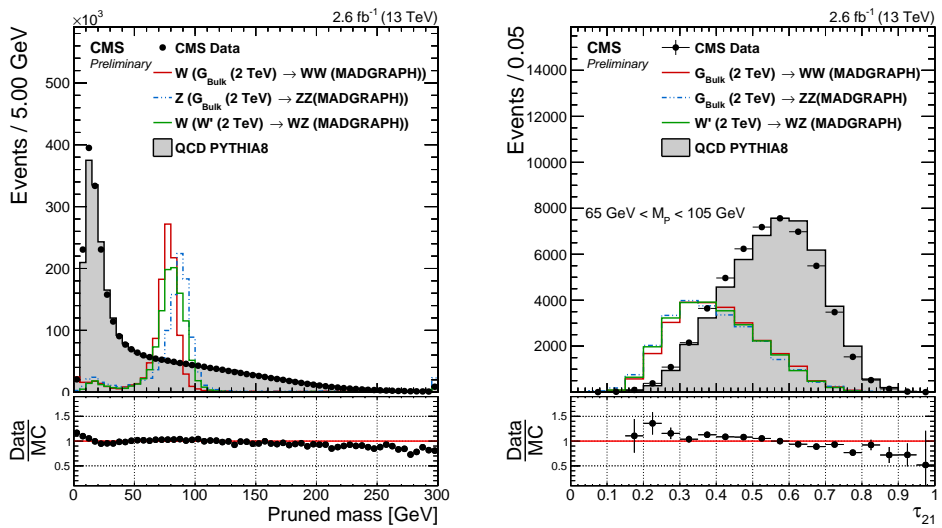


Figure 7.16: Pruned jet mass (left) and τ_{21} (right) distributions for data and simulated samples. Simulated samples are scaled to match the distribution in data. The τ_{21} distribution is shown for jets after a cut on the pruned jet mass of $65 \text{ GeV} < m_p < 105 \text{ GeV}$ has been applied.

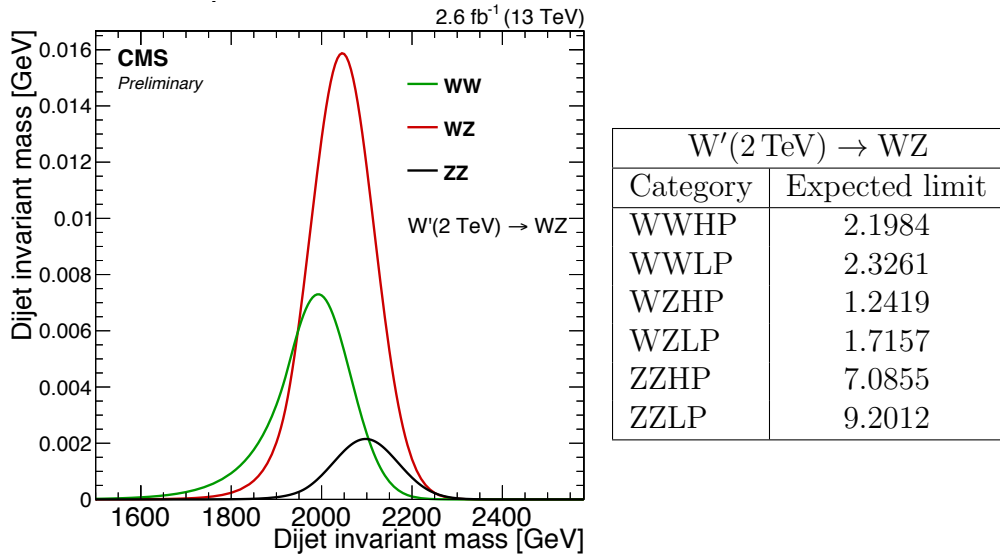


Figure 7.17: The expected signal yield per mass category for a W' (2 TeV) decaying to a W and a Z (left) together with the expected limit per mass category for the same signal (right).

1717 7.4.4 Analysis categorization

1718 As the analysis requires two W/Z -tags, we always require one HP-tagged jet and then divide into
 1719 LP and HP categories depending on whether the other jet is of high or low purity. In addition, in
 1720 order to further enhance the analysis sensitivity, we further split the pruned jet mass window
 1721 into a W and a Z boson window where the W window is defined as $65 \text{ GeV} < m_p < 85 \text{ GeV}$ and
 1722 the Z boson window as $85 \text{ GeV} < m_p < 105 \text{ GeV}$. This has the added benefit of allowing us to
 1723 discriminate between a G_{bulk} decaying to WW or ZZ , and a W' decaying into WZ by separating
 1724 these events into categories. The signal yield will be higher in the WZ category for a W' decaying
 1725 to a W and Z boson than for a G_{bulk} decaying to WW or ZZ . Figure 7.17 shows the relative
 1726 expected signal yield (left) and expected limits (left) in the different mass categories for a W' with
 1727 a mass of 2 TeV. All categories are combined in the end, leading to the same or better sensitivity
 1728 at each resonance mass value than when using the whole pruned mass window. Figure 7.18 shows
 1729 the expected 95% CL upper limits on the production cross section of a W' decaying to WZ (left)
 1730 and a G_{bulk} decaying to WW (right) as a function of the resonance mass in the HP category.
 1731 The blue line corresponds to the expected limits obtained when not splitting into mass categories
 1732 and the red line corresponds to the limit using the combination of two categories. The dotted
 1733 and solid black lines are the limits for the W and Z categories, respectively. The combination of
 1734 two mass categories leads to slightly better (10%) or similar sensitivity as when using one large

mass window. The real benefit of splitting into mass categories becomes obvious when defining

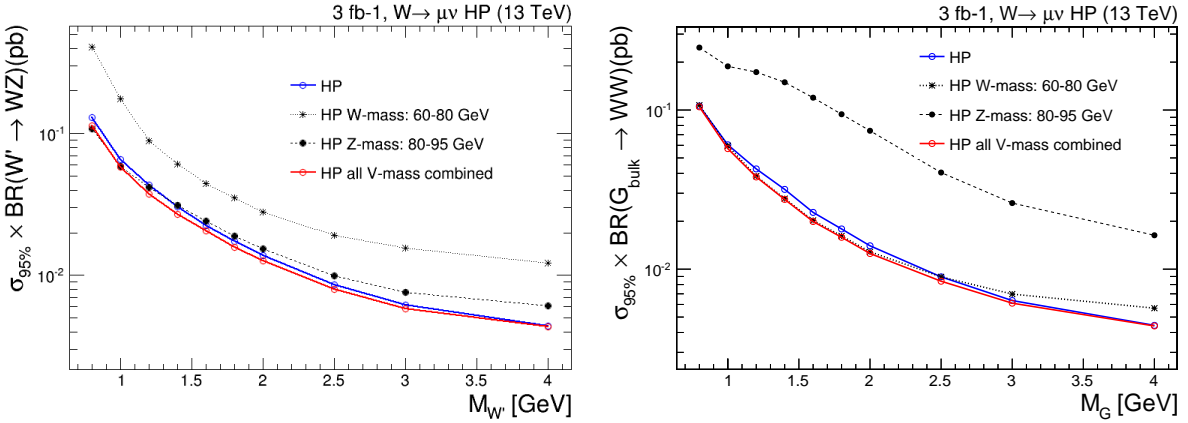


Figure 7.18: Expected 95% CL upper limits on the production cross section of a W' (left) and G_{bulk} (right) signal as a function of the resonance mass for the different mass categories for events passing the high-purity τ_{21} selection.

1735
1736 a test statistics based on the likelihood ratios of each signal hypothesis, $q = -2 \ln(L_{G_{\text{bulk}}}/L_{W'})$,
1737 shown in Figure 7.19. For a signal with a signal strength corresponding to a 3-4 σ excess, the test
1738 statistics for each signal hypothesis are well separated ($\sim 3.5\sigma$), allowing us to make a statement
of whether a possible signal is more likely due to a G_{bulk} or a W' particle. With the high-purity

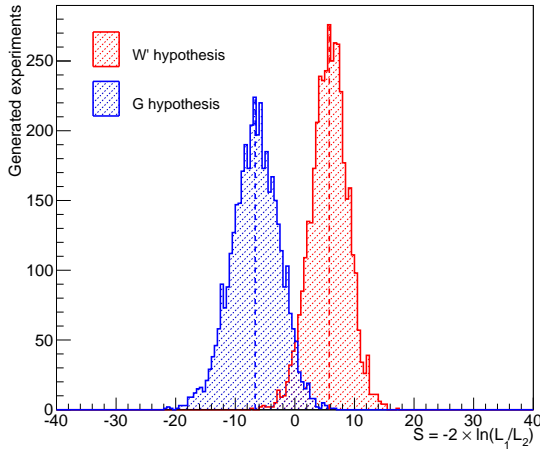


Figure 7.19: Distribution of the test statistic $q = -2 \ln(L_{G_{\text{bulk}}}/L_{W'})$ for a G_{bulk} (blue) and W' signal hypothesis.

1739
1740 and low-purity categories as defined above for each mass window combination, this leaves us with

1741 six different signal categories: HP with 3 mass categories corresponding to WW, WZ, and ZZ, and
1742 the same 3 mass categories for LP. In parallel to the mass-category based analysis, we perform an
1743 analysis without categorization in mass (similar to the 8 TeV analysis) as a cross-check. We found
1744 the sensitivity with mass categories to be higher and hence will not present these studies here.
1745 The final tagging efficiency for different signal hypotheses (top) together with the QCD mistag
1746 rate (bottom) in the different signal categories is shown in Figure 7.20. The solid lines represent
1747 the tagging efficiency in the full mass window ($65 \text{ GeV} < m_p < 105 \text{ GeV}$) before splitting into
1748 mass categories. A lower signal efficiency in the ZZ mass category is observed in all cases. This
1749 can be explained from the pruned jet mass distribution on the left in Figure 7.16, where a lower
1750 pruned jet mass selection of 85 GeV leaves a large fraction of the Z peak in the W mass window.
1751 The main benchmark models under consideration preferably decay to W bosons, since in the
1752 Bulk Graviton model the branching ratio $\text{BR}(G_{\text{Bulk}} \rightarrow \text{WW}) = 2 * \text{BR}(G_{\text{Bulk}} \rightarrow \text{ZZ})$ and in the
1753 HVT model $\text{W}'/\text{Z}' \rightarrow \text{WZ}/\text{WW}$ (but not ZZ). Therefore, the tagging procedure is optimized for
1754 a high efficiency to tag W bosons. In the limit-setting procedure all the categories are combined
1755 and the overall signal efficiency is maintained. For the combined mass-categories (solid line) the
1756 signal efficiency is between 16 and 23% in the double-tag categories, and between 20 and 34 % in
1757 the single-V tag categories. The mistagging rate is below 1% in the high-purity category. The
1758 full analysis selections and final signal categories are listed in Table 7.1, where m_{jet_1} and m_{jet_2}
1759 refers to the jet with the highest and second highest jet p_T , respectively.

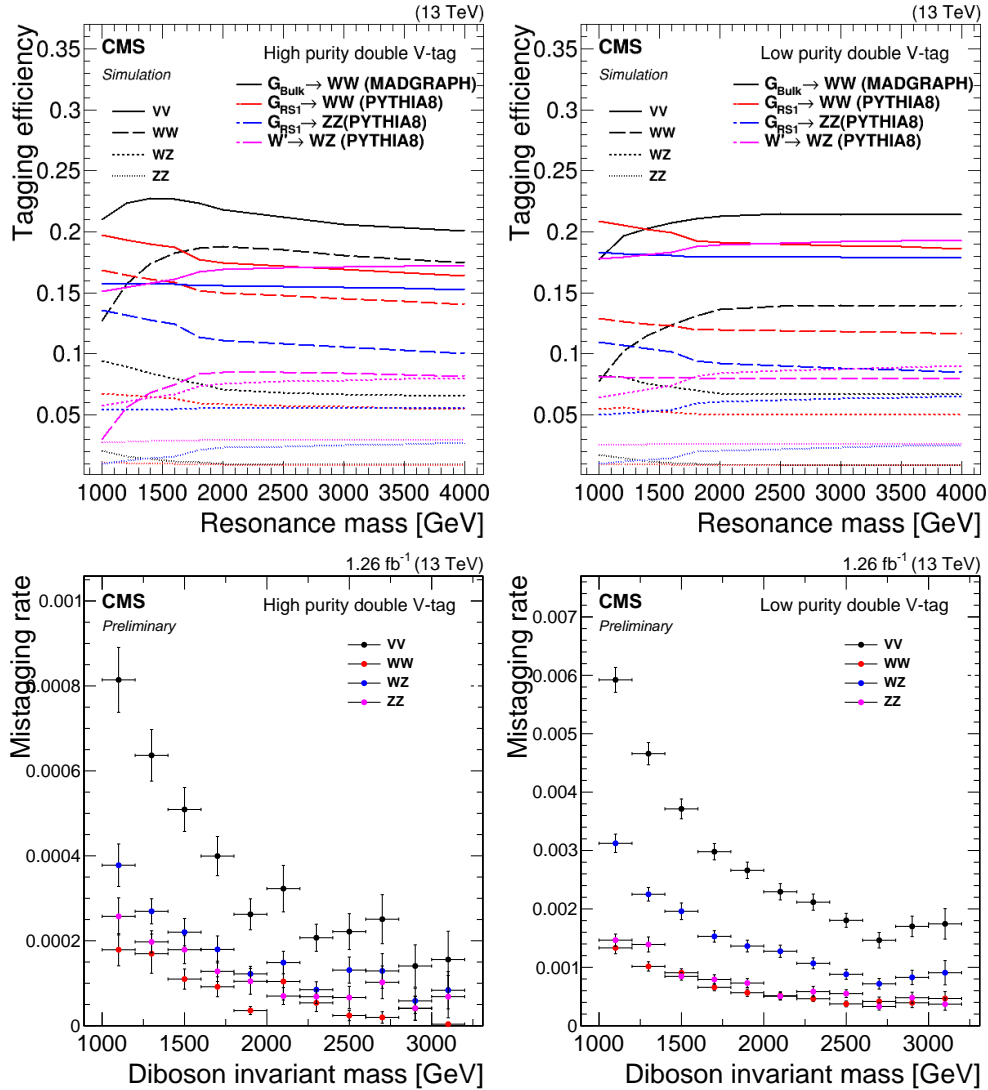


Figure 7.20: Tagging efficiency (top) and mistagging rate (bottom) in the different pruned mass categories in the high-purity category (left) and in the low-purity category (right).

Selection	Value
Boson selections	
$V \rightarrow q\bar{q}$ (2 AK8 jets)	$p_T > 200 \text{ GeV}$ $ \eta < 2.4$
Pruned jet mass	$65 < m_{\text{jet}_1}, m_{\text{jet}_2} < 105 \text{ GeV}$
Topology	$ \Delta\eta_{jj} < 1.3$
Dijet invariant mass	$m_{jj} > 1 \text{ TeV}$
2- to 1-subjettiness ratio	$\tau_{21} < 0.75$
<i>m_{jet}</i> categories	
WW	$65 < m_{\text{jet}_1} < 85 \text{ GeV}, 65 < m_{\text{jet}_2} < 85 \text{ GeV}$
WZ	$65 < m_{\text{jet}_1} < 85 \text{ GeV}, 85 < m_{\text{jet}_2} < 105 \text{ GeV}$
ZZ	$85 < m_{\text{jet}_1} < 105 \text{ GeV}, 85 < m_{\text{jet}_2} < 105 \text{ GeV}$
τ_{21} categories	
High-purity	$\tau_{21,\text{jet}1} < 0.45, \tau_{21,\text{jet}2} < 0.45$
Low-purity	$\tau_{21,\text{jet}1} < 0.45, 0.45 < \tau_{21,\text{jet}2} < 0.75$

Table 7.1: The full analysis selections, and the signal categories based on the pruned jet mass and τ_{21} values.

1760 7.5 Background modeling

1761 We assume that the QCD multijets background can be described by a smooth, monotonically
 1762 decreasing function, which is parametrizable. This is similar to what is done in previous CMS
 1763 analyses looking for bumps in the dijet invariant mass spectrum [66, 67]. The search is then
 1764 performed by fitting the sum of the functions for background and signal to the dijet invariant
 1765 mass spectrum in data. Neither data control regions nor simulated samples are used directly by
 1766 this method. The background functions are of the following form:

$$\frac{dN}{dm_{jj}} = \frac{P_0}{(m_{jj}/\sqrt{s})^{P_2}} \quad \text{and} \quad \frac{dN}{dm_{jj}} = \frac{P_0(1 - m_{jj}/\sqrt{s})^{P_1}}{(m_{jj}/\sqrt{s})^{P_2}}, \quad (7.1)$$

where m is the dijet invariant mass, \sqrt{s} is the center-of-mass energy, P_0 is a normalization parameter for the probability density function, and P_1 and P_2 describe the shape. The number of fit parameters is decided through a Fisher’s F-test [68]. In this test, we start from the 2-parameter function and compare the goodness of fit (χ^2 divided by degrees of freedom) when fitting the data signal region with a 2, 3, 4 and 5 parameter function. If the confidence level is less than 10%, we add additional parameters to model the background distribution. The 4- and 5-parameter functions are

$$\frac{dN}{dm_{jj}} = \frac{P_0(1 - m_{jj}/\sqrt{s})^{P_1}}{(m_{jj}/\sqrt{s})^{P_2 + P_3 \times \log(m_{jj}/\sqrt{s})}} \quad \text{and} \quad (7.2)$$

$$\frac{dN}{dm_{jj}} = \frac{P_0(1 - m_{jj}/\sqrt{s})^{P_1}}{(m_{jj}/\sqrt{s})^{P_2 + P_3 \times \log(m_{jj}/\sqrt{s}) + P_4 \times \log(m_{jj}/\sqrt{s})^2}}, \quad (7.3)$$

1767 where P_3 and P_4 are additional free parameters. As an additional crosscheck, an alternative fit
 1768 function is also tested:

$$\frac{dN}{dm_{jj}} = \frac{P_0(1 - m_{jj}/\sqrt{s} + P_3(m_{jj}/\sqrt{s})^2)^{P_1}}{(m_{jj}/\sqrt{s})^{P_2}}. \quad (7.4)$$

1769 The fit range is chosen such that it starts where the trigger efficiency has reached its plateau to
 1770 avoid bias from trigger inefficiency, and extends to the bin after the highest m_{VV} mass point.
 1771 The binning chosen for the fit follows the detector resolution as in Refs. [66, 67], and is referred to
 1772 as the “dijet binning”. Before unblinding the signal region, we check that the QCD dijet invariant
 1773 mass spectrum is expected to be smooth from the distribution in QCD MC as well as exercise
 1774 the F-test in QCD MC and in a data sideband.

1775 The fits to data in the signal region using the different fit functions are shown in Figure 7.21,

and the corresponding F-test output are given in Tables 7.2 through 7.4. The findings can be summarized as follows: for the WW enriched category, a 2-parameter fit is sufficient to describe the data in both the high- and low-purity categories. In the WZ category, a 2-parameter fit is sufficient in the high-purity category, while three parameters are needed for the low-purity category. For the ZZ category, a 3-parameter fit is needed for both purity categories. The 2- and 3-parameter fit functions as defined in Equation C.2 will therefore be used to model the background component in the simultaneous signal and background fit.

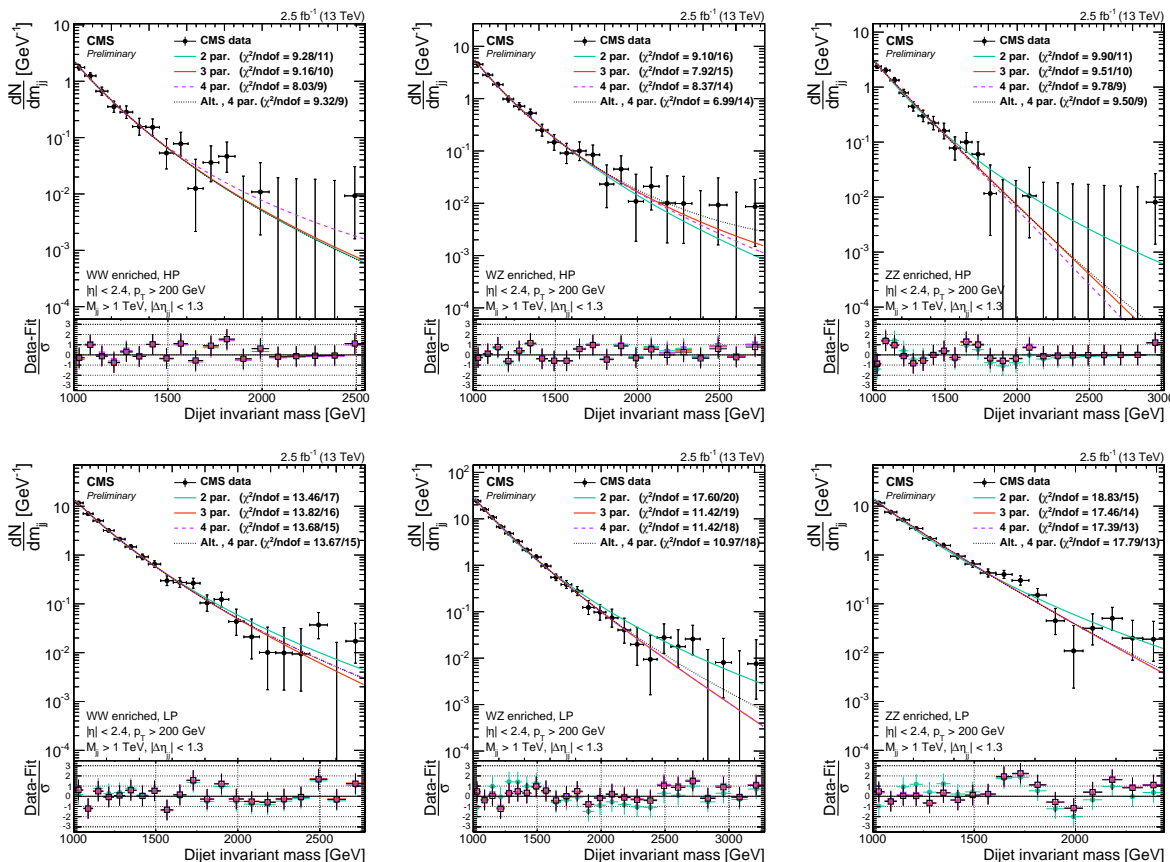


Figure 7.21: Fitted dijet mass spectrum in the different mass and purity categories in data. A 2-parameter fit is sufficient to describe the data in the WW- (HP and LP) and WZ-enriched (LP) categories. For the ZZ- (HP and LP) and WZ-enriched (HP) categories, a 3-parameter fit is needed.

WW-enriched, HP				WW-enriched, LP			
Function	Residuals	χ^2	ndof	Function	Residuals	χ^2	ndof
2 par	0.034	9.279	11	2 par	0.270	13.462	17
3 par	0.034	9.160	10	3 par	0.300	13.819	16
4 par	0.040	8.030	9	4 par	0.324	13.680	15
Fishers23	-0.053	CL	1.0	Fishers23	-1.723	CL	1.0
Fishers34	-1.456	CL	1.0	Fishers34	-1.191	CL	1.0

Table 7.2: Residuals, χ^2 , and degrees of freedom for the WW-enriched HP and LP categories. A 2-parameter fit is needed to describe the data in both categories.

WZ-enriched, HP				WZ-enriched, LP			
Function	Residuals	χ^2	ndof	Function	Residuals	χ^2	ndof
2 par	0.039	9.105	16	2 par	1.016	17.602	20
3 par	0.047	7.915	15	3 par	0.270	11.424	19
4 par	0.048	8.370	14	4 par	0.269	11.421	18
Fishers23	-2.598	CL	1.0	Fishers23	55.258	CL	0.0
Fishers34	-0.491	CL	1.0	Fishers34	0.078	CL	0.783

Table 7.3: Residuals, χ^2 , and degrees of freedom for the WZ-enriched HP (left) and LP (right) categories. A 2-parameter fit is sufficient to describe the data in the high-purity category, while three parameters are needed for the low-purity category.

ZZ-enriched, HP				ZZ-enriched, LP			
Function	Residuals	χ^2	ndof	Function	Residuals	χ^2	ndof
2 par	0.220	9.901	11	2 par	0.448	18.832	15
3 par	0.140	9.511	10	3 par	0.121	17.463	14
4 par	0.124	9.781	9	4 par	0.118	17.394	13
Fishers23	6.302	CL	0.029	Fishers23	40.438	CL	0.0
Fishers34	1.246	CL	0.290	Fishers34	0.356	CL	0.56

Table 7.4: Residuals, χ^2 , and degrees of freedom for the ZZ-enriched LP and HP categories. A 3-parameter fit is sufficient to describe the data in both categories.

₁₇₈₃ **7.6 Signal modeling**

₁₇₈₄ The signal shape is extracted from signal MC with resonance masses in the range from 1 to 4 TeV.
₁₇₈₅ A linear interpolation provides shapes for the mass points in between in steps of 100 GeV. From
₁₇₈₆ these shapes, signal shape models are constructed as composite models with a Gaussian core due
₁₇₈₇ to detector resolution and an exponential tail to account for parton distribution function effects.
₁₇₈₈ Parametric shape uncertainties due to jet energy scale and resolution uncertainties are inserted by
₁₇₈₉ variations of the Gaussian peak position and width. The dijet invariant mass shape for different
₁₇₉₀ benchmark model signals is shown in Figure 7.22. The signal and background components are
 then simultaneously fitted to the data points.

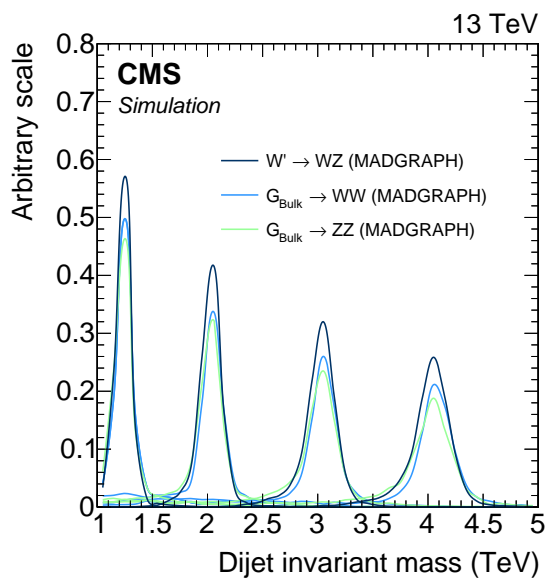


Figure 7.22: Dijet invariant mass from signal MC used to extract the signal shape, shown here for resonances with masses of 1.2, 2, 3, and 4 TeV.

1792 7.7 V-tagging scale factors

1793 As seen in Figure 7.16, a discrepancy is observed in the τ_{21} distribution between data and MC.
1794 This could lead to a bias in the signal efficiency estimation so we must measure the real signal
1795 efficiency in data in an orthogonal data sample. The W-tagging efficiency is measured using real
1796 boosted W-jets in a data sample enriched in $t\bar{t}$ decays with a hadronically decaying W boson.
1797 This region is mainly quark-enriched, as opposed to the gluon-enriched QCD region previously
1798 studied, and substructure variables are better described here. The sample is obtained by requiring
1799 a final state compatible with two b-jets and two W bosons, where one of the bosons decays
1800 leptonically and the other one hadronically. There are several good reasons to use this channel:
1801 Top-quark pair production events are plentifully produced at the LHC; we can ensure a high
1802 purity of the sample by requiring a high-energy lepton, b-tag and missing energy requirements;
1803 and lastly, we can ensure that the W jets are boosted by requiring the leptonic leg, together
1804 with the hadronic W boson candidate, to have high transverse momentum. The final state is
1805 illustrated in Figure 7.23, with the object of interest being the AK R=0.8 jet containing the two
 quark daughters of the hadronically decaying W boson.

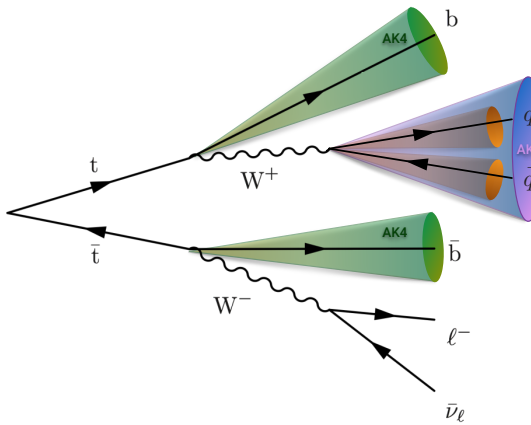


Figure 7.23: A top quark pair decaying into two b quarks and two W bosons, one of which decays leptonically and one of which decays hadronically.

1806

1807 7.7.1 Event selection

The W boson can decay to a neutrino and either an electron or muon, and both final states (“channels”) are used in the analysis. We select events by triggering and event selection on the leptonic W decay. First, we require a high-energy lepton at trigger level, with an online

p_T above 45 GeV for the muon or 135 GeV for the electron. This requires an offline muon (electron) p_T threshold of 53 (120) GeV. The leptons are further required to pass the lepton requirements defined in Section 6.2.2, and events containing additional leptons (passing the same ID requirements, but looser cuts as defined in Table 7.5) are vetoed. Offline, we further require a high missing energy of 40 (80) GeV in the muon(electron) channel. To ensure a high signal purity of boosted, hadronically decaying W bosons, the four-vector of the leptonically decaying W boson is reconstructed such that we can put tight momentum requirements on the leptonic W boson (ensuring that both tops, and therefore vector bosons, have a high momentum). The leptonic W boson is reconstructed in two steps: First, the unknown z component of the neutrino momentum must be solved for through a second order equation assuming the real W boson mass

$$M_W^2 = m_\ell^2 + 2(E_\ell E_\nu - p_{x_\ell} p_{x_\nu} - p_{y_\ell} p_{y_\nu} - p_{z_\ell} p_{z_\nu}) = (80.4)^2.$$

1808 This results in a completely defined neutrino four-vector, which is then added to the lepton
 1809 four-vector. The sum of the two defines the leptonic W boson four-momentum, and its momentum
 1810 is required to be greater than 200 GeV. Further, we require at least one AK R=0.4 jet to be
 1811 b-tagged with the Combined Secondary Vertex (CSV) algorithm [69, 70]. This algorithm exploits
 1812 the relatively long lifetime and large mass of b hadrons that leads to the presence of a displaced
 1813 vertex in order to distinguish between jets originating from b quarks and those originating from
 1814 light-flavor quarks. More information on the CSV algorithm can be found in [69, 70]. The reason
 1815 for requiring only one b-tagged jet is to ensure a high selection efficiency. Finally, we require at
 1816 least one AK R=0.8 jet in the event with a momentum greater than 200 GeV, which will be the
 1817 hadronic W boson candidate. It's pruned jet mass is required to be between 40 GeV and 150
 1818 GeV. After reconstructing and selecting all our objects, a set of angular selections are applied to
 1819 ensure a diboson-like topology. These are the following:

- 1820 • the ΔR between the lepton and the hadronic W boson candidate must be $< \pi/2$,
- 1821 • the $\Delta\phi$ between the hadronic W boson candidate and the E_T^{miss} must be > 2 , and
- 1822 • the $\Delta\phi$ between the hadronic W boson candidate and the lepton must be > 2 .

1823 With these requirements, we have a nearly pure sample of $t\bar{t}$ events, with a small contamination
 1824 from single top-quark production, W+jets, and VV events. A summary of the final selection
 1825 criteria is presented in Table 7.5. The pruned jet mass and τ_{21} variables in data and in MC are
 1826 shown in Figure 7.24.

Selection	Value	Comments
Tight Lepton selection		
Electron p_T	$p_T > 120 \text{ GeV}$	
Muon p_T	$p_T > 53 \text{ GeV}$	
Electron η	$ \eta _{\text{SC}} < 2.5$ except $[1.4442, 1.566]$	Veto ECAL barrel-endcap transition.
Muon η	$ \eta < 2.1$	
Loose Lepton selection		
Electron p_T	$p_T > 35 \text{ GeV}$	
Muon p_T	$p_T > 20 \text{ GeV}$	
Electron η	$ \eta _{\text{SC}} < 2.5$ except $[1.4442, 1.566]$	Veto ECAL barrel-endcap transition.
Muon η	$ \eta < 2.4$	
AK8 jet selections		
Jet p_T	$p_T > 200 \text{ GeV}$	For hadronic W reconstruction
Jet η	$ \eta < 2.4$	
AK4 jet selections		
Jet p_T	$p_T > 30 \text{ GeV}$	Used for b-tag jet selection
Jet η	$ \eta < 2.4$	
E_T^{miss} selections		
E_T^{miss} (electron channel)	$E_T^{\text{miss}} > 80 \text{ GeV}$	
E_T^{miss} (muon channel)	$E_T^{\text{miss}} > 40 \text{ GeV}$	
Boson selections		
Pruned jet mass	$40 < m_p < 150 \text{ GeV}$	
Leptonic W p_T	$p_T > 200 \text{ GeV}$	
Hadronic W p_T	$p_T > 200 \text{ GeV}$	
Veto		
Number of loose electrons	0	
Number of loose muons	0	
Number of b-tagged jets	> 0	CSV medium working point
Angular selections		
$\Delta R(l, W_{\text{AK8}})$	$> \pi/2$	
$\Delta\phi(W_{\text{AK8}}, E_T^{\text{miss}})$	> 2	
$\Delta\phi(W_{\text{AK8}}, W_{\text{lept}})$	> 2	

Table 7.5: Summary of the final semi-leptonic $t\bar{t}$ selections.

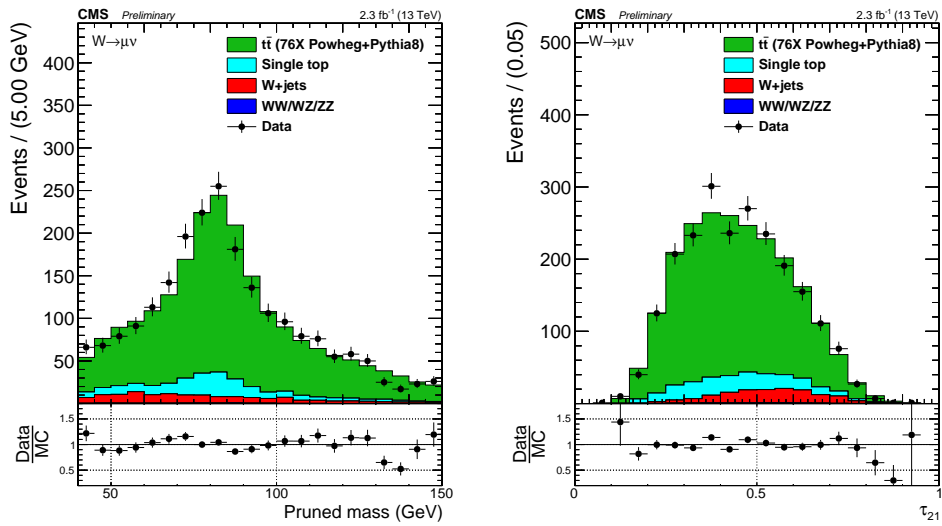


Figure 7.24: Distribution of pruned jet mass (left) and n-subjettiness (right) in the $t\bar{t}$ control sample.

¹⁸²⁷ 7.7.2 Fitting procedure

¹⁸²⁸ For this measurement, what we are interested in is to extract and compare the W-tagging efficiency
¹⁸²⁹ of the combined selection of jet mass and τ_{21} in data and MC. We are additionally interested in
¹⁸³⁰ the difference in jet-mass scale (mean of the W-jet mass peak) and jet-mass resolution (width
¹⁸³¹ of the W-jet mass peak), as this also affects the shape of the signal jet mass and therefore the
¹⁸³² tagging efficiency. In order to study these variables, we look at the pruned jet mass spectrum
¹⁸³³ between 40 and 150 GeV in two regions:

- ¹⁸³⁴ • Pass region: $0 < \tau_{21} \leq 0.45 \sim$ high purity , and
- ¹⁸³⁵ • Fail region: $0.45 < \tau_{21} \leq 0.75 \sim$ low purity.

¹⁸³⁶ Our goal is to understand what the real fraction of merged W jets is in the pass category and in
¹⁸³⁷ the fail category, assuming that the sum of the two correspond to a 100% selection efficiency (the
¹⁸³⁸ amount of W boson jets falling outside of this region is negligible). The strategy is as follows:
¹⁸³⁹ We first derive probability density functions (PDFs) which describe the distribution of fully
¹⁸⁴⁰ merged W boson jets and non-W boson jets in $t\bar{t}$, both in the pass and in the fail region. The
¹⁸⁴¹ PDFs describing real W jets and non-W jets are added with a fraction which is left floating:
¹⁸⁴² the fit decides what the fraction of real W to non-W jets is in the pass and in the fail region.
¹⁸⁴³ A simultaneous fit of pass and fail regions is then performed (using the two composite PDFs),
¹⁸⁴⁴ where the fraction of real W jets in both pass and fail regions is constrained such that, if the
¹⁸⁴⁵ signal efficiency in the pass region is ϵ_S , the signal efficiency in the fail region is $(1 - \epsilon_S)$. This
¹⁸⁴⁶ is done by letting the normalization of the PDF describing real W jets in the pass category be
¹⁸⁴⁷ defined as the total real W boson yield in the pass and fail regions combined, multiplied by some
¹⁸⁴⁸ fraction, ϵ_S . The normalization of the PDF describing real W boson jets in the fail category is
¹⁸⁴⁹ then the total real W boson yield in the pass and fail regions combined, multiplied by $(1 - \epsilon_S)$.

To understand which part of the $t\bar{t}$ jet mass distribution contains real, merged W boson jets and which are only pure combinatorial background, non-W jets, we start from $t\bar{t}$ MC. By matching the AK8 jet with quarks coming from the hadronic W boson at generator level, in a cone of $\Delta R < 0.8$, we can access the real merged W and non-merged W softdrop mass shapes. The real W and non-W PDFs for jets that pass and fail the N-subjettiness selection $\tau_{21} < 0.45$, are found to be well described by the following functions:

$$f_{\text{bkg}}(m_j) = F_{\text{ExpErf}} = e^{c_0 m_j} \cdot \frac{1 + \text{Erf}((m_j - a)/b)}{2} \quad \sim \text{for non-W jets in both pass and fail}$$

$$f^{\text{sig}}(m_j) = F_{\text{Gaus}}(m_j) + F_{\text{ExpErf}}(m_j) \quad \sim \text{for real W jets in both pass and fail}$$

Figure 7.25 shows the fitted pruned jet mass spectrum for real W jets (upper) and non-W jets (lower) in $t\bar{t}$ for jets that passed (left column) and failed (right column) the N-subjettiness selection $\tau_{21} < 0.45$.

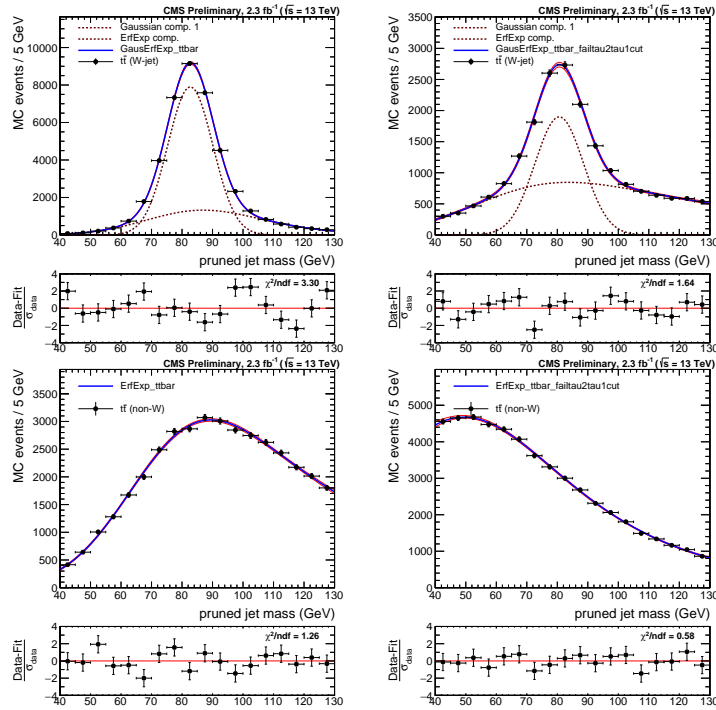


Figure 7.25: Fit to the real W (upper) and non-W (lower) boson pruned jet mass distribution for jets that pass (left) and fail (right) the cut on $\tau_{21} < 0.45$.

These shapes constitute the fit functions used for the simultaneous fit. As can be seen from the fit to real W jets in the pass region, the distribution is not purely Gaussian and has a tail at higher groomed masses. This tail depends on the matching requirements used to define real merged W jets and is unphysical. We therefore assume that the distribution of real W jets can be described by a Gaussian only, allowing the exponential error function used to describe non W-jets to cover the contribution from the tails, thereby taking the number of real W jets as the integral of the Gaussian shape only. This eliminates two additional fit functions, corresponding to six free parameters from the fit. In older estimations of the W-tagging scale factor based on the same procedure [71]), the functions used to describe the tail of the real W-jet distributions were also taken into account as contributing to the real W-jet tagging efficiency. These two calculations test two extremes: the new method assumes a Gaussian peak, absorbing the tails into the background function making the fit more robust, while the old method assumes a Gaussian peak with tails estimated from matched MC. The latter uses a more precise definition of real W jets, but yields a

less robust fit. Both methods were investigated and we found that the absorption of tails into the background function resulted in a decrease in the relative uncertainty on the final scale factor of 50% and an overall improvement on the fit quality, reducing the fit χ^2 by 15%. The fit parameters of the functions used to describe non-W jets in both the pass and in the fail region are further constrained using the values obtained from matched $t\bar{t}$ MC. The W-tagging scale factors (SF_{HP}) for the high purity selection ($\tau_{21} < 0.45$) are then extracted by estimating the selection efficiency (ϵ_{HP}) for both data and simulated samples by fitting, simultaneously, the pass and fail categories:

$$L_{\text{pass}} = \prod_i^{N_{\text{evt}}^{\text{pass}}} \left[N_W \cdot \epsilon_{HP} \cdot f_{\text{pass}}^{\text{sig}}(m_j) + N_2 \cdot f_{\text{pass}}^{\text{bkg}}(m_j) + \sum_{j=\text{ST,VV,WJet}} N_{\text{pass}}^j \cdot f_{\text{pass}}^j \right],$$

$$L_{\text{fail}} = \prod_i^{N_{\text{evt}}^{\text{fail}}} \left[N_W \cdot (1 - \epsilon_{HP}) \cdot f_{\text{fail}}^{\text{sig}}(m_j) + N_3 \cdot f_{\text{fail}}^{\text{bkg}}(m_j) + \sum_{j=\text{ST,VV,WJet}} N_{\text{fail}}^j \cdot f_{\text{fail}}^j \right],$$

where N_W is the number of real W boson jets, N_2 and N_3 are the number of combinatorial background events passing and failing the τ_{21} selection, respectively, and N_j and f_j , with $j = \text{ST, VV, WJet}$, are the normalizations and shapes of the minor backgrounds (single top, VV, W+jets), which are fixed from simulation. The fit functions used are:

$$f_{\text{pass}}^{\text{Top}} = F_{\text{ErfExpGaus}}(x) = \frac{1 + \text{Erf}((x - a)/b)}{2} \cdot e^{-(x - x_0)^2/2\sigma^2}$$

$$f_{\text{fail}}^{\text{Top}} = F_{\text{ExpGaus}}(x) = e^{ax} \cdot e^{-(x - b)^2/2s^2},$$

$$f_{\text{pass}}^{\text{VV}} = F_{\text{ExpGaus}}(x) = e^{ax} \cdot e^{-(x - b)^2/2s^2},$$

$$f_{\text{fail}}^{\text{VV}} = F_{\text{ExpGaus}}(x) = e^{ax} \cdot e^{-(x - b)^2/2s^2},$$

$$f_{\text{pass}}^{\text{wjet}} = F_{\text{ErfExp}}(x) = e^{c_0 x} \cdot \frac{1 + \text{Erf}((x - a)/b)}{2},$$

$$f_{\text{fail}}^{\text{wjet}} = F_{\text{ErfExp}}(x) = e^{c_0 x} \cdot \frac{1 + \text{Erf}((x - a)/b)}{2},$$

¹⁸⁵³ with the corresponding distributions shown in Figure 7.26. The floating parameters of the fit
¹⁸⁵⁴ (besides the PDF shape parameters themselves) are the rates N_W , N_2 and N_3 , and the mean and
¹⁸⁵⁵ sigma of the W-mass distribution defined in $f_{\text{pass}}^{\text{sig}}(m_j)$ and $f_{\text{fail}}^{\text{sig}}(m_j)$. The ratio between data and
¹⁸⁵⁶ simulation efficiencies is then taken as the W-tagging scale factor:

$$SF_{HP} = \frac{\epsilon_{HP}(\text{data})}{\epsilon_{HP}(\text{sim})}. \quad (7.5)$$

Considering that, both for data and simulation, $\epsilon_{HP} + \epsilon_{LP} + \epsilon_{fail} = 1$, the scale factor for low

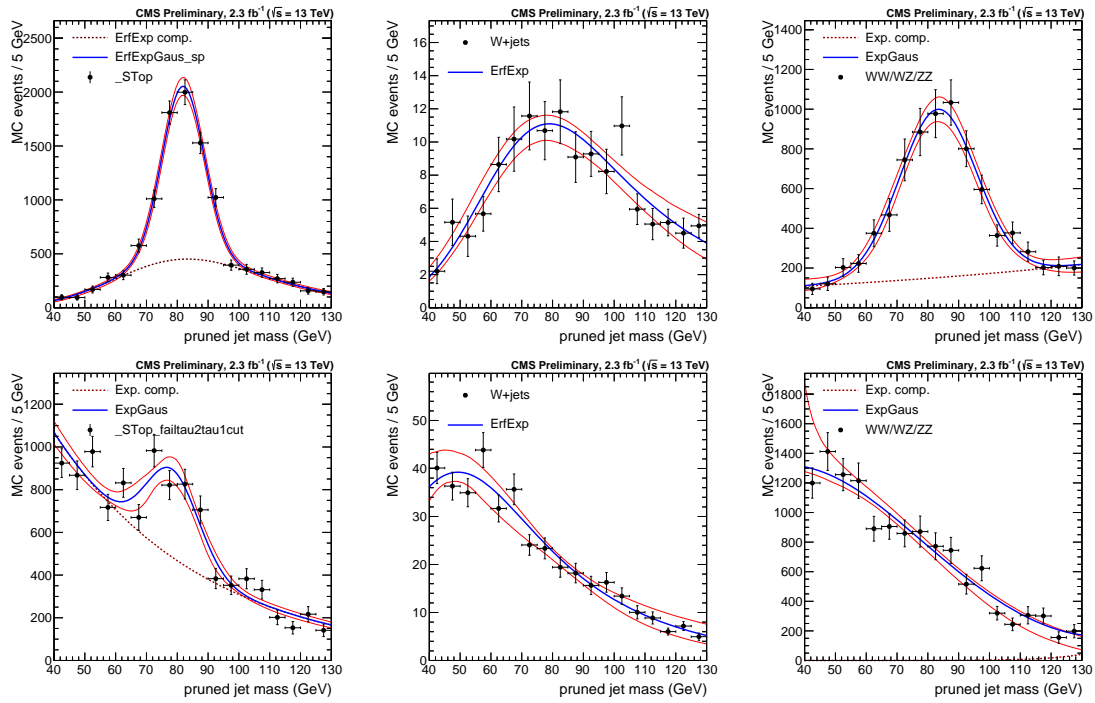


Figure 7.26: Fits to the pruned jet mass spectrum for the non-dominant backgrounds (Single top, W+jets and VV respectively) in the pass (upper) and fail (lower) regions.

purity category can be defined as:

$$SF_{LP} = \frac{1 - \epsilon_{HP}(\text{data}) - \epsilon_{fail}(\text{data})}{1 - \epsilon_{HP}(\text{sim}) - \epsilon_{fail}(\text{sim})},$$

where ϵ_{fail} is the ratio between the number of events with $\tau_2/\tau_1 > 0.75$ and the total number of events. As mentioned previously, the number of real W jets with $\tau_2/\tau_1 > 0.75$ is negligible and the definition of the low purity scale factor simplifies to

$$SF_{LP} = \frac{1 - \epsilon_{HP}(\text{data})}{1 - \epsilon_{HP}(\text{sim})}. \quad (7.6)$$

7.7.3 Systematic uncertainties

As systematic uncertainties, we consider effects due to differences between $t\bar{t}$ simulation as well as effects due to the choice of fit method. The former is evaluated by comparing the extracted scale factor when using $t\bar{t}$ MC samples produced with three different combinations of matrix element (ME) and shower generators: POWHEG (NLO) interfaced with PYTHIA8, MADGRAPH (LO) QCD

interfaced with HERWIG++, and POWHEG interfaced with HERWIG++. The uncertainty due to different ME generators (POWHEG versus MADGRAPH) corresponds to 3(13)% and is listed in Table 7.6 as the first quoted systematic uncertainty. The uncertainty due to parton showering (PYTHIA8 versus HERWIG++) is 8.6%, but is not relevant for analyses where no HERWIG++ based simulation is used, as is the case for the search presented in this chapter. For the systematic uncertainty accounting for effects due to choice of fit method, we compare the estimated extracted efficiency in $t\bar{t}$ MC using the two different fit models described above: the new model, where the signal is modeled by a Gaussian peak and the tails of the distribution are absorbed in the background fit model, and the old model, including the tails when calculating the fraction of real W jets. Figure 7.27 shows the fits obtained in the pass and fail regions using the two different models. With the new model only the Gaussian component of the fit contributes to the W-tagging efficiency while, with the old model, a Chebyshev component is additionally contributing to the total W-tagging efficiency. The estimated efficiencies obtained using both methods, after

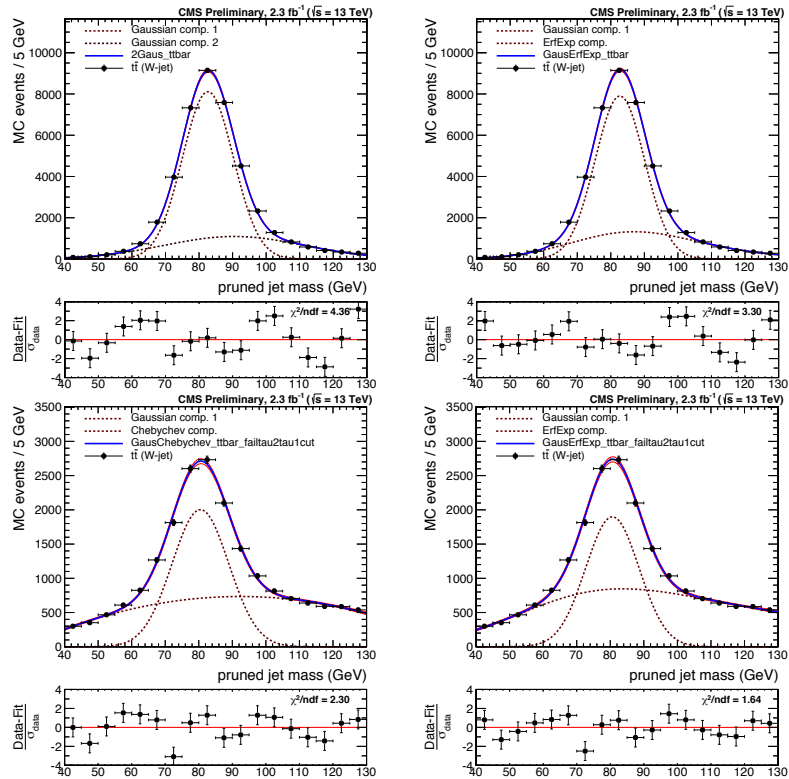


Figure 7.27: Fits obtained in the pass (top) and fail (bottom) regions using two different models: An alternative model with tails (top and bottom, left) where the tail component is contributing to the total W-tagging efficiency. When using the default model (top and bottom, right), only the Gaussian component of the fit contributes to the W-tagging efficiency.

1878 being corrected for the fraction of W jets in the tails, agree within 0.3(0.8)% and are listed as a
1879 systematic uncertainty in Table 7.6.

1880 One additional uncertainty is added. As the W-tagging scale factor is evaluated in a $t\bar{t}$ sample,
1881 the transverse momentum range is rather limited. When the W-jet p_T reaches ~ 400 GeV, the
1882 AK8 jet becomes a fully merged top jet with a mass of 170 GeV and a scale factor measurement
1883 becomes impossible. However, the jets used in the analyses presented in this thesis have very high
1884 transverse momenta, up to 2-3 TeV, and we therefore need an estimate of how the uncertainty
1885 on the W-tagging scale factor changes as a function of p_T . This is estimated by comparing
1886 the difference in tagging efficiency between $G_{\text{bulk}} \rightarrow WW$ signal MC showered by PYTHIA8 as
1887 compared to HERWIG++ as a function of jet p_T , relative to the difference in tagging efficiency
1888 between the two at a $p_T \sim 200$ GeV. This measurement was performed by a separate analysis
1889 team, and found to be $5.90\% \times \ln(p_T/200 \text{ GeV})$. Systematic uncertainties from other sources
1890 (lepton identification, b tagging, etc.) are less than 0.5% and therefore negligible.

1891 7.7.4 Fit results

1892 The simultaneous fit as described above is then performed both for data and for simulation, where
1893 we take the ratio of data and MC efficiencies as efficiency scale factors. The corresponding fits are
1894 shown in Figure 8.17, with the corresponding extracted efficiencies and scale factors summarized
 in Table 7.6. We additionally extract the jet mass scale and jet mass resolution, used to scale

	Working point	Eff. data	Eff. simulation	Scale factor
HP	$\tau_{21} < 0.45$	0.775 ± 0.041	0.822 ± 0.033	$0.94 \pm 0.05 \text{ (stat)} \pm 0.03 \text{ (sys)} \pm 0.003 \text{ (sys)}$
LP	$0.45 < \tau_{21} < 0.75$	0.225 ± 0.041	0.178 ± 0.033	$1.27 \pm 0.25 \text{ (stat)} \pm 0.13 \text{ (sys)} \pm 0.008 \text{ (sys)}$

Table 7.6: Efficiencies in data and in MC together with the corresponding W-tagging scale factors for the high purity and low purity categories.

1895
1896 and smear the jet mass signal shape in the limit setting procedure. These values are taken from
1897 the mean $\langle m \rangle$ and width σ of the Gaussian component of the simultaneous fit in the pass region
1898 and are summarized in Table 7.7. Both the jet mass scale as well as the jet mass resolution is
1899 larger in simulation than in data with a relative difference of 2 and 10%, respectively. However,
1900 the jet mass resolution scale factor has a large uncertainty attached to it and is statistically
1901 insignificant (in agreement with unity within uncertainty).

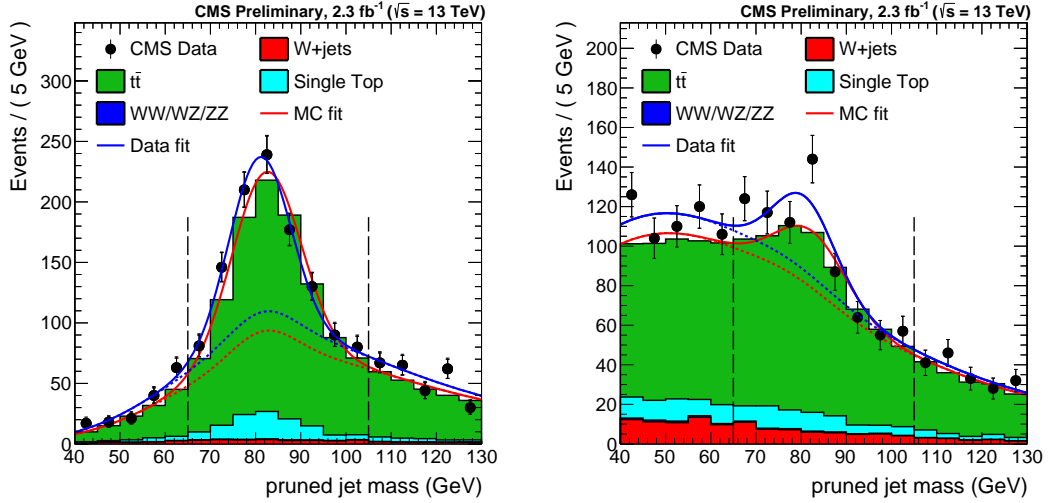


Figure 7.28: Pruned jet mass distribution that pass (left) and fail (right) the $\tau_{21} < 0.45$ selection. Results of both the fit to data (blue) and simulation (red) are shown. The background components of the fit are shown as short-dashed lines.

Parameter	Data	Simulation	Data/Simulation
Pruning $\langle m \rangle$	80.9 ± 0.6 GeV	82.5 ± 0.1 GeV	0.980 ± 0.007
Pruning σ	6.7 ± 0.7 GeV	7.5 ± 0.3 GeV	0.89 ± 0.10

Table 7.7: Jet mass scale and resolution in data and in simulation together with the relevant data-simulation scale factors.

7.7.5 Impact on search variables

The obtained W-tagging scale factors are used as a scale of the signal yield. As we require two W-tagged jets, either HP or LP, the actual scale factors for the high-purity signal yield is $SF_{HP} \times SF_{HP}$ and for the low-purity category $SF_{HP} \times SF_{LP}$. The signal yields are then

$$N_S^{HP} = N_{\text{HP tot. yield}} \times SF_{HP} \times SF_{HP}$$

$$N_S^{LP} = N_{\text{LP tot. yield}} \times SF_{HP} \times SF_{LP}$$

¹⁹⁰³ The uncertainties on the scale factors are considered as anti-correlated between the HP and the LP categories. The jet mass scale and resolution are used to scale and smear the signal Monte Carlo. An uncertainty on the signal yield based on the uncertainty on jet mass scale and

1906 resolution is also considered by scaling and smearing the jet mass up and down within the quoted
1907 uncertainties and then recomputing the signal efficiency. The results are listed in Table 7.8.

1908 7.8 Systematic uncertainties

1909 The uncertainty on the background parametrization is statistical only and is taken as the
1910 covariance matrix of the dijet fit function. As demonstrated in the F-test, we study different
1911 background parameterizations and we have found these to be within the fit uncertainty of the
1912 nominal fit. The remaining uncertainties concern the signal shape and yield and are listed in
1913 Table 7.8. Jet reconstruction uncertainties affect both the signal yield and the signal shape. These
1914 are evaluated by rescaling the jet four-momenta according to uncertainties on the jet energy scale
1915 and resolution and recomputing the signal efficiency. The difference in efficiency with and without
1916 smearing/scaling is taken as a systematic uncertainty, as described above. The jet mass/energy
1917 scale and resolution also affect the signal shape, and are added as uncertainties in the peak
 position and width of the Gaussian component of the signal PDFs.

Source	Relevant quantity	HP uncertainty (%)	LP uncertainty (%)
Jet energy scale	Resonance shape	2	2
Jet energy resolution	Resonance shape	10	10
Jet energy and m_{jet} scale	Signal yield	0.1–4	
Jet energy and m_{jet} resolution	Signal yield	0.1–1.4	
Pileup	Signal yield	2	
Integrated luminosity	Signal yield	2	
PDFs (W')	Signal yield	4–19	
PDFs (Z')	Signal yield	4–13	
PDFs (G_{bulk})	Signal yield	9–77	
Scales (W')	Signal yield	1–14	
Scales (Z')	Signal yield	1–13	
Scales (G_{bulk})	Signal yield	8–22	
Jet energy and m_{jet} scale	Migration	1–50	
V tagging τ_{21}	Migration	14	21
V tagging p_T -dependence	Migration	7–14	5–11

Table 7.8: Summary of the systematic uncertainties and the quantities they affect. Migration uncertainties result in events switching between the purity/mass categories and change the efficiency in each category, but do not affect the total signal efficiency.

¹⁹¹⁹ 7.9 Results

¹⁹²⁰ The background fits for each analysis category in the data signal region are shown in Figure
¹⁹²¹ 7.29. Here a background-only fit is performed while, as described above, a simultaneous fit is
¹⁹²² used for the limit-setting procedure. The filled area corresponds to the 1σ error band of the
¹⁹²³ background fit, obtained using linear error propagation. No excess is observed, and we proceed
¹⁹²⁴ by setting upper limits on the cross section times branching ratio of the process $X \rightarrow VV$, using
¹⁹²⁵ the asymptotic CL_S method [72]. The binned likelihood is defined as

$$L = \prod_i \frac{\mu_i^{n_i} e^{-\mu_i}}{n_i!}, \quad (7.7)$$

¹⁹²⁶ with

$$\mu_i = \sigma \cdot N_i(S) + N_i(B). \quad (7.8)$$

¹⁹²⁷ Here σ is the signal strength scaling the expected number of signal events in the i -th dijet invariant-
¹⁹²⁸ mass bin $N_i(S)$, $N_i(B)$ is the expected number of background events in dijet invariant-mass bin i
¹⁹²⁹ and n_i is the observed number of events in the i th dijet invariant-mass bin. The background per
¹⁹³⁰ bin $N_i(B)$ is estimated from the background component of the best signal and background fit to
¹⁹³¹ the data points, with the signal cross section set to zero. The number of signal events in the i -th
¹⁹³² dijet invariant mass bin, $N_i(S)$, is estimated from the signal templates, considering only dijet
¹⁹³³ invariant massed in a 20% window around the resonance mass, containing most of the signal
¹⁹³⁴ contribution while making sure to keep a good description of the core.

¹⁹³⁵ 7.10 Limits

¹⁹³⁶ 7.10.1 All-hadronic analysis only

¹⁹³⁷ As mentioned in Section 7.3, we set limits on three different signal scenarios: $G_{\text{bulk}} \rightarrow WW$,
¹⁹³⁸ $G_{\text{bulk}} \rightarrow ZZ$, and $W' \rightarrow WZ$, with a $\tilde{k} = 0.5$ for the G_{bulk} . Figure 7.30 shows the asymptotic
¹⁹³⁹ limits at 95 % confidence level on the signal cross section as a function of its resonance mass
¹⁹⁴⁰ obtained with 2.7 fb^{-1} of 13 TeV CMS data after combining all mass and purity categories
¹⁹⁴¹ (top). The corresponding p-values are shown in the bottom panel. The statistics are too low to
¹⁹⁴² exclude the excess around 2 TeV observed in the corresponding Run 1 analysis and, in addition,
¹⁹⁴³ an under-fluctuation in data is present in this region. The largest excess of 2.8σ is observed for a
¹⁹⁴⁴ $G_{\text{bulk}} \rightarrow ZZ$ hypothesis at a resonance mass of 2.8-3 TeV. This is driven by the high-purity ZZ

mass category, the category with the lowest statistics, and is caused by one event. A 3-parameter fit is the default background fit function for this category, however, a 2-parameter fit could also be used to describe these data. In Figure 7.31 we compare the limits and p-values obtained using a 2-parameter and a 3-parameter fit to describe the background in this category. The significance at 3 TeV is reduced from 2.8 to 1.5 σ with a 2-parameter fit, reflecting the fact that the fit is poorly constrained in the high mass tail due to low statistics. The fit to data using both a 2 and 3-parameter fit in the ZZ high-purity category is shown in Figure 7.32, where we see that the 2-parameter fit lies within the fit uncertainties of the nominal fit. The lack of constraint on the fit in the dijet invariant mass tail when statistics are very low is a drawback of a method relying fully on a parametric fit and reduces the analysis sensitivity in the high- m_{jj} region. In Search II (Section 8) we will keep taking advantage of the dijet fit, however, the integrated luminosity is ~ 15 times higher, resulting in more datapoints in the m_{jj} tail which further constrains the fit. In Search III (Section 9), we will explore alternate methods which allow more control over the background shape across the full mass spectrum.

7.10.2 Semi-leptonic and all-hadronic combination

To maximize the search sensitivity, we combine the results obtained above with those of the corresponding semi-leptonic analysis. We assume the uncertainties on luminosity, V-tagging efficiency, and jet mass scale and resolution to be fully correlated. The obtained exclusion limits in Figure 7.33 show the resulting expected and observed exclusion limits after combining the two analyses. As before, we consider a scenario where only either a W' or Z' resonance is expected, called the singlet hypothesis (upper two plots). In addition, we set limits on the triplet hypothesis, assuming the W' and Z' bosons to be degenerate in mass (bottom left plot). The all-hadronic analysis sets stronger upper limits than the semi-leptonic analysis above 1.7 TeV for a Z' and > 1.3 TeV for a W' . The improvement in sensitivity is due to the higher branching fraction, such that $\mathcal{B}(WW \rightarrow q\bar{q}q\bar{q}) = 44\%$, $\mathcal{B}(WW \rightarrow \ell\nu q\bar{q}) = 31\%$, $\mathcal{B}(WZ \rightarrow q\bar{q}q\bar{q}) = 46\%$, and $\mathcal{B}(WZ \rightarrow \ell\nu q\bar{q}) = 16\%$. The analysis sensitivity for G_{bulk} is too weak to set limits, but cross sections between 3–1200 fb are excluded. For the HVT models A and B, a W' is excluded below 2.0 and 2.2 TeV, respectively, and Z' resonances are excluded below 1.7 (1.6) TeV assuming a HVT model A(B). Assuming a HVT Model A(B) triplet hypothesis, resonances below 2.3 (2.4) TeV are excluded. The combined results would therefore just exclude a W' with a mass around 2 TeV, the favored candidate to explain the diboson excess observed in 8 TeV data. However, Bulk Graviton signals were still far from excluded and, with the expected increase in luminosity of a factor of ten in 2016, we were excited to keep on searching.

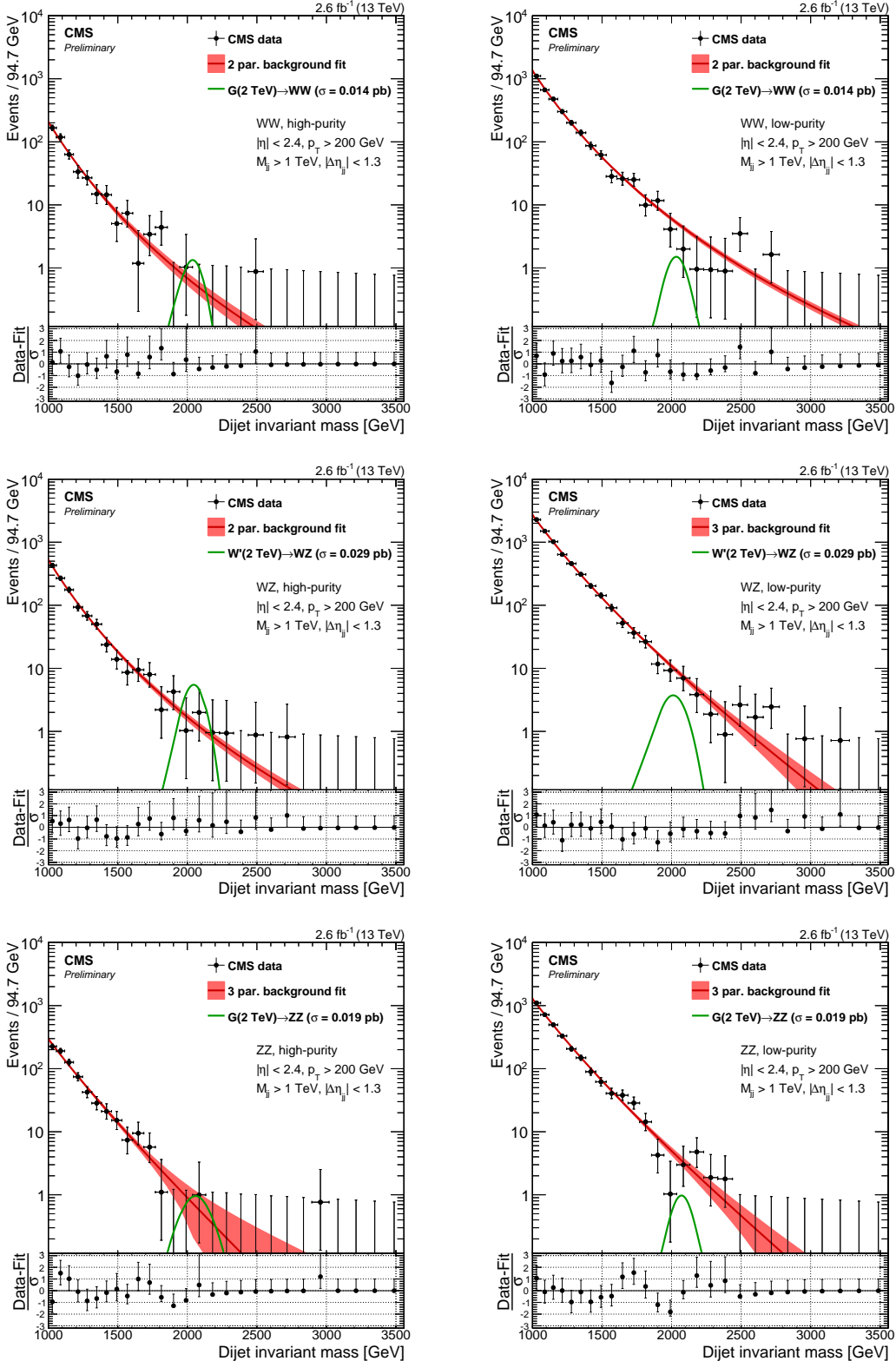


Figure 7.29: Fit to data in the signal region using the background fit only for the different mass and purity categories. The filled red area correspond to the 1σ statistical error of the fit.

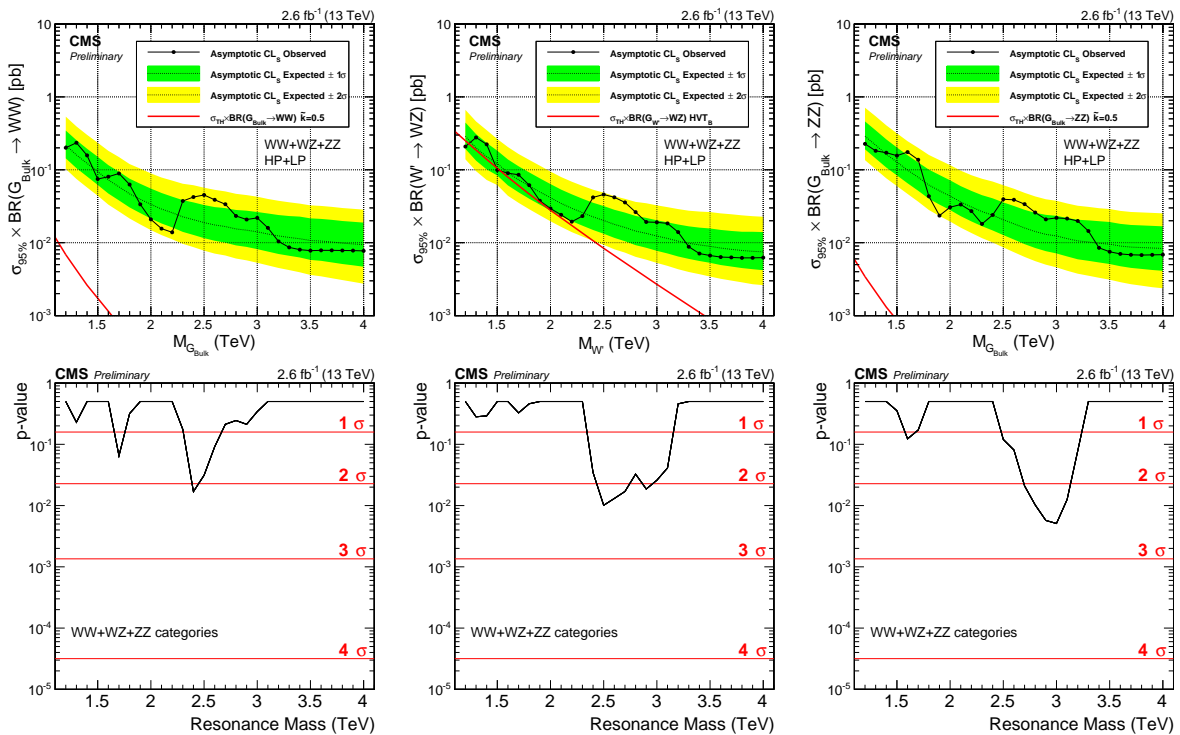


Figure 7.30: Expected and observed limits with corresponding p-values obtained using 2.7 fb^{-1} of CMS data after combining all mass and purity categories. Here for a Bulk $G \rightarrow WW$ (left), $W' \rightarrow WZ$ (middle), and $G \rightarrow ZZ$ (right) signal.

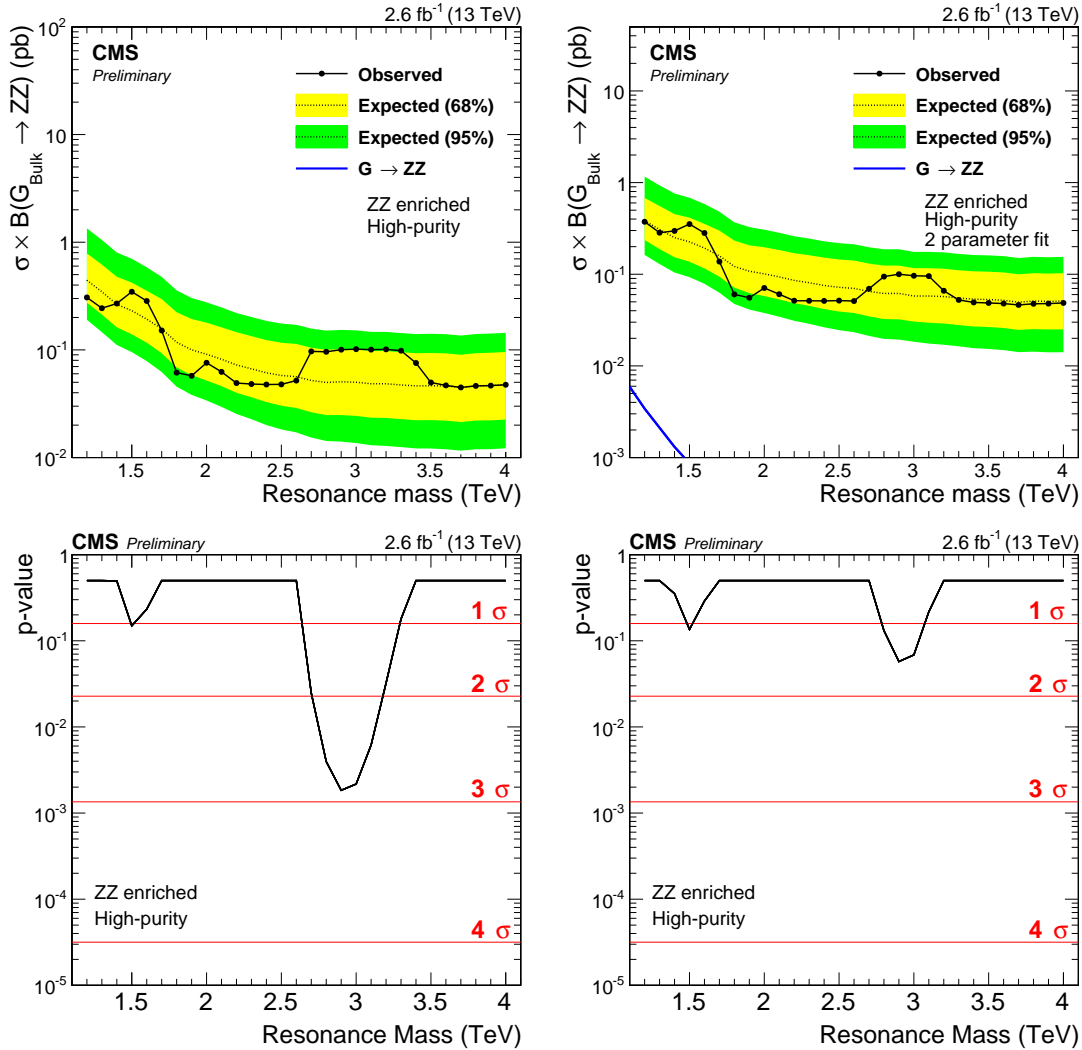


Figure 7.31: Expected and observed limits (top) and the corresponding p-values (bottom) obtained in the ZZ high-purity category using a 3- (left) and 2-parameter (right) fit to describe the background. The significance at 3 TeV is reduced from 2.8 to 1.5 σ .

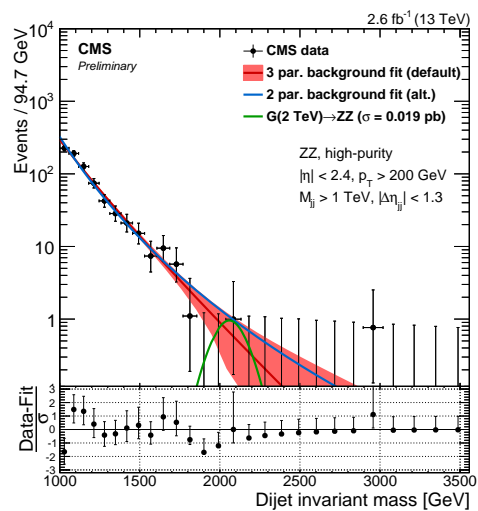


Figure 7.32: Background fit to data in the ZZHP category using the nominal 3- (red) and an alternate 2-parameter (blue) fit to describe the background.

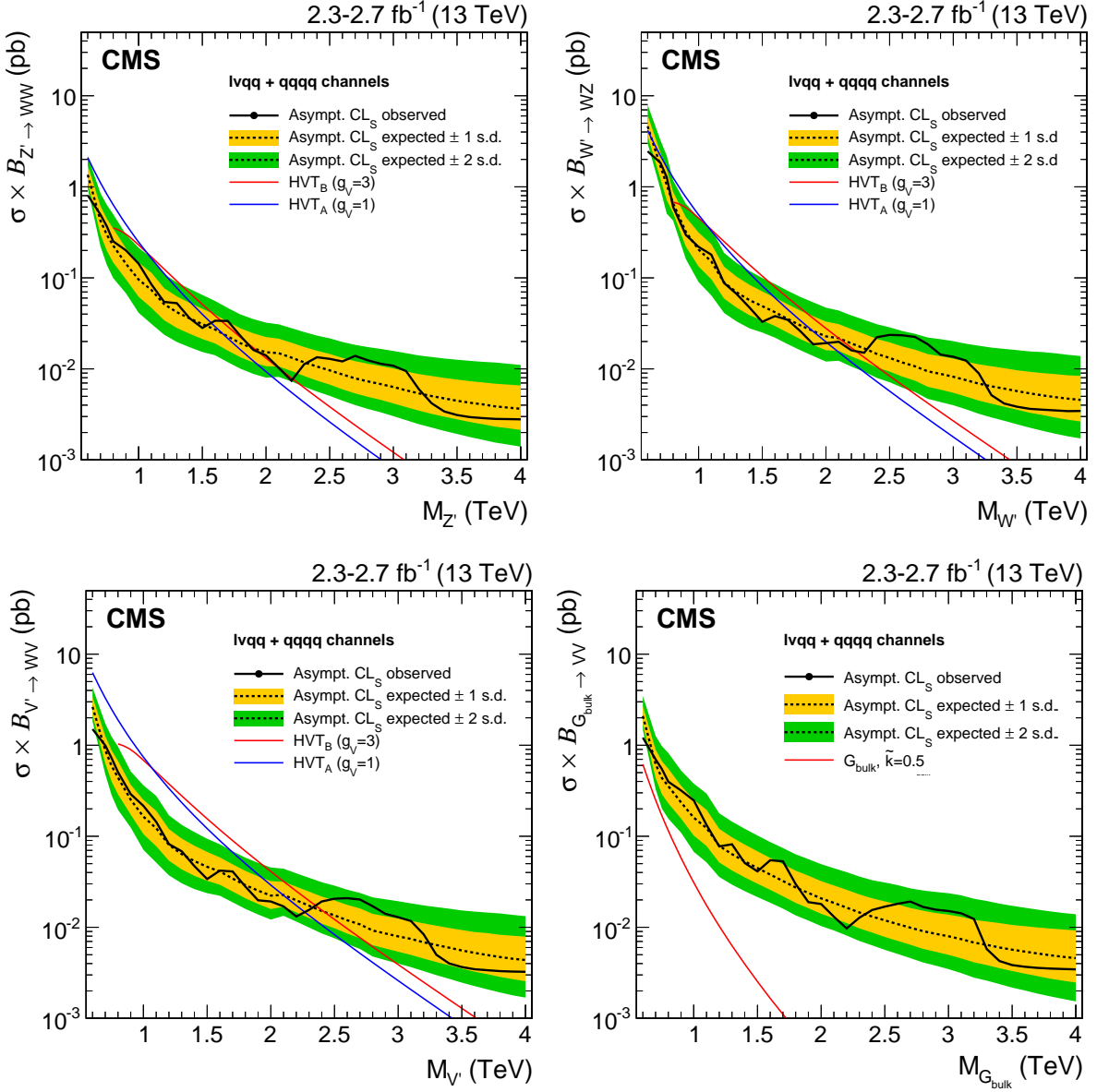


Figure 7.33: Observed (black solid) and expected (black dashed) 95% CL upper limits on the production of a narrow-width resonance decaying to a pair of vector bosons for different signal hypotheses. In the upper plots, limits are set in the context of a spin-1 neutral Z' (left) and charged W' (right) resonance, and compared with the prediction of the HVT Models A and B. In the lower left plot, limits are set in the same model under the triplet hypothesis (W' and Z' of degenerate mass). In the lower right plot, limits are set in the context of a bulk graviton with $\tilde{k} = 0.5$ and compared with the prediction.

1978

CHAPTER 8

1979

Search II: A new pileup resistant and perturbative safe tagger

1980

1981 *With the first diboson resonance search with a center-of-mass energy of 13 TeV published, we*
1982 *concluded that more data would be needed in order to fully exclude the excess observed in Run 1.*
1983 *Data from 2016 was right around the corner and, with the LHC planning to reduce β^* from 80 to*
1984 *40 cm, the machine was expected to deliver an instantaneous luminosity three times that of the*
1985 *peak luminosity in 2015. This higher instantaneous luminosity, however, meant double the pileup.*

1986

1987 *We knew that a novel pileup-subtraction algorithm had been developed, which provided far better*
1988 *pileup and underlying event rejection than the current default algorithm that used charged hadron*
1989 *subtraction. We also knew that there had been made progress on the theory side in the development*
1990 *of a groomer which was completely insensitive to correlated soft emissions (non-global logarithms),*
1991 *allowing jet grooming to be accomplished in a theoretically calculable way, softdrop with $\beta = 0$*
1992 *($mMDT$).*

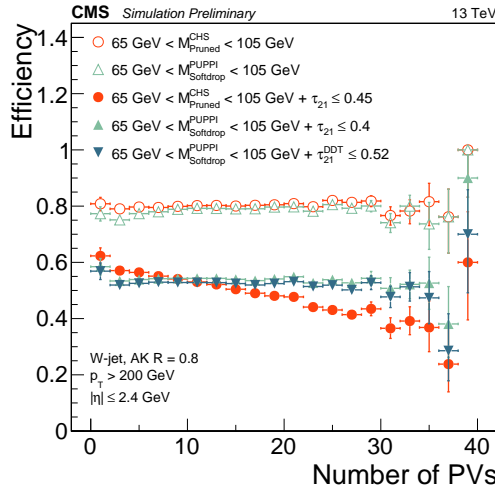
1993

1994 *With more time at hand than in 2015, I therefore decided to pursue a novel W-tagger for*
1995 *this second search. This meant studying and optimizing new approaches for pileup rejection and*
1996 *grooming, developing dedicated jet-mass corrections, as well as validating this new tagger in MC*
1997 *and data. This tagger, together with the mass corrections, became the default and recommended*
1998 *W-tagging algorithm of CMS.*

1999

2000 *Search II was the first published analysis to use a novel combination of PUPPI and softdrop*
2001 *grooming algorithms, now default for W-tagging in CMS. Through this search, the tagger was*
2002 *optimized, commissioned and validated, making it available for several analysis to come. In*

addition, the search was extended to consider three additional signal hypothesis. Two of these were in a final state never before explored with a center-of-mass energy of 13 TeV, the excited quark scenario where q^* decays to qW or qZ , and the vector boson is boosted and identified through V -tagging. It was published with 35.9 (12.9) fb^{-1} of 2016 data.



Published in PRD, DOI: 10.1103/PhysRevD.97.072006; CMS-PAS-B2G-16-021; CMS-PAS-JME-16-003

2007 8.1 Towards robust boosted jet tagging

2008 When we first studied W tagging with 13 TeV data, in the context of the analysis conducted
 2009 with the 2015 dataset, Section 7.4.3, two interesting correlations were observed:

- 2010 1) a strong dependence of the jet mass on the jet p_T , when using the AK8 jet clustering algorithm
 2011 with CHS pileup removal and softdrop with $\beta = 0$ (mMDT) grooming, and
- 2012 2) a strong dependence of the τ_{21} selection efficiency on pileup, when using the AK8 jet clustering
 2013 algorithm with CHS pileup removal.

2014 The reason we studied the softdrop algorithm with $\beta = 0$, hereafter just referred to as “softdrop”,
 2015 as an alternative to the pruning algorithm used in the 2015 analysis was that, besides the
 2016 possibility that it might perform better, we knew it had certain favorable qualities compared to
 2017 other groomers; the softdrop algorithm, in addition to removing sensitivity to the soft divergences
 2018 of QCD as all groomers do (they are IRC safe, see Section 6.4.1), eliminates all correlated soft
 2019 emissions in the jet which are wider than the dominant two-prong substructure, leading to no
 2020 non-global logarithmic terms (NGLs) in the jet mass [44]. NGLs arise from configurations where,
 for instance, a soft gluon is radiated into the jet cone, as illustrated in Figure 8.1. The benefit of

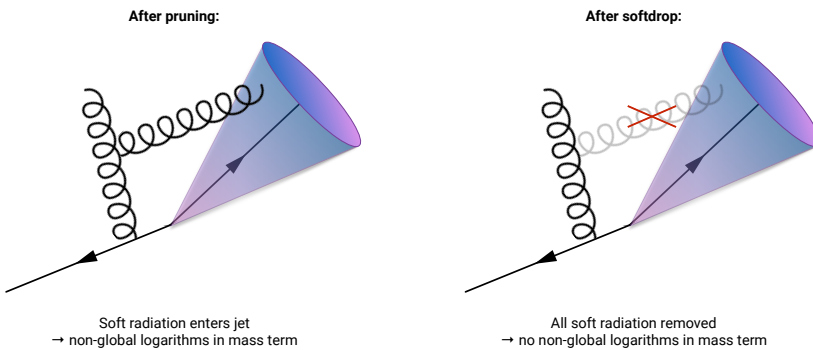


Figure 8.1: The pruning algorithm does not remove all soft emission and therefore has non-global logarithmic terms in the jet mass. Softdrop with $\beta = 0$ removes all soft emissions wider than the dominant two-prong substructure and is therefore free of non-global logarithms.

2021 being NGL-free, is that one can calculate the softdrop jet mass to a significantly higher precision
 2022 than what is possible for other grooming algorithms or for the plain jet mass (NGLs are the main
 2023 reason a full resummation of the plain jet mass beyond NLL accuracy does not exist). There
 2024

were therefore theoretically well-motivated reasons for wanting the baseline CMS vector boson tagger to be softdrop-based.

However, as was discussed in Section 7.4.3, the softdrop jet-mass of signal jets displayed a large dependence on jet p_T , both for reconstructed and generator-level jets. One hypothesis was that this was due to pileup and that perhaps softdrop was more sensitive to contribution from additional interaction vertices than pruning. A study in Ref. [73] had also shown mMDT to be more sensitive to the underlying event, but using a different asymmetry criteria than softdrop (see Appendix A.1).

In parallel to the ongoing theoretical work on groomers, a novel pileup removal algorithm had been proposed: Pileup per particle identification (PUPPI) [35]. Described in detail in Section 6.3.2, PUPPI considers not only charged pileup, but also reweights neutral particles in the jet with its probability of arising from pileup. PUPPI had proven itself far superior to the current CHS algorithm in terms of jet observables for large radius jets, and therefore seemed like a good candidate to address both issues listed above: the softdrop p_T dependence and the strong pileup dependence of τ_{21} . The focus of Search II would therefore be on the commissioning of a novel W-tagger. There are interesting additions to the analysis strategy as well: the inclusion of a $Z' \rightarrow WW$ signal hypothesis and the addition of a completely new analysis, the single V-tag analysis.

8.2 Analysis strategy

The analysis strategy for this search is conceptually the same as for Search I. In addition, we take advantage of the n-subjettiness categorization and do an additional analysis in parallel: a search for excited quark resonances q^* [74, 75] decaying to qW or qZ . We call this the single V-tag analysis, and the analysis selection only differs in that one jet is not required to pass the V-tag selection (groomed mass and n-subjettiness). The VV analysis is hereby referred to as the double V-tag analysis. The difference between the two analyses is illustrated in Figure 8.2. In addition, limits are set on a $Z' \rightarrow WW$ signal hypothesis in the double V-tag analysis, another first with data collected at 13 TeV center-of-mass energy. This analysis was published in two steps: an early CMS physics analysis summary document (PAS) based on 12.9 fb^{-1} of 2016 data [71], describing the new PUPPI softdrop based V tagger as well as the single V-tag analysis, and a second analysis considering the full 2016 dataset [76]. The commissioning of the new V tagger has also been documented in a jet performance PAS [77]. In this chapter, the main emphasis will be on the work presented in CMS-PAS-B2G-16-021 [71] since this was where the new V tagger and single V-tag analysis was first presented. The second part of the results chapter, Section 8.10.2,

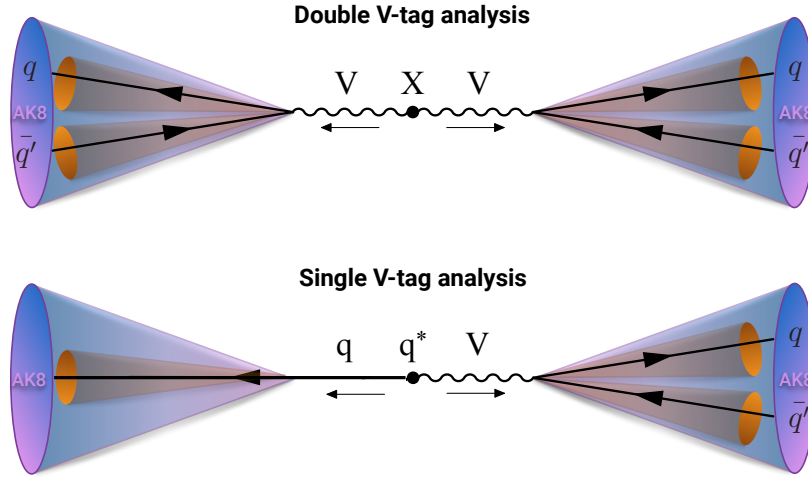


Figure 8.2: The double (top) and single (bottom) W/Z-tag analysis.

2058 includes the results obtained using the full 2016 dataset of 35.9 fb^{-1} .

2059 8.3 Data and simulated samples

2060 As mentioned above, the analysis of the 2016 dataset was done in two steps corresponding
 2061 to two different datasets: one analysis based on 12.9 fb^{-1} of early 2016 data, describing the
 2062 new W-tagger and single V-tag category, and a second paper considering the full 2016 dataset,
 2063 corresponding to 35.9 fb^{-1} . Both were collected at a center-of-mass energy of 13 TeV.

2064 The G_{bulk} and HVT signal samples are modeled in the same way as in 2015. The q^* samples
 2065 are simulated assuming unpolarized bosons and a compositeness scale Λ set equal to the resonance
 2066 mass. These are generated at leading order using PYTHIA version 8.212 [63].

2067 The standard model background processes of QCD, W+jets, and Z+jets are all simulated to
 2068 leading order. The W and Z+jets backgrounds are simulated with MADGRAPH5_AMC@NLO [62, 78].
 2069 Three different combinations of matrix element and shower generators are used for QCD as these
 2070 predictions are known to differ: PYTHIA-only, the leading order mode of MADGRAPH5_AMC@NLO
 2071 matched with PYTHIA, and HERWIG++ 2.7.1 [50] with the CUETHS1 tune [57].

2072 8.4 Event selection

2073 8.4.1 Triggering

2074 The triggers used in this analysis are the same ones as in 2015 (see Section 7.4.1), however, due
 2075 to the new single V-tag analysis, the trigger turn-ons have been reevaluated separately with the
 2076 requirement that either one or two jets have an offline softdrop jet mass above 65 GeV. Figure 8.3
 2077 shows the trigger turn-on curves as a function of dijet invariant mass for jets passing one of the
 2078 H_T -based triggers only (pink markers), one of the grooming triggers only (green markers), and
 2079 when combining all of them (purple markers). The turn-on curves are shown for all jet pairs
 2080 passing loose selections as described in Section 7.4.2 (top), and for jet pairs where one (bottom
 2081 left) or both (bottom right) of the jets additionally are required to have a softdrop mass larger
 2082 than 65 GeV. Including the grooming triggers lowers the 99% trigger efficiency threshold by
 2083 around 50 (80) GeV in the single-tag (double-tag) category once substructure is required on the
 2084 analysis level. Using a combination of either of the triggers, we are safely on the trigger plateau
 2085 for dijet invariant masses above 955 (986) GeV in the double (single) tag category, so that the
 2086 dijet invariant-mass threshold can be set at 955 GeV for the double-tag analysis and 990 GeV for
 2087 the single-tag analysis. For control plots, where no groomed-mass window is applied, a trigger
 2088 threshold of 1020 GeV is used. Figure 8.4 shows the trigger efficiency as a function of the offline
 2089 PUPPI softdrop-jet mass (left) and pruned-jet mass (right) for the trigger requiring an online
 2090 trimmed-jet mass of at least 30 GeV. Here, the jet transverse momentum of one of the jets is
 2091 required to be at least 600 GeV and no other mass cut is applied. The trigger turn-on is sharp
 2092 and the plateau is reached for offline groomed-jet masses around 50 GeV.

2093 8.4.2 Preselection

2094 The same preselections as in Search I, described in Section 7.4.2, are used; we require two AK8 jets
 2095 with CHS pileup subtraction applied, and that are required to pass the tight jet-ID requirement,
 2096 $p_T > 200$ GeV and $|\eta| < 2.5$. The same selection requirement that suppresses t-channel QCD
 2097 production is required, $|\Delta\eta| < 1.3$, together with thresholds on the dijet invariant mass of 955
 2098 GeV for the double-tag and 990 GeV for the single-tag analyses. The jet p_T (top left), η (top
 2099 right), $\Delta\eta_{jj}$ (bottom left) and dijet invariant mass (bottom right) for the two leading jets in the
 2100 event after loose preselections are applied is shown in Figure 8.5. A large difference in slope in
 2101 the jet p_T and dijet invariant mass spectrum depending on the QCD matrix element or shower
 2102 generator is observed. Pure PYTHIA QCD MC describes the data best, while HERWIG++ tends to
 2103 underestimate and MADGRAPH5_AMC@NLO+PYTHIA tends to overestimate the number of high
 2104 p_T/m_{jj} jets. Pure PYTHIA8 QCD MC is therefore used for all background checks in this analysis.

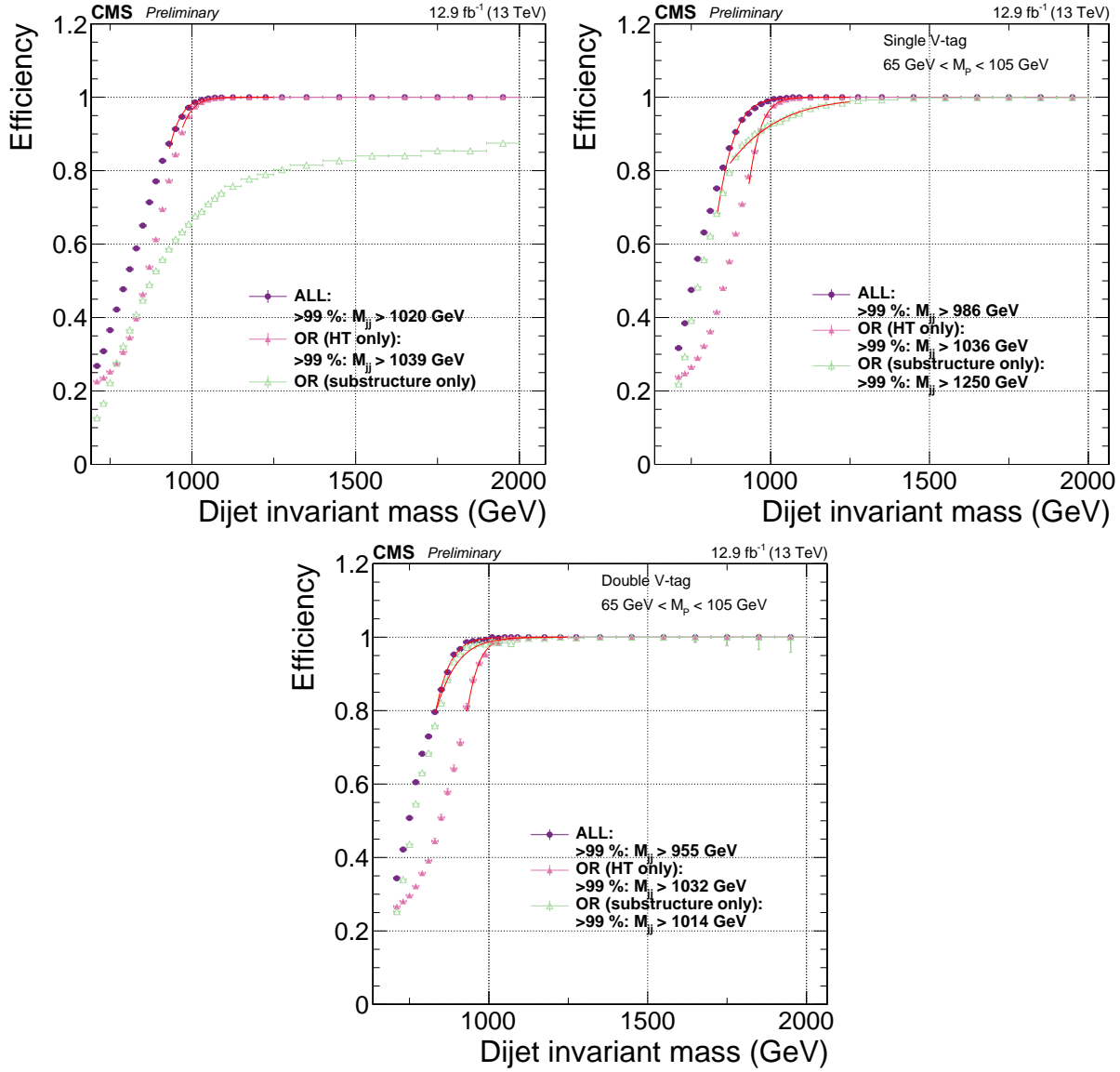


Figure 8.3: Comparison of trigger efficiencies for jets passing one of the HT-triggers only (pink), for jets passing one of the grooming-triggers only (green), and for jets passing one of the HT-triggers or one of the grooming triggers (purple). It is shown here as a function of the dijet invariant mass for all jet pairs passing loose selections (top), where one jet additionally is required to have a softdrop mass larger than 65 GeV (bottom left), and where both jets are required to have a softdrop mass larger than 65 GeV (bottom right).

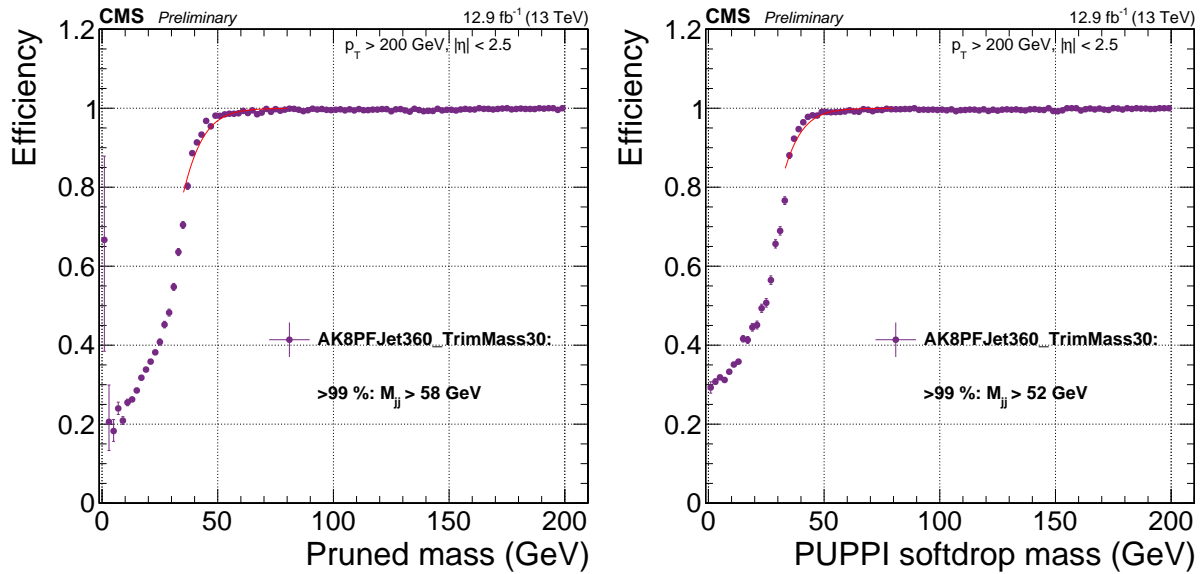


Figure 8.4: Efficiency for the trigger requiring an online trimmed jet mass of at least 30 GeV as a function of the pruned-jet (left) and softdrop-jet (right) mass for jets with $p_T > 600$ GeV.

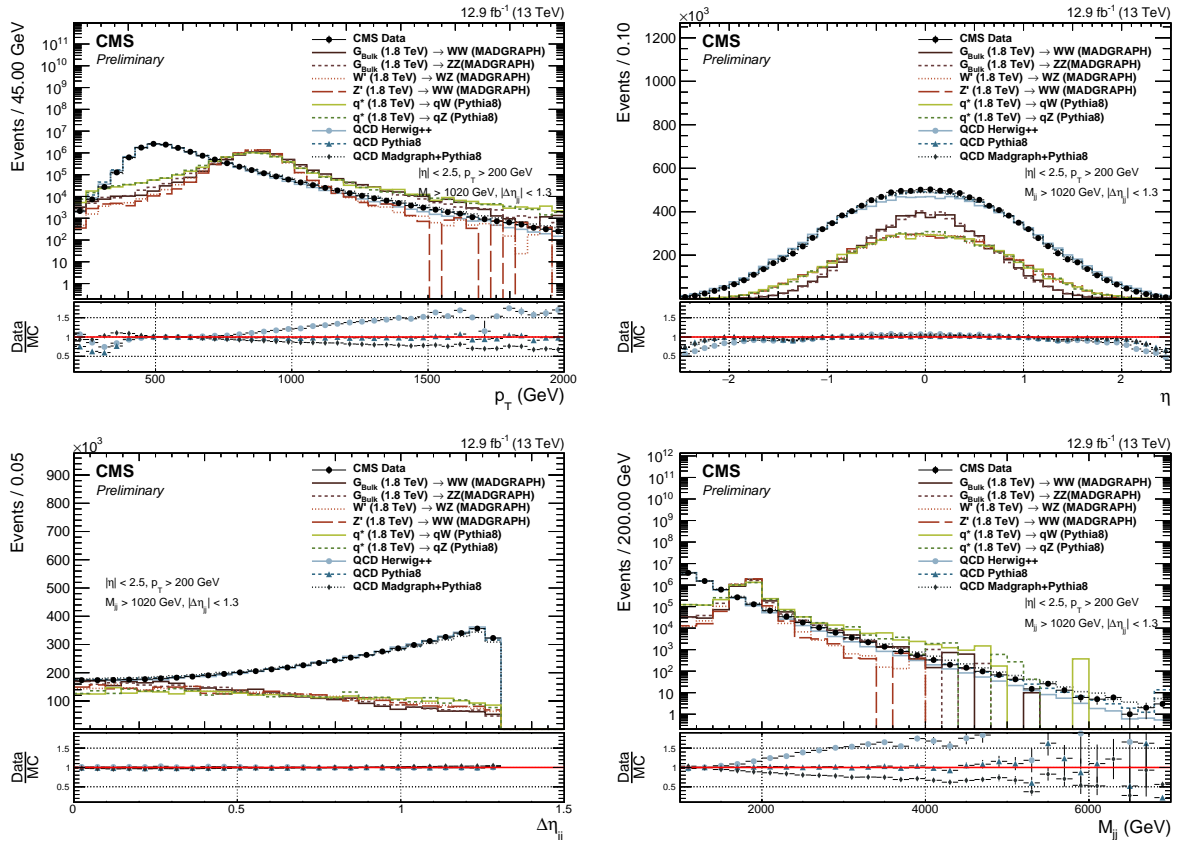


Figure 8.5: Jet p_T (top left), η (top right), $\Delta\eta_{jj}$ (bottom left) and dijet invariant mass (bottom right) for the two leading jets in the event after loose preselections are applied. The signal is scaled by an arbitrary number.

2105 8.5 Developing a new W-tagger

2106 As mentioned in the introduction to this chapter, studies had shown that the PUPPI pileup
 2107 subtraction algorithm yielded superior resolution on large-cone jet observables like the jet mass.
 2108 We therefore wanted to check whether the softdrop jet mass, and its observed sensitivity to the
 2109 underlying event and pileup, would be improved if a better pileup subtraction algorithm was
 2110 applied pre-clustering.

2111 Two interesting observations were made. Softdrop used together with PUPPI pileup subtraction
 2112 displayed a much smaller p_T -dependent shift than the combination of CHS and softdrop.
 2113 Figure 8.6 shows the PUPPI softdrop jet mass for W-jets from a 1 TeV resonance, corresponding
 2114 to a jet $p_T \sim 500$ GeV, and a 4 TeV resonance, corresponding to a jet $p_T \sim 2$ TeV, exhibiting the
 desired reduced p_T dependence on jet mass scale. However, when applying the recommended L2

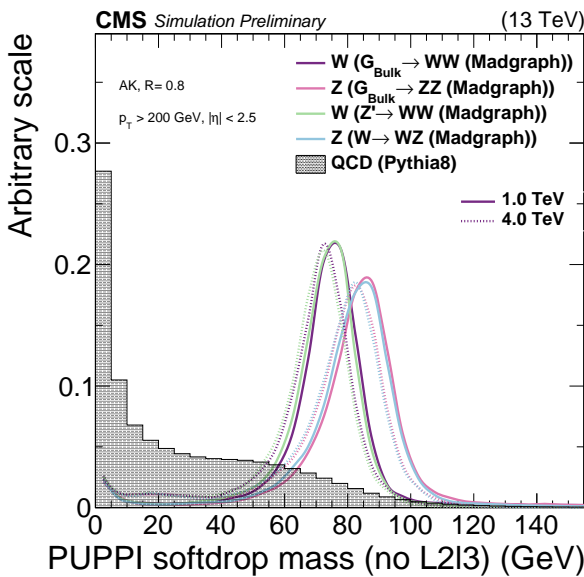


Figure 8.6: The PUPPI softdrop jet mass distribution for W boson jets coming from a 1 and 4 TeV resonance assuming different signal hypothesis. The QCD multijet background is shown in gray. No jet energy corrections have been applied to the jets.

2115 and L3 jet energy corrections (see Section 6.4.3) to the jet groomed mass, a strong p_T dependent
 2116 shift is re-introduced. This effect is not present for the pruned jet mass. Figure 8.7 shows
 2117 the softdrop (top left) and pruned (top right) jet mass distributions with recommended L2L3
 2118 corrections applied. Here, the PUPPI softdrop jet mass shift as a function of p_T is significantly
 2119 increased with respect to what was observed for the uncorrected mass, while the CHS pruned
 2120 jet mass remains stable. This points to the PUPPI jet energy corrections not being optimal for
 2121

2122 PUPPI soft-dropped jets. Indeed, there is no reason to expect the CMS JEC corrections to work
 2123 for groomed jets at all as they were derived from un-groomed PUPPI or CHS jets. The fact that
 2124 they work well for CHS pruned jets is not a given. The jet energy corrections derived for CHS
 2125 and PUPPI jets as a function of jet p_T are shown in the bottom plot in Figure 8.7. A significant
 slope in JEC as a function of p_T is measured for PUPPI, while not present for CHS.

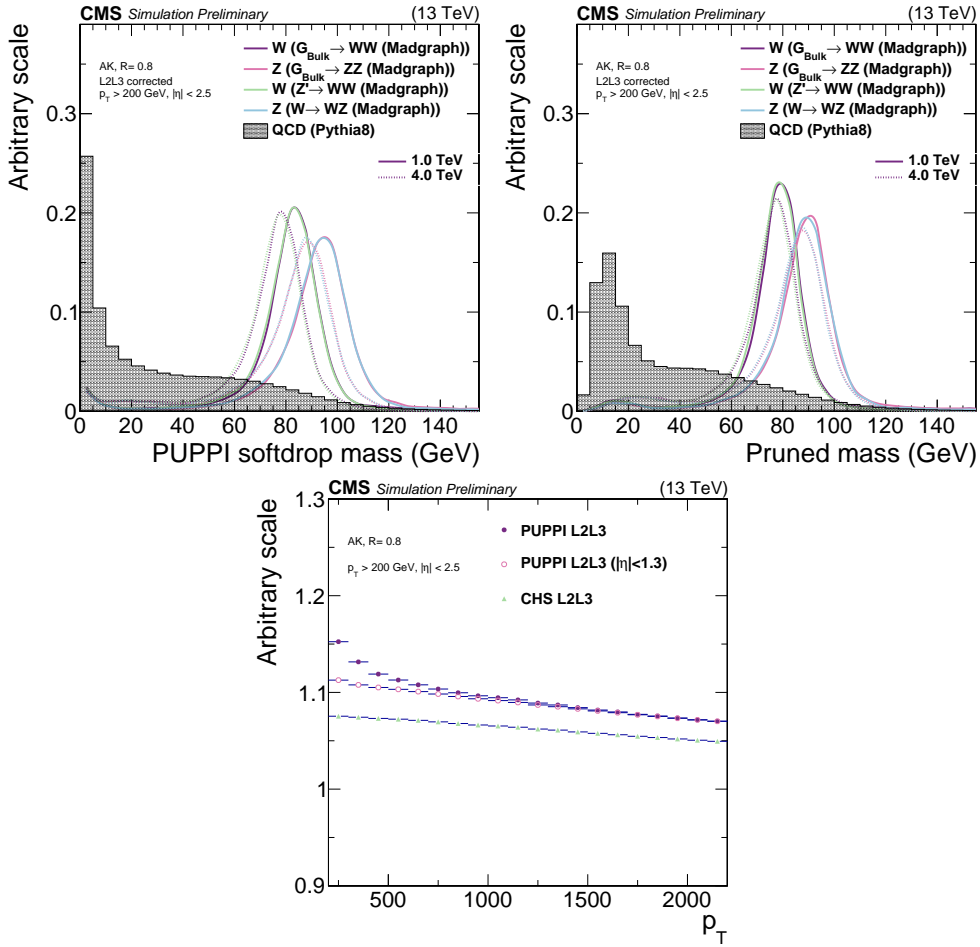


Figure 8.7: Top: PUPPI softdrop jet mass distribution (top left) and pruned jet mass distribution (top right) with L2 and L3 corrections applied. Bottom: The projection of CHS and PUPPI jet energy corrections versus jet p_T .

2126

2127 8.5.1 Dedicated PUPPI softdrop jet mass corrections

In order to remove the PUPPI softdrop jet mass dependence on jet p_T , all jet energy corrections to the softdrop jet mass are removed. However, this still leaves a residual p_T -dependent shift and,

in addition, the uncorrected mass does not peak near the correct W-mass of 80.4 GeV. Figure 8.8 shows the mean of a Gaussian fit to the uncorrected PUPPI softdrop mass as a function of jet p_T in two different η bins (smaller or greater than $|\eta| = 1.3$) for W-jets coming from a Bulk Graviton signal sample. A mass shift both as a function of η and p_T is observed, together with an average mean shifted significantly lower than the W boson mass. In order to use PUPPI softdrop for

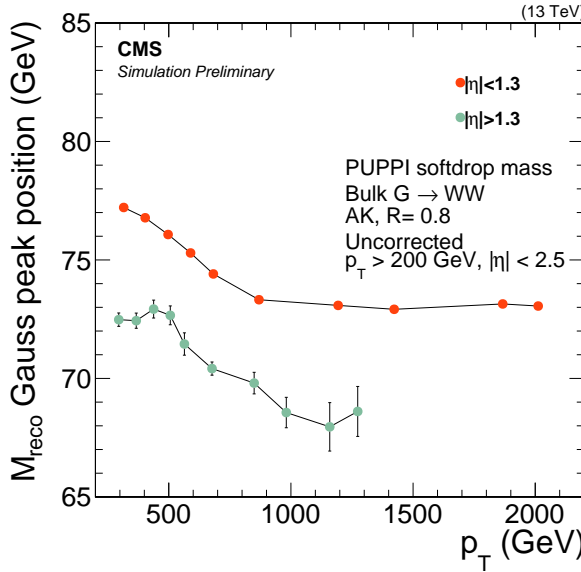


Figure 8.8: The mean of a Gaussian fit to the W-jet PUPPI softdrop mass peak as a function of jet p_T in two different η bins (smaller or greater than $|\eta| = 1.3$). No jet energy corrections have been applied to the softdrop mass.

W tagging, we therefore derive dedicated jet-mass corrections to compensate for two factors: a generator-level p_T -dependence, as first observed in Section 7.4.3, and a reconstruction-level p_T - and η -dependence, most likely due to calibration (recall, the PUPPI jet energy corrections have been removed). Figure 8.9 shows the mean of the generated softdrop jet mass (left) and the normalized difference in reconstructed and generated softdrop jet mass (right) as a function of jet p_T . The shift in generated softdrop mass at lower p_T is of the order of 2-3% while the difference between reconstructed and generated softdrop mass is a 5-10% effect. The mass shift introduced at generator-level is corrected by a fit to $M_{\text{PDG}}/M_{\text{GEN}}$ as a function of jet p_T , where $M_{\text{PDG}} = 80.4$ GeV and M_{GEN} is the fitted mean of the generator-level mass as shown in the left plot in Figure 8.9. To correct for the residual shift between generated and reconstructed softdrop mass, a fit to $(M_{\text{RECO}} - M_{\text{GEN}})/M_{\text{RECO}}$, where M_{RECO} is the reconstructed mass shown in the right plot in Figure 8.9 and M_{GEN} is as defined above, as a function of jet p_T in two η bins (smaller or greater than $|\eta| = 1.3$) is performed. Polynomial fit functions of the following forms

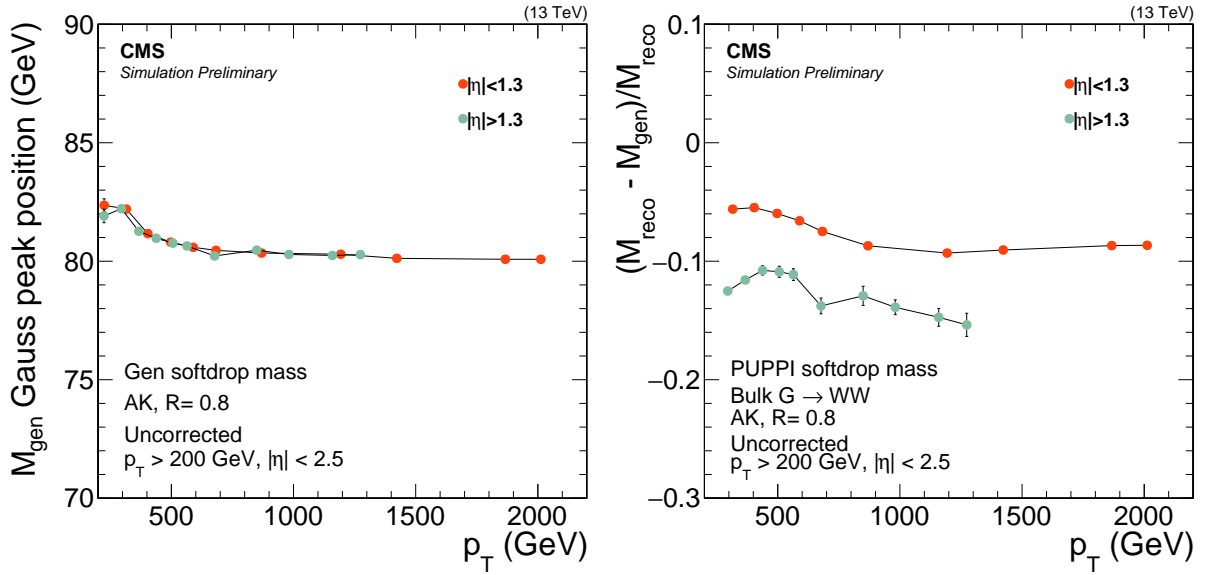


Figure 8.9: The mean of the fitted generator level W-jet softdrop mass distribution as a function of jet p_T (left) and the normalized difference in reconstructed and generated softdrop jet mass (right).

are used:

$$\begin{aligned} w(p_T) &= A + B(x^2)^{-C} && \sim \text{"gen correction" and} \\ w(p_T) &= A + Bx + Cx^2 + Dx^3 + Ex^4 + Fx^5 && \sim \text{"reco correction".} \end{aligned}$$

2128 The distribution and corresponding parametrization of the two corrections is shown in Figure 8.10
 2129 for the “gen correction” (left) and “reco correction” (right). The two corrections are then applied
 2130 to the uncorrected PUPPI softdrop mass both in data and in MC as

$$M_{SD} = M_{SD,\text{uncorr}} \times w_{GEN} \times w_{RECO} \quad (8.1)$$

2131 where w_{GEN} and w_{RECO} correspond to the generator and reconstructed level corrections, respec-
 2132 tively, and $M_{SD,\text{uncorr}}$ is the uncorrected PUPPI softdrop mass.

2133 A closure test is performed in order to check that the corrected PUPPI softdrop W-jet mass
 2134 peaks at 80.4 GeV and is stable with respect to the jet p_T and η . The fitted mean of the corrected
 2135 PUPPI softdrop mass peak as a function of jet p_T in two different η bins is shown in Figure 8.11.
 2136 Good closure is observed, with the corrected mass peaking around 80 GeV independent of the jet
 2137 p_T and η . The PUPPI softdrop jet mass peak for W, Z, and Higgs boson jets from different signal
 2138 samples after jet mass corrections have been applied is shown in Figure 8.12, for resonances with

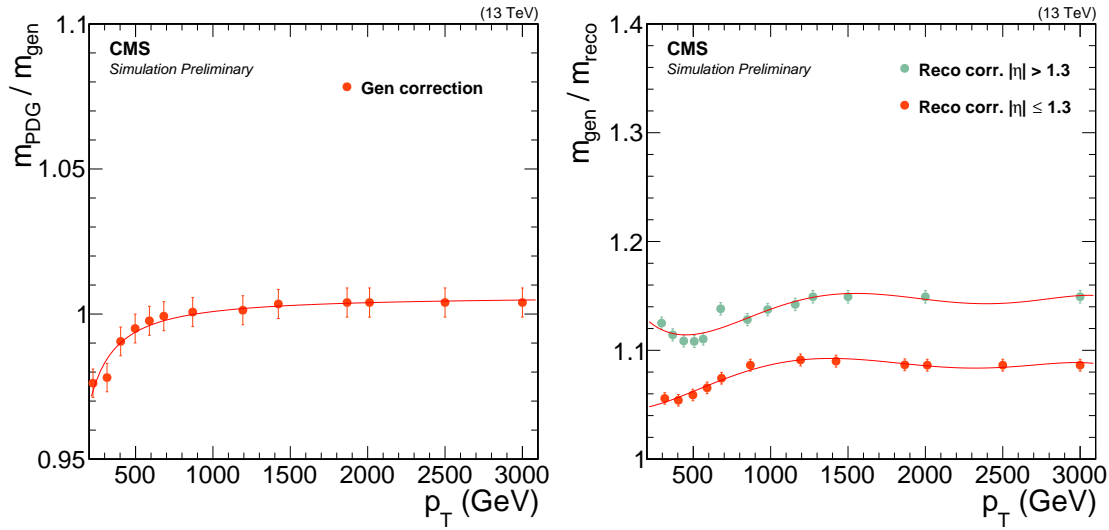


Figure 8.10: Left: fit to $M_{\text{PDG}}/M_{\text{GEN}}$ as a function of jet p_T , where $M_{\text{PDG}} = 80.4$ GeV and M_{GEN} is the fitted mean of the generator level mass. Right: fit to $(M_{\text{RECO}} - M_{\text{GEN}})/M_{\text{RECO}}$, where M_{RECO} is the reconstructed softdrop mass, as a function of jet p_T in two η bins.

2139 a mass of 1 and 4 TeV. The corrections yield a mass stable with p_T , peaking around the boson mass, for all three boson-jets under consideration.

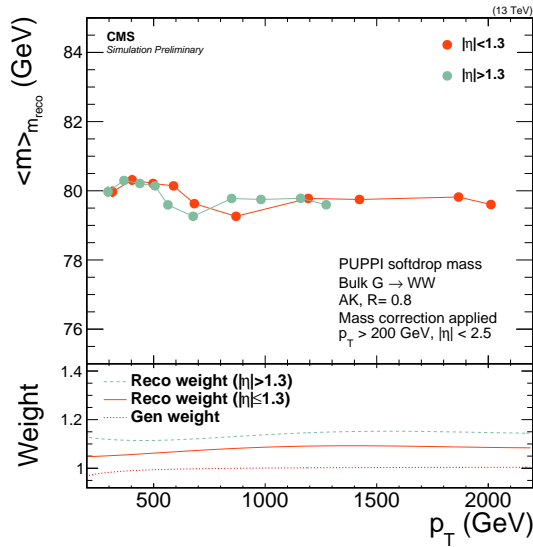


Figure 8.11: The mean of a Gaussian fit to the corrected PUPPI softdrop mass peak for real W-jets as a function of jet p_T in two different η bins.

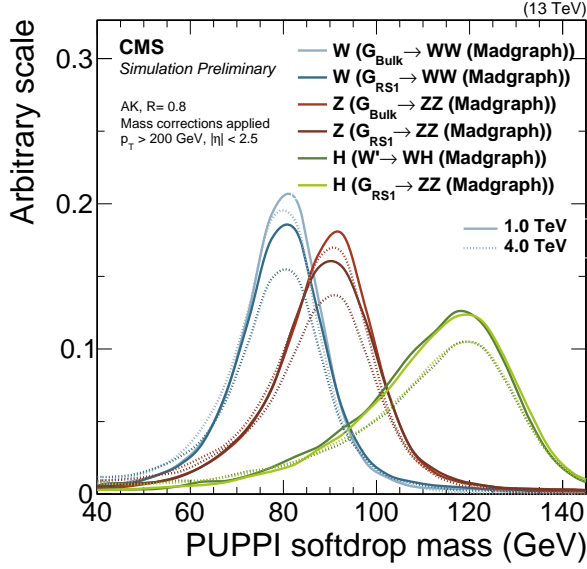


Figure 8.12: The corrected PUPPI softdrop jet mass for W, Z, and H jets from different signal samples with masses of 1 and 4 TeV.

8.5.2 W-tagging performance

The new PUPPI softdrop based V tagger uses a softdrop jet mass window of $65 \text{ GeV} < m_{SD} < 105 \text{ GeV}$ in combination with a selection of PUPPI $\tau_{21} < 0.4$. The CMS default is to compute the τ_{21} variable starting from un-groomed jets, but it can also be computed from already groomed jets. I briefly studied calculating τ_{21} starting from soft-dropped jets, summarized in Appendix A.2, where I found a small gain in performance when calculating τ_{21} starting from jets groomed with softdrop $\beta = 0$. This is something that needs further study, and is left for future work. We compare the performance of the PUPPI softdrop based V tagger to that of the CHS pruning-based tagger used in Search I, as well as to that of a “DDT-transformed” τ_{21} -based tagger [79]. The τ_{21}^{DDT} variable is a linear transformation of τ_{21} given as

$$\tau_{21}^{DDT} = \tau_{21} + M \times \log \left(\frac{m^2}{p_T \times 1 \text{ GeV}} \right) \quad (8.2)$$

where $M = -0.063$ is obtained from a fit of τ_{21} against the variable $\rho' = \log(m^2/p_T/\mu)$ in QCD Monte Carlo, where $\mu = 1 \text{ GeV}$. The purpose of this is to decorrelate τ_{21} from the QCD jet softdrop mass and p_T , yielding a mass and dijet invariant mass spectrum minimally sculpted by a cut on the τ_{21}^{DDT} tagging variable. This tagger will be further explored, and described in detail, in the context of Search III in Section 9.6.

2156 The background rejection efficiency for QCD light-flavor jets as a function of W-jet signal
 2157 efficiency is shown in Figure 8.13. The efficiency is measured after requiring a softdrop jet mass
 selection of $65 \text{ GeV} < m_{SD} < 105 \text{ GeV}$, while scanning the cut on τ_{21} . The general performance

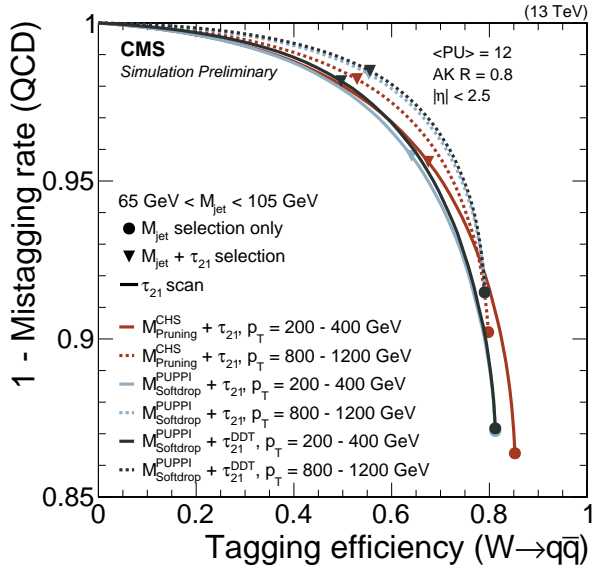


Figure 8.13: The background rejection efficiency for QCD light-flavor jets as a function of W-jet signal efficiency. A cut on CHS pruned or PUPPI softdrop jet mass of $65 < m_{p/sd} < 105 \text{ GeV}$ is applied while scanning the cut on τ_{21} . The cuts corresponding to $\tau_2/\tau_1 < 0.45$ for CHS pruned jets, PUPPI $\tau_{21} < 0.4$ or $\tau_{21}^{DDT} < 0.52$ for PUPPI softdrop jets are indicated with triangles, while the solid circles represent the efficiency and mistag rate for a mass cut only.

2158 of each tagger is very similar, with the PUPPI softdrop-based taggers displaying a slightly higher
 2159 signal efficiency for a given mistag rate at high p_T and CHS pruning-based taggers performing
 2160 slightly better at low p_T . In order to better understand the difference between each tagger, we
 2161 look at the tagging performance as a function of jet p_T and pileup, as shown in Figure 8.14
 2162 and 8.15. In Figure 8.14 we observe that the signal efficiency for a PUPPI softdrop or a CHS
 2163 pruned jet mass selection is flat and around 80% as a function of jet p_T . The QCD mistagging
 2164 rate, on the other hand, falls off as a function of p_T , with a 1-3% lower mistagging rate when using
 2165 PUPPI softdrop jet mass than when using CHS pruned jet mass. Once applying an n-subjettiness
 2166 cut, the signal efficiency as well as the mistag rate for the τ_{21} -based taggers becomes smaller
 2167 as a function of jet p_T , with an average signal efficiency of around 50% for a ~ 2% mistag rate.
 2168 An interesting behavior is observed for the τ_{21}^{DDT} tagger: while the mistagging rate is flat as a
 2169 function of p_T , by construction, the signal efficiency gets higher as the p_T increases, outperforming
 2170 the other taggers above 1 TeV.

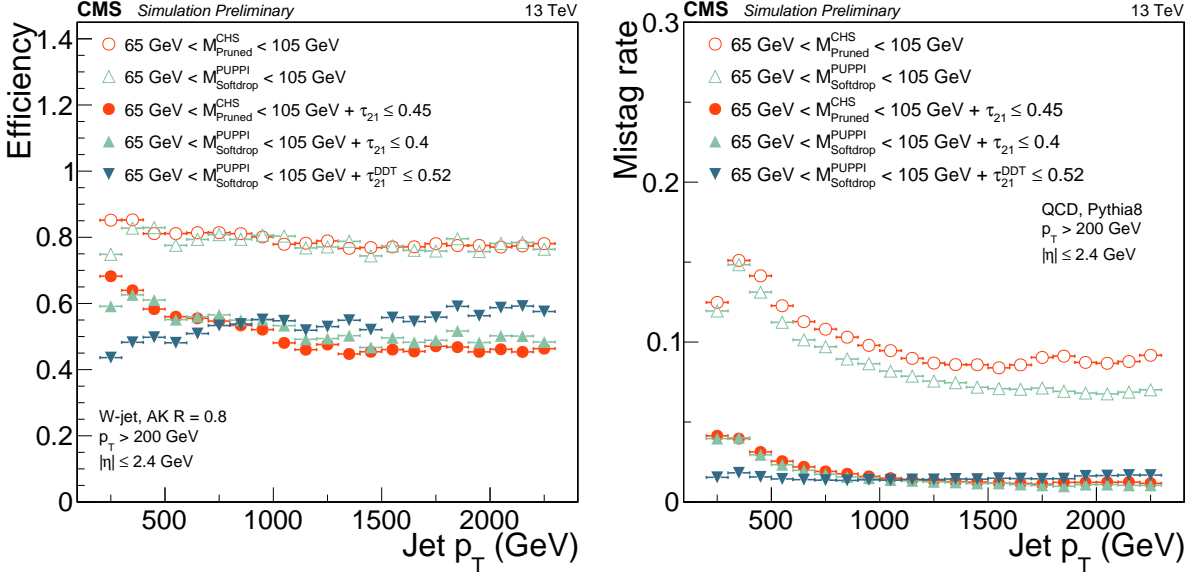


Figure 8.14: W-jet efficiency (left) and QCD light-flavor jet mistag rate (right) for a PUPPI softdrop or CHS pruned jet mass selection only (hollow circles) and the combined $m_{\text{p/sd}}$ + (PUPPI) τ_{21} (DDT) selection (solid circles) as a function of jet p_T .

2172 Figure 8.15 shows the W-jet tagging efficiency (left) and QCD light-flavor jet mistagging rate
2173 (right) as a function of the number of interaction vertices in the event. The tagging efficiency
2174 of the CHS pruned jet tagger (red solid circles) falls off steeply versus the number of primary
2175 vertices in the event, while the PUPPI softdrop taggers (light and dark blue solid circles) are
2176 more or less insensitive to pileup. The per-jet efficiency of the PUPPI softdrop and PUPPI τ_{21}
2177 tagger is around 50-55% for a 1-2% mistag rate. Based on the observed general performance,
2178 tagging stability versus pileup, and due to theoretical considerations, PUPPI softdrop jet mass
2179 with dedicated mass corrections applied, together with PUPPI τ_{21} , is chosen as the W tagger for
2180 this analysis.

2181 8.5.3 Efficiency scale factors, jet mass scale and resolution

2182 In order to measure the W-tagging efficiency, and jet-mass scale and resolution for the new
2183 PUPPI softdrop jet mass tagger, we use the same procedure as outlined in Section 7.7. The
2184 first commissioning of the new tagger was done using 2.3 fb^{-1} of data collected in 2015, and
2185 was published in a jet algorithms performance note [77]. The measurements were then redone
2186 using 12.9 and 35.9 fb^{-1} of data collected in 2016 for the two analyses presented in this chapter
2187 (the latter measurement was performed by a separate analysis team). The results shown in the

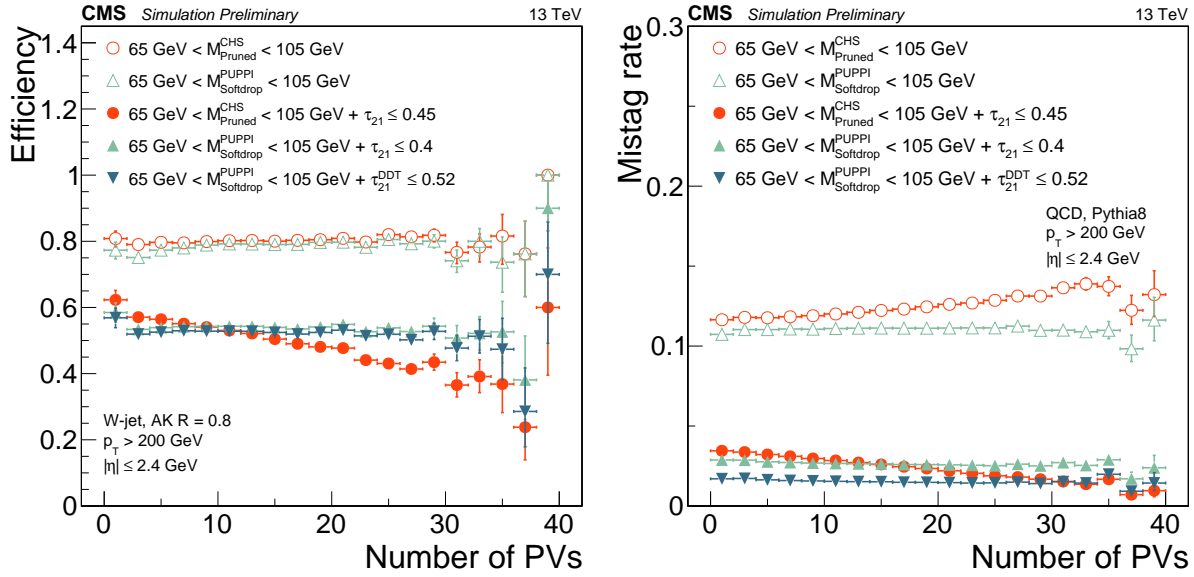


Figure 8.15: W-jet efficiency (left) and QCD light-flavor jet mistag rate (right) for a PUPPI softdrop or CHS pruned jet mass selection only (hollow circles) and the combined $m_{\text{p/sd}} + (\text{PUPPI}) \tau_{21}$ (DDT) selection (solid circles) as a function of the number of interaction vertices in the event.

following will be those obtained when the V tagger was first presented in an analysis context, corresponding to the PAS based on 12.9 fb^{-1} of data collected in the beginning of 2016. Since the fit method is outlined in detail in Section 7.7, fits to matched $t\bar{t}$ MC and minor backgrounds for the PUPPI softdrop based tagger are skipped here and can be found in Appendix C.1.

The PUPPI softdrop jet mass and the PUPPI τ_{21} variable in data and MC are shown in Figure 8.16. These can be compared to the corresponding plots for the CHS pruned jet mass and τ_{21} distributions in Figure 8.16. The softdrop and pruned jet mass distributions, as well as the PUPPI and CHS τ_{21} variables, are very similar and the variables are described equally well in simulation. Following what was done in Section 7.7, we extract and compare the W-tagging efficiency, jet mass scale and jet mass resolution of the combined jet mass and τ_{21} selection in data and in MC. This is done through a simultaneous fit of the the softdrop jet mass spectrum between 40 and 150 GeV in two regions:

- pass region: $0 < \tau_{21} \leq 0.40 \sim \text{high purity, and}$
- fail region: $0.40 < \tau_{21} \leq 0.75 \sim \text{low purity.}$

The fits are shown in Figure 8.17, with the corresponding extracted efficiencies from the Gaussian component of the total fit and scale factors summarized in Table 8.1. The quoted systematic

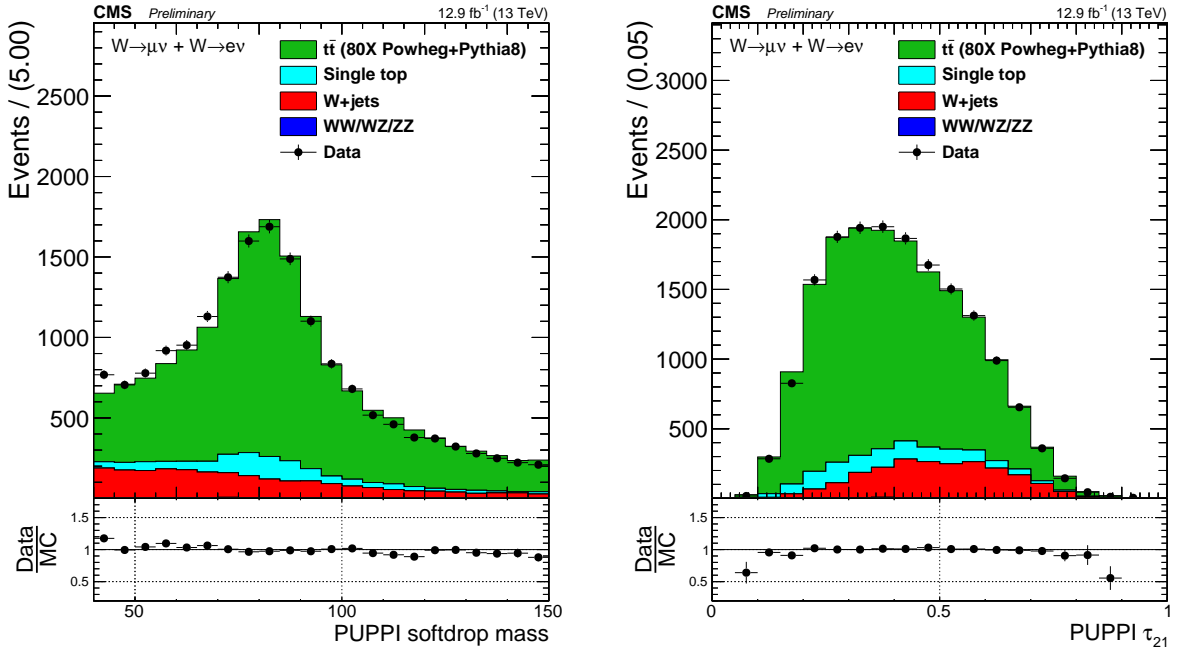


Figure 8.16: Distribution of the PUPPI softdrop mass (left) and PUPPI n-subjettiness (right) distribution in the $t\bar{t}$ control sample.

uncertainties are evaluated in the same way as was described in Section 7.7.3, and correspond to the uncertainty due to the choice of ME generator and due to the choice of fit method.

	Working point	Eff. data	Eff. simulation	Scale factor
HP	$\tau_{21} < 0.4$	0.839 ± 0.020	0.817 ± 0.012	$1.03 \pm 0.03 \text{ (stat)} \pm 0.04 \text{ (sys)} \pm 0.06 \text{ (sys)}$
LP	$0.4 < \tau_{21} < 0.75$	0.154 ± 0.020	0.176 ± 0.012	$0.88 \pm 0.12 \text{ (stat)} \pm 0.17 \text{ (sys)} \pm 0.12 \text{ (sys)}$

Table 8.1: W-tagging scale factors for both categories the high purity and low purity categories for two taggers: Pruned jet mass + τ_{21} and PUPPI softdrop jet mass + PUPPI τ_{21} .

Both scale factors are compatible with unity within uncertainties. We additionally extract the jet-mass scale and jet-mass resolution from the mean and width of the Gaussian component of the total fit in the pass region. These are summarized in Table 8.2. We find that the W-jet mass scale for PUPPI softdrop jet mass is identical in simulation and in data, whereas for pruning (Table 7.7) the difference was around 2%, The jet mass resolution, on the other hand, is larger in data for PUPPI softdrop jet mass, by roughly 8%, whereas for pruning the resolution is larger in simulation (11%). However, both are statistically insignificant and compatible with unity within uncertainties. The W-tagging efficiency scale factors, jet-mass and resolution scales affect the signal yield and are included in the analysis in the same way as was described in Section 7.7.5, by

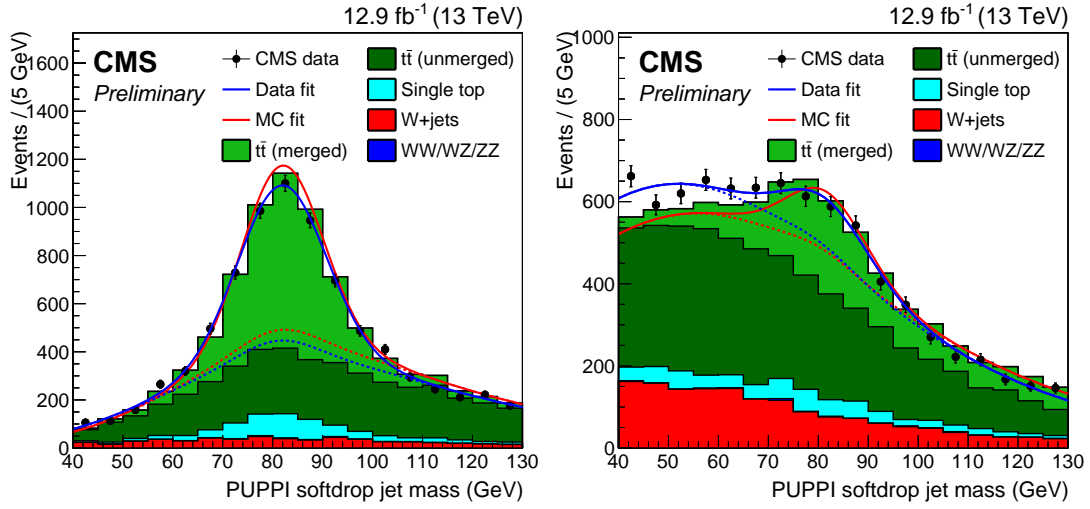


Figure 8.17: PUPPI softdrop jet mass distribution that pass (left) and fail (right) the PUPPI $\tau_{21} < 0.40$ selection. Results of both the fit to data (blue) and simulation (red) are shown and the background components of the fit are shown as short-dashed lines.

Parameter	Data	Simulation	Data/Simulation
PUPPI softdrop $\langle m \rangle$	81.9 ± 0.3 GeV	82.0 ± 0.2 GeV	0.999 ± 0.004 (stat) ± 0.0006 (sys)
PUPPI softdrop σ	8.9 ± 0.4 GeV	8.3 ± 0.3 GeV	1.08 ± 0.07 (stat) ± 0.08 (sys)

Table 8.2: Summary of the fitted W-jet mass peak parameters.

scaling the total signal yield and incorporating an uncertainty on the signal efficiency due to a shift and broadening of the W-jet mass peak.

8.5.4 W-tagging mistag rate measurement

The W-tagging light-flavor jet mistagging rate is measured in a QCD dijet-enriched region in data and is compared to the prediction from QCD MC using three different combinations of generators: HERWIG++, PYTHIA8, and MADGRAPH+PYTHIA8. Figure 8.18 shows the mistagging rate as a function of jet p_T for three different taggers: CHS pruning and τ_{21} , PUPPI softdrop and τ_{21} , and PUPPI softdrop and τ_{21}^{DDT} . We find a substantial difference in the modeling of substructure variables between the different generators, most likely coming from their very different description of gluon radiation (dominant in QCD multijet events). The best description is obtained with HERWIG++, while all three generators model the p_T -dependence of the tagger well.

We additionally study how a selection on τ_{21} and τ_{21}^{DDT} affect the total quark and gluon content of the QCD background. Figure 8.19 shows the stacked relative quark and gluon content

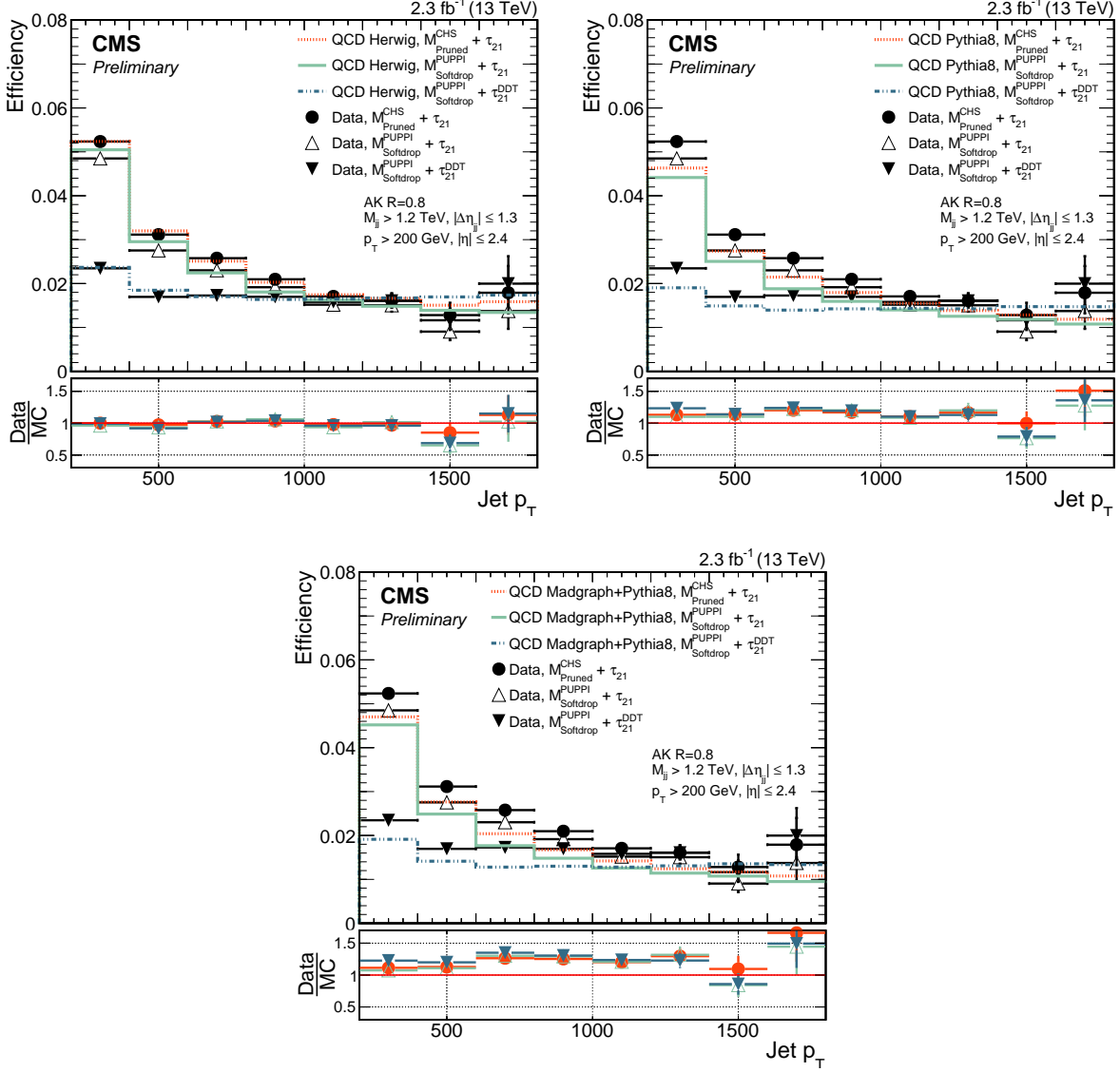


Figure 8.18: The fraction of jets that pass the $m_{p/\text{sd}}$ and τ_{21} selections in a dijet enriched sample for data and for simulation as a function of jet p_T . Here the comparison is between HERWIG++ (top left), PYTHIA8 (top right), and PYTHIA8 with MADGRAPH as the matrix-element generator (bottom).

in a PYTHIA8 QCD dijet sample for selection requirements based on PUPPI τ_{21} and τ_{21}^{DDT} . We see that the quark content increases as a function of jet p_T when applying a selection on τ_{21}^{DDT} , while it decreases when applying a selection on τ_{21} . This can be attributed to the fact that the distribution of jet mass divided by the jet p_T , m/p_T , for quark and gluon jets are very different

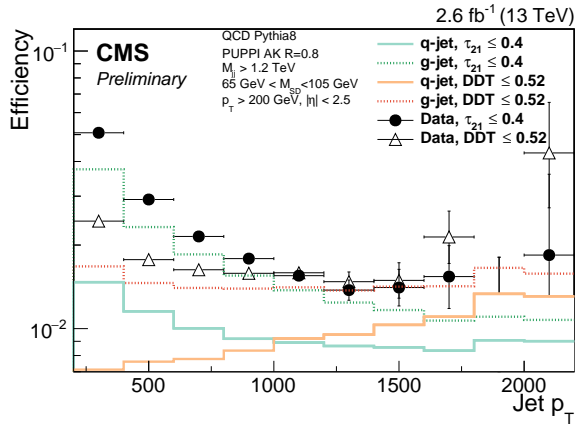


Figure 8.19: The fraction of jets that pass the PUPPI softdrop jet mass selection and a selection on τ_{21} (turquoise) or τ_{21}^{DDT} (orange) in a dijet-enriched sample. The jets from QCD MC are split into two contributions: jets originating from gluons (dotted line) and jets originating from quarks (solid line).

from one another, and these differences increase as the jet p_T increases. Figure 8.20 shows the mass divided by p_T for jets originating from a quark (blue) or a gluon (red), for jets with a p_T of 200 GeV (left) or 1600 GeV (right). We see that the jet mass divided by the jet p_T peaks at significantly higher values for gluon jets than for quark jets. From the definition of the τ_{21}^{DDT} tagger in Equation 8.2, it can therefore be seen that a selection on τ_{21}^{DDT} will act more aggressively on jets with a high m/p_T , effectively removing more gluon jets.

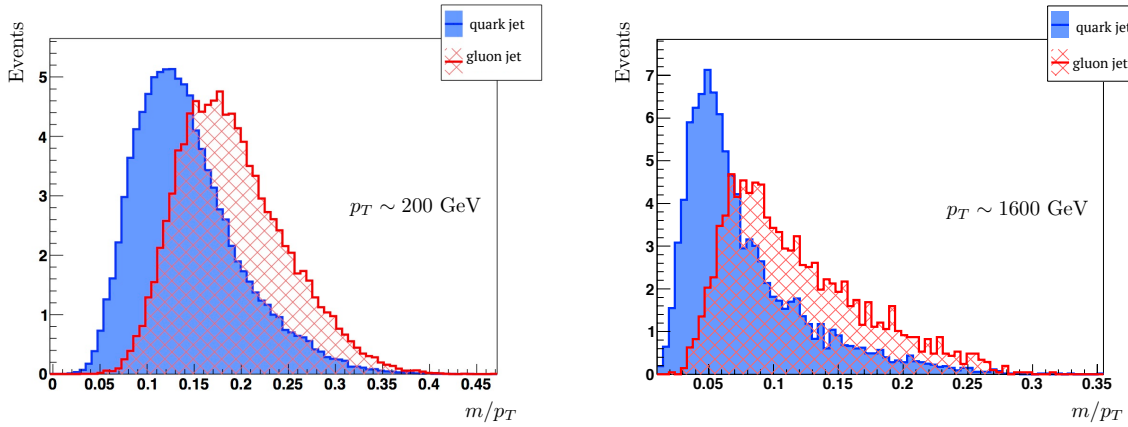


Figure 8.20: The jet mass divided by the jet p_T for quark (blue) and gluon (red) jets for a jet p_T of 200 (left) and 1600 GeV (right). Generated using [80].

8.6 Mass and purity categorization

The PUPPI softdrop jet mass and PUPPI τ_{21} distributions after loose analysis preselections, as outlined in Section 8.3, have been applied are shown in Figure 8.21. We see some disagreement between data and MC, especially in the high-purity region ($\text{PUPPI } \tau_{21}^{DDT} < 0.4$), confirming what was observed in Section 8.5.4. As this analysis is sensitive to both heavy resonances

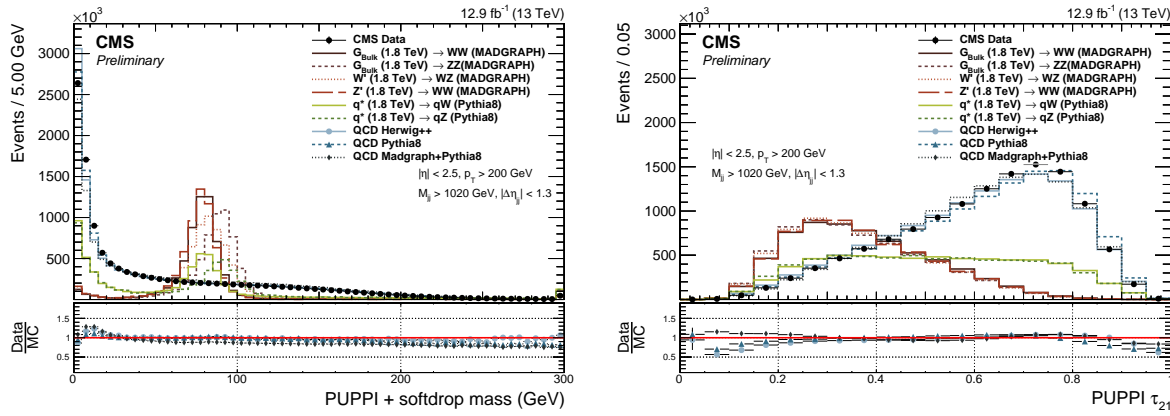


Figure 8.21: PUPPI softdrop jet mass (left) and PUPPI n-subjettiness τ_{21} (right) distribution for data and simulated samples. Simulated samples are scaled to match the distribution in data.

decaying into two vector bosons and excited quark resonances q^* decaying to qW and qZ, we look for events with both a single V-tag and events with two V-tags. Vector boson candidates are selected with a PUPPI softdrop jet mass of $65 \text{ GeV} < m_{sd} < 105 \text{ GeV}$. Further, and similar to what was done in Search I, we select “high-purity” (HP) W and Z jets by requiring PUPPI $0 < \tau_{21} \leq 0.40$ and “low-purity” (LP) W and Z jets with $0.40 < \tau_{21} \leq 0.75$. The events with one W/Z-tag are classified in HP and LP categories according to the two categories described above. Events with two W/Z-tagged jets are always required to have one HP tagged jet, and are further divided into LP and HP categories depending on whether the other jet is of high or low purity. We additionally split events into two mass categories in order to enhance the analysis sensitivity, with the W-window defined as $65 \text{ GeV} < m_{sd} < 85 \text{ GeV}$ and the Z boson window as $85 \text{ GeV} < m_{sd} < 105 \text{ GeV}$. This results in ten different signal categories: for the double W/Z-tag analysis, there are 3 mass categories corresponding to WW, WZ, and ZZ for HP, and the same 3 mass categories for LP. For the single W/Z-tag analysis, there are 2 mass categories corresponding to qW and qZ in HP, and the same for LP.

2257 8.7 Background modeling

2258 The background is modeled using a parametric fit of the dijet invariant mass spectrum in the
2259 data signal region in the same way as described in Section 7.5. We determine the number of
2260 necessary fit parameters in order to describe the background through a Fishers F-test, comparing
2261 the same fit functions as in Section 7.5. This test is first exercised in QCD MC and then in a
2262 data sideband before the final determination is performed in the data signal region. As the F-test
2263 method was presented in detail in the context of Search I, only a brief summary of the findings
2264 as well as a presentation of the fits in the single-tag categories will be presented here. Fits and
2265 F-test results for all categories can be found in Appendix C.3. A two- or three-parameter fit
2266 is sufficient to describe the background for all the double-tag categories: a two-parameter fit is
2267 sufficient for the “high-purity” WZ and ZZ categories, as well as the “low-purity” WW category,
2268 while the remaining analysis categories require a three-parameter background fit. From the fits of
2269 the single-tag categories, shown in Figure 8.22, a three-parameter fit is sufficient for all categories
2270 except for the “high-purity” qW category. In the qW category, the improvement in fit quality
2271 when increasing the number of parameters is so large that adding an additional fit parameter is
2272 justified, and we continue by using a 5-parameter fit for this category. A summary of what fit
2273 functions are used for each analysis category is listed in Table 8.3.

Mass category	N pars.	
	HP	LP
WW	3	2
WZ	2	3
ZZ	2	3
qW	5	3
qZ	3	3

Table 8.3: The number of fit parameters used in the background fit to the dijet invariant mass distribution for each analysis category as determined through an F-test.

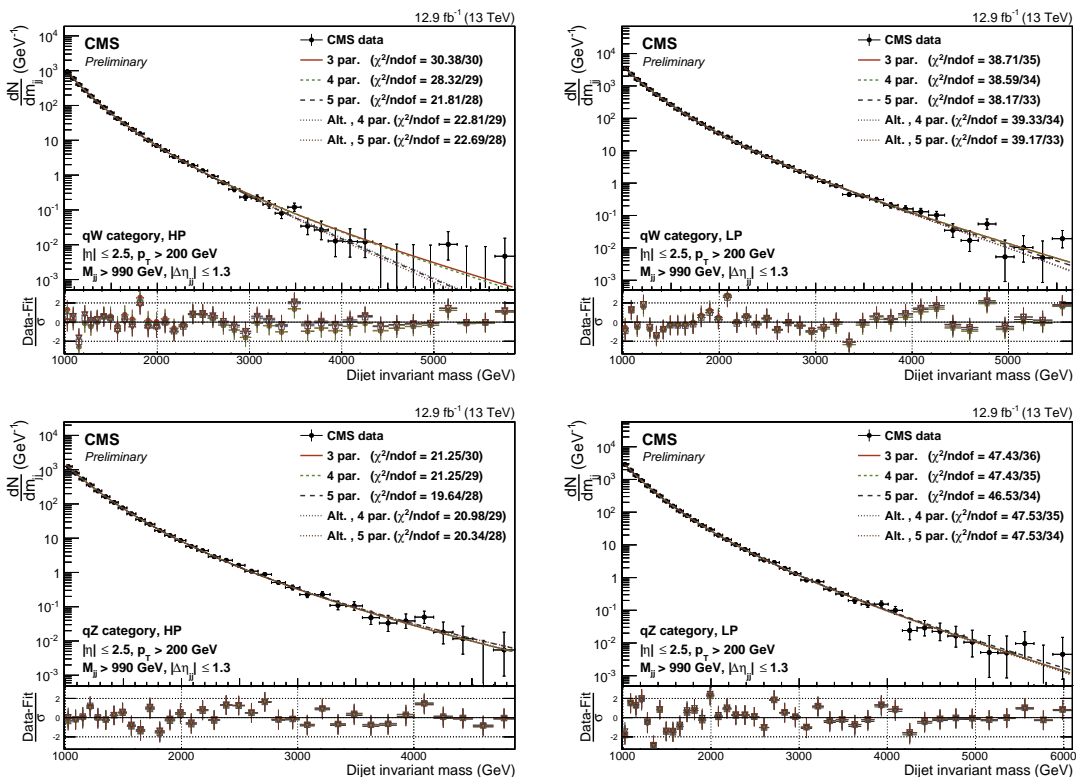


Figure 8.22: Background-only fit of the dijet invariant mass distribution in the data signal region used to establish the number of parameters of the background shape for the single-tag analysis. Here for the high- (left) and low-purity (right) single V-tag categories qW (top) and qZ (bottom).

²²⁷⁴ **8.8 Signal modeling**

²²⁷⁵ The dijet invariant mass distribution for signal is modeled from MC in the same way as in
²²⁷⁶ Section 7.6, where we assume the shape can be described by a Gaussian core and an exponential
²²⁷⁷ tail. The interpolated signal shapes for $q^* \rightarrow qW$ and $q^* \rightarrow qZ$ in their most sensitive analysis
²²⁷⁸ categories (qW and qZ , respectively) are shown in Figure 8.23. The signal shapes for the
 double-tag categories can be compared to those in Figure 7.22.

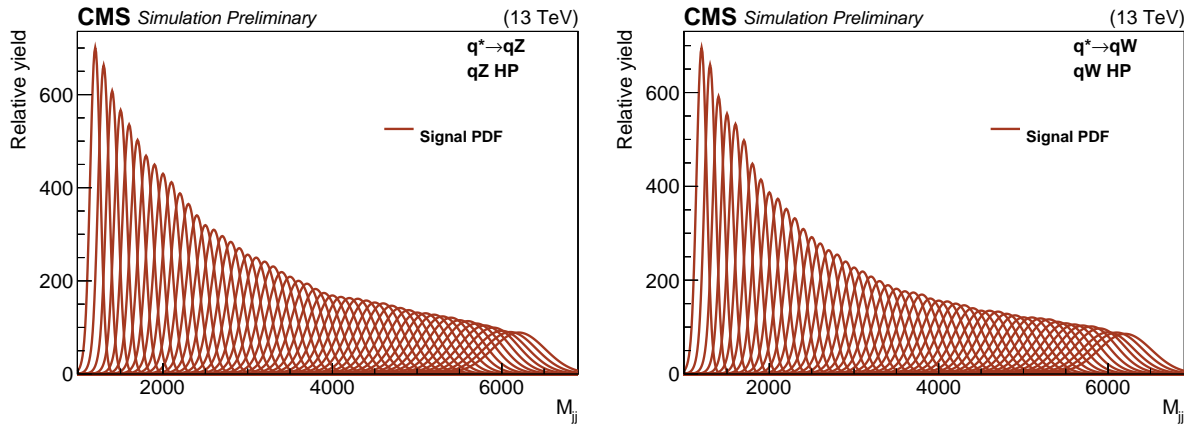


Figure 8.23: Interpolated signal shapes for a $q^* \rightarrow qZ$ (left) and $q^* \rightarrow qW$ (right) signal.

2280 8.9 Systematic uncertainties

2281 The largest sources of systematic uncertainty for this analysis are, as for Search I, related to the
 2282 signal modeling and are due to the uncertainty in the tagging efficiency of the V-tagger, the jet
 2283 energy and mass scale, the jet energy and mass resolution and the integrated luminosity. The
 2284 V-tagging uncertainty is estimated as described in Section 8.5.3, and yield uncertainties on the
 2285 scale factors for the HP and LP tagging categories. The p_T - and η -dependent jet energy scale
 2286 and resolution uncertainties on the resonance shape are approximated by a constant 2% and 10%.
 2287 The jet energy scale and resolution uncertainty are taken into account as shape uncertainties by
 2288 shifting and widening the signal resonance model, while all other signal uncertainties only affect
 the yield. The most relevant systematic uncertainties are listed in Table 8.4.

Source	Relevant quantity	HP+HP unc. (%)	HP+LP unc. (%)
Jet energy scale	Resonance shape	2	2
Jet energy resolution	Resonance shape	10	10
Jet energy scale	Signal yield	<0.1–4.4	
Jet energy resolution	Signal yield	<0.1–1.1	
Jet mass scale	Signal yield	0.02–1.5	
Jet mass resolution	Signal yield	1.3–6.8	
Pileup	Signal yield	2	
Integrated luminosity	Signal yield	6.2	
PDFs (W')	Signal yield	4–19	
PDFs (Z')	Signal yield	4–13	
PDFs (G_{bulk})	Signal yield	9–77	
Scales (W')	Signal yield	1–14	
Scales (Z')	Signal yield	1–13	
Scales (G_{bulk})	Signal yield	8–22	
Jet mass scale	Migration	<0.1–16.8	
Jet mass resolution	Migration	<0.1–17.8	
W-tagging τ_{21}	Migration	15.6	21.9
W-tagging p_T -dependence	Migration	7–14	5–11

Table 8.4: Summary of the systematic uncertainties on the signal and their impact on the event yield in the signal region and on the reconstructed dijet invariant mass shape (mean and width).

2290 8.10 Results

2291 As mentioned in the introduction to this chapter, the analysis of the 2016 dataset was done in
 2292 two steps: one based on 12.9 fb^{-1} of data collected early in 2016, demonstrating the new PUPPI
 2293 softdrop V-tagger and the new single-tag analysis categories, and one utilizing the full 35.9 fb^{-1}
 2294 of data collected in 2016. The results from both will be presented in the following sections.

2295 8.10.1 Early analysis

2296 The dijet invariant mass distributions in the analysis signal regions using 12.9 fb^{-1} of data
 2297 collected in 2016, are shown in Figure 8.24 for the double-tag and in Figure 8.25 for the single-tag
 2298 analysis. No significant excess is observed and we proceed to set upper limits on the signal cross
 2299 section using the method described in Section 7.9. Exclusion limits are set in the context of
 2300 the bulk graviton model, the HVT model B, and excited-quark resonance models, assuming the
 2301 resonances have a natural width negligible with respect to the experimental resolution (as in
 2302 Search I). Figure 8.26 shows the expected and observed upper exclusion limits at 95% confidence
 2303 level (CL) on the signal cross section times the branching fraction as a function of the resonance
 2304 mass for the different signal hypotheses in the double-tag analysis. The limits are compared
 2305 with the theoretically predicted cross section times branching fraction to WW and ZZ for a bulk
 2306 graviton with $\tilde{k} = 0.5$, and with the cross section times branching fraction to WZ and WW
 2307 for spin-1 particles predicted by the HVT model B. For the HVT model B, we exclude W' (Z')
 2308 resonances with masses below 2.7 (2.6) TeV. The signal cross section uncertainties are displayed
 2309 as a red checked band and result in an additional uncertainty on the resonance mass limits of
 2310 0.05 (0.04) TeV. The cross section limits for $Z' \rightarrow WW$ and $G_{\text{bulk}} \rightarrow WW$ are not identical due
 2311 to the different acceptance for those two signal scenarios. Figure 8.31 shows the corresponding
 2312 exclusion limits for excited quarks decaying to qW and qZ , excluding a q^* decaying into qW and
 2313 qZ with masses below 5.0 and 3.9 TeV, respectively. The signal cross section uncertainties are
 2314 displayed as a red checked band and result in an additional uncertainty on the resonance mass
 2315 limits of 0.1 TeV.

2316 8.10.2 Full 2016 dataset

2317 Figure 8.28 shows the dijet invariant mass distributions in the analysis signal regions using the
 2318 full dataset of 35.9 fb^{-1} collected in 2016 for the double-tag and in Figure 8.29 for the single-tag
 2319 analysis. No significant excess is observed and we proceed with setting upper limits on the signal
 2320 cross section times branching ratio as in Section 7.9.

2321 For a G_{bulk} we exclude production cross sections in a range from 36.0 fb, at a resonance mass
2322 of 1.3 TeV, to 0.6 fb at a resonance mass of 3.6 TeV. The W' (Z') resonances are excluded with
2323 masses below 3.2 (2.7) TeV for the HVT model B, in addition to W' resonances with a mass
2324 between 3.3 and 3.6 TeV. For excited quark resonances, we can exclude the production of q^*
2325 decaying to qW or qZ for masses below 5.0 and 4.7 TeV, respectively. Figure 8.30 and 8.31 show
2326 the resulting expected and observed upper limits at 95% confidence level on the signal cross
2327 section times branching ratio as a function of the resonance mass for VV and qV resonances,
2328 respectively.

2329 The sensitivity improvement in terms of mass reach with respect to Search I for a W' resonance
2330 of the HVT model B, improved from excluding resonances below 2 TeV to excluding resonances
2331 below 3.2 TeV.

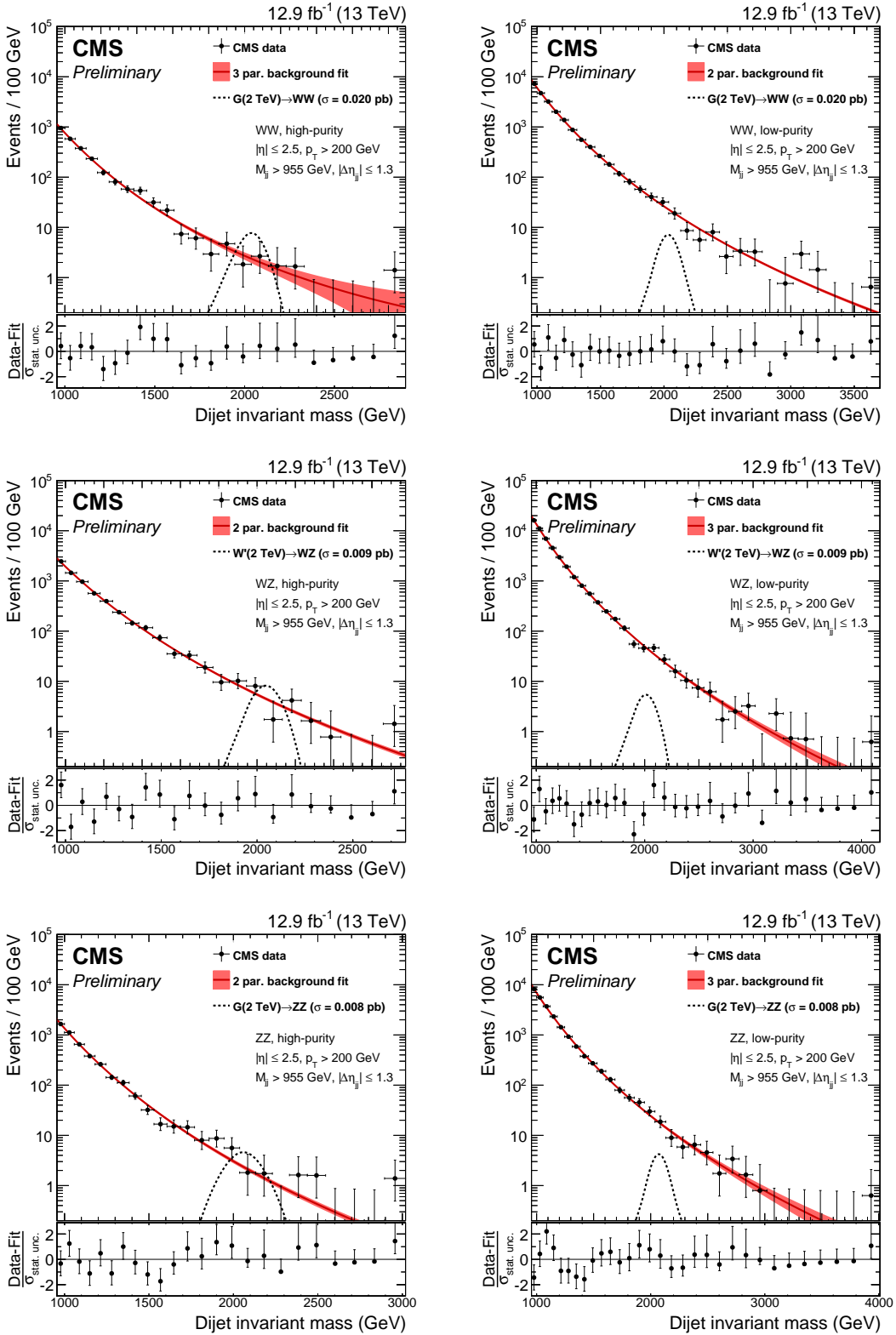


Figure 8.24: Observed dijet invariant mass spectrum for the double-tag analysis in the high-purity (left) and low-purity (right) categories using 12.9 fb^{-1} of data collected in 2016.

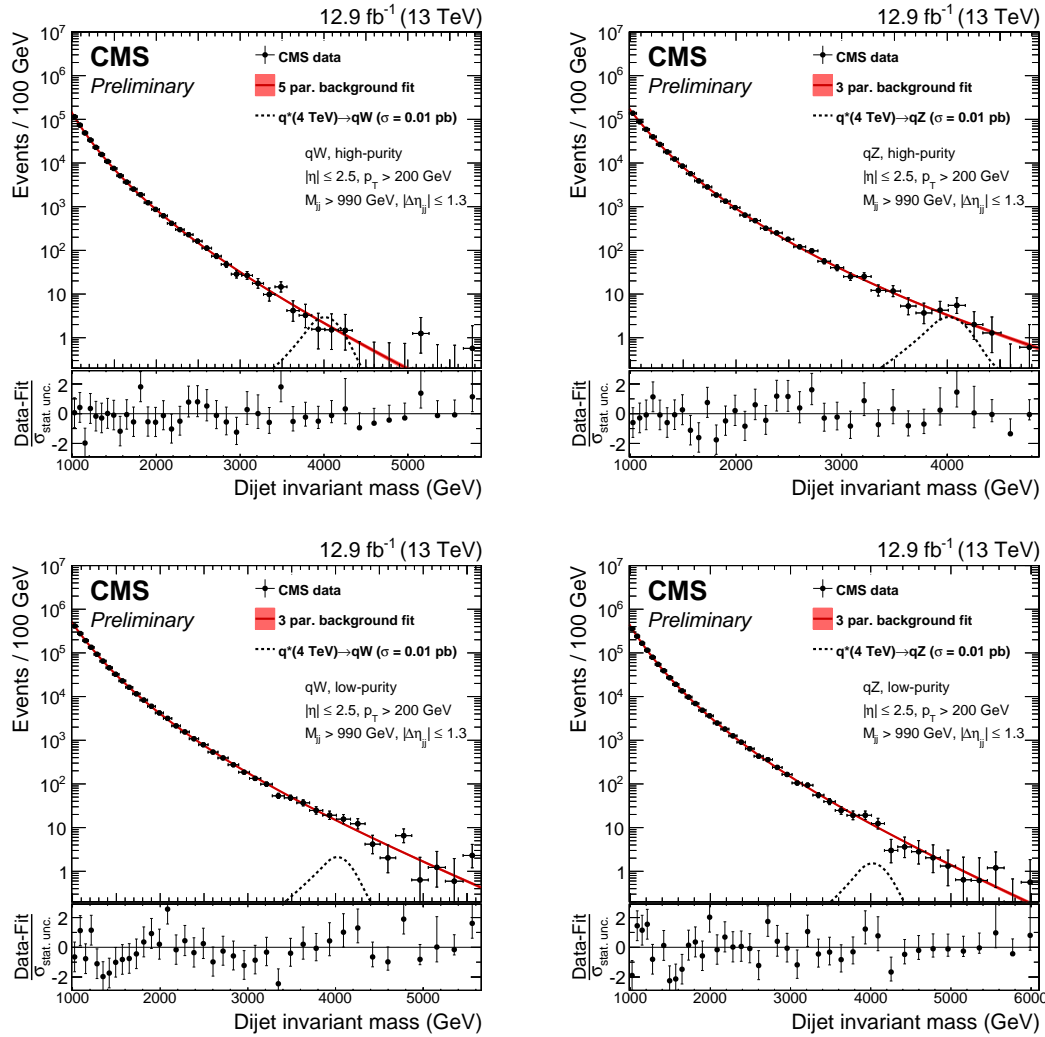


Figure 8.25: Observed dijet invariant mass spectrum for the single-tag analysis in the high-purity (top) and low-purity (bottom) categories using 12.9 fb^{-1} of data collected in 2016.

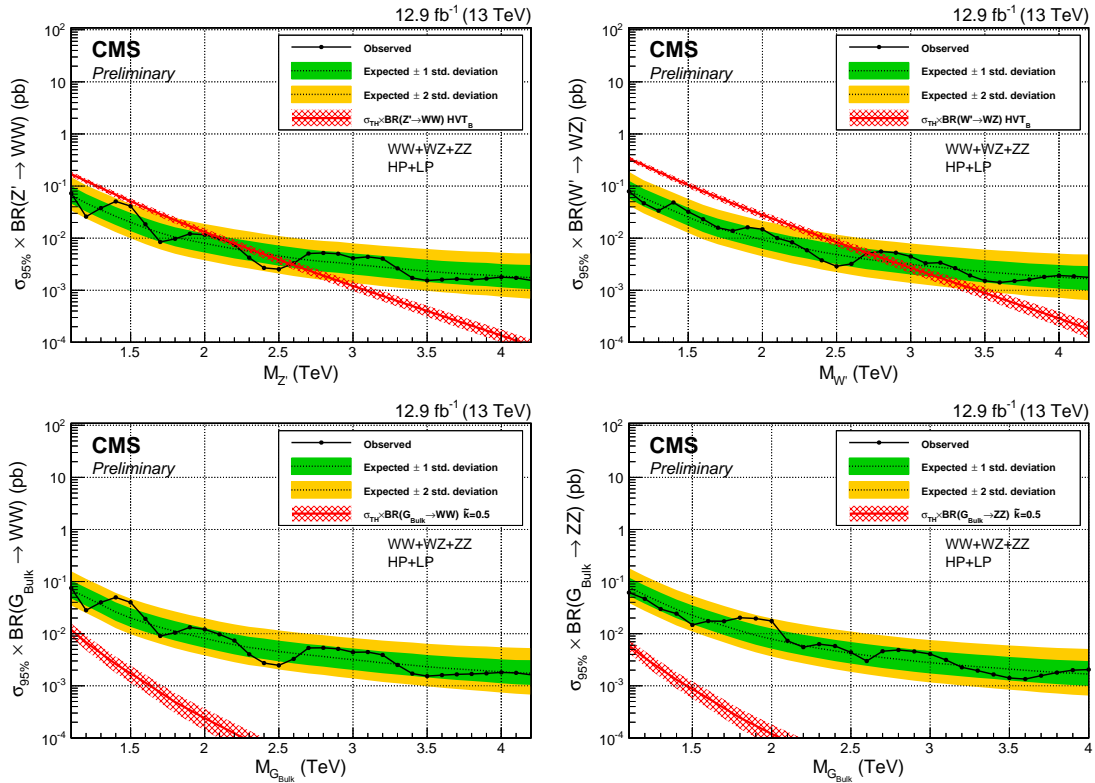


Figure 8.26: Observed (black solid) and expected (black dashed) 95% CL upper limits on the production of a narrow-width resonance decaying to a pair of vector bosons for different signal hypotheses. Limits are set in the context of a spin-1 neutral Z' (left) and charged W' (right) resonance, and compared with the prediction of the HVT model B. On the bottom, limits are set in the context of a bulk graviton decaying into WW (left) and ZZ (right) with $\tilde{k}=0.5$ and compared with the model prediction. Signal cross section uncertainties are displayed as a red checked band.

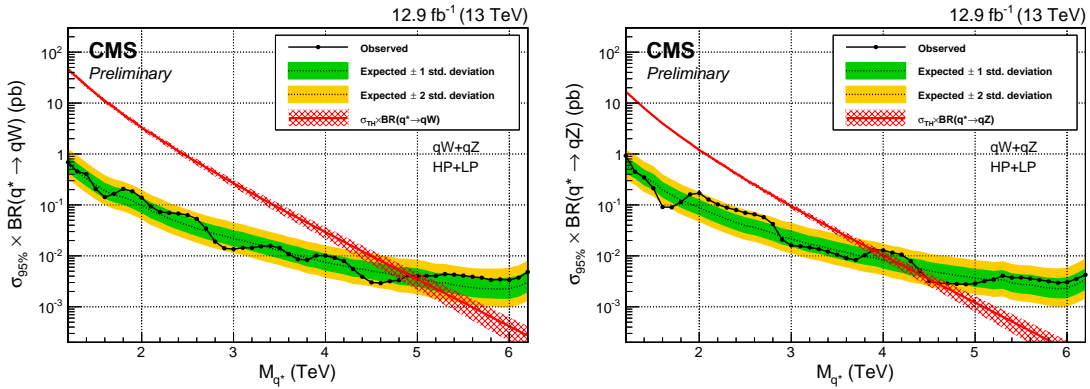


Figure 8.27: Observed (black solid) and expected (black dashed) 95% CL upper limits on the production of an excited quark resonance decaying into qW (left) or qZ (right). Signal cross section uncertainties are displayed as a red checked band.

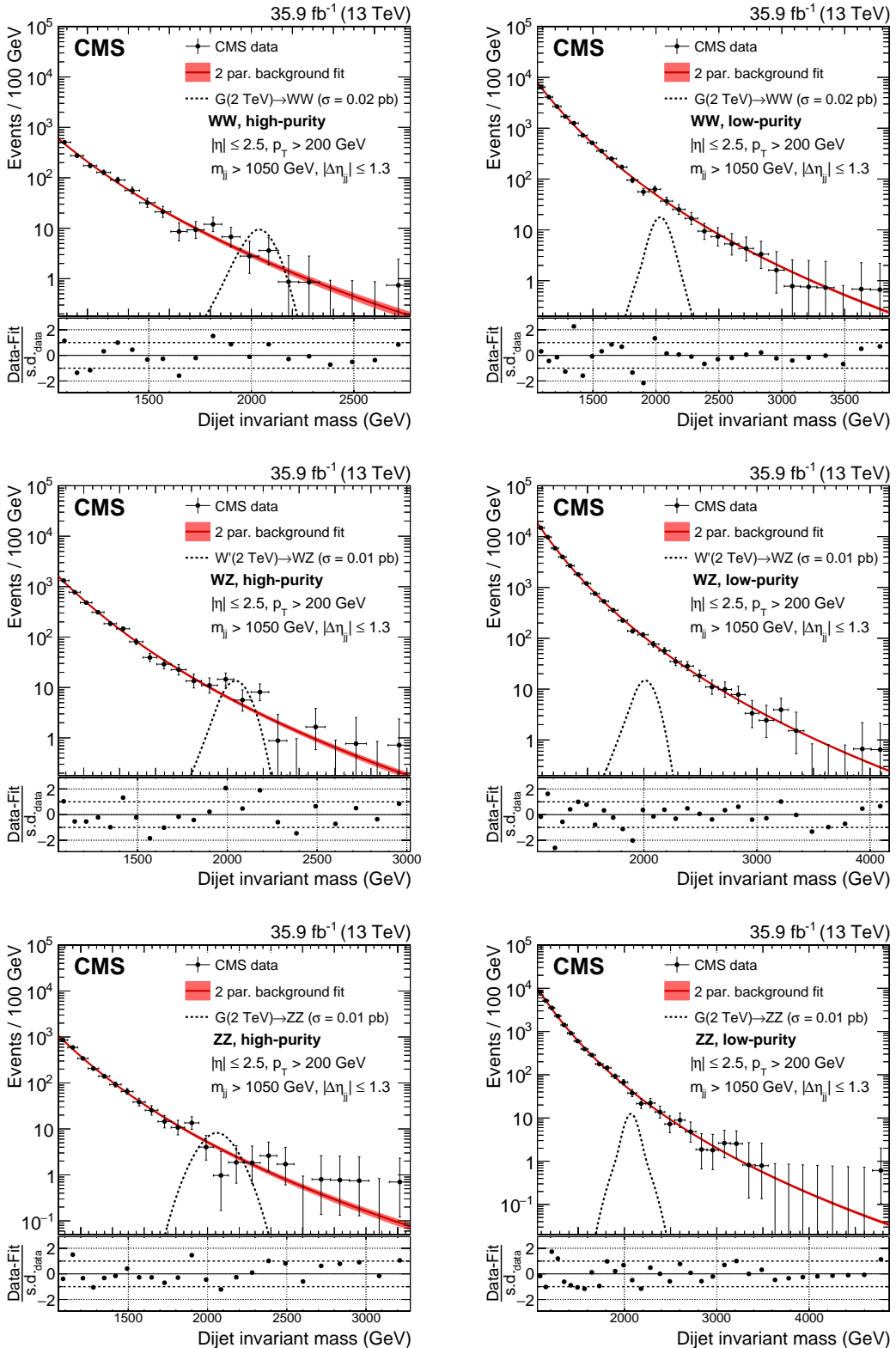


Figure 8.28: Observed dijet invariant mass spectrum for the double-tag analysis in the high-purity (left) and low-purity (right) categories using 35.9 fb^{-1} of data collected in 2016.

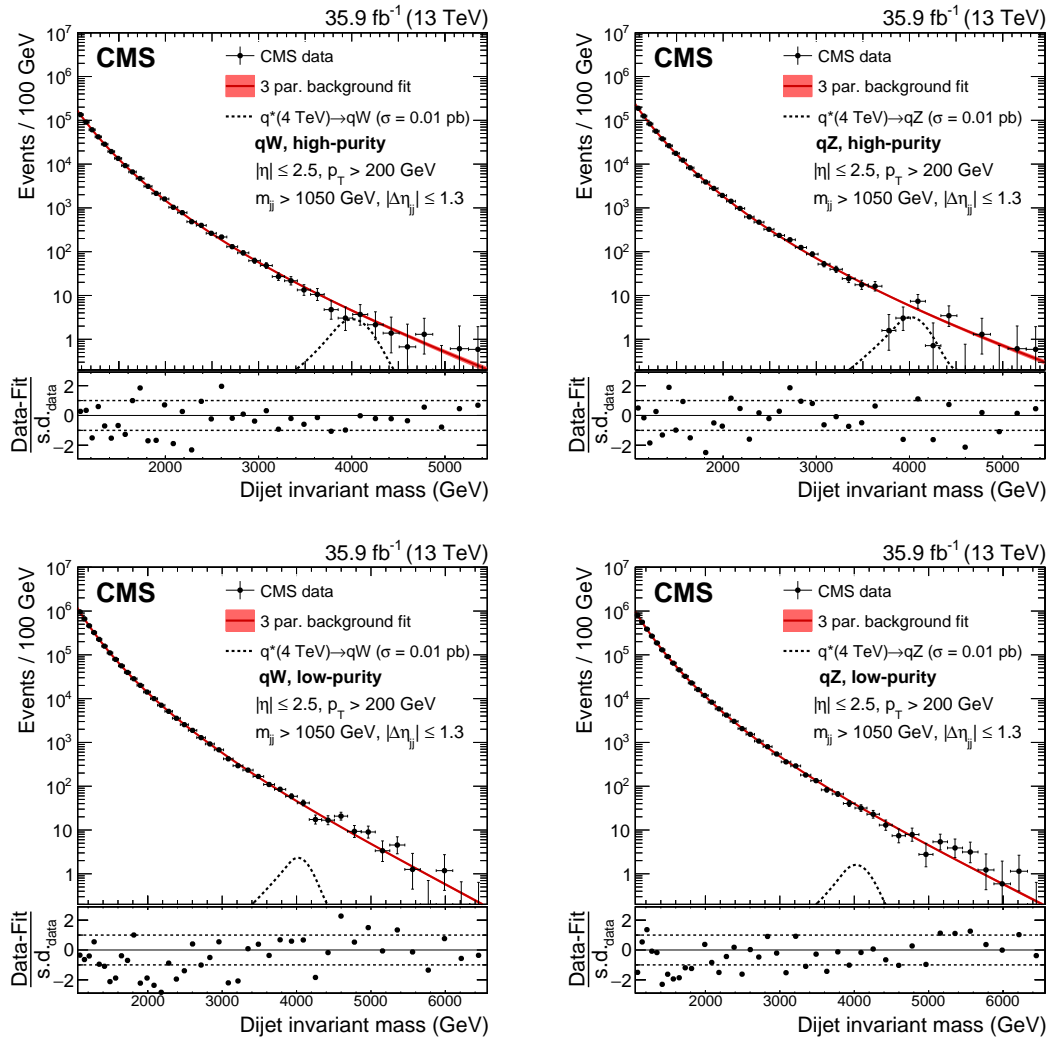


Figure 8.29: Observed dijet invariant mass spectrum for the single-tag analysis in the high purity (top) and low purity (bottom) categories using 35.9 fb^{-1} of data collected in 2016.

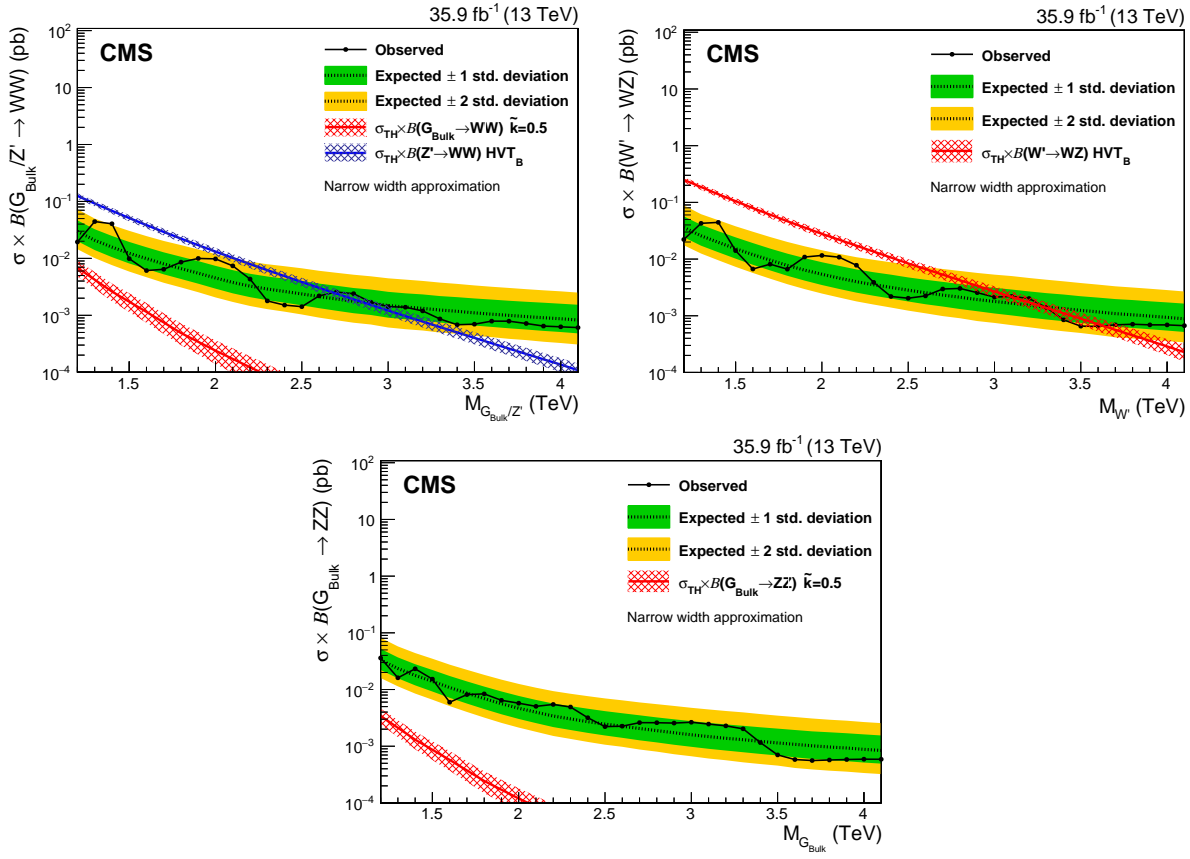


Figure 8.30: Observed (solid line) and expected (dashed line) 95% CL upper limits on the production cross section of a narrow resonance decaying into two vector bosons for different signal hypotheses: a Z' or G_{bulk} resonance decaying into WW (top left), a Z' decaying into WZ (top right) and a bulk graviton decaying into ZZ (bottom).

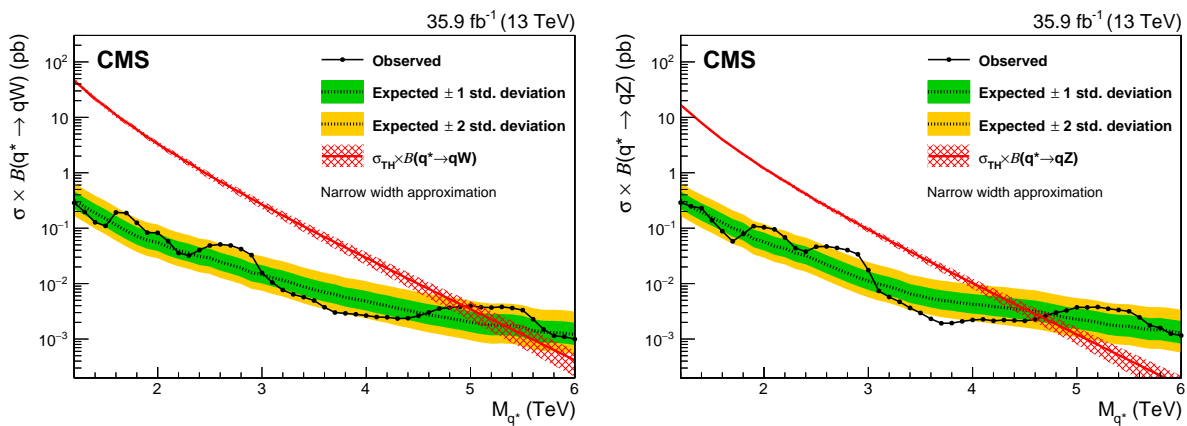


Figure 8.31: Observed (solid line) and expected (dashed line) 95% CL upper limits on the production of an excited quark resonance decaying into qW (left) or qZ (right).

2332

CHAPTER 9

2333

Search III: A novel framework for multi-dimensional searches

2334

2335 After two successful analysis using the LHC data collected at a center-of-mass energy of 13
2336 TeV, there was no confirmation of the excess observed at a center-of-mass energy of 8 TeV,
2337 and the prospect of observing new physics in diboson analyses was bleak. However, this was not
2338 a source of concern to some theorists, who considered whether the small bumps that had been
2339 observed were due to us observing the tail of another type of boson with a mass slightly different
2340 from that of a W or a Z boson, and that perhaps these bosons were not 2-prong, but 4-prong objects.

2341

2342 With no significant excess observed with the 2016 dataset of 36 fb^{-1} , we were expecting to
2343 collect a total dataset of 150 fb^{-1} in Run 2 (2015-2018) that would allow us to probe alternative
2344 BSM models, and we wanted to do so as efficiently as possible. More specifically, we wanted a
2345 way of looking for any heavy resonance decaying to any two jets with substructure, with masses
2346 anywhere in the jet mass spectrum. We decided to do so by taking advantage of the fact that we
2347 are looking for bumps in a three-dimensional space: the mass of the two jets as well as their dijet
2348 invariant mass. The one-dimensional dijet fit can therefore be replaced by a three-dimensional fit,
2349 looking for bumps in all three dimensions simultaneously. This would allow us to easily search for
2350 resonances decaying to any object peaking in jet mass; $W(qq)$, $Z(qq)$, $H(qq)$, as well as non-SM
2351 bosons; in one common framework.

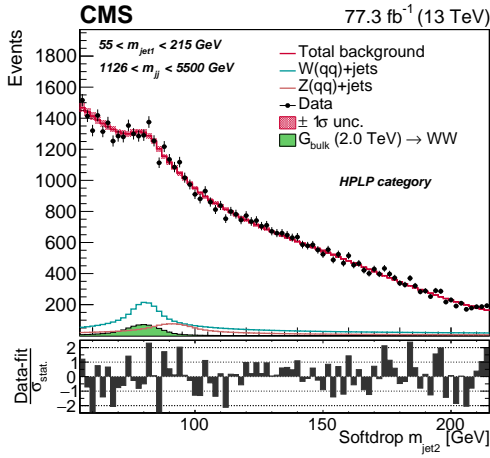
2352

2353 An additional benefit of the method, was that the modeling of the QCD multijet background
2354 would start from simulation rather than relying on a parametric fit to data. This had the benefit
2355 of allowing more control over the background shape across the full dijet invariant mass spectrum,
2356 making the fit less prone to fluctuations in the low statistics tail of the distribution, something we

2357 found to be problematic with the 1D dijet fit method.

2358

2359 Search III introduces a novel three-dimensional fit method that can be used to search for heavy
 2360 resonances decaying to any two jets with substructure peaking in the jet groomed mass spectrum.
 2361 It is validated in the context of a diboson resonance search in the all-hadronic final state, but is
 2362 easily extendable to other signals. The fit method has allowed for the first measurement of the
 2363 jet mass scale and resolution simultaneously from a $W(qq)+\text{jets}$ and $Z(qq)+\text{jets}$ mass peak, and
 2364 could also allow for the extraction of the SM $W/Z+\text{jets}$ cross section. It was published with data
 2365 collected in 2016 and 2017, corresponding to a total integrated luminosity of $\sim 80 \text{ fb}^{-1}$.



In progress. To be submitted to The European Physical Journal C

2366 9.1 Small bumps and tri-bosons

2367 In addition to the observation of a 3.4σ excess in the search for diboson resonances in the
 2368 all-hadronic final state by ATLAS [52], not confirmed by subsequent searches, several little
 2369 bumps near 2 TeV were observed in data collected at center-of-mass energies of 8 and 13 TeV, as
 2370 illustrated by the dijet invariant mass distributions observed by ATLAS and CMS in Figure 9.1.
 2371 These were not statistically significant, and are expected due to statistical fluctuations, however,
 2372 only a coherent analysis would be able to determine if a new physics signal could be partly
 responsible for any of these excesses in the dijet invariant mass of V jets. Due to their small size

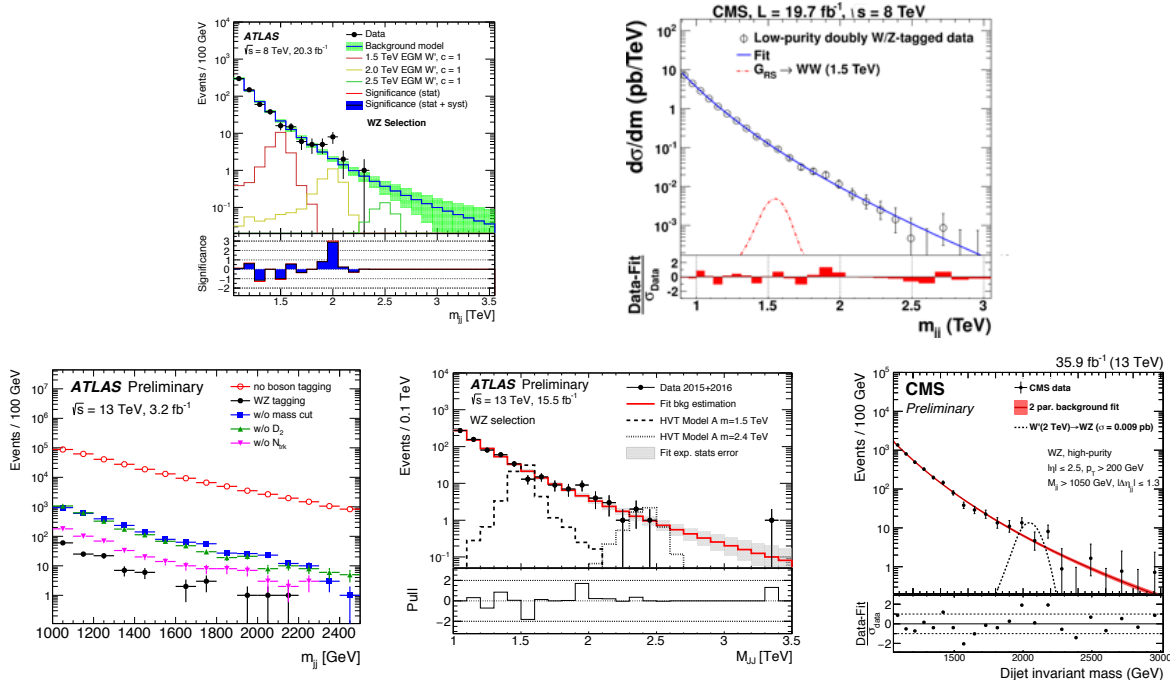


Figure 9.1: Several small bumps have been observed in diboson resonance searches in the all-hadronic final state, both in ATLAS and in CMS [81].

2373 and the way the excesses appeared to slightly shift around, these were obviously not diboson
 2374 resonances. However, a proposal was made that they could be caused by the observation of
 2375 a non-SM boson, such that jets with a mass several standard deviations away from the new
 2376 particle's mean, its so-called *tail*, were being observed, as illustrated in Figure 9.2. Further, these
 2377 could be 4-pronged objects rather than 2-prong, which would cause the excess to vary in size
 2378 depending on the 4-prong efficiency of the analysis specific W-tagger in use. An explanation for
 2379 the observed excesses was proposed in [82]. This paper pointed out that, if particles like W' and

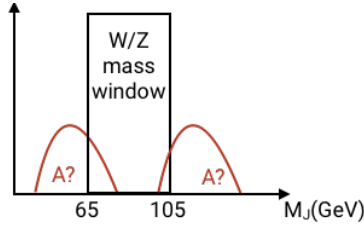


Figure 9.2: The small excesses in diboson searches could be caused by the observation of the tail of a non-SM object, peaking at a groomed jet mass slightly higher or lower than that of a W or Z boson.

Z' exist, an extended scalar sector is needed in order to give mass to the vector bosons. These heavy scalars would decay to lighter bosons, if kinematically allowed, leading to a cascade of decays that produced signals of multiple bosons in a single jet. Some example signatures are illustrated in Figure 9.3. Signatures like these would peak in the groomed-jet mass spectrum and,

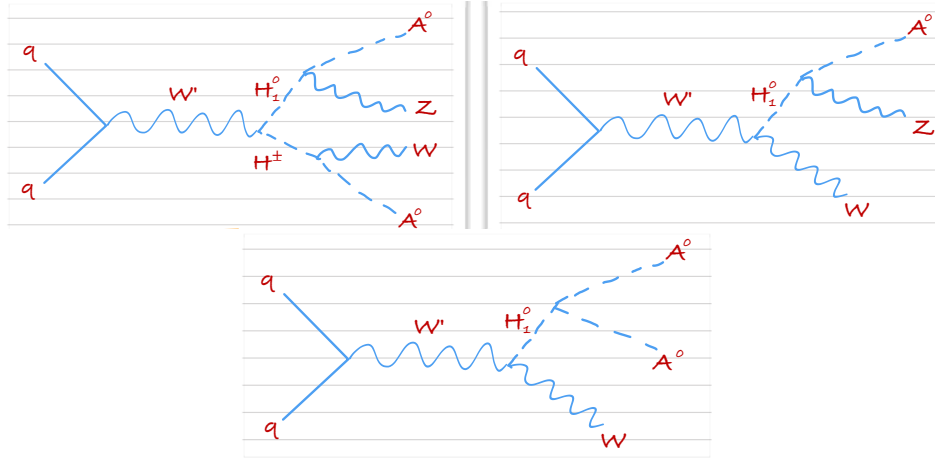


Figure 9.3: A W' decaying to a neutral H^0 and a charged H^\pm scalar particle leading to a quadriboson final state (left), and a W' decaying to a neutral scalar particle H^0 and a W leading to a triboson final state (middle and right) [82].

depending on what the final bosons decay into, have very different substructure profiles. In order to efficiently search for such types of signals, or any signal peaking in the jet mass spectrum, we decided to build a generic framework that would allow searching for peaks anywhere in the jet-mass and dijet invariant mass spectrum. Rather than selecting jets with a groomed mass between 65 and 105 GeV and then searching for resonances peaking in the dijet invariant mass, we would attempt to look for resonances peaking anywhere in the three-dimensional space formed by the groomed mass of each jet and their dijet invariant mass, scanning the full groomed mass spectrum in a single analysis. We would first demonstrate the new method in context of

2393 the diboson all-hadronic search since this was an analysis we were familiar with and which would
2394 allow for a straight forward comparison of the obtained results.

2395 **9.2 Analysis strategy**

2396 The background estimation used in Search I and Search II relies on a one-dimensional fit of
2397 the dijet invariant mass of the signal region after a tight selection on the jet mass has been
2398 applied. Since the signal will peak in all three dimensions, mainly the dijet invariant mass
2399 M_{VV} , and the mass of jet 1 and jet 2 (M_{jet1} and M_{jet2}), we will extract the signal from the
 three-dimensional plane of M_{VV} - M_{jet1} - M_{jet2} . The benefits of doing so are that we can search for

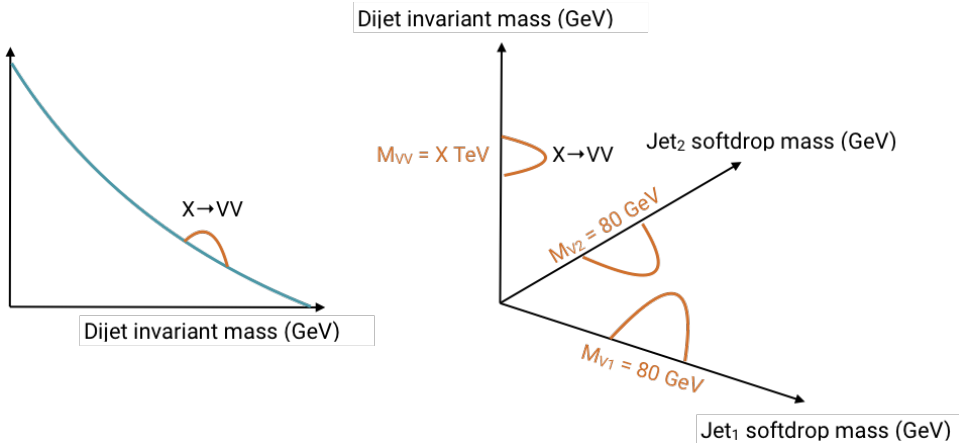


Figure 9.4: The one dimensional diboson analysis versus the three dimensional fit.

2400
2401 resonances decaying to VV ($V=W/Z$), VH ($H=$ Higgs), HH, VX, VH, XX, or XY, where X and
2402 Y are new hypothetical bosons, in the same analysis. Additionally, a jet-mass selection is no
2403 longer needed as we fit the full jet mass line-shape to extract the signal. This effectively increases
2404 the signal statistics since a large fraction of the W and Z signal falls outside the mass window.
2405 Fitting the groomed-jet mass and resonance mass together also allows for the addition of nuisance
2406 parameters that simultaneously affect both in order to fully account for the correlation between
2407 the variables. Finally, we would model the background starting from simulation, rather than
2408 from a dijet fit to data. This allows the background shape to assume non-smooth distributions,
2409 and could allow the search to probe lower dijet masses, something we will discuss further in
2410 Section 9.5. Replacing the parametric fit by a simulation-based model would also reduce the fit
2411 sensitivity to background fluctuations in the extreme tails of the dijet invariant mass spectrum.

2412 This chapter presents a novel three-dimensional fit method in the search for diboson resonances

2413 in the all-hadronic final state, and is based on 77.3 fb^{-1} of data collected in 2016 and 2017. The
2414 data collected in 2016 was already analyzed in the context of Search II, but is reanalyzed here in
2415 order to compare the performance of the three-dimensional fit to that of the one dimensional
2416 search.

2417 9.3 Data and simulated samples

2418 The data analyzed in this search consists of 35.9 fb^{-1} of data collected in 2016 and 41.4 fb^{-1} of
2419 data collected in 2017, yielding a total of 77.3 fb^{-1} .
2420 The simulated samples are the same as those described in Section 8.3.

2421 9.4 Event selection

2422 Events are selected following the same criteria as in Search I and Search II (see Section 7.4.2)
2423 and can be summarized as follows: we require two AK8 jets with PUPPI pileup subtraction
2424 applied, and with $\eta < 2.5$ and $p_T > 200 \text{ GeV}$. The two jets are further required to be separated
2425 by $|\Delta\eta|_{jj} < 1.3$. The softdrop algorithm is applied, and the two jets with the highest jet mass in
2426 the event are selected as potential vector boson candidates. In order to avoid any bias in the
2427 jet mass shapes when performing the three-dimensional fit, the two jets are randomly sorted
2428 after the above selections have been applied. In addition, the dijet invariant mass is required
2429 to be greater than 1126 GeV in order to be on the trigger plateau. As already mentioned in
2430 the introduction, the background modeling used in this analysis is capable of modeling trigger
2431 turn-ons. We explored the possibility of starting the analysis below the trigger plateau, however,
2432 while the background modeling was found to be reliable, the extraction of a signal peaking on
2433 top of a turn-on was difficult, and we therefore had to abandon the modeling of the trigger
2434 turn-on for this first demonstration of the method. More details will be given in Section 9.5. The
2435 dijet invariant mass and $|\Delta\eta|_{jj}$ distribution for the two leading jets in the event after the above
2436 preselections have been applied are shown in Figure 9.5 and the jet p_T and η distributions for
2437 signal and for background is shown in Figure 9.6.

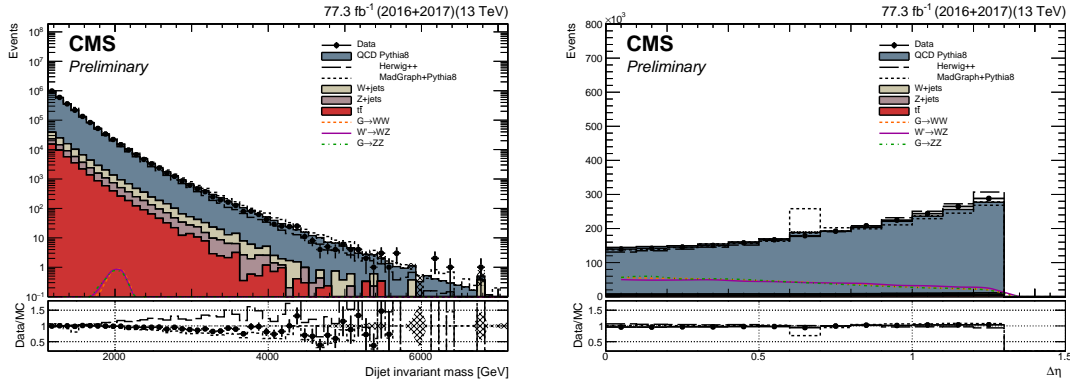


Figure 9.5: The dijet invariant mass (left) and $|\Delta\eta|_{jj}$ (right) for the two leading jets after preselections are applied. The signal is scaled by an arbitrary number to be visible.

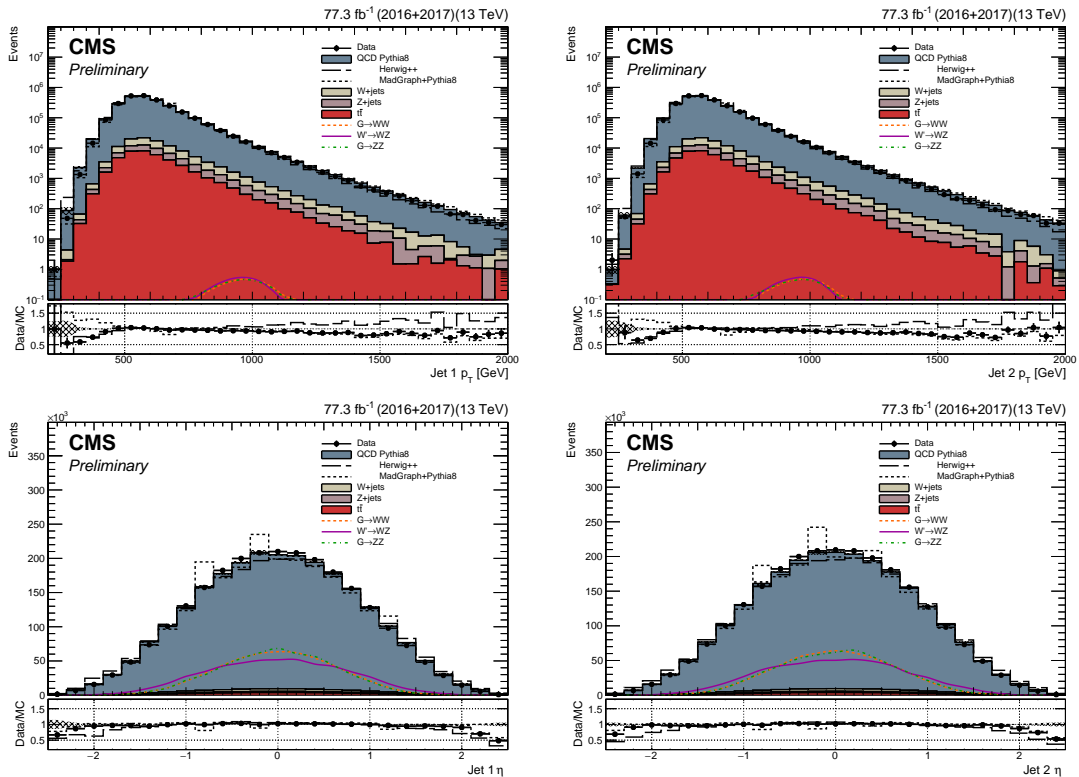


Figure 9.6: Jet p_T (top) and η (bottom) of the first (left) and second (right) selected jet in the event. The signal is scaled by an arbitrary number.

2438 9.5 Triggering

2439 The triggers used for the data collected in 2016 are the same as in Section 7.4.1, while the
 2440 thresholds in 2017 have increased in order to push the trigger rate to a level acceptable for the
 2441 increased luminosity. The triggers used for 2017 data are

- 2442 • HLT_PFHT1050
- 2443 • HLT_AK8PFJet500
- 2444 • HLT_AK8PFJet360/380/400/420_TrimMass30
- 2445 • HLT_AK8PFHT750/800/850/900_TrimMass50.

2446 As in Section 7.4.1, the trigger names indicate the primary selection criteria, with the terms “PF”,
 2447 “HT”, and “AK8” being previously explained. The term “JetXXX” refers to the lower value of
 2448 the p_T selection criteria of the jet, “HTXXX” refers to the HT requirement, and “TrimMassYY”
 2449 refers to the trimmed-jet mass selection applied to least one jet. For the results presented here,
 2450 the analysis threshold is set by the value of M_{VV} such that the combination of all triggers are
 2451 greater than 99% efficient. The trigger turn-on is evaluated in an orthogonal data set in which
 2452 the presence of a single muon with a p_T above 27 or 50 GeV is required. The trigger efficiency as
 2453 a function of dijet invariant mass using a combination of all triggers (left), and as a function of
 2454 the jet soft drop mass for the grooming-based triggers only (right) are shown in Figure 9.7. The
 2455 grooming-based triggers in the 2017 data set do not fully reach the trigger plateau as the triggers
 where unavailable during one data taking period, corresponding to 4.8 fb^{-1} . The corresponding

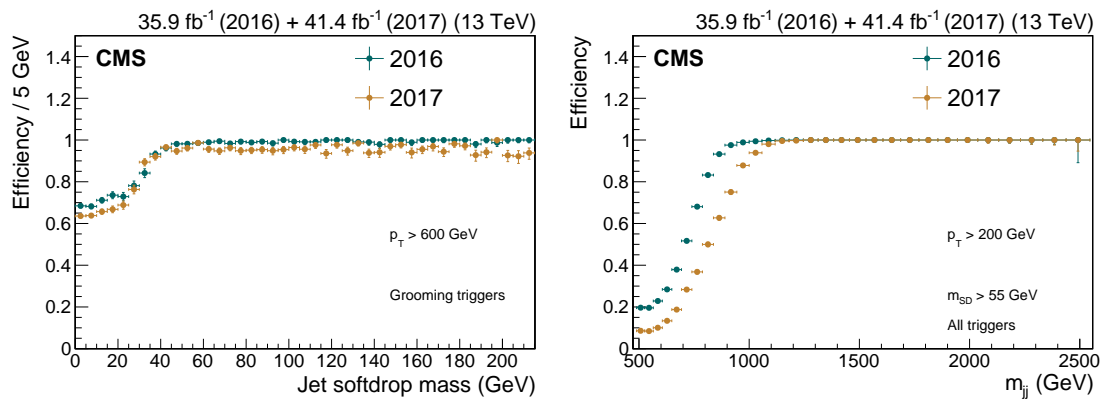


Figure 9.7: Left: trigger efficiency as a function of the dijet invariant mass using a combination of all analysis triggers. Right: trigger efficiency as a function of the jet softdrop mass for triggers requiring an online trimmed mass of at least 30 or 50 GeV.

²⁴⁵⁷ turn-on excluding the data taken without grooming-based triggers included, is shown in Figure 9.8.
²⁴⁵⁸ Here we see the that the trigger efficiency as a function of jet softdrop mass reaches the trigger plateau at the same point as in 2016. The combination of all triggers are > 99% efficient above

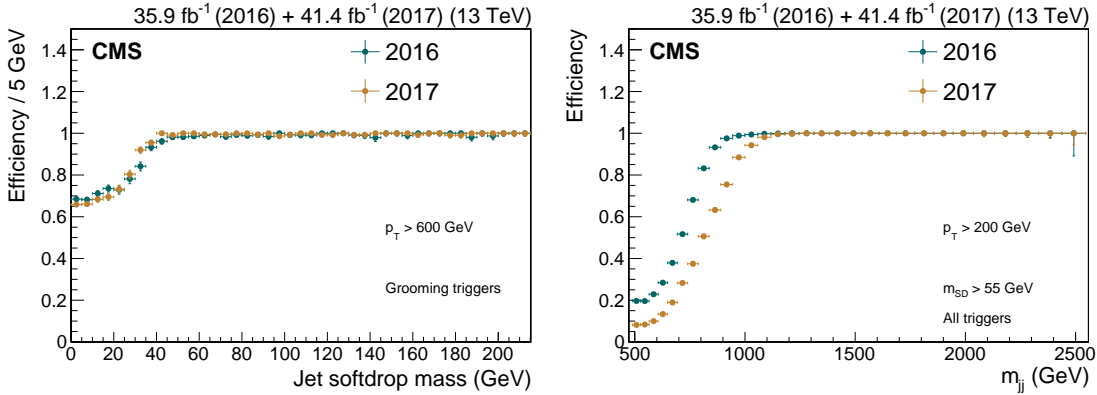


Figure 9.8: Left: trigger efficiency as a function of the dijet invariant mass using a combination of all analysis triggers. Right: trigger efficiency as a function of the jet softdrop mass for triggers requiring an online trimmed mass of at least 30 or 50 GeV. Here after excluding the data taken in 2017 without grooming-based triggers included.

²⁴⁵⁹
²⁴⁶⁰ a dijet invariant mass of 1126 (990) GeV for the 2017 (2016) dataset. Since the point of full
²⁴⁶¹ efficiency is largest in the 2017 dataset, this sets the analysis threshold.

²⁴⁶² 9.5.1 Trigger turn-on modeling

The threshold in the dijet mass at which resonances can be searched for depends on the value which the trigger can efficiently select events. The threshold used in the previous analyses was required to be high enough so that the dijet mass spectrum could be described with a smoothly falling function. Since the background modeling for this analysis does not depend on a smoothly falling dijet invariant-mass spectrum, as will be described in detail in Section 9.7, and in order to compensate for a loss in acceptance due to the increased trigger thresholds, we sought to model the trigger turn-on directly from data. This would allow us to search for diboson resonances with masses below the value at which the trigger is fully efficient. To model the trigger turn-on we derive a three dimensional histogram of the trigger efficiency versus dijet invariant mass (M_{VV}) and the groomed-jet mass of jet 1 and jet 2 (M_{jet1} and M_{jet2}), where each bin corresponds to the trigger efficiency for a small range of values of M_{VV} , M_{jet1} and M_{jet2} . The procedure is as follows. From the one-dimensional trigger turn-on histograms shown in Figure ??, values of M_{VV} , M_{jet1} and M_{jet2} at which the signal efficiency is above 99% are determined. For every bin above this

threshold, the trigger efficiency is fixed to one, corresponding to a 100% efficiency. For all bins below this threshold, we fit slices of M_{VV} in bins of M_{jet1} and M_{jet2} with a sigmoid function, determine the trigger efficiency to be used as a weight for simulated events to pass the trigger, and set the value from this function, and set the bin content of the three dimensional weight histogram accordingly. Since the trigger efficiency falls below 50 percent around a dijet invariant mass of 800 GeV, as seen from the right-hand plot in Figure ??, searching for resonances with masses below this point is not feasible due to low acceptance. In addition, the full signal shape needs to be contained within the dijet invariant mass spectrum, requiring the search to consider dijet invariant masses 10% lower than the actual value of the lowest resonance mass being probed. These two factors dictate that the minimum resonances mass we can search for is 1 TeV, and that the background modeling must begin around 900 GeV in order to fully contain the signal. Starting from a dijet invariant mass of $M_{VV} = 893$ GeV, the “dijet bin” closest to 900 GeV (where the “dijet binning” is as described in Section 7.5), and a jet mass of $M_{jet} = 40$ GeV, a coarsely binned three-dimensional histogram is filled with the fraction of events that pass one of the signal triggers,

$$w_{ijk}^{Bin} = \frac{\text{PASS}(m_{jj}^i, m_{j1}^j, m_{j2}^k)}{\text{ALL}(m_{jj}^i, m_{j1}^j, m_{j2}^k)}.$$

From this three-dimensional coarse histogram, a finer binned histogram is achieved through interpolation. In bins of M_{jet1} and M_{jet2} , each slice in M_{VV} is fitted with a sigmoid function,

$$s(x) = \frac{1}{1 + e^{-p_1(x-p_2)}},$$

and the trigger weight is extracted in dijet invariant mass bins of 10 GeV. This fine binning in dijet invariant mass is sufficient to yield a smooth distribution after trigger reweighting, as will be demonstrated below, and no additional interpolation is done. Figure 9.9 shows the total projections on the M_{VV} , M_{jet1} and M_{jet2} axes for the full trigger weight histogram. The M_{jet} and

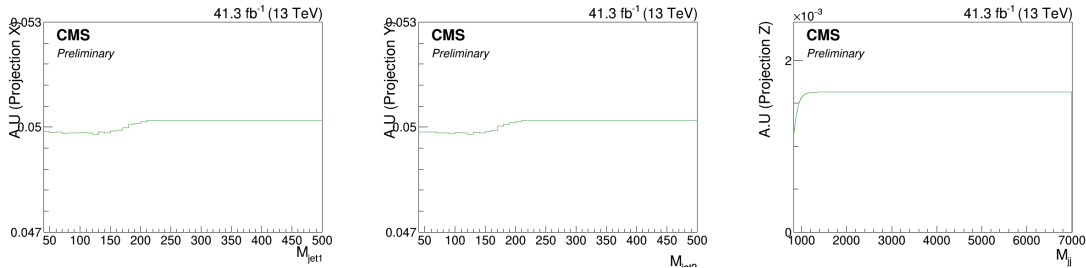


Figure 9.9: One-dimensional projections of the trigger weight histogram for M_{jet1} , M_{jet2} and M_{VV} , respectively.

2467 M_{VV} spectra for the signal sample with the lowest resonance mass, and for the QCD background
2468 before and after trigger weights have been applied, are shown in Figure 9.10 and are compared to
2469 data. A greater than 95% the signal efficiency is retained after the trigger weights have been
 applied, and the reweighted QCD simulation agrees well with data. The modeling of the trigger

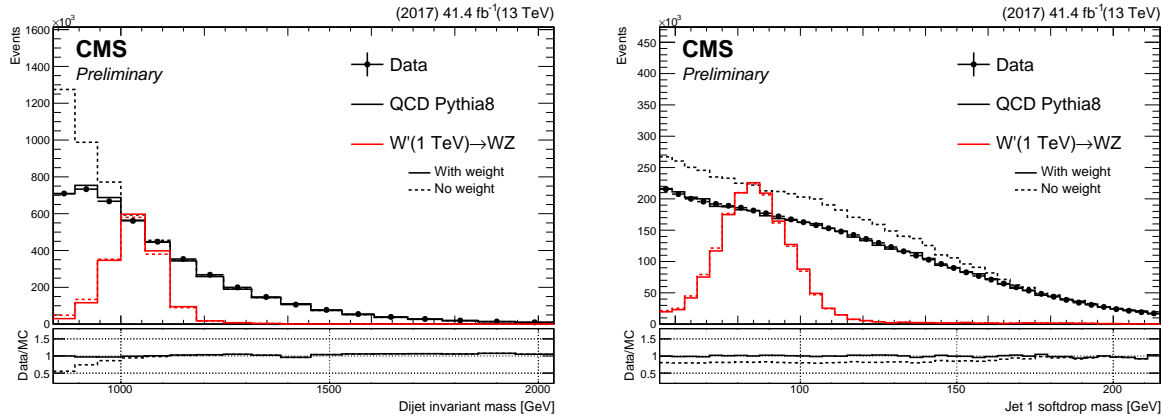


Figure 9.10: The M_{VV} (left) and M_{jet} (right) spectra for signal and background before and after trigger weights have been applied.

2470
2471 turn-on was then implemented in the background fit method in the 3D analysis and we found
2472 that the method could model the turn-on well. However, when studying the bias on the extracted
2473 signal rate for a possible signal in this turn-on region, we found this to be large due to the
2474 difficulties involved with fitting a signal peak on top of a background that is peaking. Since
2475 the intention of the analysis presented here was to introduce the 3D fit method and allow it to
2476 become available as soon as possible, we therefore abandoned the modeling of the trigger turn-on
2477 for this paper. However, we still wish to pursue this strategy in the future.

2478 9.6 A mass- and p_T -decorrelated tagger

2479 In order to identify W-jet and Z-jet candidates we utilize the softdrop algorithm and calculate
 2480 the n-subjettiness ratio τ_{21} for AK8 jets that are clustered with PUPPI constituents. As before,
 2481 the softdrop jet mass is used to improve the mass resolution of the jet, while n-subjettiness serves
 2482 as a discriminant by yielding a probability of how compatible the jet is with having N axes. For
 2483 this search we require the softdrop jet mass to be between $55 < m_{sd} < 215$ GeV, removing as
 2484 much as possible of the low-mass QCD background and going high enough to encompass all
 2485 searches for resonances decaying to W, Z, H or tops (the SM particles known to produce jets
 2486 with substructure in the final state). Since the analysis is done in bins of jet mass and dijet
 2487 invariant mass, the background must be modeled for a very wide range of mass and transverse
 2488 momenta. It is therefore desirable that the QCD background spectrum is minimally sculpted as a
 2489 function of p_T and mass, such that the background shapes in all regions are similar to one another
 2490 and remains smoothly falling in all three analysis dimensions and in all bins of M_{VV} , M_{jet1} and
 2491 M_{jet2} . In order to ensure minimal sculpting, we therefore decorrelate the τ_{21} variable from the
 2492 jet softdrop mass and the jet p_T following what was done in Ref. [79], and briefly discussed in
 2493 Section 8.5.2. This decorrelation is performed by flattening the τ_{21} profile dependence on ρ' ,
 2494 where ρ' is defined by

$$\rho' = \log(m^2/p_T/\mu), \text{ where } \mu = 1 \text{ GeV.} \quad (9.1)$$

2495 Figure 9.11 shows the profile distribution of τ_{21} as a function of ρ' for QCD jets after applying
 the preselections listed above together with a softdrop mass selection of $55 < m_{sd} < 215$ GeV. A

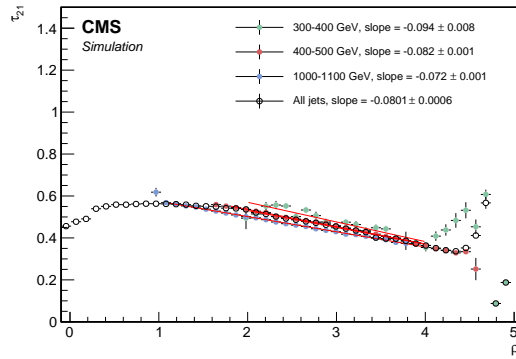


Figure 9.11: Profile distributions of τ_{21} as a function of $\rho' = \log(m^2/p_T/\mu)$ after applying a softdrop mass selection of $55 < m_{sd} < 215$ GeV.

2497 linear transformation is then defined as

$$\tau_{21}^{DDT} = \tau_{21} - M \times \rho', \quad (9.2)$$

2498 where the slope M is fitted from the linear part of the τ_{21} profile versus ρ' for the inclusive p_T
2499 spectrum, shown in Figure 9.11. The resulting slope is $M = -0.080$. The profile of the retuned
2500 τ_{21}^{DDT} versus ρ' is shown in Figure 9.12, exhibiting the desired flattened spectra for QCD jets
 versus ρ' . Which selections on τ_{21}^{DDT} to be used are chosen in the following way. First, we

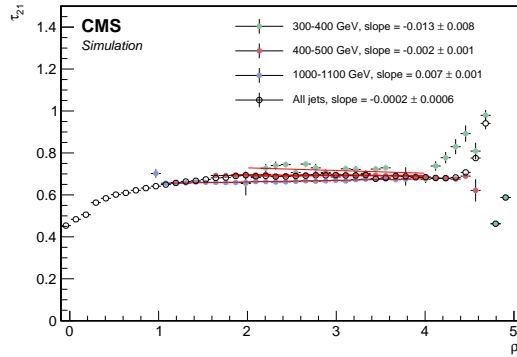


Figure 9.12: Profile distributions of τ_{21}^{DDT} as a function of $\rho' = \log(m^2/p_T/\mu)$, where $\mu = 1$ GeV.

2501

2502 check which τ_{21}^{DDT} selection corresponds to the highest Punzi significance as a function of the
2503 resonance mass for different signal samples, as shown in Figure 9.13. All other analysis selections,
 including a selection on the groomed-jet mass of $55 < m_{sd} < 215$ GeV, have been applied. The

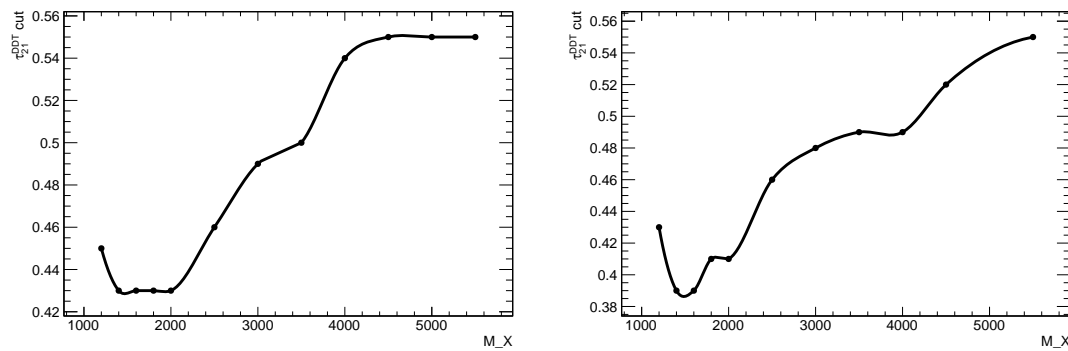


Figure 9.13: The τ_{21}^{DDT} cut corresponding to the highest Punzi significance for a given signal resonance mass, here for a Bulk $G \rightarrow WW$ (left) and a Bulk $G \rightarrow ZZ$ (right) signal.

2504

2505 cut maximizing the Punzi significance at lower resonance mass, where the background is highest,
 2506 is chosen as the “high-purity” (HP) working point. This corresponds to $\tau_{21}^{DDT} \leq 0.43$. We then
 2507 proceed by finding which selections on τ_{21}^{DDT} contains at least 95% of the signal, and out of those
 2508 select the one that optimizes the Punzi significance. This is found to be $0.43 < \tau_{21}^{DDT} \leq 0.79$,
 2509 and is classified as the low purity (LP) category. The purpose of this category is to enhance the
 2510 overall sensitivity of the analysis, especially where the background is low.

2511 Figure 9.14 shows the performance of τ_{21} and τ_{21}^{DDT} (2016 and 2017 tune) in the background-
 2512 signal efficiency plane (top). We observe a significant gain in signal efficiency at a fixed mistag-
 2513 rate with the decorrelated taggers, when not using a tight jet groomed mass selection (recall: a
 2514 window of $55 \text{ GeV} < M_{SD} < 215 \text{ GeV}$ is used in this analysis). That is because we are taking
 2515 advantage of far more information when computing the DDT: subjetiness, and the ratio of
 2516 jet groomed mass and momentum. All these have a distribution which is different between
 2517 quark/gluon jets and W-jets, leading to a larger separation between signal and background,
 2518 as can be seen when comparing the distributions of the different taggers in the left plot of
 2519 Figure 9.15. The distribution of $\log(m_{SD}^2/p_T)$ is shown on the right in Figure 9.15, and it is
 clear that the variable adds discriminating power. In addition to cutting on τ_{21}^{DDT} , a selection on

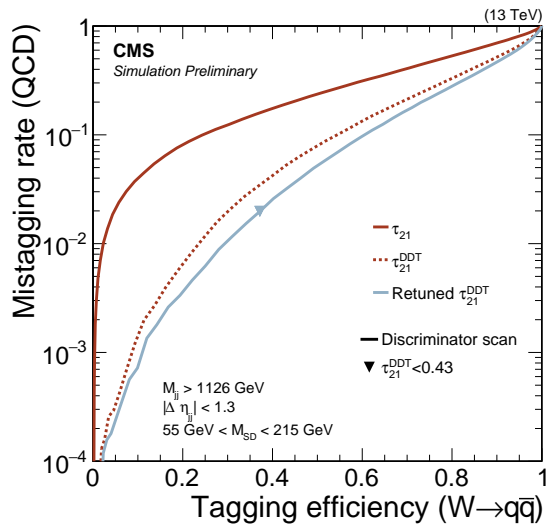


Figure 9.14: Performance of τ_{21} and τ_{21}^{DDT} (2016 and 2017 tune) in the background-signal efficiency plane.

2520
 2521 $\rho = \log(m^2/p_T^2) < -1.8$ is applied. This is in order to avoid configurations where the jet mass is
 2522 high, but the jet transverse momentum is low. In these cases, the AK8 cone size is too small
 2523 to contain the full jet, affecting both the jet mass resolution and the τ_{21}^{DDT} tagging efficiency.
 2524 These edge effects are difficult to model in simulation and we therefore avoid this region in the

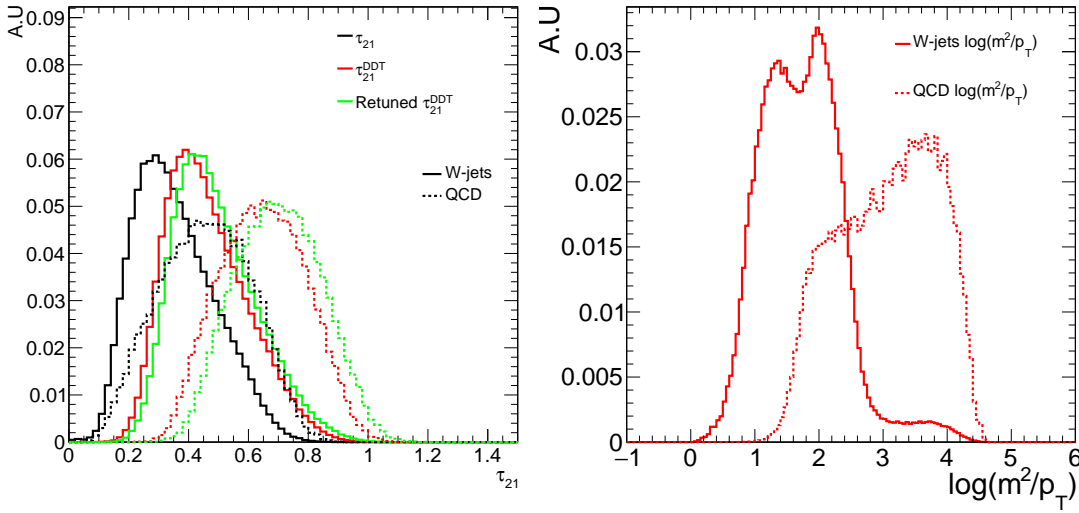


Figure 9.15: Distribution of τ_{21} and τ_{21}^{DDT} with the old and the new tune (left) and comparison of $\log(m^2/p_T)$ for signal and background jets (right).

following. Figure 9.16 shows the profile distribution of τ_{21}^{DDT} versus ρ for QCD jets, where a clear deviation from the observed linear spectra is observed above a ρ of -1.8. Note that this has a

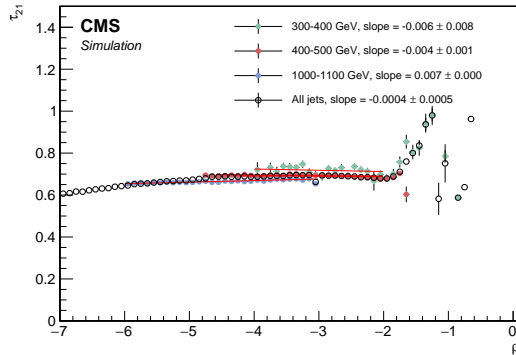


Figure 9.16: Profile distributions of τ_{21}^{DDT} as a function of $\rho = \log(m^2/p_T^2)$, where $\mu = 1$ GeV. The DDT breaks down above $\rho = -1.8$.

negligible effect on signal jets, which mainly peak around 80 GeV and have a high jet transverse momenta. Figure 9.17 shows the distributions of the PUPPI softdrop jet mass, the τ_{21}^{DDT} , and the τ_{21} variable for simulation and for data. The softdrop jet mass in the signal distribution peaks nicely around the W mass, while the multijets background spectrum is peaked at lower softdrop masses.

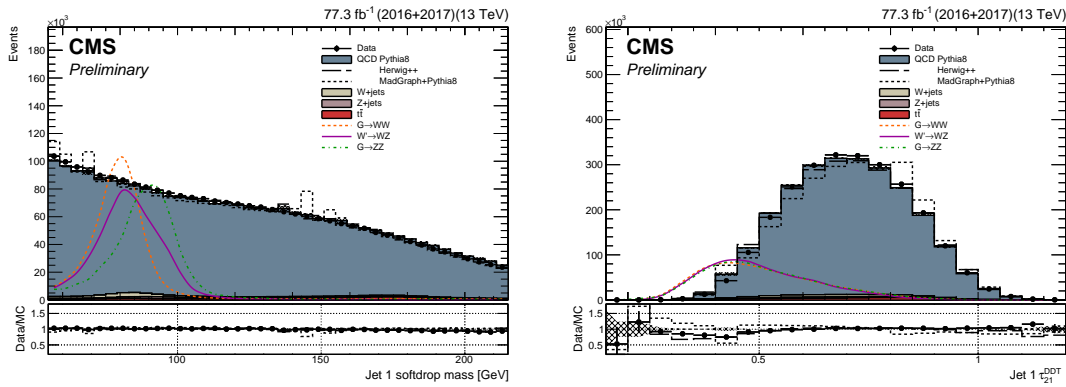


Figure 9.17: The softdrop jet mass (left) and τ_{21}^{DDT} (right) distribution in data and in simulation. Signal is scaled by an arbitrary number.

2532 9.6.1 Data to simulation scale factors

2533 Following what was done in Section 7.7 and 8.5.3, we derive W-tagging scale factors in order to
 2534 correct the efficiency in MC of the selection on τ_{21}^{DDT} , by estimating the ratio of the selection
 2535 efficiencies in data and in simulation. The softdrop jet mass range is fitted from 55 to 215 GeV,
 2536 and the two categories of purity are:

- 2537 • pass region: $0 < \tau_{21}^{DDT} \leq 0.43 \sim$ high-purity,
- 2538 • fail region: $0.43 < \tau_{21} \leq 0.79 \sim$ low purity.

2539 The obtained scale factors, jet-mass scale and resolution together with their statistical uncertainty
 2540 are listed in Tables 9.1 and 9.2 for 2016 and 2017 data, respectively. The corresponding
 2541 simultaneous fits are shown in Figure 9.18. The W-tagging efficiency in this region is lower
 2542 than what is expected for signal jets, around 7% compared to 35%. This is expected as the
 2543 measurement in $t\bar{t}$ is dominated by W-jets with a p_T of around 200 GeV, just where the W decay
 2544 products merge into a single jet, whereas the signal jets mostly have a transverse momentum
 2545 above 600 GeV. The signal efficiency for τ_{21}^{DDT} increases at a function of jet p_T , as can be seen
 2546 from Figure 9.26, whereas the background efficiency is flat by design. In addition to the statistical
 2547 uncertainty, two systematic uncertainties are evaluated: one due to generator differences and one
 2548 due to NNLO corrections. The former is evaluated by comparing the resulting scale factors when
 2549 using $t\bar{t}$ simulation produced with different generators. The latter is evaluated by comparing the
 2550 extracted efficiency with and without top- p_T reweighting. This weight is derived from data in
 2551 order to better describe the observed p_T distribution in $t\bar{t}$ and is calculated for each top jet as
 2552 $w = \exp^{0.0615 - 0.0005 * p_{T,top}}$. The W tagging scale factors, jet mass scale, and jet mass resolution,
 2553 with their total uncertainty after adding systematics, are listed in Table 9.3. As before, the scale
 2554 factor is used to scale the signal yield and the jet mass scale and resolution are used to smear the
 2555 MC. The difference in jet mass scale between data and simulation is around 2%, and the jet mass
 2556 resolution scale factor is roughly 8%.

$\tau_{21}^{DDT} < 0.43$	m [GeV]	σ [GeV]	W-tag efficiency
Data	81.999 ± 0.454 GeV	7.148 ± 0.544 GeV	0.080 ± 0.008
Simulation	80.890 ± 0.160 GeV	6.579 ± 0.149 GeV	0.085 ± 0.003
Data/simulation	1.014 ± 0.006	1.086 ± 0.086	0.937 ± 0.094
$0.43 < \tau_{21}^{DDT} < 0.79$			
Data			0.920 ± 0.008
Simulation			0.915 ± 0.003
Data/simulation			1.006 ± 0.009

Table 9.1: Jet mass scale, jet mass resolution, and τ_{21}^{DDT} scale factors, as evaluated in the full 2016 single-muon dataset.

$\tau_{21}^{DDT} < 0.43$	m [GeV]	σ [GeV]	W-tag efficiency
Data	80.784 ± 0.391 GeV	7.694 ± 0.445 GeV	0.065 ± 0.006
Simulation	82.208 ± 0.293 GeV	7.127 ± 0.284 GeV	0.068 ± 0.005
Data/simulation	0.983 ± 0.006	1.080 ± 0.076	0.955 ± 0.113
$0.43 < \tau_{21}^{DDT} < 0.79$			
Data			0.935 ± 0.006
Simulation			0.932 ± 0.005
Data/simulation			1.003 ± 0.008

Table 9.2: Jet mass scale, jet mass resolution, and τ_{21}^{DDT} scalefactors as evaluated in the full 2017 single-muon dataset.

	SF $\pm \sqrt{\text{Stat.} + \text{Sys}_{\text{Generator}} + \text{Sys}_{\text{NNLO}}}$	SF \pm Total Unc.
$HPSF_{DDT}^{2017}$	$0.955 \pm \sqrt{0.113^2 (\text{stat.}) + 0.003^2 (\text{sys.}) + 0.043^2 (\text{sys.})}$	0.955 ± 0.121
$HPSF_{DDT}^{2016}$	$0.937 \pm \sqrt{0.094^2 (\text{stat.}) + 0.003^2 (\text{sys.}) + 0.043^2 (\text{sys.})}$	0.937 ± 0.103
$LPSF_{DDT}^{2017}$	$1.003 \pm \sqrt{0.008^2 (\text{stat.}) + 0.003^2 (\text{sys.}) + 0.02^2 (\text{sys.})}$	1.003 ± 0.008
$LPSF_{DDT}^{2016}$	$1.006 \pm \sqrt{0.009^2 (\text{stat.}) + 0.003^2 (\text{sys.}) + 0.02^2 (\text{sys.})}$	1.006 ± 0.009
JMS^{2017}	$0.983 \pm \sqrt{0.006^2 (\text{stat.}) + 0.002^2 (\text{sys.}) + 0.001^2 (\text{sys.})}$	0.983 ± 0.007
JMS^{2016}	$1.014 \pm \sqrt{0.006^2 (\text{stat.}) + 0.002^2 (\text{sys.}) + 0.001^2 (\text{sys.})}$	1.014 ± 0.007
JMR^{2017}	$1.080 \pm \sqrt{0.076^2 (\text{stat.}) + 0.027^2 (\text{sys.}) + 0.001^2 (\text{sys.})}$	1.080 ± 0.081
JMR^{2016}	$1.086 \pm \sqrt{0.086^2 (\text{stat.}) + 0.027^2 (\text{sys.}) + 0.001^2 (\text{sys.})}$	1.086 ± 0.090

Table 9.3: Final jet mass scale, jet mass resolution, and τ_{21}^{DDT} scalefactors with statistical and systematic uncertainties.

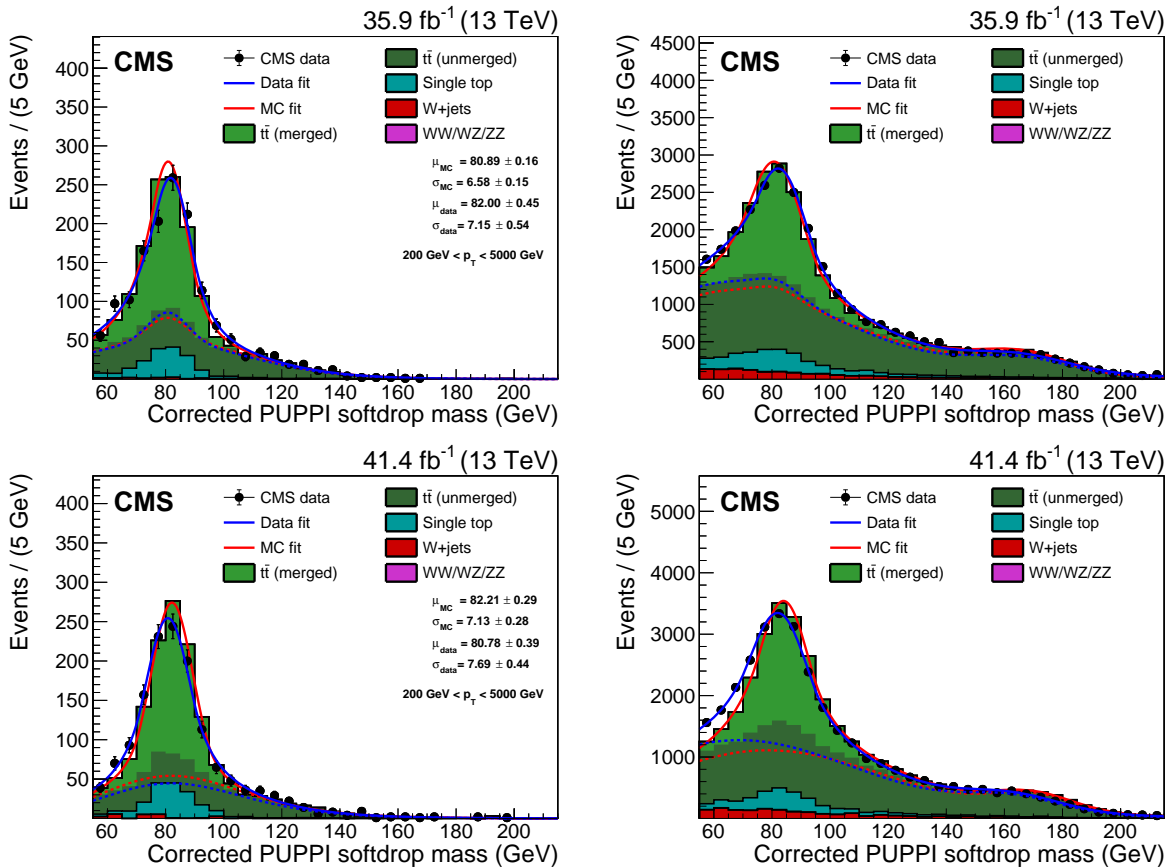


Figure 9.18: PUPPI softdrop jet mass distribution for events that pass (left) and fail (right) the $\tau_{21}^{DDT} < 0.43$ selection in the $t\bar{t}$ control sample. The result of the fit to data and simulation is shown by the solid blue and solid red line, respectively. The background components of the fit are shown as dashed-dotted lines. The fit to 2016 data is shown in the upper panels and the fit to 2017 data in the lower panels.

2557 9.6.2 p_T -dependence

2558 The τ_{21}^{DDT} selection criteria used for this search is restrictive to favor better signal significance, but
 2559 results in small event samples of the data and simulation needed to produce the scale factors. In
 2560 order to determine the dependence of the W-tagging efficiency, and the PUPPI softdrop jet-mass
 2561 scale and resolution on the transverse momentum of the jets, we divide the sample into 4 different
 2562 jet- p_T bins using the looser softdrop + τ_{21} tagger, and compute the scale factors per bin. The
 2563 systematic uncertainties are evaluated the same way as above (one due to top- p_T reweighting and
 2564 one comparing different $t\bar{t}$ samples). Figure 9.19 shows the extracted W-tagging efficiency for
 2565 data (black markers) and for simulation (red markers) using a tagger based on PUPPI softdrop
 2566 with a requirement of $\tau_{21} < 0.4$, as a function of jet p_T . The inclusive efficiency measurement
 2567 is marked with triangles. The lower panel shows the efficiency ratio of data over simulation,
 2568 corresponding to the W-tagging scale factor. All scale factors are compatible with unity, but
 2569 the uncertainty on the measurement grows as statistics decrease. The corresponding extracted
 scale factors are listed in Table 9.4. With the observation of this clear trend of an uncertainty

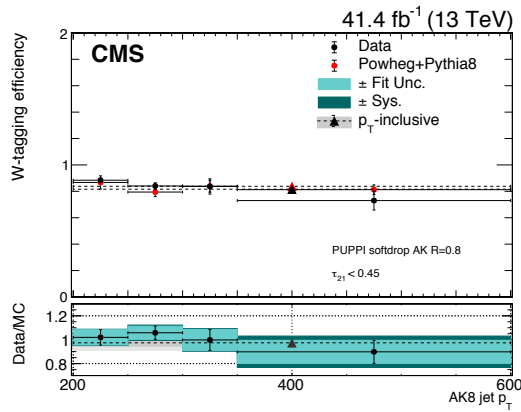


Figure 9.19: The W-tagging efficiency in data (black circles) and in simulation (red circles) as a function of jet p_T . The p_T -inclusive measurement is marked with triangles. The lower panel shows the efficiency in data divided by the efficiency in simulation, corresponding to the W-tagging uncertainty. The blue bands mark the fit and systematic uncertainties.

2570
 2571 increase as a function of p_T , we evaluate a p_T -dependent W-tagging scale factor uncertainty in the
 2572 following way: using signal Monte Carlo generated with two different shower generators, PYTHIA8
 2573 and HERWIG++, we compute the difference in tagging efficiency between the two samples at
 2574 low- p_T , where we have a real measurement in data, and compare that to the difference in tagging

Bin	$SF \pm \sqrt{\text{Stat.} + \text{Sys}_{\text{Generator}} + \text{Sys}_{\text{NNLO}}}$	$SF \pm \text{Total Unc.}$
200 - 250 GeV	$1.019 \pm \sqrt{0.064^2 + 0.005^2 + 0.022^2}$	1.02 ± 0.07
250 - 300 GeV	$1.058 \pm \sqrt{0.055^2 + 0.033^2 + 0.002^2}$	1.06 ± 0.06
300 - 350 GeV	$0.998 \pm \sqrt{0.087^2 + 0.035^2 + 0.007^2}$	1.00 ± 0.09
350 - 600 GeV	$0.898 \pm \sqrt{0.097^2 + 0.089^2 + 0.007^2}$	0.90 ± 0.13
≥ 200 GeV	$0.974 \pm \sqrt{0.029^2 + 0.055^2 + 0.015^2}$	0.97 ± 0.06

Table 9.4: The data to simulation scale factors in bins of jet p_T for a tagger based on PUPPI softdrop with a requirement of $\tau_{21} < 0.4$. All scalefactors are compatible with unity.

efficiency between the two at high- p_T . In other words, we take a double ratio

$$\sigma_{p_T, \text{Bin}=i} = \frac{\left(\frac{\epsilon_{\text{HERWIG}}}{\epsilon_{\text{PYTHIA}}}\right)_{p_T, \text{Bin}=i}}{\left(\frac{\epsilon_{\text{HERWIG}}}{\epsilon_{\text{PYTHIA}}}\right)_{p_T=300 \text{ GeV}}} - 1, \quad (9.3)$$

where $\sigma_{p_T, \text{Bin}=i}$ is the uncertainty on the scale factor on p_T bin i . In contrast with what was found for the τ_{21} -based tagger in Section 7.7.3, where this uncertainty grew logarithmically with p_T , we find that the corresponding double ratio stabilizes around 1 TeV in the high-purity category when using τ_{21}^{DDT} , and it can be approximated as a flat 28%. The uncertainty for the low-purity category is still well described by a logarithmic function. The uncertainty σ_{p_T} and resulting parametrization is shown in Figure 9.20. In my personal opinion, this way of defining

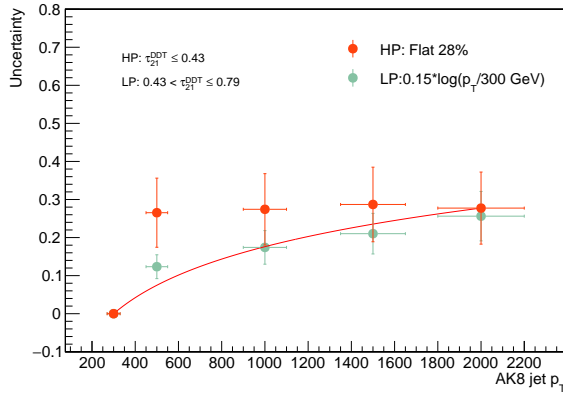


Figure 9.20: The parametrized uncertainty on the W-tagging efficiency scale factor as a function of the jet p_T .

an uncertainty is rather random and ad hoc. We already know there is a large difference in the modeling of substructure variables between generators, and there is no good reason to believe the difference between PYTHIA8 and HERWIG++ provides a reasonable description of the magnitude

of the uncertainty. In an analysis using two jets this is a very large and overly conservative systematic uncertainty that is impossible to constrain from data. I would rather prefer to use the measured scale factor uncertainties in data and extrapolate these, but the above method was used in previous searches and is therefore the method of choice for the Jet Physics Object Group at CMS. I will therefore continue using these uncertainties for the presented analysis, but will attempt to change this for future searches. In addition to measuring the dependence of the tagging efficiency on jet p_T , we also extract the change in softdrop jet-mass scale and resolution as a function of p_T . We find that the jet-mass scale in data divided by MC ranges between 0.5 and 2.5% for the p_T bins considered, and the jet-mass resolution varies between 4 and 10%, the latter measurement not being statistically significant as the uncertainties are large, around 10%. For this analysis, we therefore use a fixed uncertainty of 2 and 10% for the softdrop jet-mass scale and resolution, respectively, to cover any broadening or shift at high p_T not described by the simulation.

2598 9.7 The multidimensional fit

2599 The three-dimensional fit method is based on the assumption that the signal peaks in three
 2600 dimensions: the dijet invariant mass (M_{VV}), the groomed jet mass of the first jet (M_{jet1}), and
 2601 the groomed jet mass of the second jet (M_{jet2}), in order to extract a possible signal from the
 2602 three-dimensional M_{jet1} - M_{jet2} - M_{VV} (x,y,z) plane.

In order to obtain a complete three-dimensional model, four different types of probability density

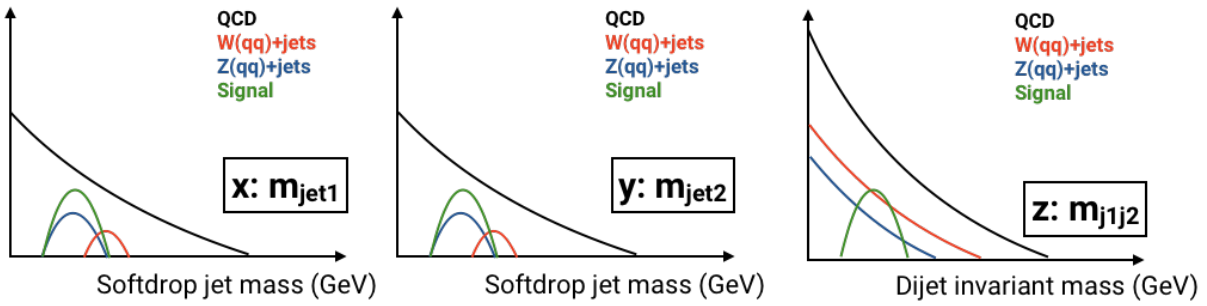


Figure 9.21: An illustration of the shape of the signal and the relative background contributions in the three dimensions $M_{jet1}(x)$, $M_{jet2}(y)$ and $M_{VV}(z)$.

2603 functions (PDF's) need to be derived:
 2604

- 2605 • **signal:** a PDF resonant in M_{jet1} , M_{jet2} and M_{VV} ,
- 2606 • **non-resonant background:** PDF for the dominant QCD multijet background. Non-
 2607 resonant in M_{jet1} , M_{jet2} and M_{VV} ,
- 2608 • **resonant background:** PDF describing of W+jets and Z+jets. Resonant in M_{jet1} and
 2609 M_{jet2} , but smoothly falling in M_{VV} , and
- 2610 • **alternative shapes:** five additional shape uncertainties for the non-resonant background.

2611 These are illustrated in Figure 9.21 and will be described in detail in the following.

2612 9.7.1 Modeling of the signal

2613 The signal shape in three dimensions is defined as the product of the resonance mass shape and
 2614 the jet mass shapes:

$$P_{sig}(M_{VV}, M_{jet1}, M_{jet2} | \theta(M_X)) = P_{VV}(M_{VV} | \theta_1(M_X)) \times P_{j1}(M_{jet1} | \theta_2(M_X)) \times P_{j2}(M_{jet2} | \theta_2(M_X)). \quad (9.4)$$

2615 The shapes for M_{VV} , M_{jet1} and M_{jet2} all depend on the hypothesized mass of the new particle
 2616 (M_X) and a set of parameters $\theta = (\theta_1, \theta_2)$ that in principle depend on M_X . The modeling of M_{jet}
 2617 is done separately for the high-purity and the low-purity category, while the modeling of M_{VV}
 2618 is done with no selection on τ_{21}^{DDT} applied (M_{VV} was found to be decorrelated from τ_{21}^{DDT} for
 2619 signal jets).

2620 The signal is parametrized by fitting the resonance mass and jet-mass line shapes for each
 2621 resonance mass value, extracting the fitted parameters and then interpolating these as a function
 2622 of the resonance-mass hypothesis. For the resonance mass M_{VV} , the sum of a crystal-ball
 2623 function and a Gaussian shape is used for each mass point, following the shapes used in Search
 2624 II. Figure 9.22 shows the derived parameters and interpolation as a function of resonance mass,
 and the final M_{VV} shapes as extracted from the parametrization are shown in Figure 9.23.

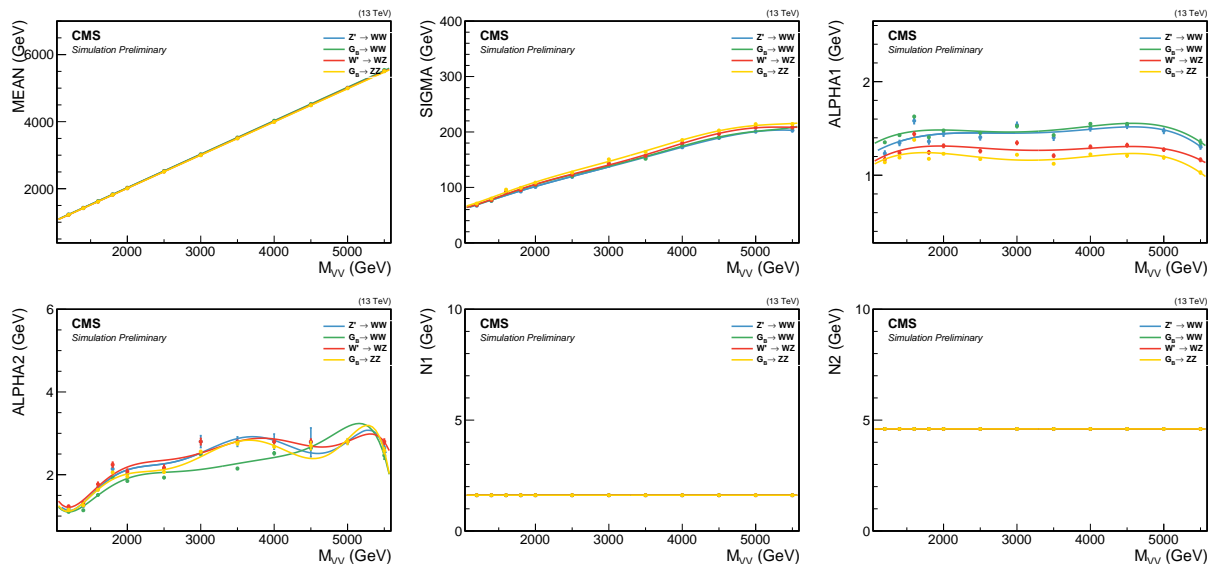


Figure 9.22: The interpolated fit parameters of a crystal-ball fit to the dijet invariant mass as a function of M_X . The small variations for ALPHA2 have been shown to have no effect on the overall modeling.

2625

2626 The same procedure is used to model the jet mass; the M_{jet} spectrum for each resonance mass

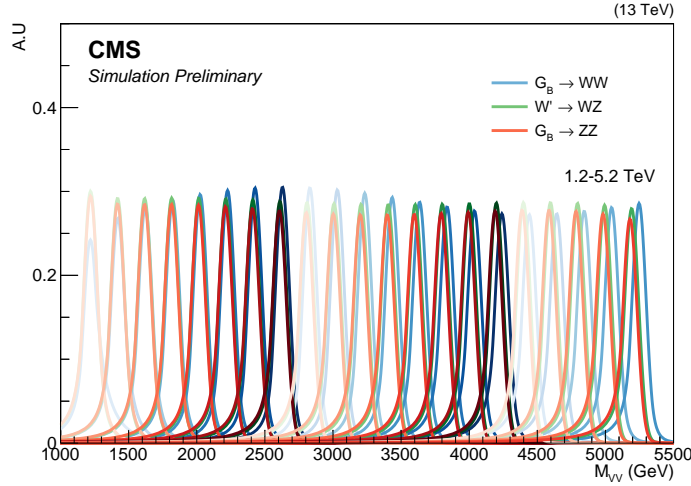


Figure 9.23: Final M_{VV} signal shapes extracted from the parametrization. Here for a G_{bulk} decaying to WW (blue), ZZ (red), and for a W' decaying to WZ (green).

hypothesis is fitted using a double Crystal-ball function, and the fitted parameters are extracted and interpolated as a function of the resonance mass. This is done separately for $M_{\text{jet}1}$ and $M_{\text{jet}2}$. The fitted parameters and interpolations are shown in Figure 9.24 for $M_{\text{jet}1}$, and the corresponding distributions for $M_{\text{jet}2}$ can be found in Appendix D.1. The final $M_{\text{jet}1}$ shapes, as extracted from

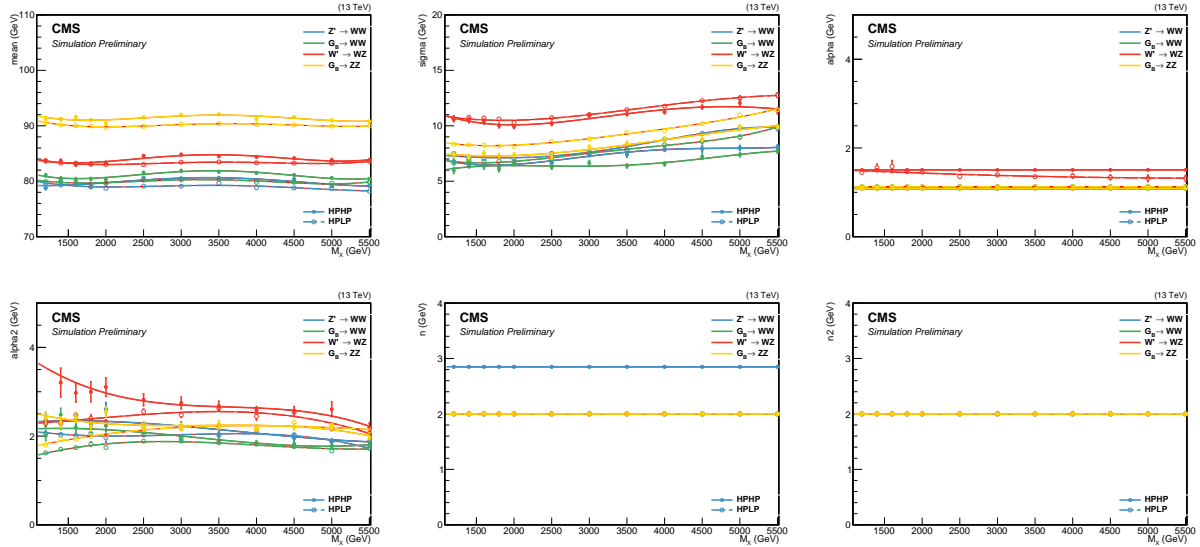


Figure 9.24: The interpolated double Crystal-ball parameters for the softdrop jet mass as a function of M_X . To improve the stability of the fit some parameters are set constant.

the parametrization are shown in Figures 9.25. Finally, the signal yield is parametrized as a

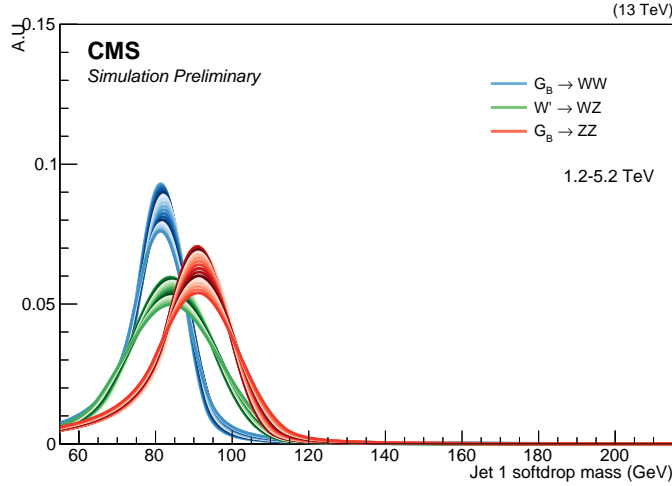


Figure 9.25: Final M_{jet} signal shapes extracted from the parametrization for a G_{bulk} decaying to ZZ (red), a G_{bulk} decaying to WW (blue), and for a W' decaying to WZ (green).

2631 function of the resonance mass. For each mass point M_X and each purity category, the signal
 2632 function of the resonance mass. For each mass point M_X and each purity category, the signal
 2633 yield per picobarn of cross section is calculated as the integral of the resulting Monte Carlo
 2634 histogram after all analysis selections have been applied. The yields are then interpolated as a
 function of M_X . The signal efficiency as a function of resonance mass is shown in Figure 9.26.

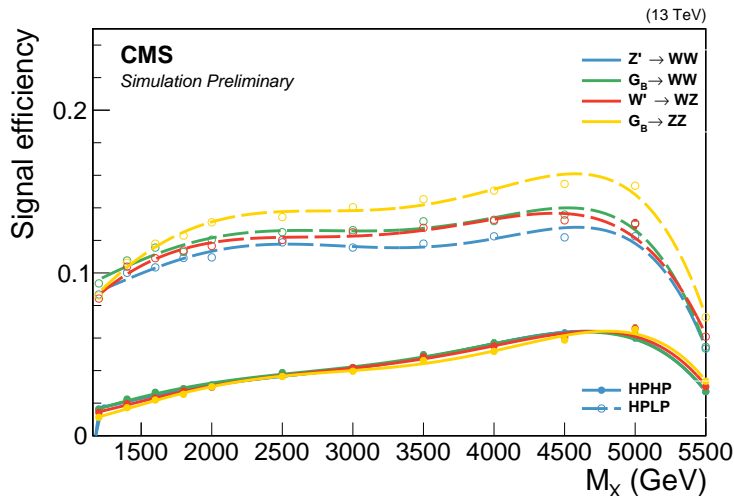


Figure 9.26: Signal efficiency as a function of resonance mass.

2636 9.7.2 Modeling of the non-resonant background

2637 In order to model the QCD multijets background in the three-dimensional M_{VV} - M_{jet1} - M_{jet2}
 2638 plane, we use the following conditional product:

$$P(M_{VV}, M_{jet1}, M_{jet2}) = P_{VV}(M_{VV}|\theta_1) \times P_{cond,1}(M_{jet1}|M_{VV}, \theta_2) \times P_{cond,2}(M_{jet2}|M_{VV}, \theta_2). \quad (9.5)$$

2639 This probability density requires a computation of the conditional two-dimensional shapes of
 2640 M_{jet1} or M_{jet2} , given M_{VV} , as well as a one dimensional shape of the M_{VV} distribution. The
 2641 reason for requiring a conditional jet-mass shape, is due to the high correlation between the jet
 2642 mass and the dijet invariant mass for quark and gluon jets. The modeling is done separately for
 2643 the high-purity and the low-purity category.

2644 The following fit ranges are used for the three axes: the jet masses M_{jet1} and M_{jet2} are fitted
 2645 from 55 to 215 GeV using 2 GeV bins, and the dijet invariant mass M_{VV} is fitted from 1126 to
 2646 5500 GeV. The lower M_{VV} bound is chosen to avoid complications in the fitting procedure due
 2647 to trigger turn-on effects, while the upper M_{VV} bound is chosen by considering the highest dijet
 2648 invariant mass event found in data. For M_{VV} , the “dijet binning”, corresponding to the dijet
 2649 mass resolution, is used. In units of GeV, the binning is as follows:

2650
 2651 Dijet binning = 1126, 1181, 1246, 1313, 1383, 1455, 1530, 1607, 1687, 1770, 1856, 1945,
 2652 2037, 2132, 2231, 2332, 2438, 2546, 2659, 2775, 2895, 3019, 3147, 3279, 3416, 3558, 3704,
 2653 3854, 4010, 4171, 4337, 4509, 4686, 4869, 5058, 5253, 5500.

2654
 2655 The background model is built starting from simulation using a “forward-folding” approach. To
 2656 build the one-dimensional template for the dijet invariant mass, $P_{VV}(M_{VV}|\theta_1)$, a 1D Gaussian
 2657 kernel is built starting from generator level quantities where, for each MC event, a Gaussian con-
 2658 tributes to the total one-dimensional probability density function. To build the two-dimensional
 2659 conditional templates, $P_{cond,1}(M_{jet1}|M_{VV}, \theta_2)$ and $P_{cond,2}(M_{jet2}|M_{VV}, \theta_2)$, a two-dimensional
 2660 Gaussian kernel is created for each MC event, where each 2D kernel contributes to the to-
 2661 tal conditional PDF.

2662 In order to define the Gaussian kernel, the dijet invariant mass scale and resolution, and the
 2663 softdrop jet-mass scale and resolution, must be derived. This is done by comparing the generated
 2664 jet-mass $M(\text{gen})$ to the reconstructed jet-mass $M(\text{reco})$. The M_{jet} and M_{VV} scale and resolution
 2665 are extracted from a Gaussian fit to either $M_{jet}(\text{reco})/M_{jet}(\text{gen})$ or $M_{VV}(\text{reco})/M_{VV}(\text{gen})$, in
 2666 bins of generator-level jet p_T . Figure 9.27 shows the fit to $M_{jet}(\text{reco})/M_{jet}(\text{gen})$ (left) and
 2667 $M_{jj}(\text{reco})/M_{jj}(\text{gen})$ (right) for an arbitrary p_T bin. The mean of the Gaussian yields the jet-mass
 2668 scale and the width yields the jet-mass resolution, for a given bin in generator-level jet p_T .

The M_{jet} and M_{VV} jet mass scale and resolution as a function of generator jet p_{T} is shown in

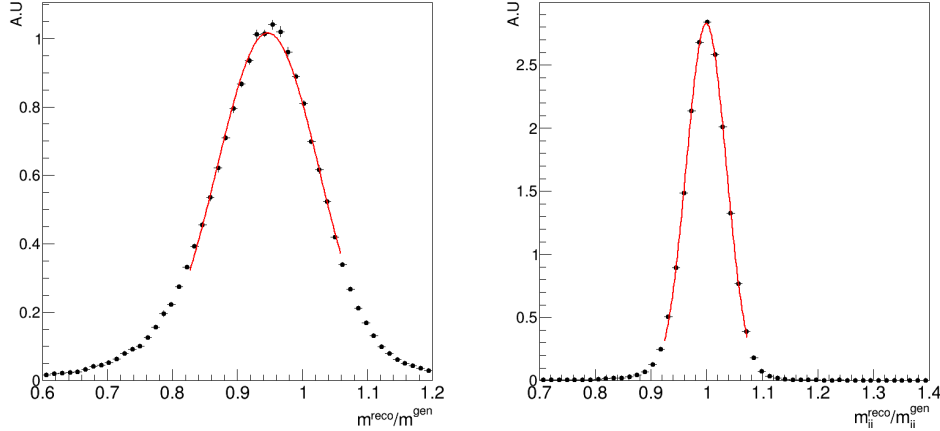


Figure 9.27: Left: fit to $M_{\text{jet}}(\text{reco})/M_{\text{jet}}(\text{gen})$. Right: fit to $M_{\text{VV}}(\text{reco})/M_{\text{VV}}(\text{gen})$. The mass resolution is taken as the width of the fitted Gaussian, while the Gaussian mean yields the mass scale.

2669
2670 Figure 9.28, and the total projection of these resolution functions are shown in Figure 9.29.
2671 The jet-mass and the dijet invariant mass scale and resolution are then used to populate the
2672 conditional 2D histogram as follows. Each generated event is smeared with a 2D Gaussian kernel
2673 of the form

$$k(M_{\text{jet}}, M_{\text{VV}}) = \frac{w_i}{\sqrt{2\pi} r_{M_{\text{VV}},i} \cdot r_{M_{\text{jet}},i}} \exp \left(-\frac{1}{2} \left(\frac{M_{\text{VV}} - s_{M_{\text{VV}},i}}{r_{M_{\text{VV}},i}} \right)^2 - \frac{1}{2} \left(\frac{M_{\text{jet}} - s_{M_{\text{jet}},i}}{r_{M_{\text{jet}},i}} \right)^2 \right), \quad (9.6)$$

2674 where s_i, r_i are the scale and the resolution derived in the previous step and w_i is the event weight
2675 product due to effects such as PU-reweighting and cross-sections. The resulting kernel values are
2676 then filled into a 2D histogram. This procedure is performed separately for $M_{\text{jet}1}$ and $M_{\text{jet}2}$. To
2677 build the one-dimensional template for the dijet invariant mass, the same procedure as above is
2678 used with the exception that the smearing is done with a one-dimensional Gaussian kernel only
2679 depending on M_{VV} . The three templates are then added together to form a three-dimensional
2680 PDF, and this PDF is fitted to QCD MC in order to remove any residual bias. The result is a
2681 smooth shape, covering the entire search range, that can be used in place of the prediction from
2682 simulation.

2683 As the high-purity category is limited by statistics, we instead build this template starting
2684 from the low-purity templates. This is done by fitting the low-purity 3D template, obtained using
2685 the method described above, to QCD MC in the high-purity category. Figure 9.30 shows the final

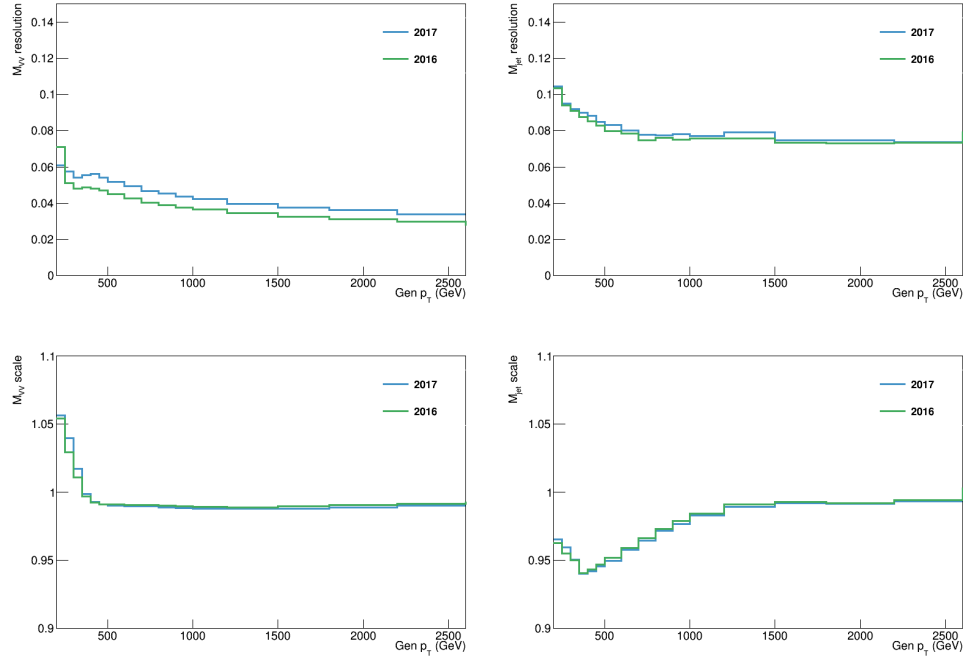


Figure 9.28: The M_{VV} resolution (top left) and scale (bottom left), and the M_{jet} resolution (top right) and scale (bottom right) as a function of generator-level jet p_T .

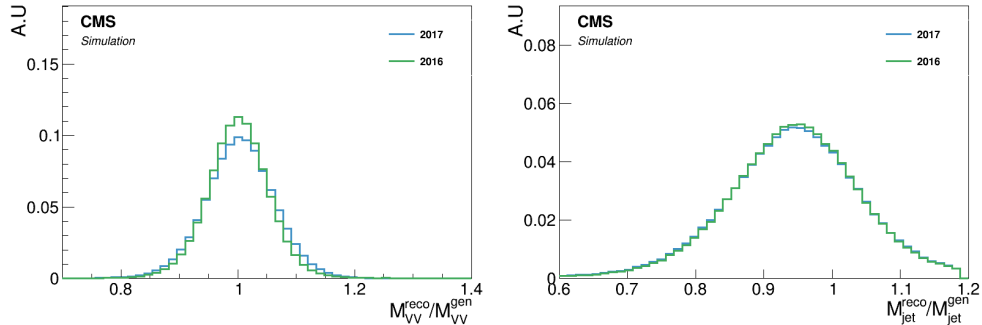


Figure 9.29: Projections of the resolution functions for all generator-level jet p_T bins for M_{VV} (left) and M_{jet} (right).

2686 templates (solid lines) together with the QCD MC (data points) derived from the 2017 MC in
 2687 the low-purity (top) and high-purity (bottom) category. Good agreement between simulation and
 2688 templates in all three dimensions is observed, within statistical uncertainties. The corresponding
 2689 distributions for 2016 MC can be found in Appendix D.2.

2690 In order to validate the kernel-transfer method, we check that we can fit a higher-statistics

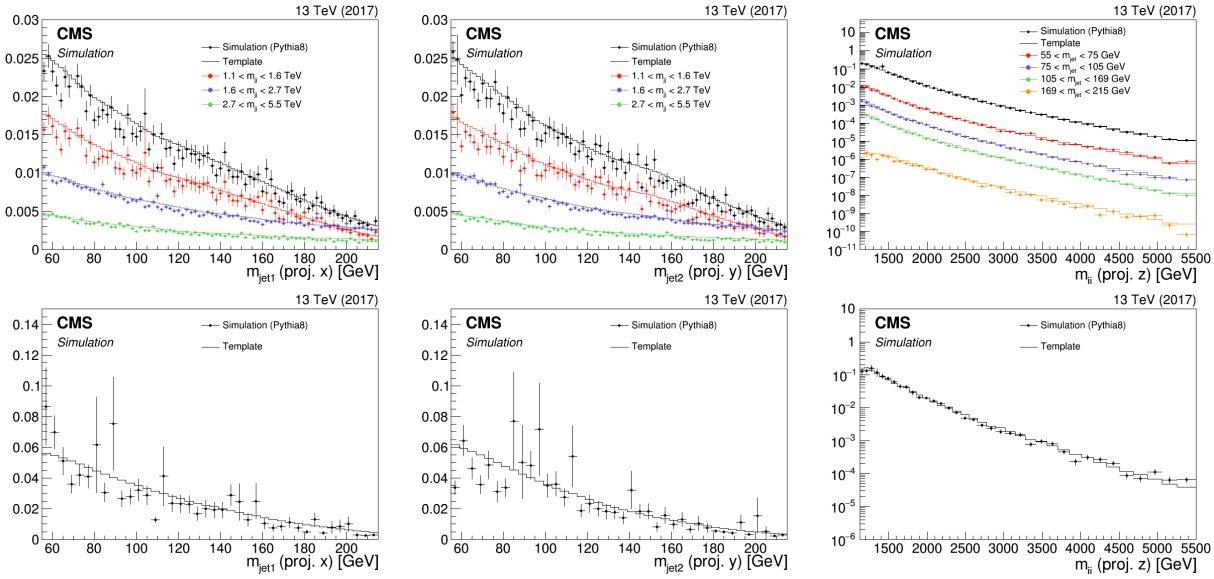


Figure 9.30: Comparison between QCD MC simulation (markers) and kernels derived from generator-level quantities (lines) for the HP (top) and LP (bottom) categories using 2017 MC. The kernels are shown for $M_{\text{jet}1}$ (left), $M_{\text{jet}2}$ (middle) and M_{VV} (right).

2691 high-purity region by loosening the τ_{21}^{DDT} cut to 0.49. This results in 12 times more background
 2692 events, and should uncover whether any degeneracy is present in the fits themselves and whether
 2693 the low-purity kernel indeed is capable of modeling the high-purity region. The resulting kernel-
 2694 versus-MC spectra are shown in Figure 9.31. Good closure is observed in all three dimensions,
 2695 demonstrating that the LP kernels adapt well to the HP MC data points even when statistics are
 sufficient, and we therefore consider the method to be sound.

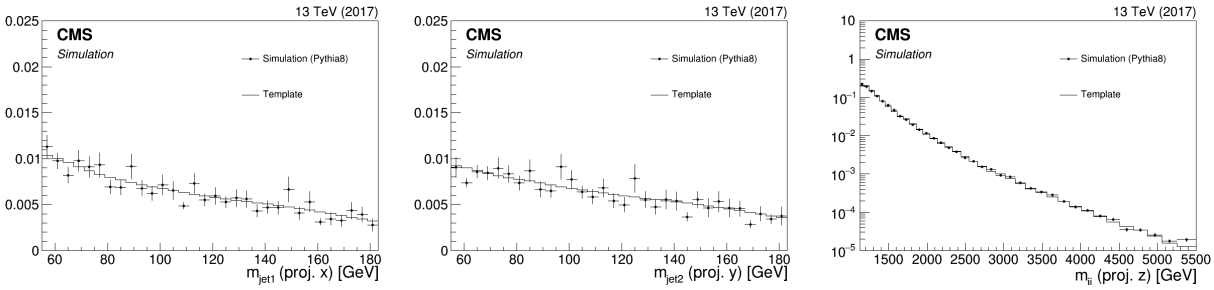


Figure 9.31: Comparison between QCD MC simulation (markers) and kernels derived from generator-level quantities (lines) in the HP category, using a looser cut on τ_{21}^{DDT} .

2697 9.7.3 Modeling of the resonant background

In addition to the QCD multijet background, there are a few sub-dominant processes which contain one real vector boson and at least one QCD-jet that must be accounted for. These are W+jets, Z+jets and events from $t\bar{t}$ processes. These events are resonant in M_{jet1} and M_{jet2} and must therefore be treated differently than the non-resonant QCD background. Figure 9.32 shows the projections on M_{jet1} (left), M_{jet2} (middle) and M_{VV} (right) for the resonant backgrounds under consideration. As the jets are randomly sorted, each jet mass distribution contains two

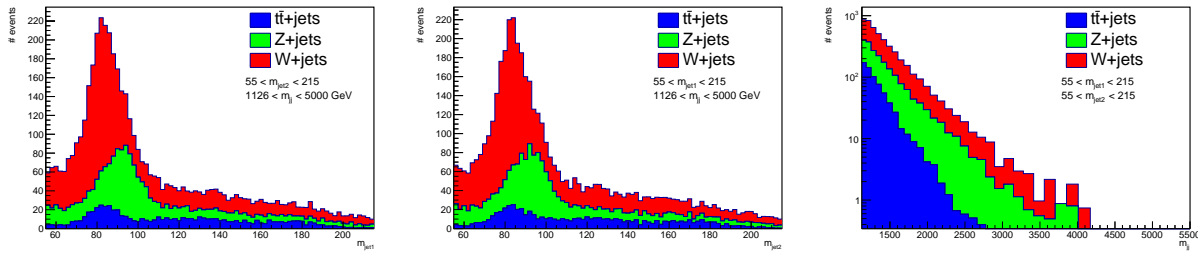


Figure 9.32: Projections of the sub-dominant backgrounds on the jet mass axes M_{jet1} (left) and M_{jet2} (middle), as well as on the dijet invariant mass M_{VV} (right). Here in the low-purity category.

contributions: a resonant part consisting of real vector-boson jets, peaking around the W or Z boson mass; and a non-resonant part composed of jets originating from a quark or a gluon, similar to the QCD-multijets background. These two contributions are modeled separately since we know that the non-resonant part of the jet mass spectrum is correlated with the dijet invariant mass (as was the case for QCD), while the resonant part is not (as was the case for the signal PDF). We additionally want to encode the information that these backgrounds in reality have only one real vector boson and so only peak in one jet-mass dimension, by requiring the PDFs to consist of a resonant part on one axis, and a non-resonant part on the other axis. A three-dimensional PDF for the resonant backgrounds is built as a product of three one-dimensional PDFs as follows:

$$P_{res}(M_{jet1}, M_{jet2}, M_{VV}) = P_{VV}(M_{VV}) \times P_{jet1}(M_{jet1}, M_{jet2}) \times P_{jet2}(M_{jet2}, M_{jet1}), \quad (9.7)$$

where

$$P_{jet1}(M_{jet1}, M_{jet2}) = f \times R(M_{jet2}) \times P_{res,1}(M_{jet1}) + (1 - f)P_{non-res,1}(M_{jet1}) \text{ and} \quad (9.8)$$

$$P_{jet2}(M_{jet2}, M_{jet1}) = (1 - f) \times R(M_{jet1}) \times P_{res,2}(M_{jet2}) + fP_{non-res,2}(M_{jet2}). \quad (9.9)$$

2698 Here, $R(M_{\text{jet}})$ parametrizes the correlation between $M_{\text{jet}1}$ and $M_{\text{jet}2}$ and f is a fit parameter
 2699 that is used to adjust the fraction of real vector boson jets in $M_{\text{jet}1}$ compared to $M_{\text{jet}2}$. Its value
 2700 can vary by 10% around $f = 0.5$, the expected median when using a random jet sorting. $P_{\text{res},1}$
 2701 and $P_{\text{res},1}$ are PDFs describing the resonant part of the jet mass spectrum, while $P_{\text{non-res},1}$ and
 2702 $P_{\text{non-res},2}$ describe the non-resonant part. The functional form of these will be described below.
 2703 As the contribution of background from $t\bar{t}$ is much smaller than the one coming from V+jets
 2704 (less than 2%), this background is modeled together with the W+jets contribution. Therefore
 2705 only two PDFs are built for the resonant background: one for the W+jets and $t\bar{t}$ processes, and
 2706 one for the Z+jets process.

2707 The available MC statistics in the high-purity category are very low and therefore the parametriza-
 2708 tion of the resonant background is done for the low-purity category only, and the resulting shapes
 2709 are then used for both purity categories. The uncertainties for the different purity categories are,
 2710 however, included as separate nuisance parameters in the fit.

2711 The non-resonant M_{VV} PDF is constructed using the same kernel approach as is used to
 2712 model the QCD multijet background with one minor difference: due to the low statistics in the
 2713 high- M_{VV} tail, an additional smoothing of the jet mass tail using a leveled exponential of the
 2714 form

$$\frac{dN}{dm_{jj}} = \frac{P_0(1 - m_{jj}/s)^{P_1}}{(m_{jj}/s)^{P_2}} \quad (9.10)$$

2715 is performed. Here, s is the center-of-mass energy. The function is fitted to the spectrum starting
 2716 from a dijet mass of 1.1 (2.1) TeV for the high-purity (low-purity) category. Two uncertainties
 2717 on the shape are added in order to accommodate possible MC mis-modeling due to higher order
 2718 QCD and electroweak corrections: one proportional to M_{VV} and one proportional to $1/M_{\text{VV}}$. The
 2719 resulting M_{VV} kernels (solid lines) for the W+jets background are shown in Figure 9.33 and are
 2720 compared to MC simulation (markers). The blue line corresponds to the nominal shape, while the
 2721 red and green lines correspond to the uncertainties proportional to M_{VV} and $1/M_{\text{VV}}$, respectively.
 2722 The corresponding distributions for the Z+jets background are shown in Appendix D.3.

As mentioned above, the modeling of the M_{jet} spectrum is split into two different PDFs: one
 2723 describing the resonant and one describing the non-resonant part. We distinguish between the two
 2724 by requiring the resonant contribution to consist of jets matched to a generated boson within a
 2725 cone of $\Delta R = 0.8$. A double-sided crystal-ball function is then fitted to the resonant spectrum for
 2726 W+jets and Z+jets separately. The uncertainty on the mean and width of the M_{jet} distribution
 2727 are fully correlated between signal and the resonant background, as these uncertainties affect
 2728 all jets generated by a real vector bosons in the same way. This effectively gives us a way of
 2729 constraining these parameters directly from data. The parametrization of the resonant part of the

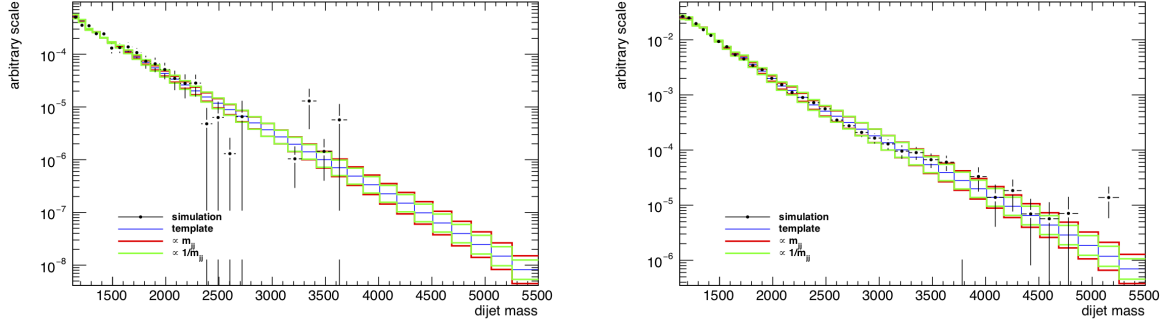


Figure 9.33: One-dimensional M_{VV} kernels (solid line) compared to MC (markers) for the W+jets background in the HP (left) and LP (right) categories. The blue line corresponds to the nominal shape, while the red and green lines correspond to uncertainties proportional to M_{VV} and $1/M_{VV}$, respectively.

jet mass spectrum for M_{jet1} is shown in Figure 9.34 for W+jets and $t\bar{t}$ (left), and Z+jets (right). The small enhancement around 170 GeV is caused by fully merged top jets, but is so small (< 2% in the low-purity and < 0.5% in the high-purity category) that we do not take it into account in the final PDF. The non-resonant part of the V+jets background is modeled using a simple

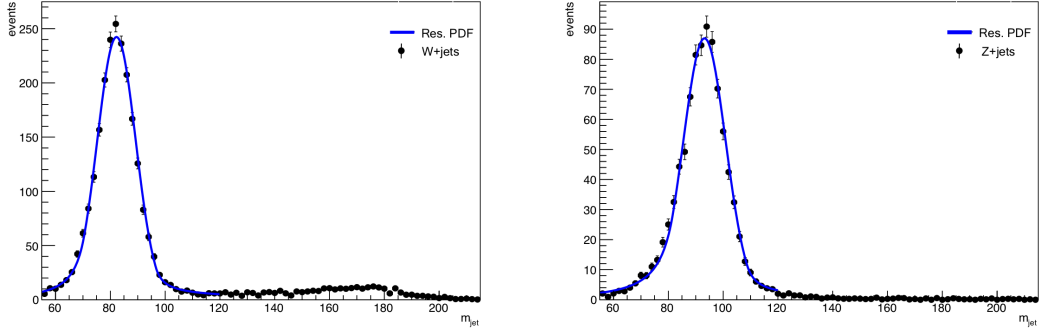


Figure 9.34: Fit to the resonant part of the V+jets and $t\bar{t}$ spectrum for W+jets and $t\bar{t}$ (left) and Z+jets (right).

Gaussian fit to the spectrum of jets not matched to real vector bosons, as shown in Figure 9.35. For the resonant modeling, correlations between the jet mass M_{jet} and dijet invariant mass M_{VV} have been found small enough to be neglected; the jet mass spectrum does not, within statistical uncertainties, depend on the jet p_T . However, there is a strong correlation between the softdrop jet mass of each jet due to the fact that when one of the two jets originate from a real boson peaking around the V mass, the other is bound to be a quark jet. Therefore, the fraction of real

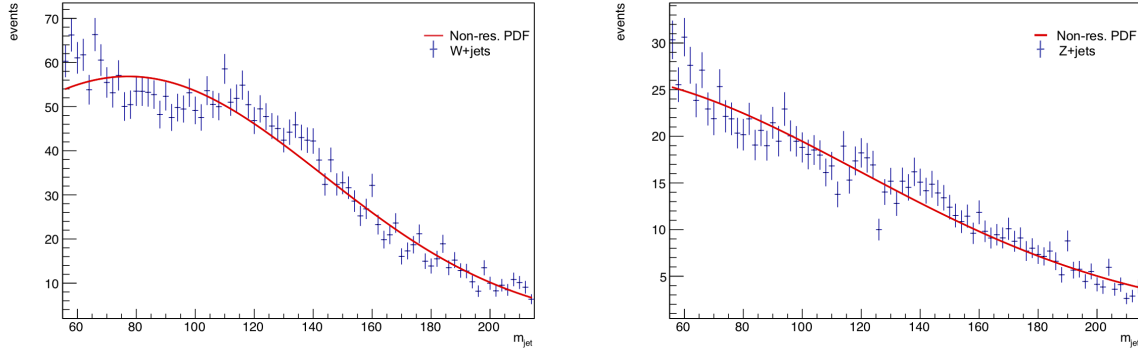


Figure 9.35: Fit to the non-resonant part of the $V+jets$ and $t\bar{t}$ spectrum for $W+jets$ and $t\bar{t}$ (left) and $Z+jets$ (right).

boson jets contained in M_{jet1} affects the fraction of real boson jets in M_{jet2} . To account for this, the fraction of real V jets versus quark or gluon jets is parametrized as a function of the jet mass. As the jets are randomly sorted, we define the parametrization as

$$R(M_{jet}) = \frac{N_{res,jet1}(M_{jet2}) + N_{res,jet2}(M_{jet1})}{N_{non-res,jet1}(M_{jet2}) + N_{non-res,jet2}(M_{jet1})}, \quad (9.11)$$

where $N(M_{jet})$ denotes the number of events within a given M_{jet} window. The resulting ratio is then fitted with a polynomial function, as shown in Figure 9.36. As a closure test, the three-

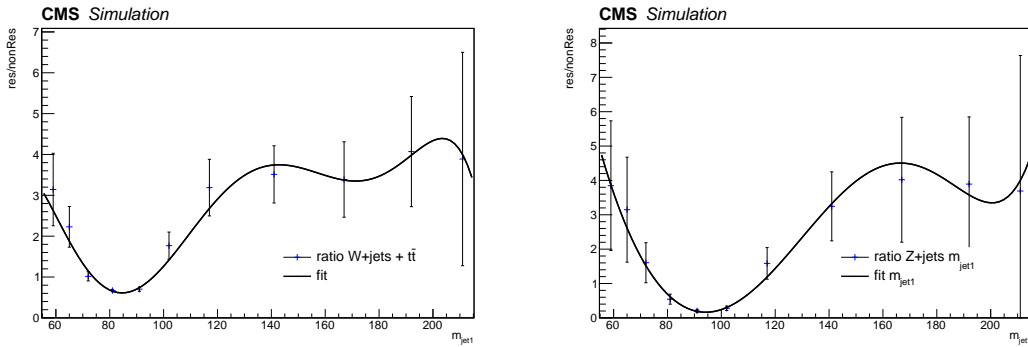


Figure 9.36: Ratio of resonant to non-resonant events in $W+jets$ (left) and $Z+jets$ (right) as a function of jet mass.

dimensional kernel as defined in Equation 9.7 is fitted to the $V+jets$ and $t\bar{t}$ simulation. Figure 9.37 shows the fitted kernel (red) together with the MC data points (black markers) in the low-(top) and high-purity (bottom) categories. Mostly good agreement is observed along all dimensions,

2728 with some deviations in the very high M_{VV} tail in the high-purity category. This is, however,
 2729 a region populated with very few events and is completely overwhelmed by the QCD multijets
 background that has the same shape.

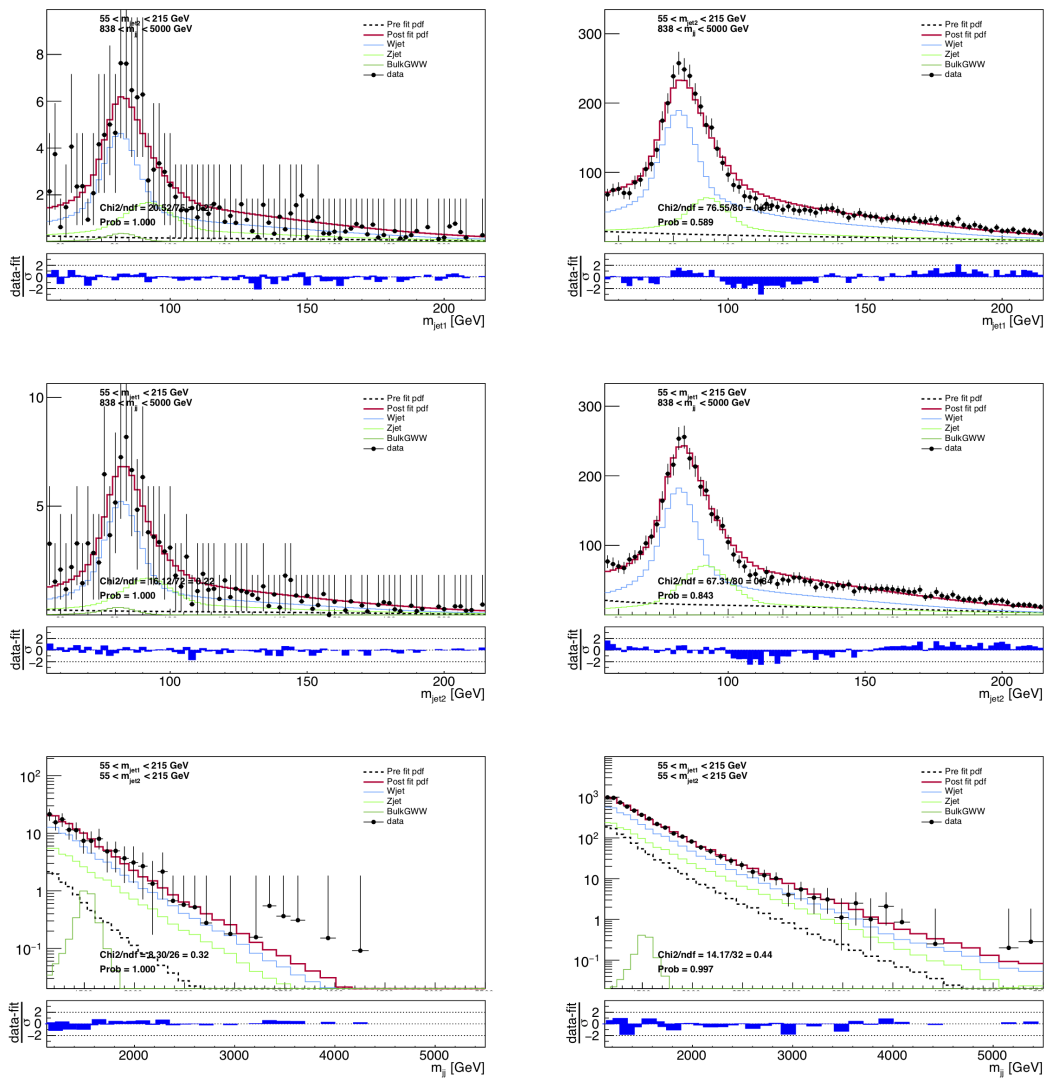


Figure 9.37: Fits using the complete resonant background model (red line) to the V+jets MC simulation (black markers) for the high- (left) and low-purity (right) category. Here for $M_{\text{jet}1}$ (top), $M_{\text{jet}2}$ (middle) and M_{VV} (bottom).

²⁷³¹ **9.8 Systematic uncertainties**

²⁷³² The background estimate for each signal mass hypothesis is obtained by fitting the signal and
²⁷³³ background three-dimensional probability density functions obtained above, to the observed
²⁷³⁴ data in each analysis category. We follow the modified frequentist prescription (CLs) criterion,
²⁷³⁵ evaluated using asymptotic expressions described in Ref. [72]. Systematic uncertainties are
²⁷³⁶ treated as nuisance parameters and profiled in the statistical interpretation using log-normal
²⁷³⁷ priors, while Gaussian priors are used for shape uncertainties. The uncertainties entering the fit
are listed in Table 9.5. Here, V+jets ratio describes the ratio between W+jets and Z+jets events

Source	Relevant quantity	HPHP unc. (%)	HPLP unc. (%)
PDFs	Signal yield	3	
W-tagging efficiency	Signal+ V+jets yield	25 (21)	13 (11)
W-tagging p_T -dependence	Signal+ V+jets yield	5-60	5-44
Integrated luminosity	Signal+ V+jets yield	2.3 (2.6)	
QCD normalization	Background yield	50	
V+jets normalization	Background yield	10	
V+jets ratio	Migration	10	
PDFs	Signal M_{VV}/M_{jet} shape	< 1	
Jet energy scale	Signal M_{VV} shape	2	
Jet energy resolution	Signal M_{VV} shape	5	
Jet mass scale	Signal + V+jets M_{jet} shape	1	
Jet mass resolution	Signal + V+jets M_{jet} shape	8	
QCD HERWIG++	QCD shape	33	
QCD MADGRAPH+PYTHIA8	QCD shape	33	
p_T -variations	QCD shape	33	
Scale-variations	QCD shape	33	
High- M_{jet} turn-on	QCD shape	33	
p_T -variations	V+jets M_{VV} shape	33	

Table 9.5: Summary of the systematic uncertainties and the quantities they affect. Numbers in parenthesis correspond to uncertainties for the 2016 analysis, when these differ from 2017.

²⁷³⁸ and is allowed to float by 10%. The W-tagging efficiency scale factor is fully anti-correlated
²⁷³⁹ between the HP and LP categories (3–10%), and fully correlated between signal and +jets. The
²⁷⁴⁰ p_T -dependence uncertainty of the scale factor arises from the extrapolation of the W-tagging
²⁷⁴¹ efficiency scale factors, which are measured in $t\bar{t}$ events where the jet has a p_T around 200 GeV,
²⁷⁴² towards higher transverse momenta. This uncertainty is estimated in signal MC and is based on
²⁷⁴³ the difference in tagging efficiency between PYTHIA and HERWIG++ as a function of p_T relative
²⁷⁴⁴ to the difference at 200 GeV. This is considered as correlated between the τ_{21}^{DDT} categories and is
²⁷⁴⁵ defined in Section 9.6.2. The shape uncertainties on M_{jet} are considered fully correlated between
²⁷⁴⁶ signal and V+Jets, allowing for the data to constrain these parameters. These affect the mean
²⁷⁴⁷ signal and V+Jets, allowing for the data to constrain these parameters. These affect the mean

2748 and the width of the signal and V+jets PDFs.

2749 Uncertainties on the background shape are added as alternate PDFs to the fit through vertical
2750 template morphing. This creates nuisance parameters for each shape that simultaneously affect all
2751 three dimensions. We define five shape nuisance parameters in total. The first effect corresponds
2752 to a variation of the underlying transverse momentum spectrum and the corresponding template is
2753 obtained by simultaneously varying jet masses and M_{VV} by a quantity proportional to M_{VV} and
2754 M_{jet} . The second effect is a variation of the scale and is taken into account through an alternate
2755 shape obtained by simultaneously varying the jet masses and M_{VV} by a quantity proportional
2756 to $1/M_{VV}$ and $1/M_{jet}$. Three additional alternate shapes that simultaneously affect resonance
2757 mass and jet groomed mass are also added in order to take into account differences in MC
2758 generation and modeling of parton shower. Since the choice of QCD MC used to generate the
2759 nominal template is random, we insert additional templates derived using all available QCD
2760 MC: HERWIG++, MADGRAPH+PYTHIA8 and POWHEG. This allows us to include all background
2761 knowledge we have available into the fit. Finally, in order to account for an expected M_{VV}
2762 turn-on in the extreme large- M_{jet} (> 175 GeV) and low- M_{VV} (< 1200 GeV) region, an additional
2763 shape uncertainty parametrizing any discrepancy between the three-dimensional template and
2764 QCD MC is added to the fit. Note that the latter shape uncertainty only affects the region
2765 above $M_{jet} > 175$ GeV and below $M_{VV} < 1200$ GeV, far from where signal is expected. The
2766 above nuisance parameters are assigned very large pre-fit values, allowed to float within 33–50%,
2767 effectively allowing the simulation enough flexibility to adapt to data. The alternate shapes
2768 described above are shown in Figure 9.38.

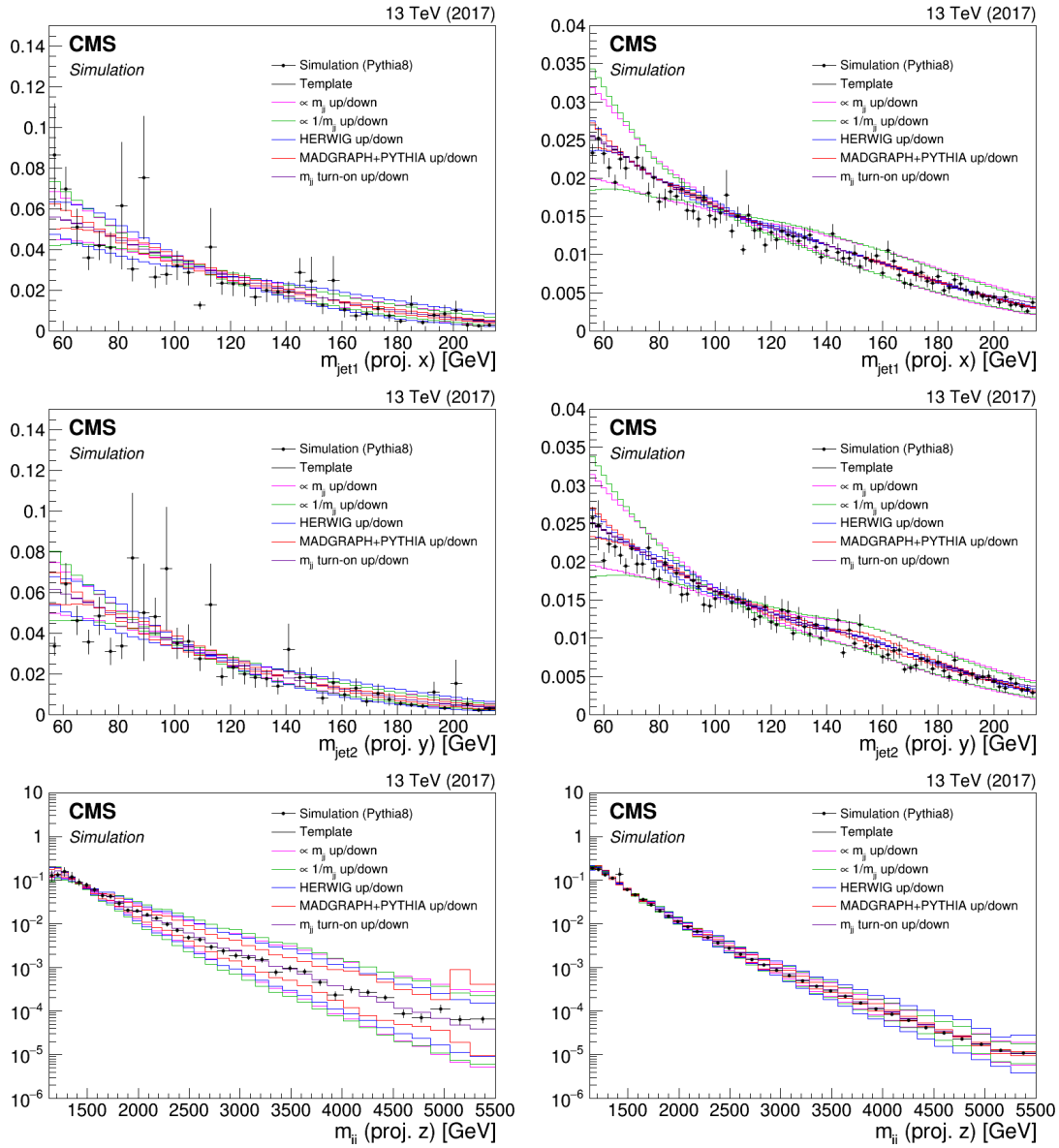


Figure 9.38: The nominal MC data (markers) and smooth nominal kernel obtained from PYTHIA8 (black line), together with the five alternate shapes added to the fit as nuisance shape parameters. Here for the high- (left) and low-purity (right) categories.

2769 9.9 Background model validation

2770 In order to test the robustness of the fit, several checks are performed in simulation and in a data
 2771 control region before unblinding the data signal region.

2772 **9.9.1 Variations of QCD multijet predictions**

2773 First, we check that the main three-dimensional background template (generated starting from
 2774 QCD PYTHIA8 MC) can fit predictions from alternate QCD multijets samples in order to
 2775 demonstrate that systematic uncertainties in the modeling of parton showers are covered by
 2776 the relevant nuisance parameters. Fits to three different QCD samples are compared: PYTHIA8
 2777 (nominal), HERWIG++ (alternate shape 1) and MADGRAPH+PYTHIA8 (alternate shape 2). To
 2778 ensure a smooth data distribution not affected by low statistics present in the MC spectra, we
 2779 generate a toy dataset from the three-dimensional templates rather than using MC events directly.
 2780 The post-fit distributions after fitting each toy is shown in Figures 9.39-9.41 for the high- (left)
 2781 and low-purity (right) category. The fit quality of these are quantified using a goodness-of-fit
 2782 (based on a saturated model, which is valid when data are non-Gaussian), shown in Figure 9.42.
 2783 The test statistics are Gaussian distributed and the toy dataset is in good agreement with the
 2784 background only hypothesis, demonstrating the fits ability to account for differences in QCD
 2785 multijet predictions.

2786 **9.9.2 Fit to data control region**

2787 To validate the method in data, the 3D fit procedure is tested in a data control region where
 2788 both jets are required to have $0.43 < \tau_{21}^{DDT} \leq 0.79$, the so-called LPLP category. The templates
 2789 are built following the procedure described in Section 9.7.2. In this category, the contribution of
 2790 the resonant background is negligible with respect to the dominant QCD multijet background
 2791 and is removed from the fit. The post-fit distributions in the data control region are shown in
 2792 Figures 9.43–9.45 for different jet mass and dijet invariant mass bins. A goodness-of-fit check is
 2793 performed, shown on the left plot in Figure 9.46, and we again find that the toys are Gaussian
 2794 distributed and the LPLP data is in good agreement with the background-only hypothesis. The
 2795 post-fit value and uncertainty of each nuisance parameter involved in the fit is also studied, where
 2796 deviations from the pre-fit value is quantified through the “pull”, defined as $p_\theta = (\theta - \theta_{in})/\sigma_\theta$,
 2797 where, θ and σ_θ are the post-fit value of the nuisance parameter and its uncertainty, and θ_{in} the
 2798 pre-fit value. The pulls for all nuisance parameters are shown in the right plot in Figure 9.46,
 2799 where the uncertainty is defined as the ratio between the post- and pre-fit uncertainties. The

2800 post-fit values show a reasonable deviation from the chosen pre-fit values of 0. The uncertainties
 2801 are strongly constrained by data, as expected given the large pre-fit uncertainty assigned to let
 2802 the shapes adjust to the real data. In addition to the goodness-of-fit check in the LPLP data
 2803 sideband region, we perform the same test on the data signal region. This is shown in Figure 9.47.
 2804 Good agreement between the observed fit result in data and the background only hypothesis from
 2805 MC simulation is observed.

2806 9.9.3 Bias test in pseudodata

2807 Finally, we study whether there is any bias on the extracted signal rate due to the background
 2808 model. A $G_{\text{bulk}} \rightarrow WW$ signal is injected on top of a toy dataset generated under either the
 2809 PYTHIA8 or the HERWIG++ template, and is fit using the full background model. The test is done
 2810 for four different signal mass values and with a signal strength chosen such that it corresponds
 2811 to a significance of 4-4.5 standard deviations for each signal mass which is tested. An example
 2812 distribution after injecting a 3 TeV signal is shown in Figure 9.48 for the high-purity category. For
 2813 each tested signal mass point, a signal plus background fit is performed. The signal normalization
 2814 is free to float in the fit, which determines the signal strength μ and its uncertainty σ_μ . For
 2815 each toy, the pull of the signal strength $p_\mu = (\mu - \mu_{in})/\sigma_\mu$ is calculated, where μ_{in} is the pre-fit
 2816 value of the signal strength. The procedure is repeated ~ 1000 times for each category, and the
 2817 cumulative distribution of the pulls is fitted with a Gaussian function to determine the mean and
 2818 its uncertainty, which represent the bias. This is shown in Figure 9.49. Ideally, the distribution
 2819 should be Gaussian distributed with a mean around 0 and a width of 1. The bias for a toy
 2820 dataset generated under the PYTHIA8 (red markers) or the HERWIG++ (black markers) template,
 2821 as shown in Figure 9.50, is consistently below 50% and therefore no additional correction/bias
 2822 term is introduced. In addition, we calculate the pull for each nuisance parameter and fit the
 2823 cumulative distribution with a Gaussian, in order to determine the mean and its uncertainty,
 2824 representing the shift of the parameters θ with respect to the pre-fit values. The results are shown
 2825 in Figure 9.51. The mean of the cumulative distributions of the pulls is found to be zero for all
 2826 nuisance parameters, as expected. The width of the distribution can range from very small values
 2827 to about 1, depending on the assigned pre-fit uncertainty and the power of the data to constrain
 2828 it.

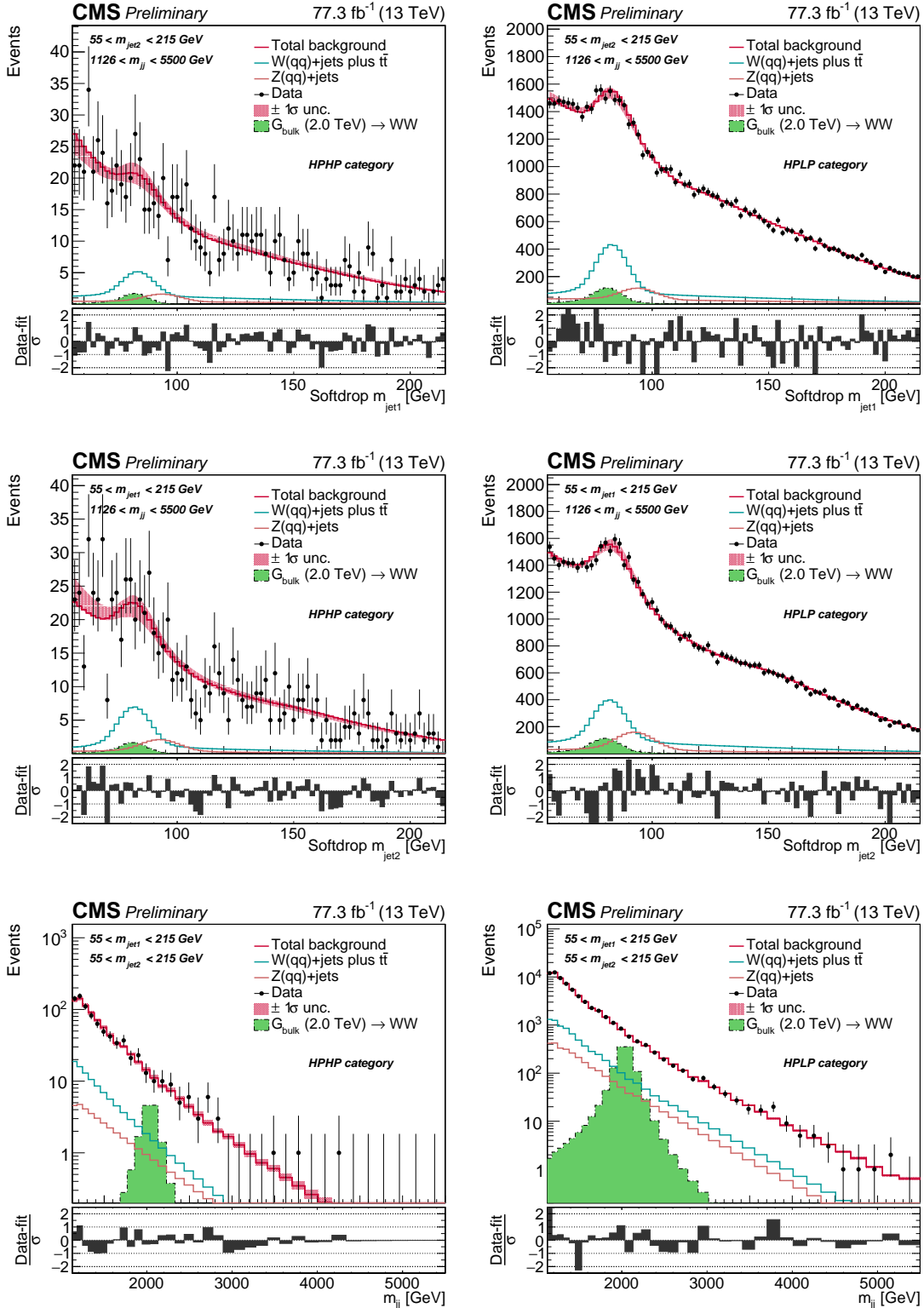


Figure 9.39: Postfit distributions after a combined fit to a toy dataset generated under the QCD PYTHIA8 template. The projections of $M_{\text{jet}1}$ (top), $M_{\text{jet}2}$ (middle) and M_{ll} (bottom) are shown for the high- (left) and low-purity (right) category.

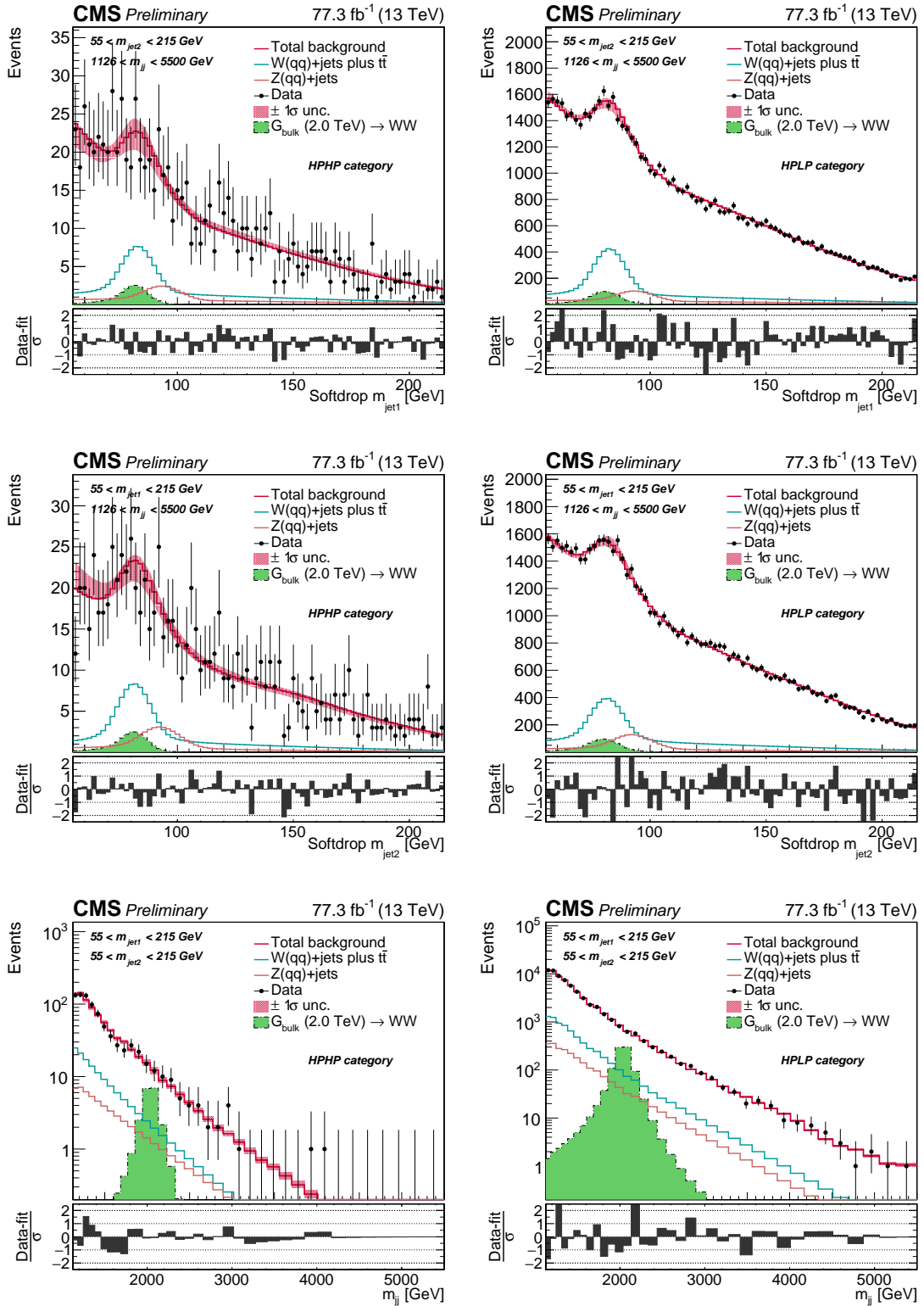


Figure 9.40: Postfit distributions after a combined fit to a toy datasets generated under the QCD HERWIG++ template. The projections of $M_{\text{jet}1}$ (top), $M_{\text{jet}2}$ (middle) and M_{vv} (bottom) are shown for the high- (left) and low-purity (right) category.

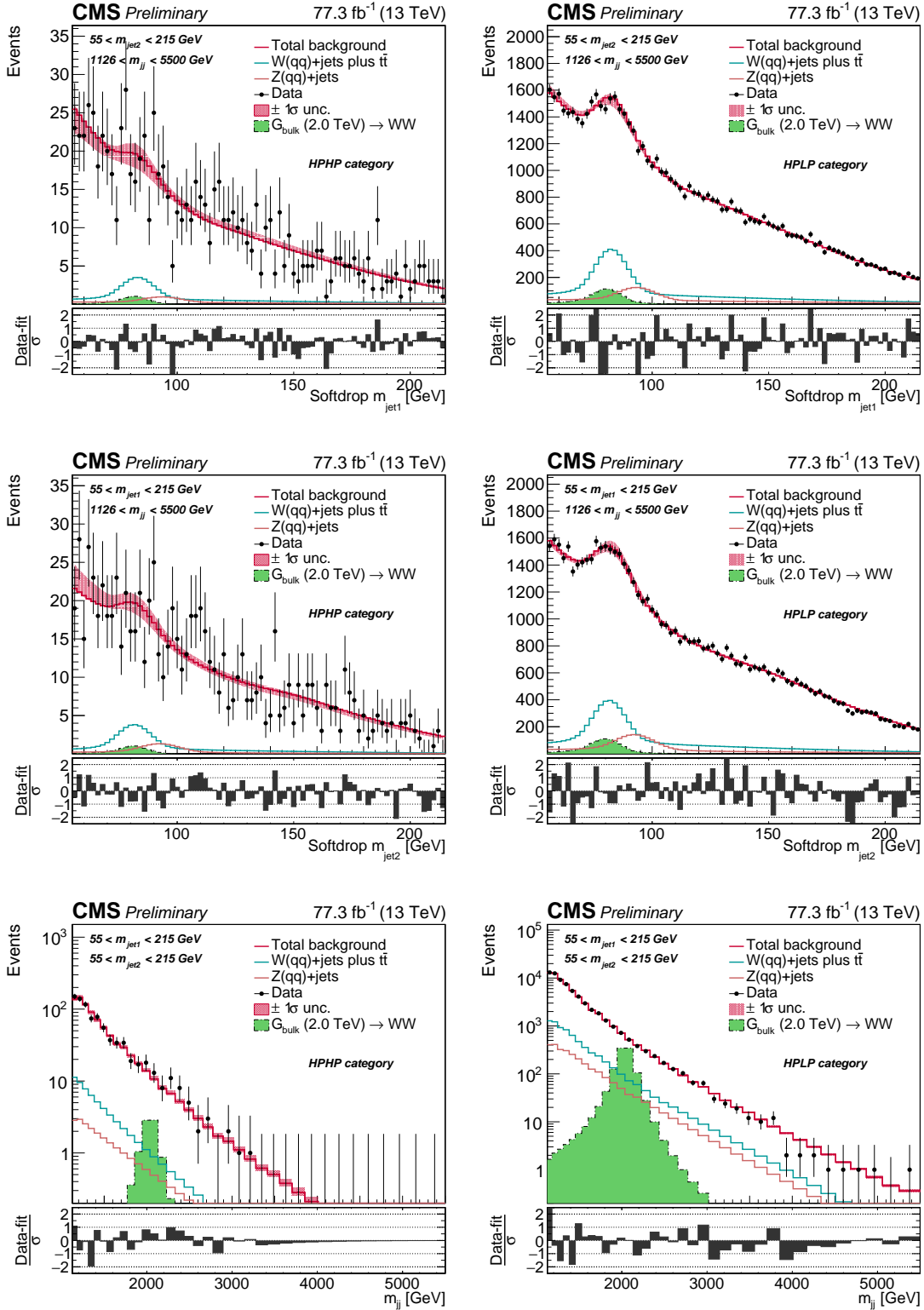


Figure 9.41: Postfit distributions after a combined fit to a toy dataset generated under the QCD QCD MADGRAPH+PYTHIA8 template. The projections of $M_{\text{jet}1}$ (top), $M_{\text{jet}2}$ (middle) and M_{VV} (bottom) are shown for the high- (left) and low-purity (right) category.

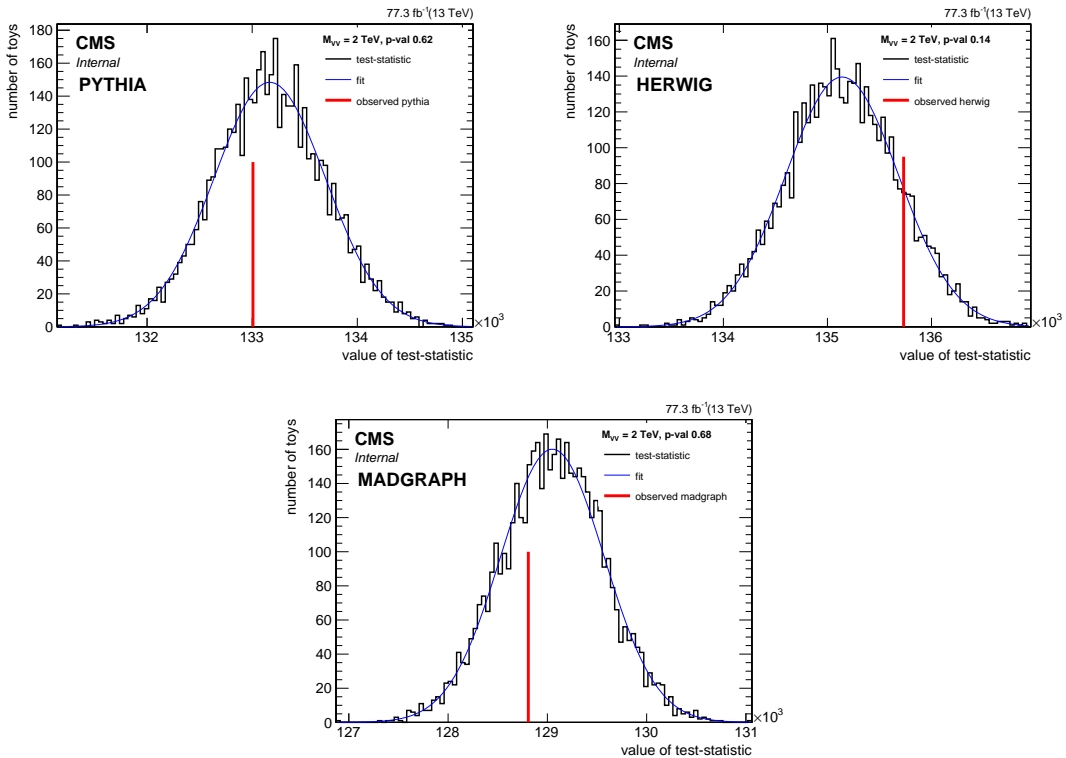


Figure 9.42: The likelihood for toys generated around the background-only hypothesis compared to the likelihood value of a toy dataset generated under the PYTHIA (top left), HERWIG++ (top right) and MADGRAPH+PYTHIA8 template (bottom).

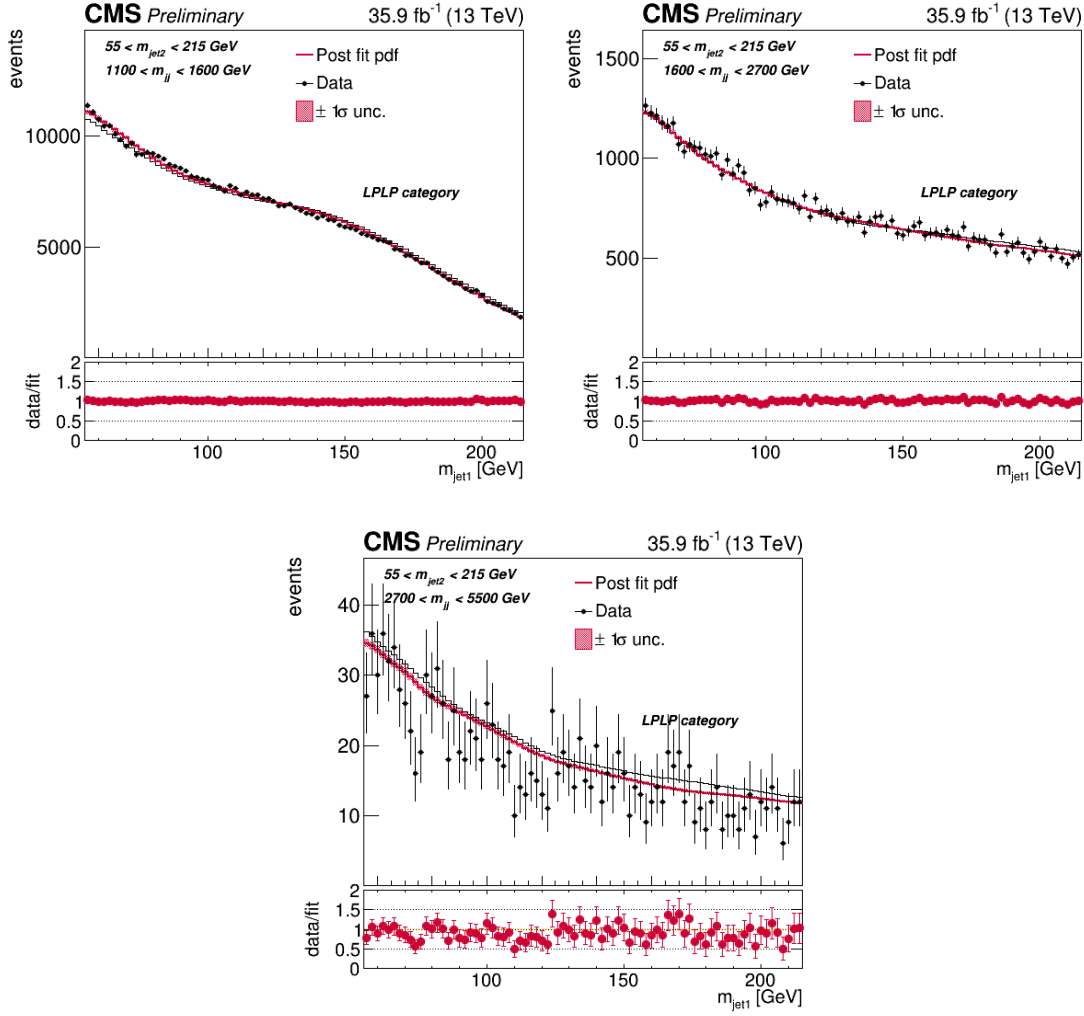


Figure 9.43: Distributions obtained from the fit to 2016 LPLP data. Here the projections of $M_{\text{jet}1}$ are shown for several ranges of M_{VV} , as labelled in the top left corner of each plot, and for the full $M_{\text{jet}2}$ range.

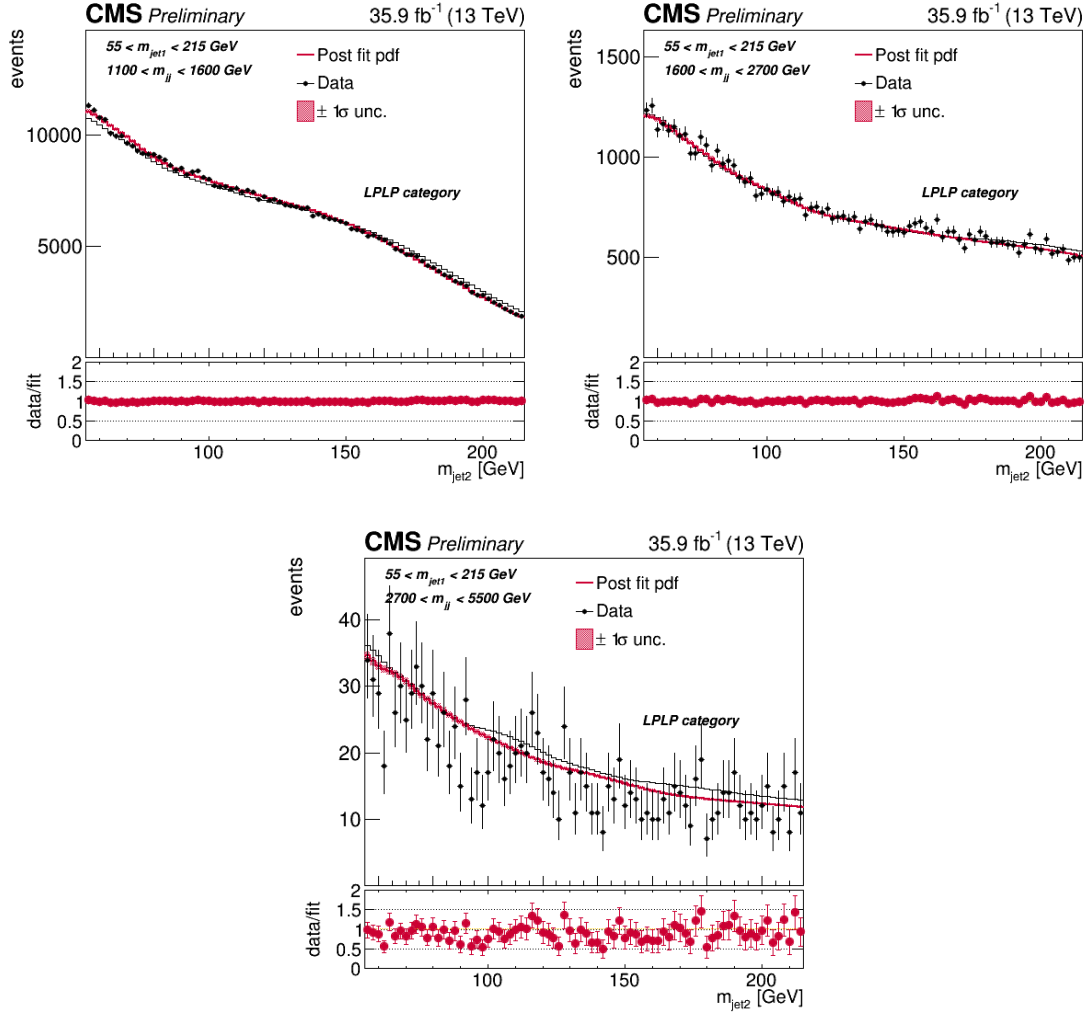


Figure 9.44: Distributions obtained from the fit to 2016 LPLP data. Here the projections of $M_{\text{jet}2}$ are shown for several ranges of M_{VV} , as labelled in the top left corner of each plot, and for the full $M_{\text{jet}1}$ range.

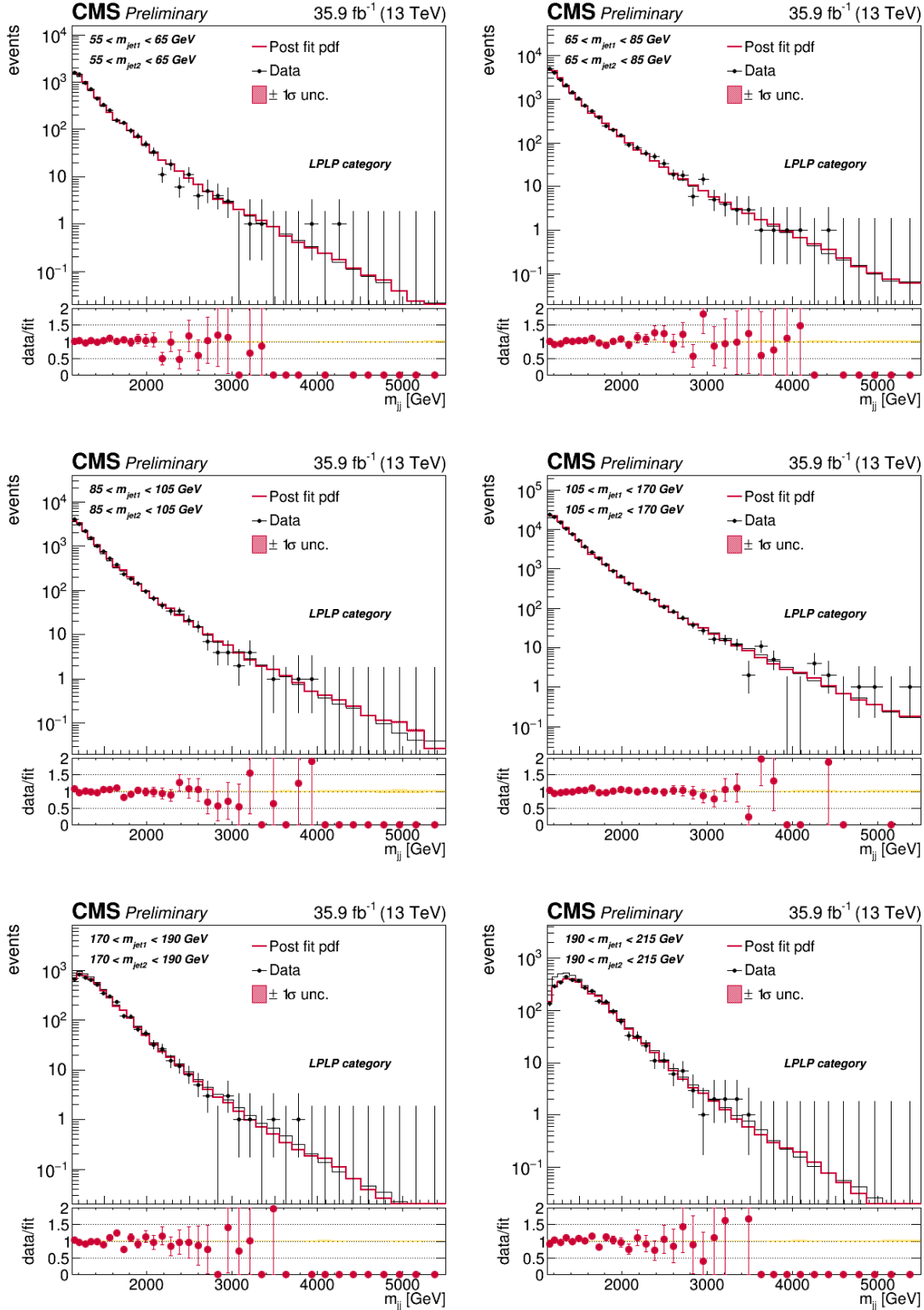


Figure 9.45: Distributions obtained from the fit to 2016 LPLP data. Here the projections of M_{VV} are shown for several equal ranges of M_{jet1} and M_{jet2} , as labelled in the top left corner of each plot.

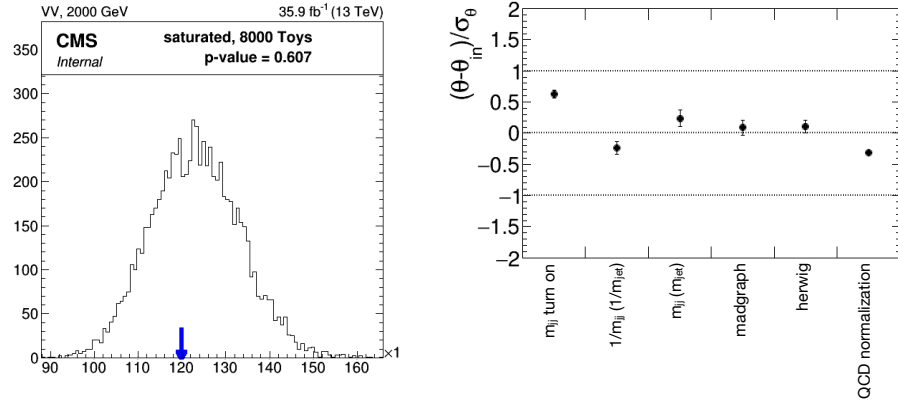


Figure 9.46: Left: the likelihood for toys generated around the background-only fit to LPLP data, compared to the likelihood on data. Data is in good agreement with the background-only hypothesis. Right: pulls of the nuisance parameters for a background-only fit.

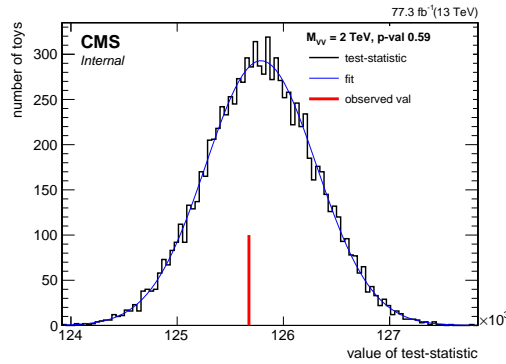


Figure 9.47: Distribution of the likelihood for toys generated around the background-only hypothesis compared to the likelihood on data for the full combination of 2016 and 2017 data.

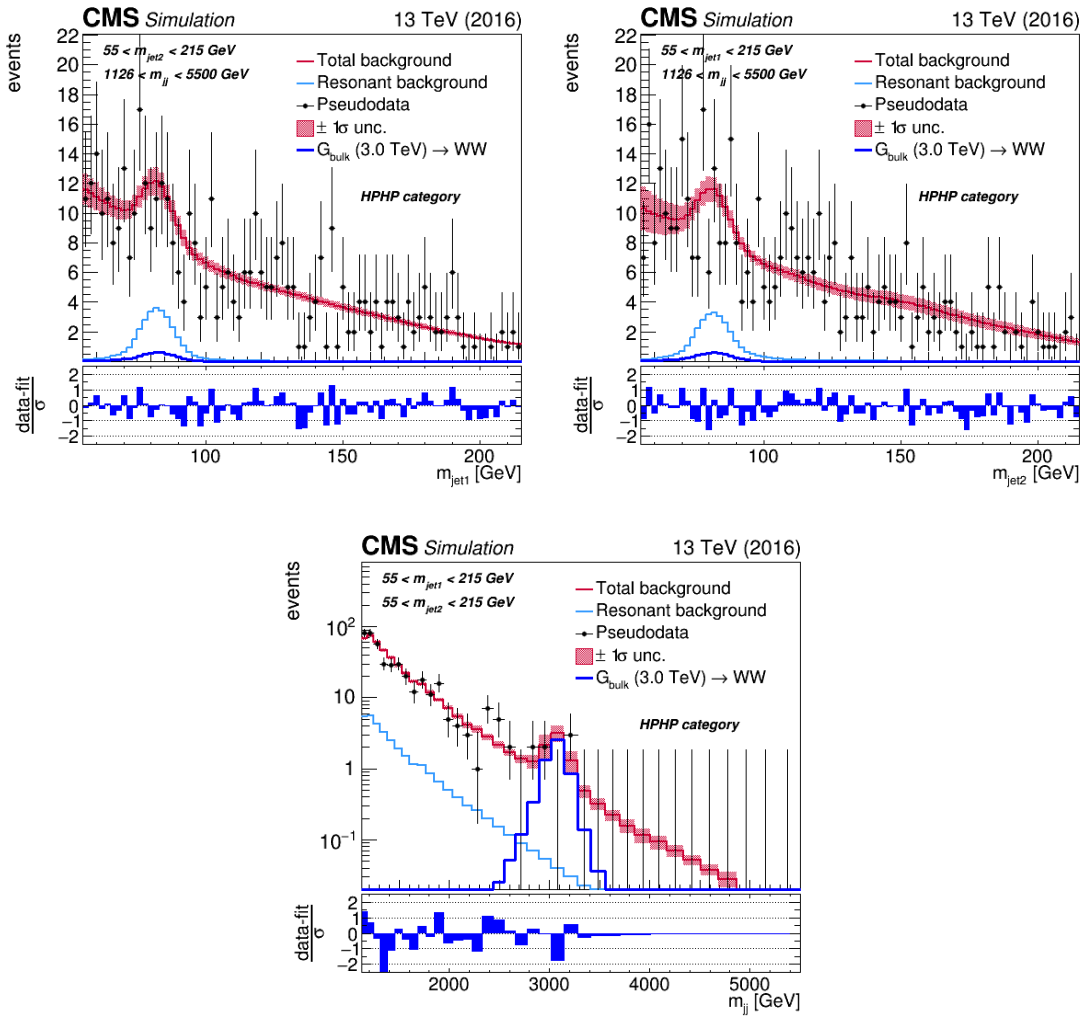


Figure 9.48: The post-fit distribution after injecting a signal with a mass of 3 TeV on top of the background in the HP category.

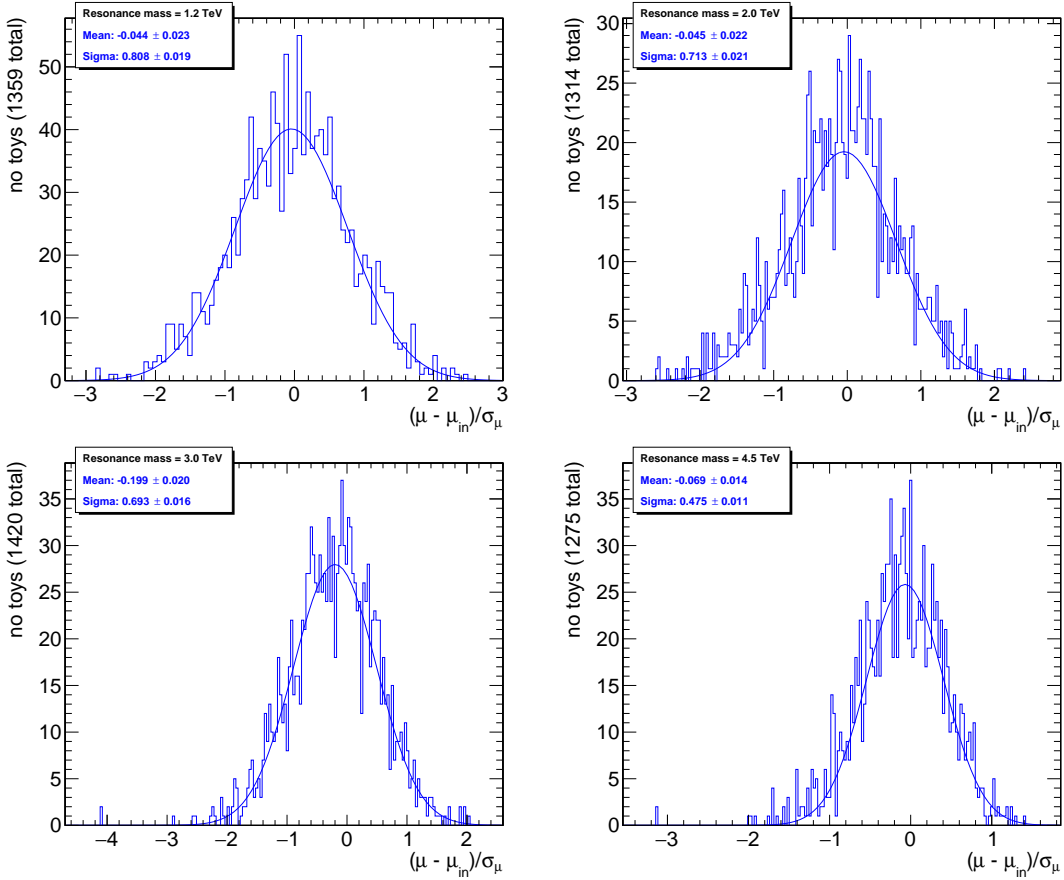


Figure 9.49: Cumulative distributions of the pulls for the signal strength for 4 different signal mass-points.

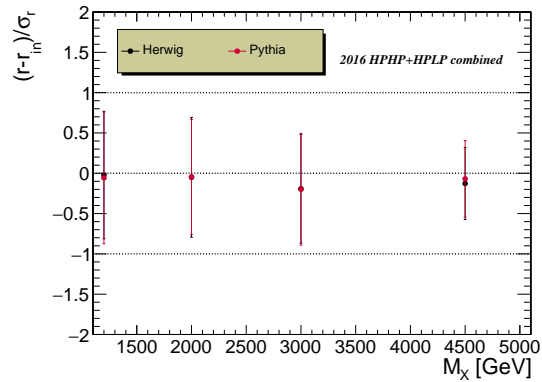


Figure 9.50: Estimated bias as a function of the resonance mass.

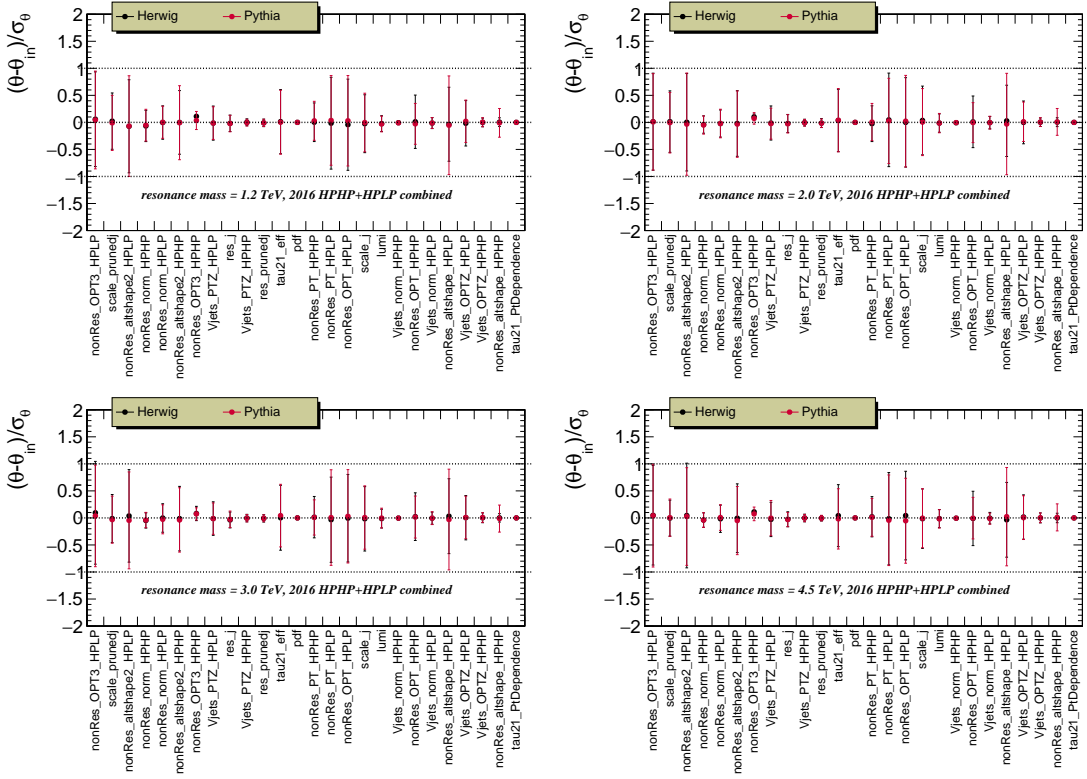


Figure 9.51: Pulls of the fit nuisance parameters after injecting signals of different mass and signal strength on top of a toy datasets generated from the nominal PYTHIA8 template (red markers) and for a toy generated under the HERWIG++ template (black markers).

2829 **9.10 Results**

2830 The distributions obtained from a combined fit to the observed data in 2016 and 2017 are shown
2831 in Figure 9.52 and 9.53, with the corresponding predicted and observed number of background
2832 events in the signal region summarized in Table 9.6. We observe a beautiful double peak from
2833 the $W(q\bar{q})$ and $Z(q\bar{q})+jets$ background, especially visible in the low-purity category. This allows
2834 us to, for the very first time, constrain the softdrop jet mass scale and resolution simultaneously
2835 from a $W(q\bar{q})+jets$ and $Z(q\bar{q})+jets$ SM background, which we will discuss in Section 9.10.2. No
2836 excess is observed and we proceed by setting upper limits on the signal cross section times the
branching ratio in the same way as in Section 7.9.

	HPHP	HPLP
$W+jets$	113.3 ± 18.1	4257.4 ± 257.0
	100.4 (exp.)	4318.0 (exp.)
$Z+jets$	46.5 ± 8.3	1747.5 ± 163.7
	50.2 (exp.)	2159.0 (exp.)
QCD	651.6 ± 4.0	51190.5 ± 313.1
	684.4 (exp.)	53767.5 (exp.)
Observed yield	778 ± 28	57227 ± 239
Post-fit total background	811.4 ± 20.3	57195.5 ± 436.8

Table 9.6: Expected and observed yields and their total uncertainty (stat.+sys.) in the two purity categories.

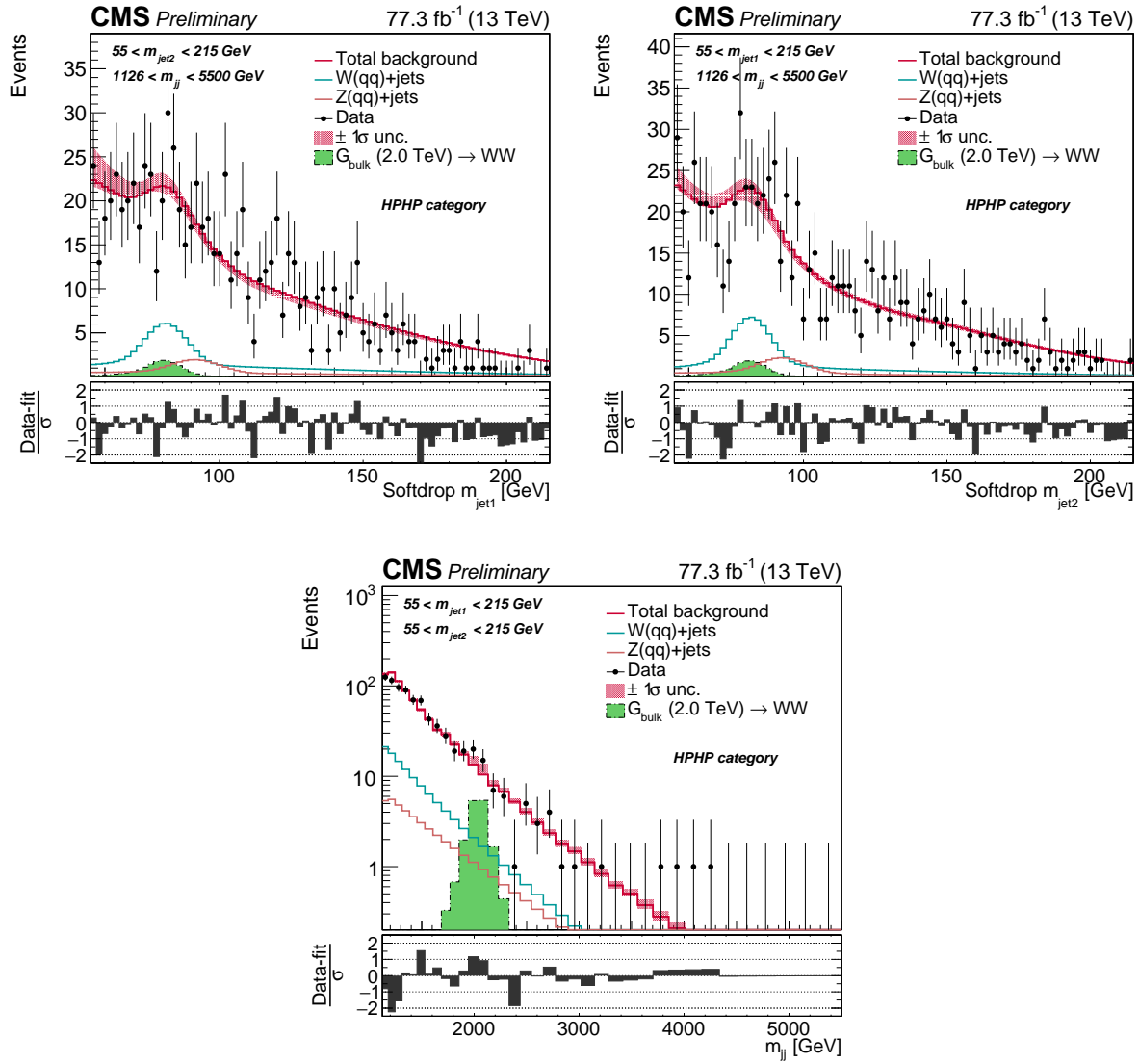


Figure 9.52: Postfit distribution after a fit to 2016 and 2017 data projected onto the $M_{\text{jet}1}$ (left), $M_{\text{jet}2}$ (middle), and M_{jj} (right) axis for the high-purity category. The background shape uncertainty is shown as a red shaded band, and the statistical uncertainties of the data are shown as vertical bars. The overlaid signal distribution is arbitrarily normalized.

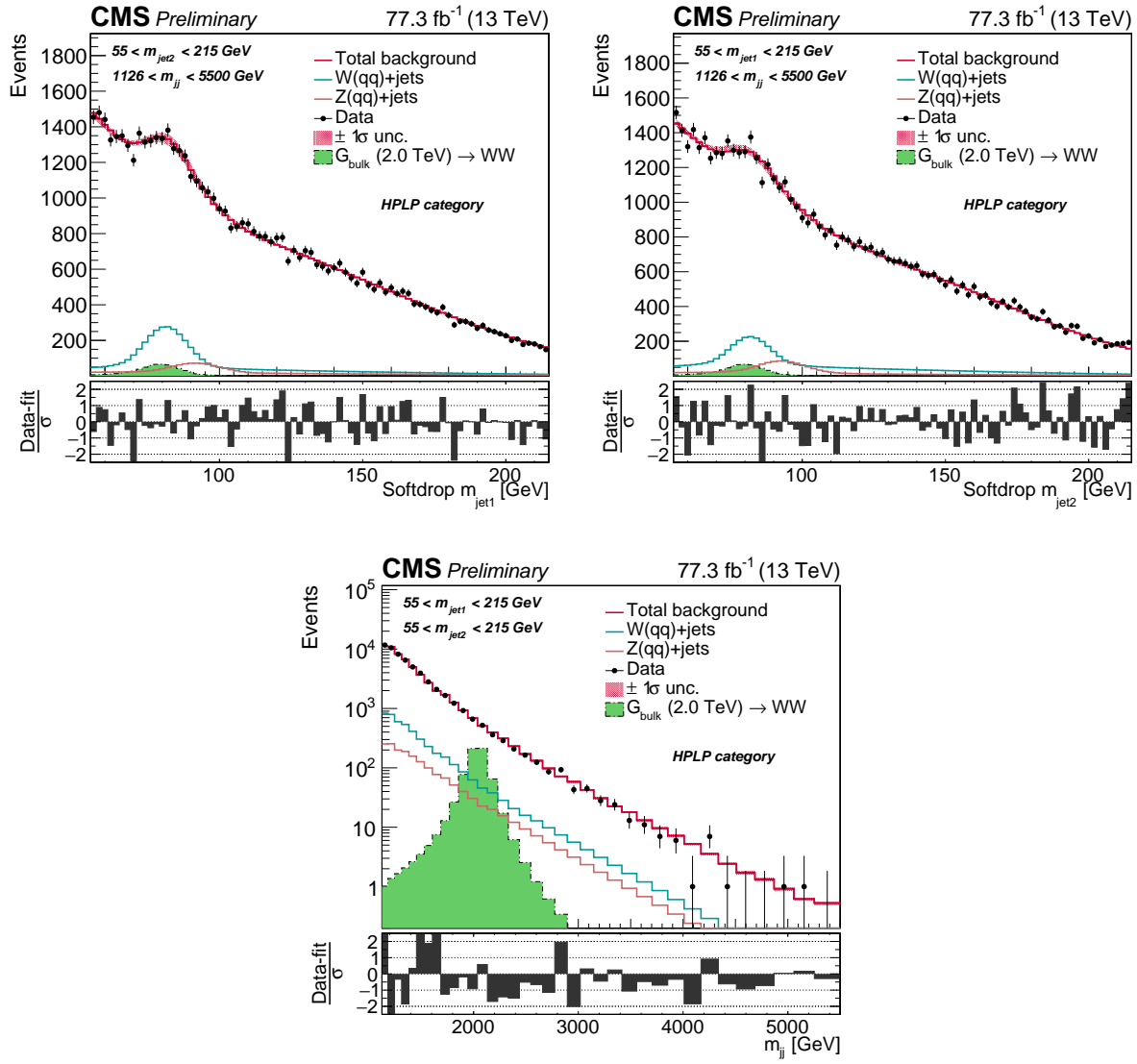


Figure 9.53: Postfit distribution after a fit to 2016 and 2017 data projected onto the $M_{\text{jet}1}$ (left), $M_{\text{jet}2}$ (middle), and M_{ll} (right) axis for the low-purity category. The background shape uncertainty is shown as a red shaded band, and the statistical uncertainties of the data are shown as vertical bars. The overlaid signal distribution is arbitrarily normalized.

2838 9.10.1 Limits

2839 As for Search I and Search II, exclusion limits on the cross section of the process $X \rightarrow VV$ are set
 2840 in the context of the Bulk Graviton model and the HVT model B scenario (again obtained using
 2841 the asymptotic CL_S method). Figure 9.54 show the resulting expected and observed exclusion
 2842 limits at 95 % confidence level on the signal cross section times branching fraction as a function of
 2843 the resonance mass for a $G_{\text{bulk}} \rightarrow WW$ (top left), $G_{\text{bulk}} \rightarrow ZZ$ (top right), $W' \rightarrow WZ$ (bottom
 2844 left) and $Z' \rightarrow WW$ (bottom right) signal. The obtained limits are compared with the resonance's
 2845 production cross section times the branching fraction to WW, ZZ and WZ. For the heavy vector
 2846 triplet model B, we exclude at 95% confidence level W' and Z' spin-1 resonances with masses
 2847 below 3.7 and 3.5 TeV, respectively. In the narrow-width bulk graviton model, lower limits on the
 2848 production cross sections are set in the range from 9 fb for a resonance mass of 1.2 TeV, down
 2849 to 0.2 fb for high resonance masses above 5.2 TeV for $G_{\text{bulk}} \rightarrow WW$. In the case of $G_{\text{bulk}} \rightarrow ZZ$,
 2850 lower cross section limits are 13 fb and 0.2 fb for bulk graviton masses of 1.2 and 5.2 TeV,
 2851 respectively.

2852 Comparison with 1D fit

2853 The analysis of the 2016 dataset and corresponding limits obtained using the 3D fit method,
 2854 can be compared to the limits using the 1D fit in Search II in order to estimate whether there
 2855 is a sensitivity gain. One caveat of this comparison is that the analysis performed using the
 2856 1D method does not apply jet energy resolution smearing to the jets, and hence uses an overly
 2857 optimistic assumption on the dijet invariant mass resolution. The difference in resonance mass
 2858 resolution with and without jet energy resolution smearing is shown in Figure 9.55 for the 2016
 2859 (left) and 2017 (right) signal samples. With JER smearing applied, the resonance mass resolution
 2860 is worse and the peak broadens by 5%. Figure 9.56 shows the expected limits based on analyses
 2861 of the 2016 dataset, either using the new 3D fit method, where the jets have been smeared (blabla
 2862 line) or not (blabla line), or using the 1D dijet method. We obtain X–X% improvement with
 2863 the 3D method, which is reduced to X% due to JER smearing being applied and about 35–40%
 2864 improvement when combining the two datasets with respect to the individual results.

2865 Comparison between datasets

2866 We additionally compare the sensitivity between the 2016 and 2017 datasets. Also here there is
 2867 one important caveat: for the 2016 analysis, pileup was removed from the jets using the charged
 2868 hadron subtraction algorithm, whereas in 2017 the PUPPI algorithm was used. In both cases,

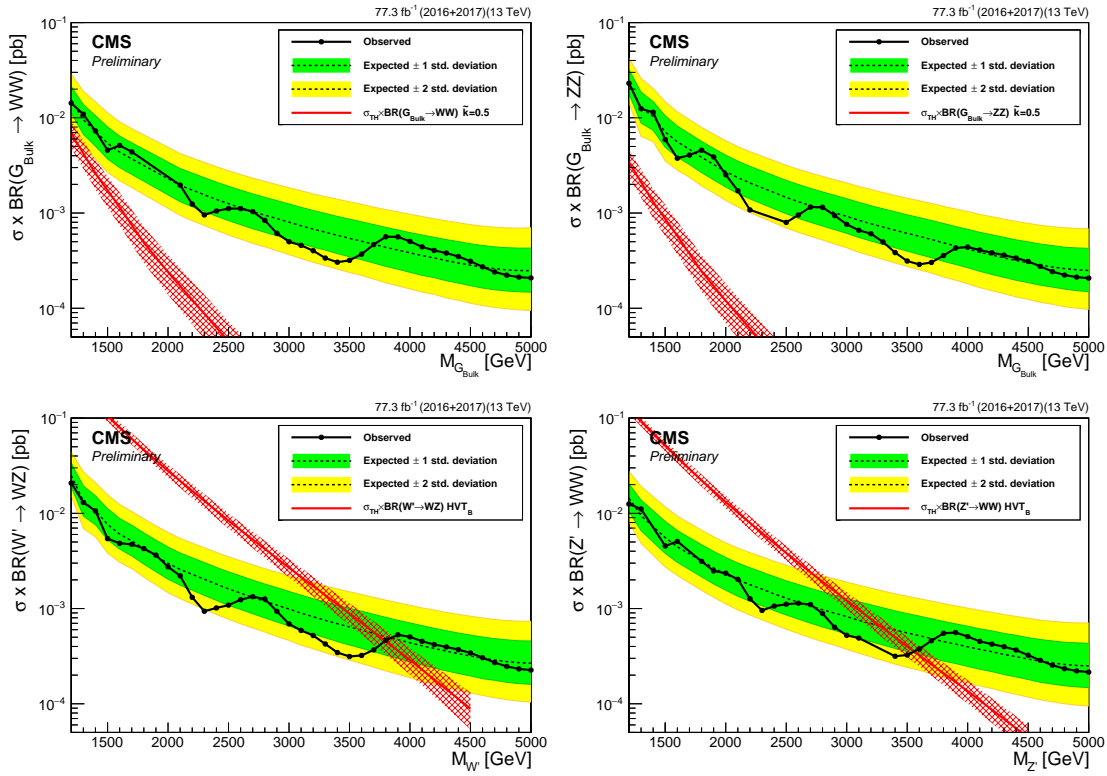


Figure 9.54: Expected limits obtained combining 35.9 fb^{-1} and 41.4 fb^{-1} of data of data after combining all purity categories for Bulk $G \rightarrow WW$ (top left), Bulk $G \rightarrow ZZ$ (top right), $W' \rightarrow WZ$ (bottom left) and $Z' \rightarrow WW$ (bottom right) signals.

the softdrop jet mass was obtained from a PUPPI cleaned soft-dropped jet (in the 2016 analysis, the CHS jet was matched to a PUPPI soft-dropped jet in order to obtain the mass. The jet four-vector still relies on CHS). The reason for this switch is that, while for a pileup between 20-30 the CHS and PUPPI algorithms have a similar performance, once the average number of interactions per event is above 30 the PUPPI algorithm has been shown to achieve a better resolution for large-radius jet observables. In 2016 the average PU was 27 whereas in 2017 it was 38, a 40 % increase. However, despite being better in term of groomed jet-mass resolution, PUPPI pileup subtraction has a worse dijet invariant mass resolution than CHS pileup subtracted jets. This is most likely due to PUPPI removing far more (PU) tracks than CHS and, if these PU tracks happen to be associated to a large calorimeter energy deposit, some of the energy might be lost. This creates a tail at lower dijet invariant masses, as shown in Figure 9.57. Figure 9.58 shows the expected limits obtained with the new 3D fit method using 35.9 fb^{-1} of 2016 data (beige dashed line), 41.4 fb^{-1} of 2017 data (pink dashed line) and when combining the two yielding a

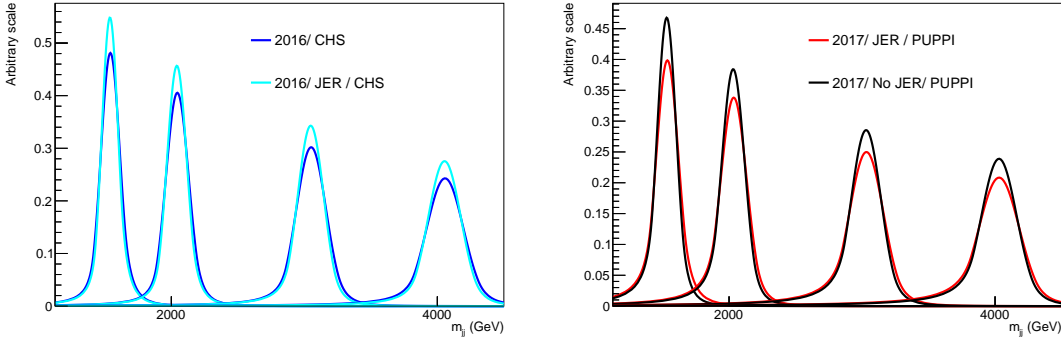


Figure 9.55: Right: A comparison of the resonance mass resolution with (turquoise) and without (blue) jet energy resolution (JER) smearing using 2016 signal samples. Left: A comparison of the resonance mass resolution with (red) and without (black) jet energy resolution (JER) smearing using 2017 signal samples. In both cases, the mass resolution is worse after smearing, and has a roughly 8–10% larger width.

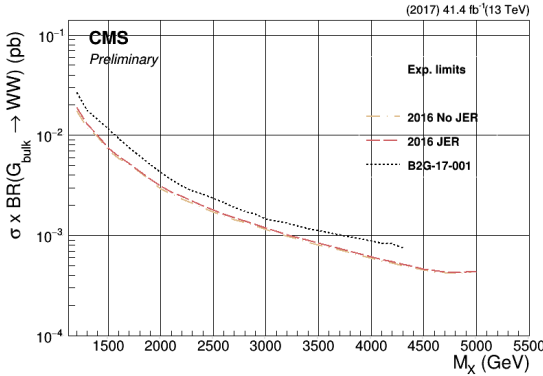


Figure 9.56: Expected limits using 35.9 fb^{-1} of data for a Bulk $G \rightarrow WW$ signal using the 3D fit method, where the jets have had JER smearing applied (red line) or not (yellow line), and using the 1D fit method (dotted black line).

total of 77.3 fb^{-1} of data (dotted black line). These are compared to the results obtained using the 1D fit in Search II (solid purple line). A 35–40% improvement is obtained when combining the two datasets with respect to the individual results, and we observe that the 2017 limits are slightly worse than the 2016 ones due to the above mentioned switch to PUPPI. For the full Run 2 legacy paper combining 2016, 2017, and 2018 data, we will perform a thorough study comparing CHS to PUPPI.

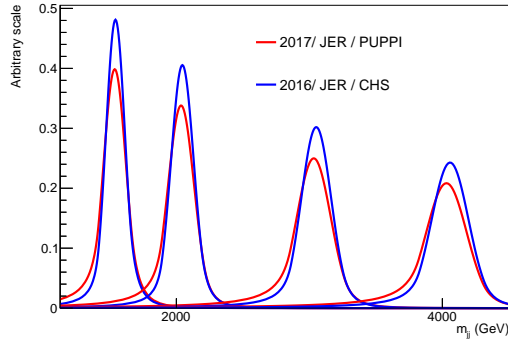


Figure 9.57: A comparison of the resonance mass resolution obtained from 2017 signal samples based on PUPPI jets (red) and 2016 signal samples based on CHS jets (blue).

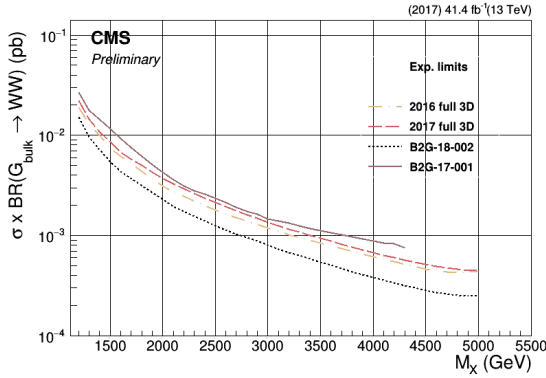


Figure 9.58: Expected limits for a Bulk $G \rightarrow WW$ signal using 35.9 (beige dashed line), 41.4 (pink dashed line), and 77.3 fb^{-1} of data using the 3D fit method (dotted black line), and using 35.9 fb^{-1} of 2016 data and the 1D fit method (solid purple line).

2888 Comparison with ATLAS

2889 Figure 9.59 shows the comparison with the expected limits obtained by the ATLAS collaboration
 2890 in a similar search for a VV resonance decaying to hadrons [83], for W' and Z' signal hypotheses.
 2891 For both signal hypotheses we obtain similar, or slightly better results by up to 35 %.

2892 Limits per category

2893 In Fig. 9.60 we also show the expected limits for a Bulk $G \rightarrow WW$ signal separately for 2016 and
 2894 2017, and for the two HPHP and HPLP categories. As a result of the jet substructure selections
 2895 optimization, the HPHP category dominates at low masses while the HPLP adds sensitivity at
 2896 higher values of the signal mass.

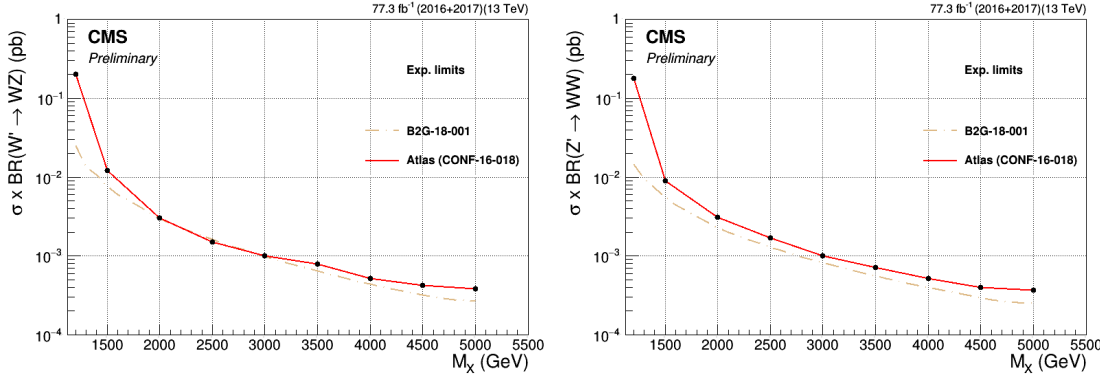


Figure 9.59: Comparison with the expected limits obtained by the ATLAS collaboration in a similar search for a VV resonance decaying to hadrons [83], for W' (left) and Z' (right) signal hypotheses.

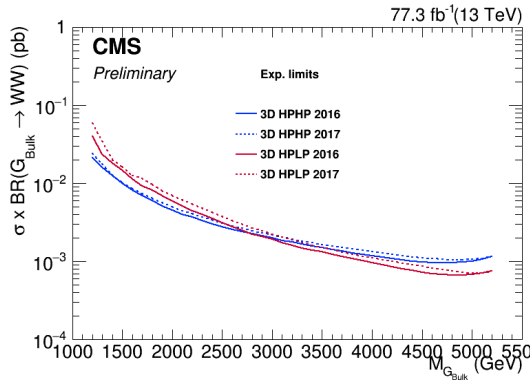


Figure 9.60: Comparison of the sensitivity of the two HPHP and HPLP categories for a Bulk $G \rightarrow WW$ signal hypothesis.

9.10.2 Pulls of nuisance parameters

As summarized in Section 9.8, we add a list of systematic uncertainties to the fit as nuisance parameters. To quantify the difference between the expected values of the systematic uncertainties and the observed values, we compute the pull of the nuisance parameters,

$$p_\theta = (\theta - \theta_{in})/\sigma_\theta, \quad (9.12)$$

where θ_{in} is the pre-fit value of the nuisance parameter under consideration, θ the corresponding parameter post-fit, and σ_θ the post-fit error. The error on p_θ is calculated as the ratio of post- and pre-fit uncertainties. Figure 9.61 shows the pulls after a signal and background fit to the

2904 combined 2016+2017 dataset (left) and when fitting the two separately (right), here using a
2905 signal hypothesis corresponding to a 2 TeV G_{bulk} . We observe that the W-tagging efficiency
2906 (“CMS_VV_JJ_tau21_eff”), the softdrop jet mass scale (“CMS_scale_prunedj”) and the resolution
2907 (“CMS_res_prunedj”) gets pulled and constrained by the W+jets and Z+jets mass peaks. In
2908 addition, the QCD shape parameters (“CMS_VV_JJ_nonRes_”*) are significantly pulled and
2909 constrained by data because of their large pre-fit uncertainty and unknown a-priori pre-fit value
2910 (again, we do not know if Nature is PYTHIA8, HERWIG++ or MADGRAPH+PYTHIA8. Though
2911 from this measurement, HERWIG++ seems to be favored by data (“altshape2”)).

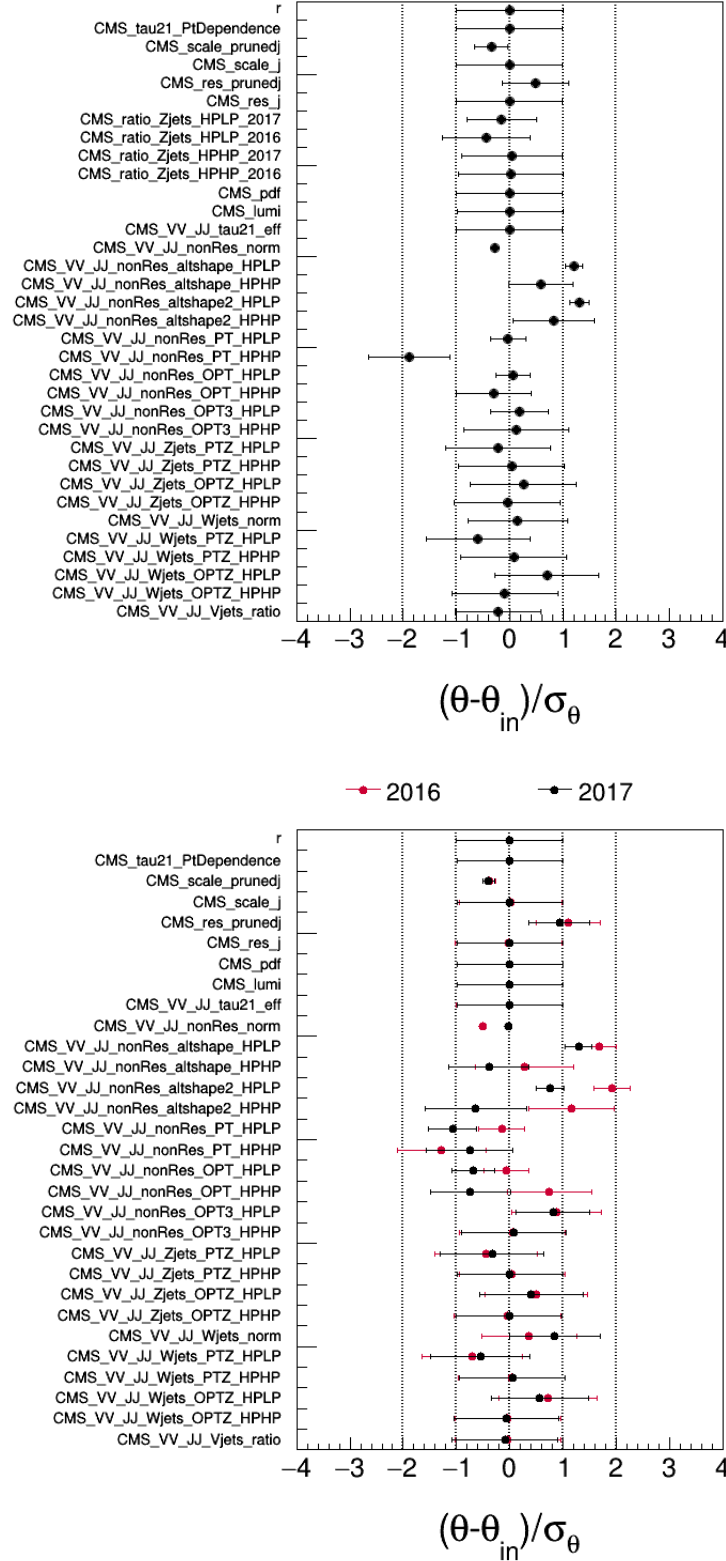


Figure 9.61: Pulls of each nuisance parameter for a combined signal+background fit to the combined 2016+2017 dataset (top) and when fitting the two separately (bottom).

2912

CHAPTER 10

2913

Summary

2914 In chapters 7, 8, and 9, we have followed the search for VV resonances in the all-hadronic final state
2915 through three stages: from being one of the first-ever analyses in the “boosted” final state with a
2916 center-of-mass energy of 13 TeV, and the very first CMS analysis to take advantage of substructure
2917 at the trigger level, through leading the development of a new W-tagging algorithm and mass
2918 corrections now default in CMS, and finally ending with the development of a multi-dimensional
2919 fit for generic searches in the groomed jet mass and dijet invariant mass.

2920 Each analysis has built on findings and improvements that came from the analysis before it:
2921 the substructure triggers and mass-corrected softdrop jet mass are both used for the 3D fit; the
2922 early discovery of the softdrop signal efficiency dependence on p_T led us to derive corrections for
2923 it; the observed lack of a constraint on the fit in the dijet invariant mass tail when statistics were
2924 low led to us exploring alternate methods that utilize simulation rather than data to create a
2925 more robust background prediction in the 3D fit; and the observation of large differences between
2926 predictions from different QCD MC generators led us to derive a clever way in which we can
2927 incorporate all of these predictions into one single fit. Now the question which remains is: *What*
2928 *comes next?*.

2929 A few ideas were already mentioned in the introduction to Search III, Section 9. The natural
2930 next step for this search is an incorporation of the VH(bb) and H(bb)H(bb) searches into the
2931 three-dimensional fit. Orthogonality between the three is guaranteed through b-tagging categories,
2932 as illustrated in Figure 10.1. This process is already underway, and we are aiming for a publication
2933 based on the full Run 2 dataset (data collected in 2016, 2017 and 2018) in one common framework.

2934 Secondly, there will be an increase in center-of-mass energy to 14 TeV in Run 3 (2020-2022).
2935 After this, there is not planned an increase in the collision energy. That means that better
2936 sensitivity will be achieved only through increases in integrated luminosity or better analysis
2937 technique, such as a better procedure for background estimation, a better fit procedure, or a

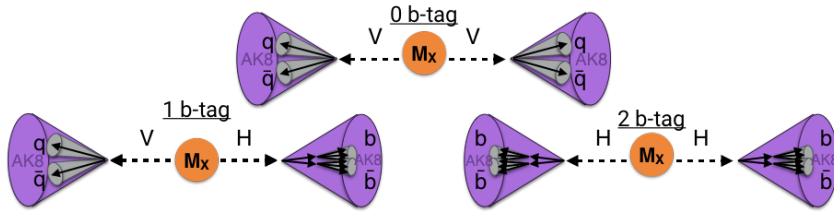


Figure 10.1: The VV , $VH(bb)$, and $H(bb)H(bb)$ analyses can all be incorporated into the multidimensional framework. Orthogonality between the analyses is ensured through b-tagging categories.

2938 better V tagger.

2939 Beyond that, and perhaps more interestingly, is the search for generic resonances peaking
 2940 anywhere in the jet mass and dijet invariant mass spectrum, where the jets themselves could
 2941 have other compositions other than two subjets (for instance, a scalar decaying to two vector
 2942 bosons, whose decay products are merged into one jet, resulting in a 4-prong object). One caveat
 2943 of the current analysis setup is that it only works for two-pronged signals due to its n-subjettiness
 2944 cut. In order for the multi-dimensional framework to be truly generic, the τ_{21} tagger needs to be
 2945 replaced by a generic anti-QCD tagger. Such a tagger works as an anomaly detector by encoding
 2946 the probability density function for quark or gluon jets as a function of certain variables, variables
 2947 for which signal jets are assumed to have a different probability density function. In our case,
 2948 good variables would for instance be groomed jet mass or substructure, as any generic signal is
 2949 assumed to be peaking in jet mass and have some (unknown) substructure. Such a tagger would
 2950 not require information about what a potential signal would look like; it would return only the
 2951 probability of any particular jet being a QCD jet. Taggers like these are usually based on deep
 2952 neural networks (DNN), where the quark and gluon jet PDFs are obtained through training of
 2953 the network, as demonstrated in Refs. [84, 85].

2954 In order for such an encoding to work, the DNN needs access to the features distinguishing
 2955 quark and gluon jets from signal jets without these features being biased towards any signal in
 2956 particular. The network must learn how to encode “non-substructure”.

2957 As a side project in parallel to working on the multi-dimensional fit, I spent the last half year of
 2958 my PhD working on a deep neural network capable of discriminating quark and gluon jets from
 2959 W jets in order to improve the W-tagging performance and improve the search sensitivity for
 2960 VV analyses to come. Based solely on the four vectors of jet constituents, the idea is to let the
 2961 neural network itself compute variables based on grooming and substructure, without feeding
 2962 it any high-level features (like softdrop mass and τ_{21}). This type of architecture is, in addition
 2963 to improving W-tagging performance, ideal for the purpose described above: encoding QCD in

²⁹⁶⁴ terms of substructure-like features. The final chapter of this thesis is therefore dedicated to the
²⁹⁶⁵ two last points: how to improve W-tagging in CMS for future analyses and how to design a neural
²⁹⁶⁶ network capable of learning jet substructure in an unbiased way.

2967

Part IV

2968

Encoding jet substructure in a deep neural network

2969

2970 Infusing deep neural networks with physics

2971 The previous chapter ended by mentioning two ingredients that will become important for future
 2972 searches with the multi-dimensional fit: a better vector-boson tagger, and a generic anti-QCD
 2973 tagger for signal-independent searches. As a side project during my final PhD semester, I worked
 2974 on a solution for the first, which has the added benefit of being a stepping stone towards the latter.
 2975 This is what I will cover in the final chapter of this thesis.

2976

2977 When applying machine learning to particle physics problems, the input has historically con-
 2978 sisted of pre-computed high-level features (quantities based on lower-level variables and certain
 2979 theoretical assumptions). With the rise of deep learning however, computational graphs have
 2980 achieved an increased capability to find even the smallest correlations in datasets, allowing them
 2981 to construct complex features on their own. The deep neural network (DNN) I will present in
 2982 the following is based on the assumption that, given sufficient instructions about the laws of
 2983 Nature, a neural network should be capable of reconstructing its own high-level features based on
 2984 lower-level quantities only. In addition, if smartly designed, the network should be capable of
 2985 finding novel correlations and physical features, *a-priori* unknown, by allocating a physical meaning
 2986 to the training weights deep within the network. The deep neural network I will present here is
 2987 trained to discriminate quark and gluon jets from W -jets. However, as I will discuss in the final
 2988 section of this chapter, it is also the perfect starting point for developing a generic anti-QCD tagger.

2989

2990 The work presented in the following has not been published and still qualifies as work in progress.
 2991 However, I believe developing taggers such as these is of great importance for future versions of
 2992 the searches presented here, and it is something I hope to continue working on in the future.

The notes show a diagram of four vectors E_1, E_2, P_1, P_2 forming a parallelogram. Below the diagram, the text 'COLA:' is written above a matrix equation:

$$k_{\text{M},i} = \begin{bmatrix} E_1 & E_2 \\ P_1^2 & P_2^2 \\ P_1^y & P_2^y \\ P_1^z & P_2^z \end{bmatrix} \quad (4,2)$$

Below this, another matrix equation is shown:

$$k_{\text{M},i} = k_{\text{M},i} \cdot L_i = \begin{bmatrix} E_1 & E_2 \\ P_1^2 & P_2^2 \\ P_1^y & P_2^y \\ P_1^z & P_2^z \end{bmatrix} \quad (4,2)$$

With a note: $(M=4)$

Further down, a large bracketed expression shows linear combinations of momenta:

$$\begin{aligned} & [E_1, E_2, E_1 + E_2, E_1 - E_2] \\ & [P_1^2, P_2^2, P_1^2 + P_2^2, P_1^2 - P_2^2] \\ & [P_1^y, P_2^y, P_1^y + P_2^y, P_1^y - P_2^y] \\ & [P_1^z, P_2^z, P_1^z + P_2^z, P_1^z - P_2^z] \end{aligned}$$

Below these, the equations for the sum of momenta components are listed:

$$\begin{aligned} & \sum E \\ & \sum P_x \\ & \sum P_y \\ & \sum P_z \end{aligned}$$

A note at the bottom right says: 'linear combinations of momenta'.

"What can we teach the machine?" → "What can we learn from the machine?".

Work in progress.

2993

CHAPTER 11

2994

A Lorentz invariance based Deep Neural Network for W-tagging

2995

2996

11.1 LoLa

2997 LoLa is a deep neural network architecture which was first introduced for top tagging [86]. It is
 2998 based on the idea that, given enough information about the laws of Nature, a neural network should
 2999 be capable of calculating jet substructure observables on its own given only low-level information.
 3000 The network is designed to discriminate between AK R=0.8 jets originating from W bosons from
 3001 those originating from quarks or gluons, solely based on the jet constituent four-vectors (variables
 with little discriminating power on their own) as illustrated in Figure 11.1. Rather than being

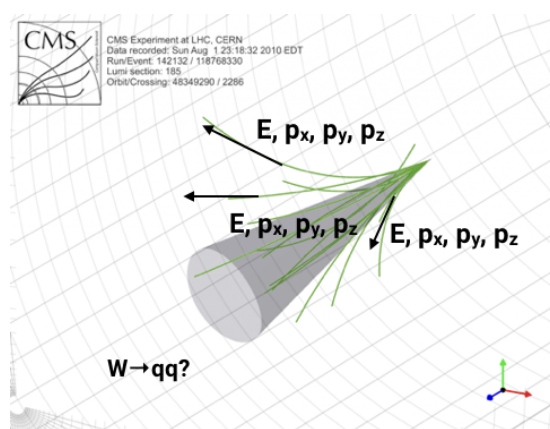


Figure 11.1: LoLa uses only jet constituent four-vectors as input to discriminate W jets from quark and gluon jets.

3002

3003 input high-level features, the neural network is given tools to perform calculations on Lorentz
 3004 vectors using the Minkowski metric. Through two novel layers, linear combinations similar to jet
 3005 clustering and jet substructure algorithms are performed, allowing the algorithm to create its
 3006 own substructure variables. Additionally, training weights deep within the network correspond
 3007 to physical quantities reconstructed by the algorithm; distance between particles, masses and
 3008 energies, linear combinations of particle four-vectors, etc. Besides the end goal of discriminating
 3009 W bosons from quarks and gluons, one could therefore hope to learn of new correlations separating
 3010 QCD from vector-boson jets.

3011 11.1.1 Architecture

3012 The LoLa architecture is designed as a four-layer deep, feed-forward sequential network doing
 3013 supervised learning on fixed-size input vectors. Two novel layers are introduced, the Combination
 3014 Layer (CoLa) and the Lorentz Layer (LoLa), which perform basic jet clustering and substructure
 3015 calculations as well as implement the Minkowski metric. These two layers are followed by two fully
 3016 connected layers, consisting of 100 and 50 nodes respectively, before the final output is computed
 3017 yielding two output probabilities between 0 and 1 (using a Softmax activation function [87]).
 3018 The loss function to be minimized is “categorical crossentropy” (or log loss) with two categories
 3019 corresponding to the probability of a given jet to be W versus non-W like. Only the W-jet
 3020 probability is stored. The optimizer used in the training is the ADAM optimizer [88], which
 3021 adapts the learning rate of the model parameters during training. The code itself is written using
 3022 the Keras [89] interface with a TensorFlow [90] backend. The full architecture with input and
 3023 output dimension per layer is shown in Figure 11.2. The three first boxes, representing the input,
 3024 CoLa and LoLa layers, correspond to tensors of rank 2, while the final four boxes correspond to
 3025 tensors of rank 1. In the following, each layer will be explained in detail.

3026 11.1.2 Input

3027 This algorithm is trained to discriminate between fully merged hadronic W-jets coming from the
 3028 process $G_{\text{bulk}} \rightarrow WW \rightarrow q\bar{q}q\bar{q}$ (where $M_{G_{\text{bulk}}} = 0.6 - 4.5 \text{ TeV}$), and quark or gluon jets from a
 3029 QCD sample generated with PYTHIA8. All jets are clustered with the anti- k_T algorithm with a
 3030 distance parameter of $R=0.8$, with the PUPPI pileup removal algorithm applied. In addition, they
 3031 are required to have $p_T > 200 \text{ GeV}$ and $|\eta| < 2.5$. Jets are defined as W jets if they are matched
 3032 to a generator-level, hadronically decaying W boson, with the following matching criteria. The
 3033 generated vector boson needs to be within $\Delta R < 0.6$ of the jet axis, and the quark decay products
 3034 need to be within $\Delta R < 0.8$ of the jet axis. The p_T and η distribution of signal and background

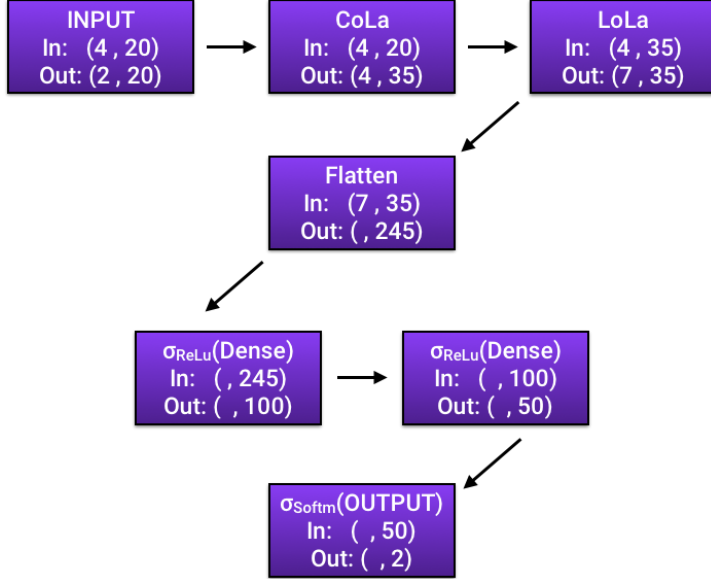


Figure 11.2: The full LoLa architecture. “In” denotes the dimension of the input tensor to the given layer, “Out” is the dimension of the output tensor.

3035 jets, is shown in Figure 11.3. From these signal and background jets, only the four-vectors of the
 3036 $N = 20$ highest- p_T jet constituents are used as input to the deep neural network: E , p_x , p_y and
 3037 p_z . I use 20 constituents since any larger number has a negligible effect on the performance, while
 3038 performance tends to drop once going below 15. The input is therefore a $4 \times (N = 20)$ matrix for
 3039 each signal and background jet, with one four-vector for each of the 20 jet constituents:

$$x_{\mu,i} = \begin{pmatrix} E^1 & E^2 & \dots & E^N \\ p_x^1 & p_x^2 & \dots & p_x^N \\ p_y^1 & p_y^2 & \dots & p_y^N \\ p_z^1 & p_z^2 & \dots & p_z^N \end{pmatrix}. \quad (11.1)$$

3040 The total number of jet constituents are shown in Figure 11.4, and the input variables (here
 3041 for all constituents) are shown in Figure 11.5. It is clear that the input variables provide
 3042 little discriminating power on their own. Therefore, the network must learn how to derive other
 3043 physical quantities where the signal and background PDFs differ to a larger extent. This is
 3044 achieved through the two custom layers described in the following.

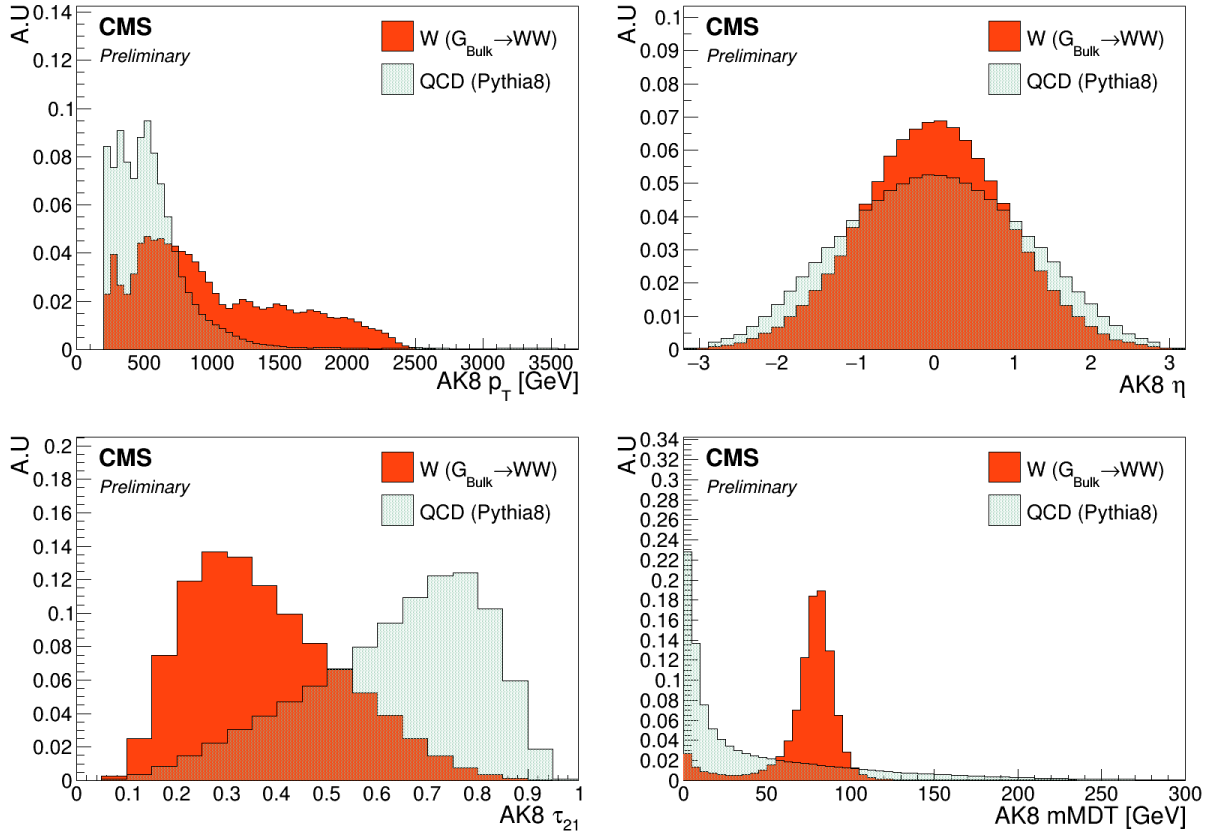


Figure 11.3: Jet p_T (top left), η (top right), τ_{21} (bottom left) and softdrop jet mass (bottom right) for signal and background jets.

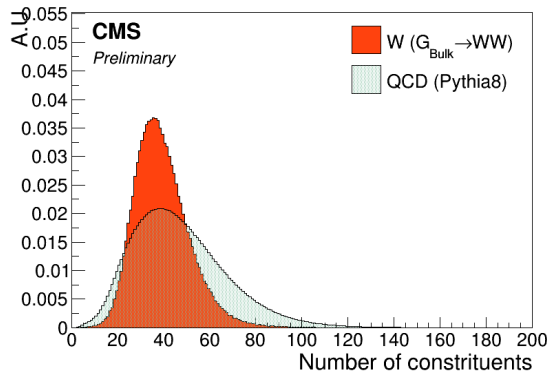


Figure 11.4: The number of jet constituents for signal (red) and background (blue). Only the 20 highest- p_T constituents are used during training.

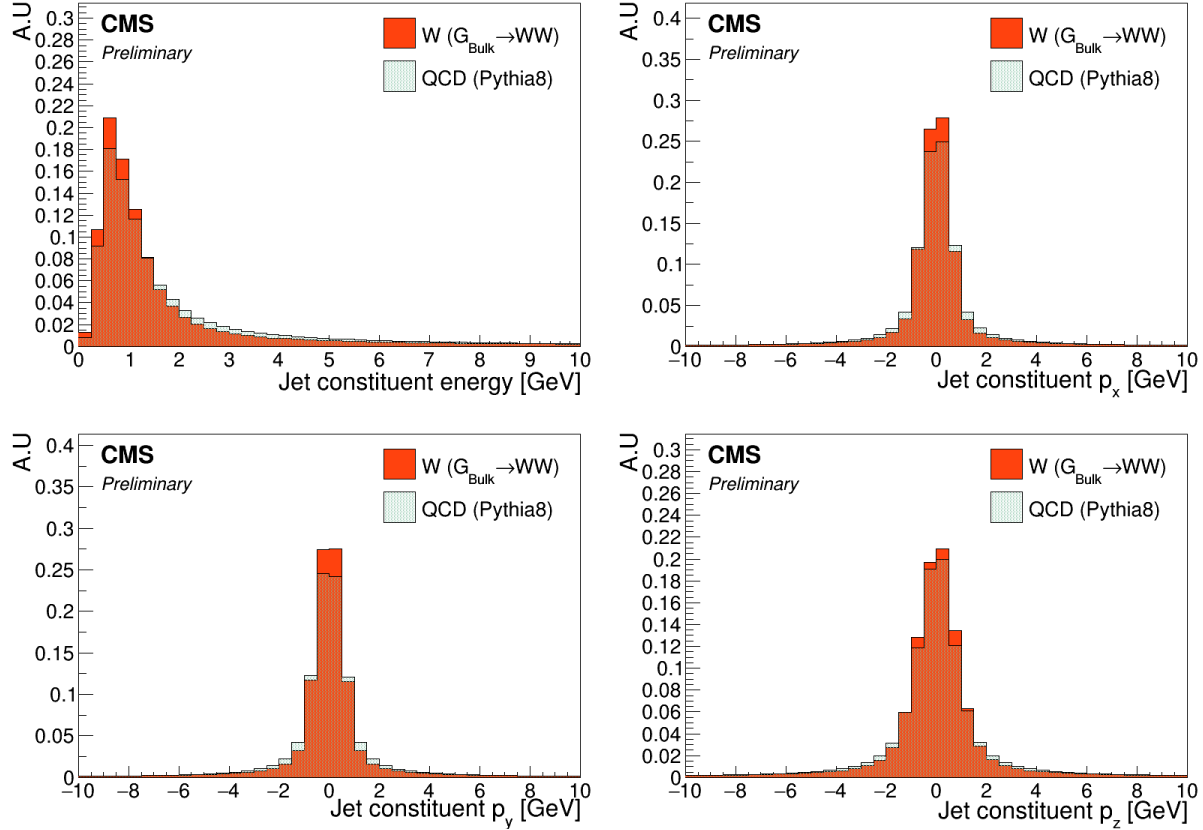


Figure 11.5: Energy (top left), p_x (top right), p_y (bottom left), and p_z (bottom right) for all jet constituents. These values are used as input to the neural network training.

11.1.3 The Combination Layer

The Combination Layer (CoLa) consists of a matrix which, when taking the scalar product with the input matrix, compute linear combinations of the jet constituents, similar to what is done in recombination jet algorithms. The main goal is to create additional four-vectors as input for the next layer. The CoLa matrix is a concatenation of the following: a vector of 1's of length N , the $N \times N$ identity matrix, and a matrix of $N \times M$ trainable weights:

$$C_{i,j} = \begin{pmatrix} 1 & 1 & 0 & \dots & 0 & w_{1,N+2} & w_{1,N+3} & \dots & w_{1,(N+2)+M} \\ 1 & 0 & 1 & \dots & 0 & w_{2,N+2} & w_{2,N+3} & \dots & w_{2,(N+2)+M} \\ \vdots & \vdots & \vdots & \ddots & \vdots & \vdots & \vdots & \dots & \vdots \\ 1 & 0 & 0 & 0 & 1 & w_{N,N+2} & w_{N,N+3} & \dots & w_{N,(N+2)+M} \end{pmatrix}. \quad (11.2)$$

3051 When performing the following multiplication

$$x_{\mu,i}^C = x_{\mu,i} C_{i,j}, \quad (11.3)$$

the resulting output matrix will have dimensions $4 \times (1 + N + M)$ and consists of the following: a first column containing the sum of all constituent momenta, the four-momenta of each individual constituent, and $M=14$ different linear combinations of particles with trainable weights. The first corresponds to the neural network computing the four-vector of the “full” jet, at least the full jet in terms of its 20 highest- p_T constituents. The second simply passes each original constituent four-momentum to the next layer. The final, and most interesting part, lets the network construct alternative subjet four-vectors by letting it weigh constituents up and down as it sees fit, in order to reach optimal discrimination power. As an example, lets look at the effect of CoLa in the simple case of only two input jet constituents and two trainable linear combinations:

$$\begin{pmatrix} E^1 & E^2 \\ p_x^1 & p_x^2 \\ p_y^1 & p_y^1 \\ p_z^1 & p_z^2 \end{pmatrix} \begin{pmatrix} 1 & 1 & 0 & w_{1,4} & w_{1,5} \\ 1 & 0 & 1 & w_{2,4} & w_{2,5} \end{pmatrix} = \begin{pmatrix} E^1 + E^2 & E^1 & E^2 & w_{1,4}E^1 + w_{2,4}E^2 & w_{1,5}E^1 + w_{2,5}E^2 \\ p_x^1 + p_x^2 & p_x^1 & p_x^2 & w_{1,4}p_x^1 + w_{2,4}p_x^2 & w_{1,5}p_x^1 + w_{2,5}p_x^2 \\ p_y^1 + p_y^1 & p_y^1 & p_y^1 & w_{1,4}p_y^1 + w_{2,4}p_y^1 & w_{1,5}p_y^1 + w_{2,5}p_y^1 \\ p_z^1 + p_z^2 & p_z^1 & p_z^2 & w_{1,4}p_z^1 + w_{2,4}p_z^2 & w_{1,5}p_z^1 + w_{2,5}p_z^2 \end{pmatrix}.$$

3052 In the two last columns, the neural network makes two “subjet” four-vectors by weighting the
 3053 relative contribution of each particle as it sees fit. This is similar to jet grooming (Section 6.5.1)
 3054 or PUPPI pileup subtraction (Section 6.3.2), and should allow the network to learn which
 3055 constituents are part of the hard scatter and which are not. The $x_{\mu,i}^C$ matrix is finally passed on
 3056 to the next layer, the Lorentz Layer.

3057 11.1.4 The Lorentz Layer

3058 The Lorentz Layer (LoLa) is responsible for encoding how particles move in space-time through
 3059 a simple set of rules. Each column (four-vector) of $x_{\mu,i}^C$, is used to compute, and afterwards is
 3060 replaced by, the following $k = 7$ features:

$$x_{k,i}^L = \begin{pmatrix} m^2(x_{\mu,i}^C) \\ p_T(x_{\mu,i}^C) \\ w_{ij}^E E(x_{\mu,j}^C) \\ w_{ij}^{s1} \sum d^2(x_{\mu,i}^C, x_{\mu,j}^C) \\ w_{ij}^{s2} \sum d^2(x_{\mu,i}^C, x_{\mu,j}^C) \\ w_{ij}^{m1} \min d^2(x_{\mu,i}^C, x_{\mu,j}^C) \\ w_{ij}^{m2} \min d^2(x_{\mu,i}^C, x_{\mu,j}^C) \end{pmatrix} \quad (11.4)$$

3061 Going through from top to bottom, these are:

- 3062 • the invariant mass and p_T of each four-vector,
- 3063 • a linear combination of all four-vector energies where each is scaled by a trainable weight,
- 3064 • two times the sum of distances between the four-vector under consideration and every other
 3065 column reweighted with a trainable weight, and
- 3066 • two times the minimum distance between the four-vector under consideration and every
 3067 other column where each distance again is reweighted by a trainable weight.

3068 The Minkowski metric enters explicitly in the first and in the last four calculations, where the
 3069 neural network is told to abide by the rules

$$m^2(x_{\mu,i}^C) = g^{\mu\nu} x_{\mu,i}^C x_{\nu,i}^C \quad (11.5)$$

3070 and

$$d^2(x_{\mu,i}^C, x_{\mu,j}^C) = (x_{\mu,i}^C - x_{\mu,j}^C)_\mu g^{\mu\nu} (x_{\mu,i}^C - x_{\mu,j}^C)_\nu \quad (11.6)$$

3071 with $g^{\mu,\nu} = [-1, 1, 1, 1]$, when calculating the invariant mass and distance between all four-vectors
 3072 produced by CoLa. This tells the neural network to use a space-time geometry in all its calculations
 3073 and to respect Lorentz invariance. The four final rows of LoLa are the most interesting: Here
 3074 the network computes quantities similar to n-subjettiness by summing up the distances between
 3075 all constituents, the jet axis and the subjets produced by CoLa. If, for instance, the network

3076 was able to reconstruct the two hard subjets in the final columns of CoLa, which create linear
3077 combinations of particles, it can create its own “ τ_2 ” variable by taking the distance between those
3078 subjets and all the jet constituents, and weighting down the column corresponding to the full
3079 jet four-vector in column one. Then it can do the same by calculating the distance between the
3080 full jet four-vector and all constituents, now weighing down the linear combinations made by
3081 CoLa, and compute “ τ_1 ”. The two custom layers, CoLa and LoLa, therefore come together in
3082 order to encode jet clustering and substructure in a novel way. They provide the network with
3083 the necessary tools in order to create its own physical quantities, through linear combinations
3084 with trainable weights, which then again are used to produce other physical quantities with
3085 new trainable weights. This allows the network full freedom to explore all interesting particle
3086 correlations, where the resulting output features have a physical meaning that can be probed.
3087 LoLa turns the question “What can we teach the machine?” around to “What can we learn from
3088 the machine?”.

3089 11.2 Performance

3090 The deep neural network is trained on 320,000 signal and background jets for up to 100 epochs,
 3091 but allow for an early stopping after ten epochs if the loss is stable. The test sample consists
 3092 of 60,000 W jets and 60,000 quark and gluon jets. To quantify the performance, we look at
 3093 the signal efficiency versus mistagging rate comparing the performance of LoLa to that of the
 3094 taggers used previously in this thesis: PUPPI softdrop with τ_{21} and PUPPI softdrop with τ_{21}^{DDT} .
 3095 The performance of these three different taggers, is shown in Figure 11.6. The point where the
 3096 blue curves end, represent the signal efficiency for a mass cut of $65 < \text{Softdrop jet mass} < 105$
 GeV, here roughly 70%. We clearly see that LoLa performs significantly better than the current

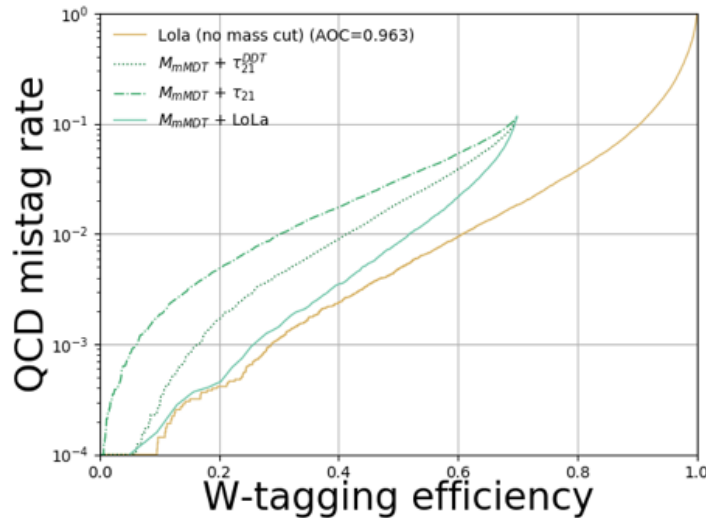


Figure 11.6: Performance of LoLa compared to other W-tagging discriminants in the background-signal efficiency plane: PUPPI softdrop + τ_{21} (dashed blue), PUPPI softdrop + τ_{21}^{DDT} (dotted blue), LoLa with a softdrop mass window applied (solid blue) and the nominal LoLa tagger with no mass cut applied.

3097
 3098 baseline W-taggers based on τ_{21} and τ_{21}^{DDT} , with a roughly 20% higher signal efficiency at a given
 3099 mistagging rate. LoLa also has a higher signal acceptance, as it can be used without a mass
 3100 window applied. If LoLa were to replace the tagger used in Search II (a better comparison than
 3101 Search III as the latter uses a rather unconventional mass window), which has a signal efficiency
 3102 of $\sim 42\%$ at a 2% mistagging rate for a single jet, the signal efficiency for the same mistagging
 3103 rate would be 65%, a 55% increase. For an analysis requiring two tagged jets, that would imply
 3104 going from an 18 to a 43% total signal efficiency, a significant gain.

3105 11.3 Dependence on jet mass and p_T

3106 Despite being a key feature, absolute performance is not all that quantifies how good one tagger
 3107 is compared to another. To use a tagger in a physics analysis, there are three key questions one
 3108 needs to consider:

- 3109 • Is the absolute performance better (compared to common methods)?
- 3110 • Is the tagger p_T -dependent?
- 3111 • Does the tagger sculpt the mass spectrum?

3112 These three measures are important in quantifying performance and, in the following, I will
 3113 attempt to explain why this is the case and which approaches are used here in order to tackle
 3114 them.

3115 Any deep neural network trained to distinguish W jets from quark and gluon jets will naturally
 3116 learn that p_T and mass are discriminating features unless it is penalized for it. Figure 11.7 shows
 the LoLa discriminant as a function of jet p_T and softdrop jet mass. A strong correlation between

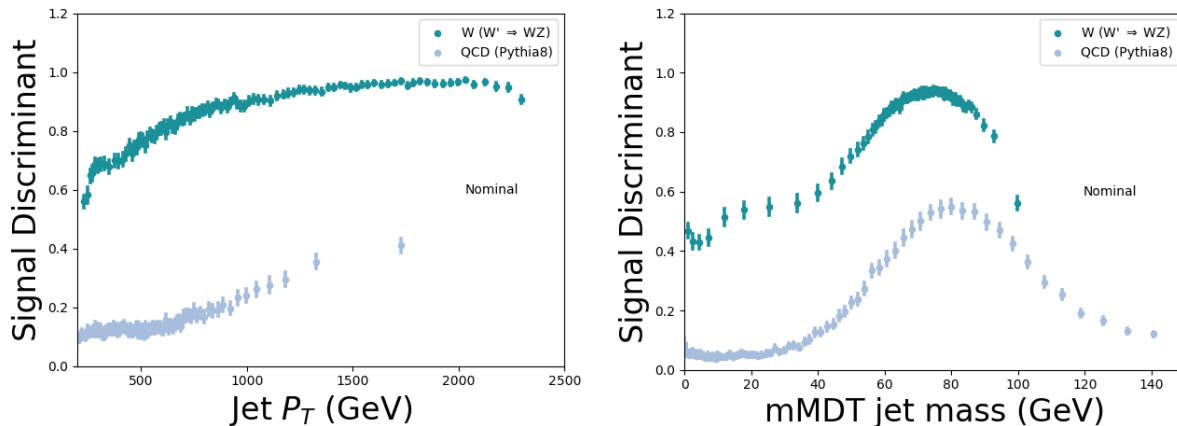


Figure 11.7: The LoLa discriminant as a function of jet p_T (left) and softdrop jet mass (right). A strong correlations with both variables is observed.

3117
 3118 the LoLa discriminant and jet mass and p_T , is observed both for signal and for background jets
 3119 (closer to 1 means more signal like), with a rising slope as a function of p_T (meaning the network
 3120 interprets a higher jet p_T as being more signal-like) and a bump around the W mass for both
 3121 signal and for background.

3122 11.3.1 p_T -decorrelation

3123 A tagger which is p_T -dependent is problematic due to the following reasons: firstly, the signal
 3124 efficiency is variable, which requires a working point that scales with p_T . That in itself is not
 3125 problematic and can easily be computed. However, it implies that when computing efficiency
 3126 scale factors from data, a range of different scale factors for different working points is required.
 3127 In addition, the scale factors are measured at low p_T , a region where the tagging efficiency can
 3128 be substantially different from the analysis signal region due to the strong p_T -correlation present.
 3129 Finally, the dijet invariant mass is intrinsically linked to the p_T -spectrum, meaning that any
 3130 p_T -dependence can introduce sculpting of the dijet invariant mass spectrum. From the top left
 3131 plot in Figure 11.3, one clearly sees that the jet p_T distribution is very different for signal and for
 3132 background. In order to avoid that the network learns jet p_T to be a discriminating feature, I
 3133 therefore compute a jet-by-jet weight intended to flatten the jet p_T spectrum. This weight is passed
 3134 as a sample weight to the training set, reweighting the contribution from each jet to the total loss
 3135 (making high-mass QCD jets and low-mass signal jets count more). Figure 11.8 shows the jet
 3136 p_T -distribution without any p_T -reweighting applied (solid lines) and after applying a p_T -weight
 (dashed lines). The training is then repeated, this time passing a sample weight with each jet,

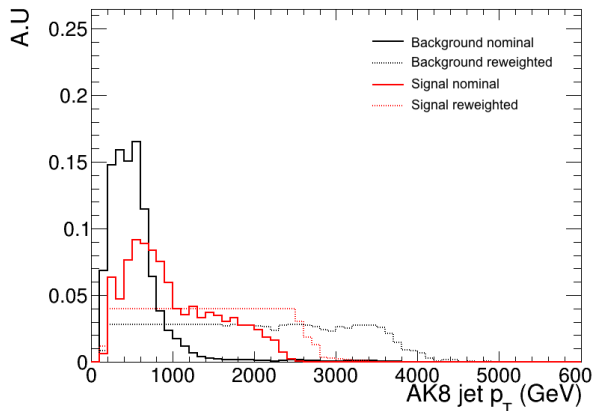


Figure 11.8: Jet p_T distribution before (solid lines) and after (dashed line) applying a weight intended to flatten the jet p_T spectrum.

3137
 3138 and the final discriminant compared to the nominal training. Figure 11.9 shows the performance
 3139 of the same taggers as above but with one additional line, which is LoLa p_T -reweighted. A
 3140 clear drop in performance is observed, as expected when removing information from the training.
 3141 However, when we again look at the discriminant output as a function of jet p_T in Figure 11.10,
 3142 the correlation we observed before has vanished and we are left with a tagger not depending

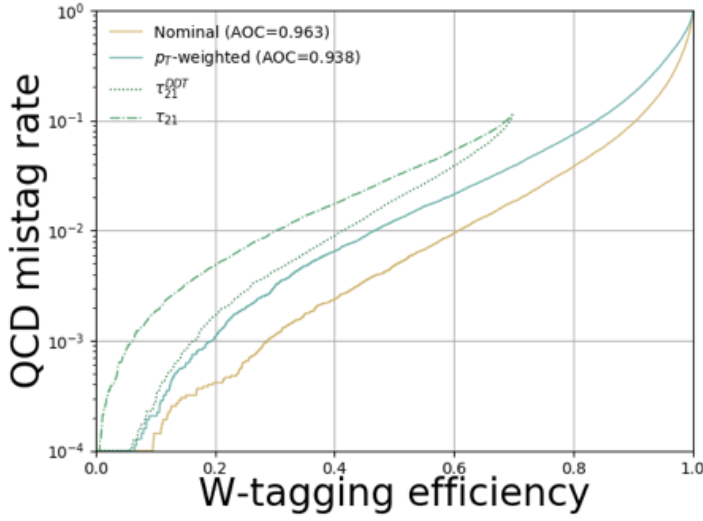


Figure 11.9: Performance of the p_T -reweighted LoLa tagger (solid blue) and the nominal LoLa tagger (solid yellow).

on the jet p_T . For completeness, Figure 11.11 shows the τ_{21} and τ_{21}^{DDT} discriminants versus jet

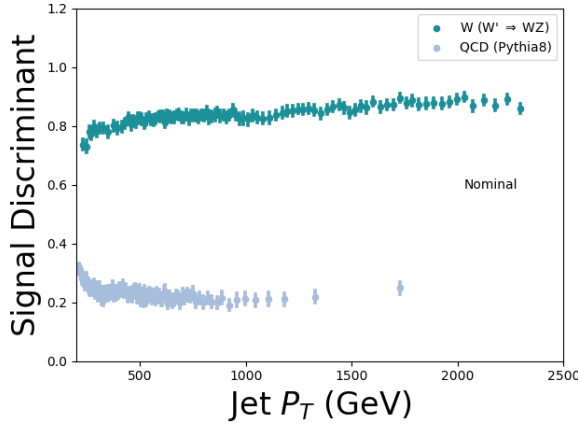


Figure 11.10: The LoLa discriminant as a function of jet p_T after training with a weight intended to flatten the sample p_T spectrum.

3143

3144 p_T . Whereas the nominal LoLa discriminant had a much larger correlation with jet p_T than
 3145 the τ_{21} -based taggers, the p_T -reweighted version is as decorrelated from p_T as the τ_{21} variables
 3146 while still exhibiting a better absolute performance than the baseline taggers. In summary,
 3147 reweighting strategies such as the one described above yield a loss in overall performance, as
 3148 expected when removing information from the training. However, the p_T dependence of the

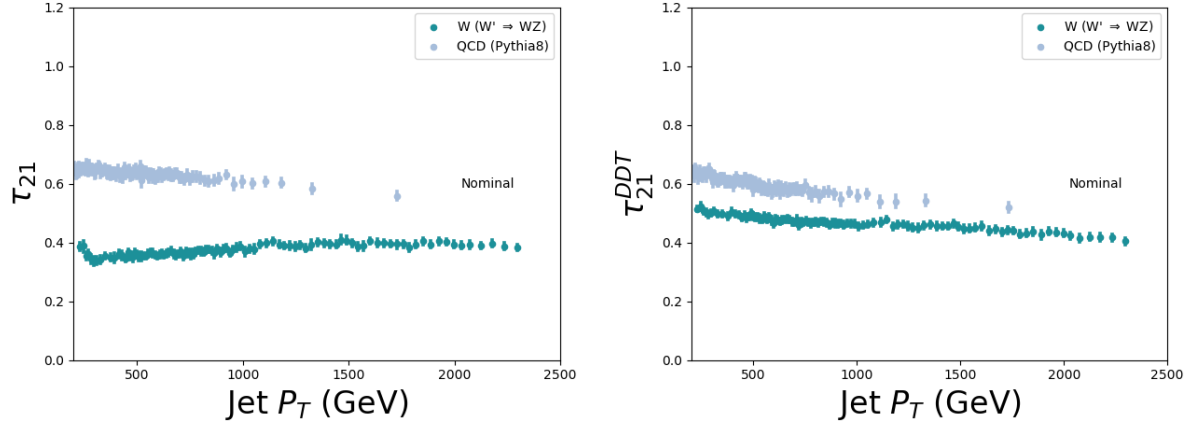


Figure 11.11: The τ_{21} (left) and τ_{21}^{DDT} (right) discriminant as a function of jet p_T .

tagger is strongly reduced, meaning that it might perform better overall in physics analysis when systematic uncertainties are taken into account. There is therefore no clear answer as to which method is better before running a full analysis including systematics for p_T -dependent tagging.

11.3.2 Mass sculpting

Any smart deep neural network intended to separate W bosons from quarks and gluons will inevitably learn the W boson mass as it clearly is very different from the quark or gluon mass. Unfortunately, as these taggers are meant to be used in physics analyses where we often estimate the background in mass sidebands, this has some undesired side effects. If a deep neural network has learned the mass then, after applying a cut on the discriminant, the background jet mass distribution becomes severely sculpted and difficult to constrain.

After applying a cut on the LoLa discriminant corresponding to a 1% mistagging rate, we see in the left plot of Figure 11.12 that the W-jet signal shape is nicely retained. In addition, there are no QCD jets left at low mass so no jet mass window is needed when using this tagger, leading to a significantly higher signal acceptance. However, when looking more closely at the QCD background on the right plot of Figure 11.12, where all histograms are normalized to unit area, we see that the bulk of the remaining 1% QCD jets is right below the W-boson mass peak and has been sculpted to look exactly like the signal. This mass sculpting is in and on its own not a problem, the tagger still manages to get rid of most of the background. However, in many physics analyses, in order to evaluate the background rate in the data signal region, mass sidebands are used. If the background distribution is peaky rather than smoothly falling, the shape and consequently the expected yield is very difficult to constrain. That leads to large uncertainties

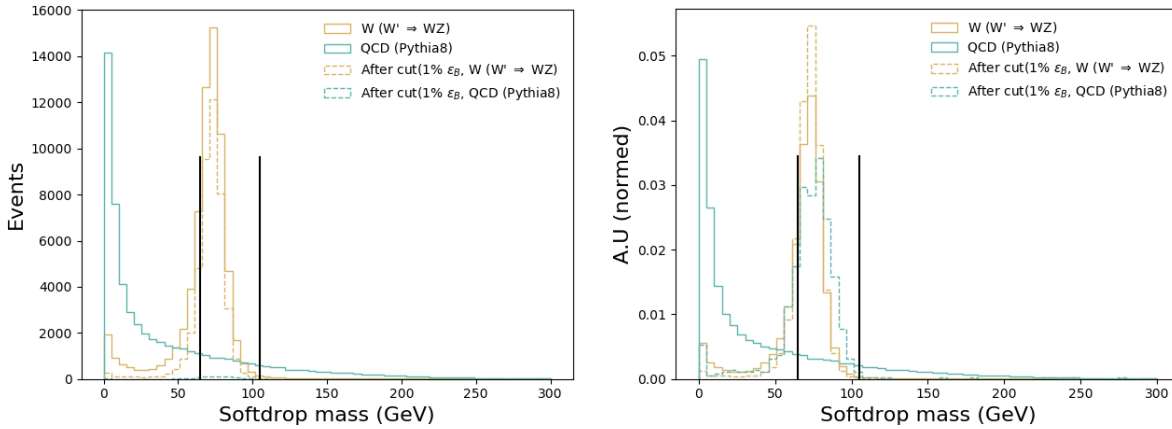


Figure 11.12: The softdrop jet mass distribution before (solid lines) and after (dotted lines) a cut on the LoLa discriminant corresponding to a 1% mistagging rate has been applied. The left plot shows the real number of events left after the cut, the right is normalized to area.

3170 on the background rate and might eventually make an analysis less sensitive than when using
 3171 a tagger with a worse absolute performance, but reduced mass correlation. In addition, if one
 3172 were to search for peaks in the softdrop jet mass, as is the case for the multidimensional fit, this
 3173 becomes increasingly difficult when attempting to fit a potential signal peak on top of a peaking
 3174 background.

3175 It should again be mentioned, that also for the baseline taggers based on τ_{21} , mass sculpting
 3176 is a known feature. Figure 11.13 shown the same softdrop jet mass spectrum before and after
 3177 a cut corresponding to a 1% mistagging rate on τ_{21} (left) and τ_{21}^{DDT} (right). Here τ_{21} clearly
 3178 exhibits mass sculpting, but is not as peaky as was the case for LoLa. The τ_{21}^{DDT} exhibits the
 3179 least amount of sculpting, but is also the tagger with the worst absolute performance.

3180 I have not yet had the chance to implement a mass decorrelation strategy for LoLa, but I
 3181 see two ways going forward: the first is, following the example of what was done to decorrelate
 3182 LoLa from jet p_T , to pass a mass-dependent sample weight to the training. LoLa would then be
 3183 trained with a weight derived to flatten the two dimensional jet mass - jet p_T plane. Another
 3184 option would be to train LoLa together with an adversarial, a dedicated deep neural network
 3185 running in parallel to LoLa and attempting to learn the jet mass from the LoLa output. The
 3186 total loss function would then be a sum of the two, where the better the adversarial is in learning
 3187 the mass, the worse the total loss function gets. Both of these options are something I would like
 3188 to explore in the future.

3189 In summary, mass- and p_T -dependence are in their own right not a problem for a tagger.
 3190 The problem occurs when using these taggers in actual physics analyses where background rate

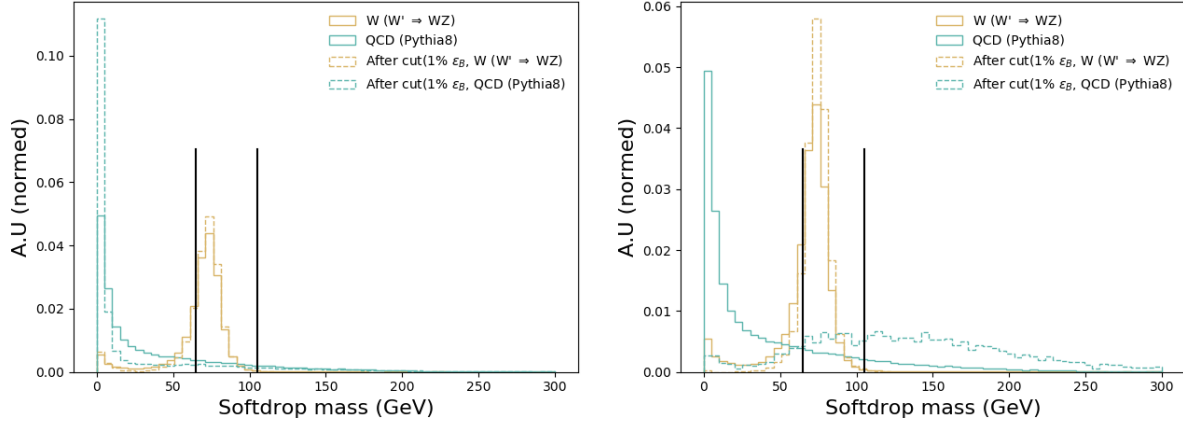


Figure 11.13: The softdrop jet mass distribution before (solid lines) and after (dotted lines) a cut on τ_{21} (left) and τ_{21}^{DDT} (right). All spectra are normalized to unit area.

3191 uncertainties and tagging p_T -dependence uncertainties have a large impact on the final sensitivity.
 3192 There is a trade-off between signal efficiency and (analysis-dependent) systematics. For LoLa,
 3193 rather than choosing, I would like to provide two different taggers: a nominal tagger, where no
 3194 mass/ p_T -decorrelation is attempted, and a decorrelated version. That would allow for both to be
 3195 tested in a full analysis chain before deciding on which tagger to use when looking at data.

3196 11.4 Validation

3197 LoLa is additionally validated on independent samples as an unbiased measure of performance,
 3198 allowing the comparison of different CMS W-tagging algorithms. The sample is based on a
 3199 $Z' \rightarrow WW$ sample with $M_{Z'} = 3$ TeV produced with MadGraph and a QCD PYTHIA 8 sample.
 3200 Here, only jets with $1000 \text{ GeV} < p_T < 1400 \text{ GeV}$ and $|\eta| < 1.5$ are used. The signal efficiency
 3201 versus mistagging rate for LoLa compared to the baseline PUPPI softdrop + τ_{21} tagger is shown
 3202 in Figure 11.14. As was pointed out in Section 11.2, a mass selection is not necessary when using
 3203 LoLa, but has been added to this plot for completeness. A significant improvement in tagging
 3204 efficiency is observed for LoLa compared to the default tagger, also when being validated on a
 3205 sample completely independent from the training sample. A selection corresponding to a 30%
 3206 signal efficiency is used as a reference working point when studying the tagging performance
 3207 as a function of jet p_T and pileup in the following, and is marked by triangles in Figure 11.14.
 3208 The signal efficiency and mistagging rate as a function of jet p_T is shown in Figure 11.15. Again
 3209 we observe the strong correlation between LoLa tagging efficiency and jet transverse momenta.

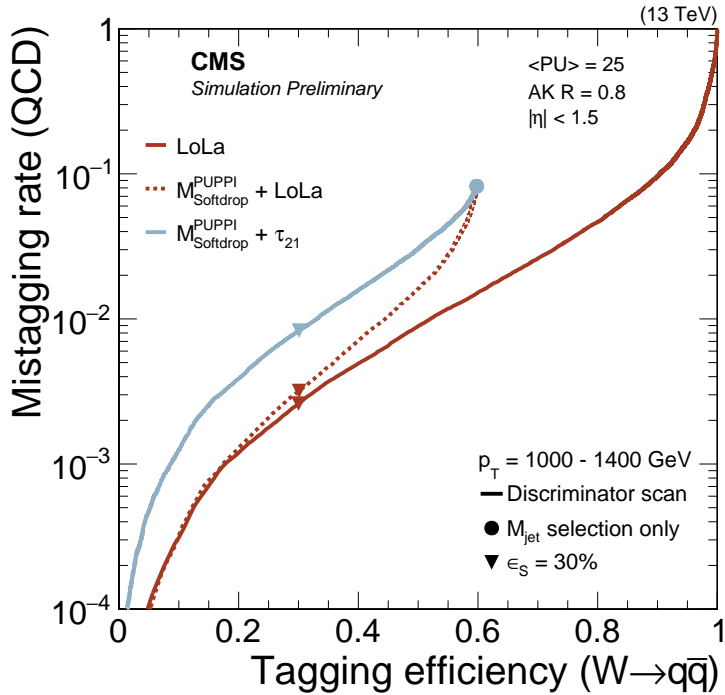


Figure 11.14: Performance of LoLa and PUPPI softdrop + τ_{21} in the background-signal efficiency plane. The PUPPI softdrop jet mass selection of $65 < M_{SD} < 105 \text{ GeV}$, and the 30 percent efficiency points are indicated with symbols.

3210 There is, however, no value for which the τ_{21} tagger has a higher signal over background ratio
 3211 than LoLa. LoLa performs its worst at very high jet p_T , but in this region the background is very
 3212 small (dijet invariant masses around 2.5-3 TeV), so the absolute performance here matters less
 3213 than at lower p_T . Figure 11.16 shows the tagging efficiency and mistagging rate as a function of
 3214 pileup. Both taggers under study are more or less decorrelated from pileup, with a flat efficiency
 3215 for up to 50 reconstructed primary vertices. In Run 3, this number is of course expected to
 3216 be significantly higher and the study should be redone up to a higher number of reconstructed
 3217 primary vertices.

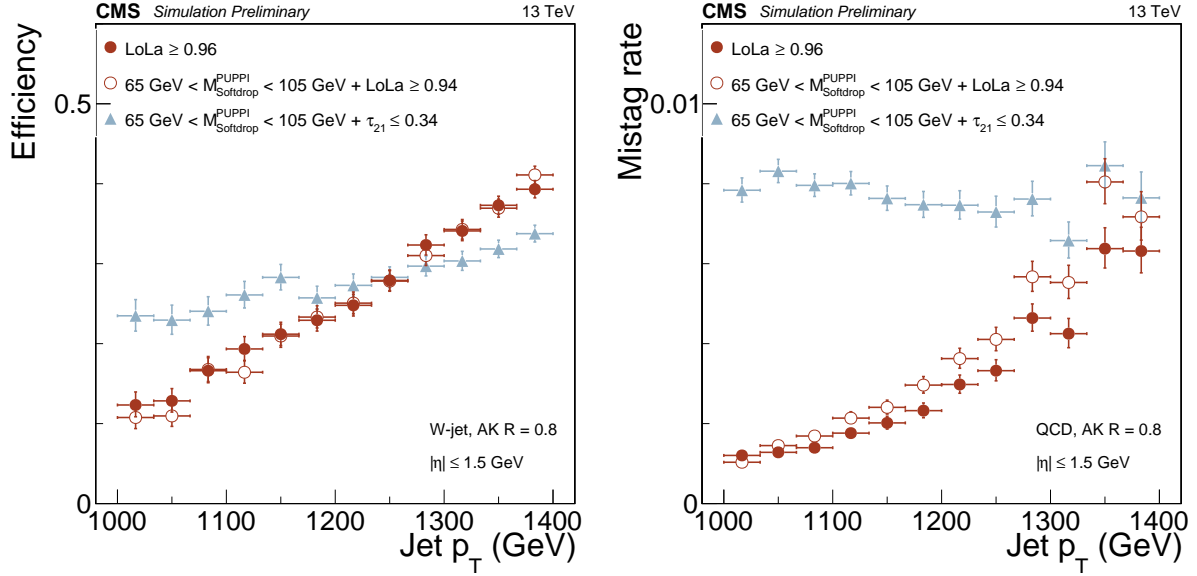


Figure 11.15: Efficiency (left) and mistagging rate (right) of the LoLa selection corresponding to a 30 percent signal efficiency as a function of jet p_T .

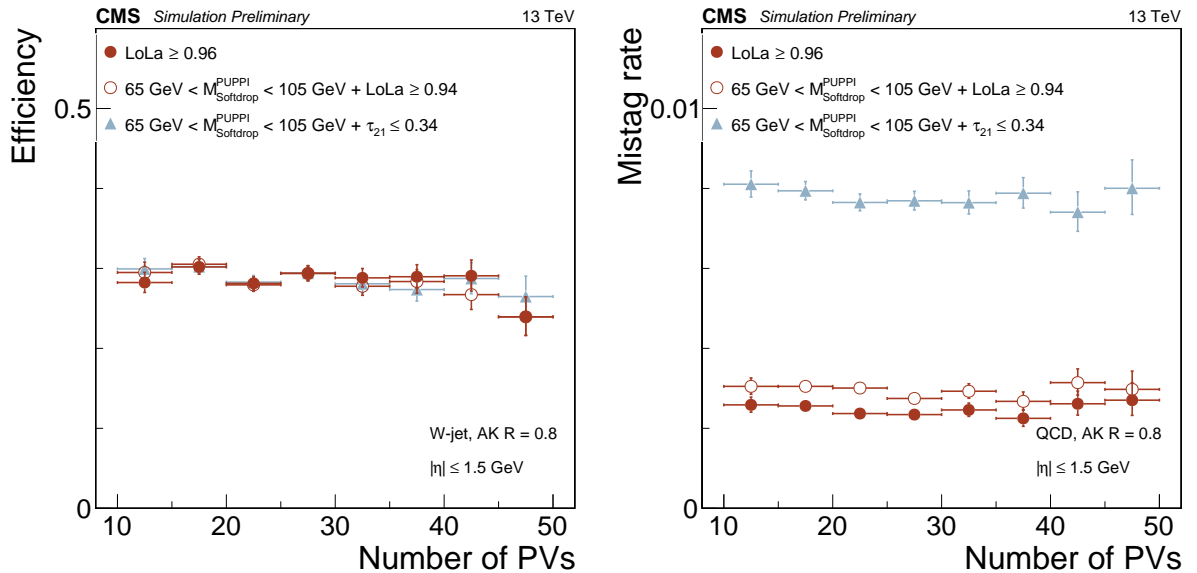


Figure 11.16: Efficiency (left) and mistagging rate (right) of the LoLa selection corresponding to a 30 percent signal efficiency as a function of the number of reconstructed vertices.

₃₂₁₈ **11.5 What *does* LoLa learn?**

₃₂₁₉ As a first study of what features LoLa learns, one can remove features in the LoLa and Cola
₃₂₂₀ layers. The first thing to check is what happens after removing variables sensitive to the jet
mass and p_T . This is shown in Figure ???. The light blue line, no $\sum p_T$, corresponds to removing

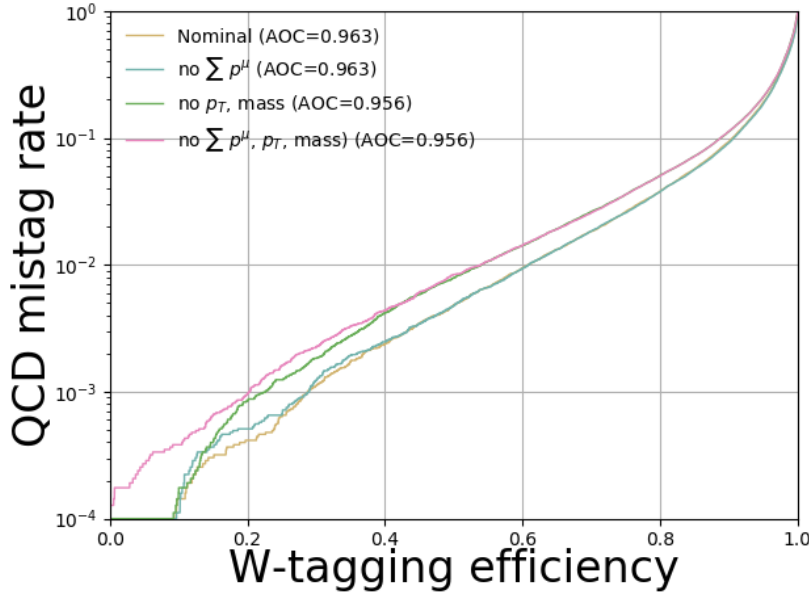


Figure 11.17: Performance after removing jet mass momentum and mass.

₃₂₂₁
₃₂₂₂ the first column of CoLa which passes the sum of all particle four-momenta to LoLa. This has
₃₂₂₃ little impact on the total performance, meaning the algorithm does not rely on the jet axis
₃₂₂₄ being defined. Removing the Lola variables that correspond to the invariant mass or p_T of the
₃₂₂₅ particles/pseudo-jets (green line) reduce the performance significantly, which explains the large
₃₂₂₆ drop in tagging efficiency that was observed in Section ?? when decorrelating the tagger from jet
₃₂₂₇ p_T . The worst performance is obtained when removing both the first CoLa column, which roughly
₃₂₂₈ corresponds to the jet axis, as well as the invariant mass and p_T LoLa variables (pink line). This
₃₂₂₉ implies that a significant part of what LoLa learns is, as suspected, related to the jet mass and p_T .
₃₂₃₀ We can also systematically go through the CoLa and LoLa variables and systematically removing
₃₂₃₁ one after the other. This is shown in Figure ??.

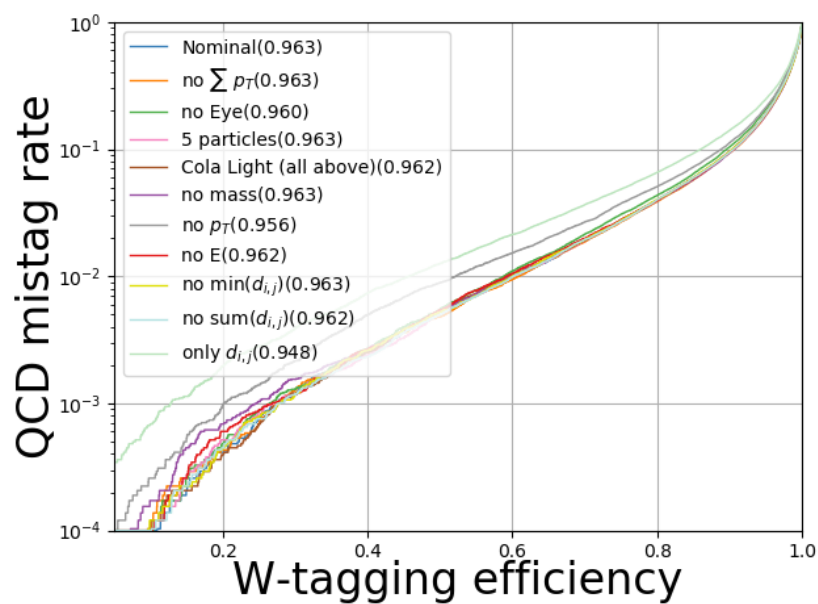


Figure 11.18: Performance after removing components of CoLa or LoLa

3232

CHAPTER 12

3233

Summary

3234 In this part of the thesis, we have seen a promising new W-tagging algorithm for future VV
3235 searches. Its absolute performance is better than that of the baseline PUPPI softdrop + τ_{21}
3236 tagger up to a jet p_T of at least 1400 GeV, roughly corresponding to a dijet invariant mass of
3237 2.5-3 TeV, and could lead to an increase in total signal efficiency from 18 to 43 % for the searches
3238 presented here. With a p_T decorrelation method already in place, it could already now be used
3239 for the one dimensional VV search presented in Search I and Search II. However, if to be used in
3240 the multidimensional search framework, a mass decorrelation method needs to be established. I
3241 have already outlined two possibilities of how to achieve this in Section 11.3.2, where one of these
3242 has already been shown to work in the context of p_T -decorrelation. This is, as of this writing, left
3243 to future studies.

3244

3245 When discussing the future of the multidimensional search, I mentioned how a deep neural
3246 network such as the one presented here could be used to encode jet substructure in a way useful in
3247 order to develop a generic anti-QCD tagger. This has already been achieved by a parallel analysis
3248 team through the use of auto-encoders, published ten days before this writing and documented
3249 in [84], and has shown very promising results. However, this strategy is to my knowledge, after
3250 discussing with the authors, no longer pursued after observing that the auto-encoder version of
3251 LoLa was very difficult to decorrelate from the jet mass. It is my belief that this can be overcome
3252 by changing some of the features calculated in the Lorentz Layer (in [84], only the invariant mass
3253 is calculated and the other features listed in Equation 11.4 are removed) and this is an idea I
3254 would like to pursue in future studies in order to achieve a truly generic search for boosted dijet
3255 resonances in the $M_{\text{jet}1}$ - $M_{\text{jet}2}$ - M_{VV} plane.

3256

Part V

3257

Final conclusions and outlook

3258 In this doctoral thesis I have presented three searches for new, heavy resonances decaying to two
 3259 vector bosons in the all-hadronic final state, using datasets collected by the CMS experiment
 3260 corresponding to an integrated luminosity of 2.7 (2015), 35.9 (2016) and 77.3 (2016+2017) fb^{-1} .
 3261 Due to the high energy (“boost”) of the vector bosons, their decay products are so collimated
 3262 that they get merged into one single jet, leading to a dijet final state topology. Dedicated jet
 3263 grooming and jet substructure techniques are therefore explored in order to discriminate vector
 3264 bosons from the overwhelming QCD multijet background.

3265 Each of the analyses presented has provided original contributions to the field: the first search
 3266 was the first of its kind to ever be performed at $\sqrt{s} = 13 \text{ TeV}$, following an observed excess
 3267 of $3.4 (1.3) \sigma$ by ATLAS (CMS) in the 8 TeV dataset, and the first time CMS demonstrated
 3268 the efficiency of using jet-grooming techniques at trigger level. It, at the time, set the most
 3269 stringent limits to date for the signal scenarios under consideration. The second search introduces
 3270 a novel pileup-resistant and perturbative-safe vector boson tagging algorithm based on using
 3271 PUPPI for pileup subtraction, and softdrop for jet grooming, ensuring a high and stable signal
 3272 efficiency up to a pileup of at least 50 interactions per event. The optimization, validation, and
 3273 full commissioning of the tagger was performed in the context of this search. Dedicated jet mass
 3274 corrections, in order to account for an observed p_T and η dependence in PUPPI softdrop jet mass,
 3275 due to the nature of the softdrop algorithm, were also developed. The tagger based on PUPPI
 3276 with softdrop, together with the jet mass corrections, became, and still is, the recommended
 3277 algorithm for W-tagging in CMS.

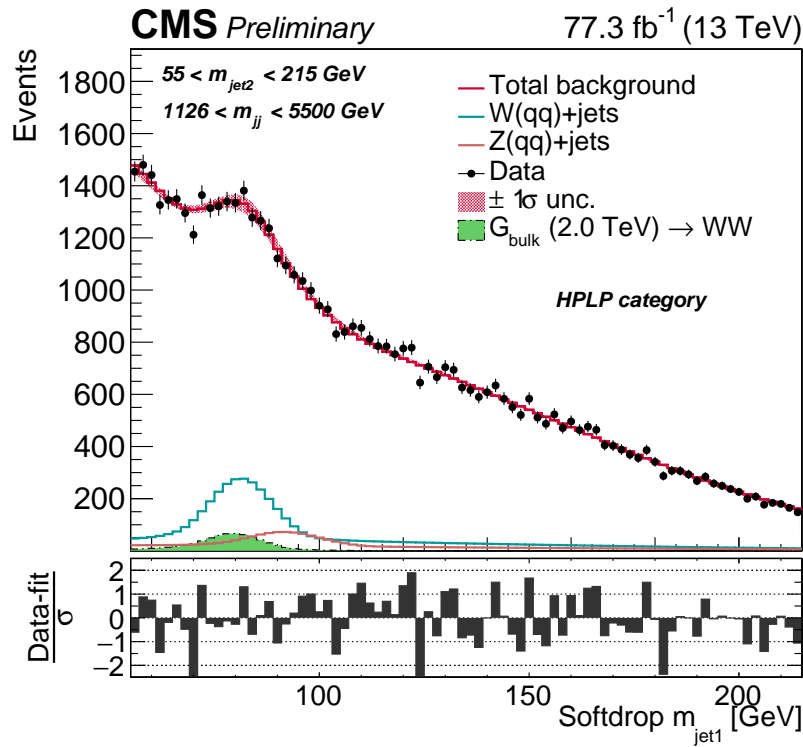
3278 The final analysis introduces a brand new way of doing diboson resonance searches through a
 3279 three-dimensional fit of the dijet invariant mass and the masses of the two jets. By optimizing
 3280 the W-tagging algorithm used in this search and due to the nature of the search method, we have,
 3281 for the first time, been able to constrain the jet mass scale and resolution from a boosted $W(\bar{q}q)$
 3282 and $Z(\bar{q}q)$ peak produced by the V+jets standard model process. The method itself leads to a
 3283 20-30 % higher sensitivity than the default search method.

3284 The benefit of using a three-dimensional fit based on dijet invariant mass and the masses of the
 3285 two jets, is that one can look for resonances peaking anywhere in the jet mass and dijet invariant
 3286 mass spectrum. The natural next step for this search is therefore the incorporation of $VH(bb)$
 3287 and $H(bb)H(bb)$ final states into the three-dimensional fit framework, where orthogonality is
 3288 guaranteed through b-tagging categories. This process is ongoing and planned for the full Run 2
 3289 dataset (including the data collected in 2018).

3290 Going further, one can incorporate searches for generic resonances peaking anywhere in the
 3291 softdrop jet mass and dijet invariant mass spectrum in the multi-dimensional fit, where the jets
 3292 themselves can have substructure compositions other than two subjets. This type of model-

3293 independent search requires a generic anti-QCD tagger in order to be truly model independent.

3294 In the final chapter of this thesis I presented ongoing work on a W-tagging algorithm
 3295 using a deep neural network for future searches, capable of more than doubling the analysis signal
 3296 efficiency by incorporating jet substructure algorithms within the deep layers. As there will be
 3297 no center-of-mass energy increase after the LHC reaches 14 TeV, achieving the best possible
 3298 analysis sensitivity for the dataset to come will be of key importance. I also showed how such a
 3299 deep neural network model is the ideal starting point for building a signal-independent anti-QCD
 3300 tagger. With $\sim 80 \text{ fb}^{-1}$ of 13 TeV data analyzed and no excess observed, the future of this
 3301 search therefore lies in increasing the analysis sensitivity through novel taggers, as the one I have
 3302 presented here, and, making the search strategy as generic as possible through multi-dimensional
 3303 scans and generic anti-QCD taggers, both of which have a foundation now built within this
 3304 doctoral work.



3306

APPENDIX A

3307

V-tagging

3308 A.1 mMDT and underlying event

3309 Signal jets groomed with mMDT using a y_{cut} definition, $\min(p_{T,s_1}^2, p_{T,s_2}^2) \Delta R(s_1, s_2) / m_j^2 > y_{cut}$,
 3310 rather than a z_{cut} definition (as is default in CMS), $\frac{\min(p_{T,i}, p_{T,j})}{p_{T,P}} > z_{cut}$, were found to be far more
 3311 sensitive to the underlying event than pruned jets [73]. Figure A.1 shows the signal efficiency for
 3312 pruning (left) and softdrop (right) as a function of jet transverse momenta when including final
 3313 state radiation (FSR) only, final and initial state radiation (ISR), hadronization, and hadronization
 with an underlying event component added. At parton level, as well as after hadronization, the

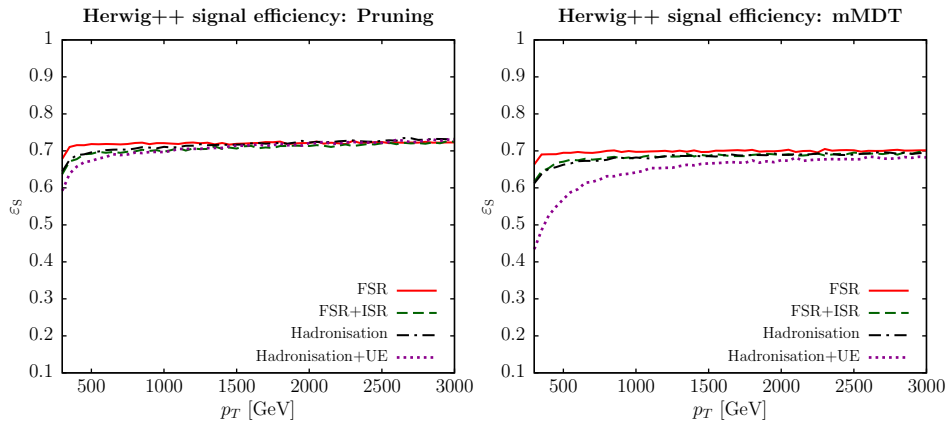


Figure A.1: The signal efficiency for pruning (left) and softdrop (mMDT) (right) as a function of jet p_T when adding FSR, ISR, hadronization and UE. The UE has a severe impact on the softdrop efficiency for signal jets [73].

3314 two algorithms perform very similar as a function of p_T . However, once UE contamination is
 3315 added, the softdrop tagging efficiency is severely affected. This can be explained by the larger
 3316 effective radius considered by the mMDT algorithm ($\propto m_V/p_T \sqrt{z_{cut}(1 - z_{cut})}$) in comparison
 3317 to pruning ($\propto m_V/p_T$), as can be seen from Equations 6.9 and 6.8. This observation corresponds
 3318 very well with the shift in jet mass we observed for softdrop as a function of p_T in Section 7.4.3:
 3319 as the jet p_T decreases, the mMDT effective radius increases and the jet mass mean shifts to
 3320 higher values, due to absorbing more background radiation.

3322 A.2 N-subjettiness on groomed jets

3323 In CMS, n-subjettiness is by default calculated on un-groomed jets. A proposal was made in
 3324 Ref. [91] to, when calculating n-subjettiness, calculate τ_2 on softdrop $\beta = 2$ jets (less aggressive
 3325 groomer) τ_1 on softdrop $\beta = 0$ jets (more aggressive groomer). This would emphasize the jet
 3326 hard substructure when calculating 1-subjettiness and the full color radiation pattern when
 3327 calculating 2-subjettiness. In the above mentioned reference, this was shown to increase the signal
 3328 significance by 25% (at 2 TeV) for a given mistagging rate, as shown in Figure A.5 and also
 reduce non-perturbative effects by a factor of 2 to 3. In this section, we study the performance

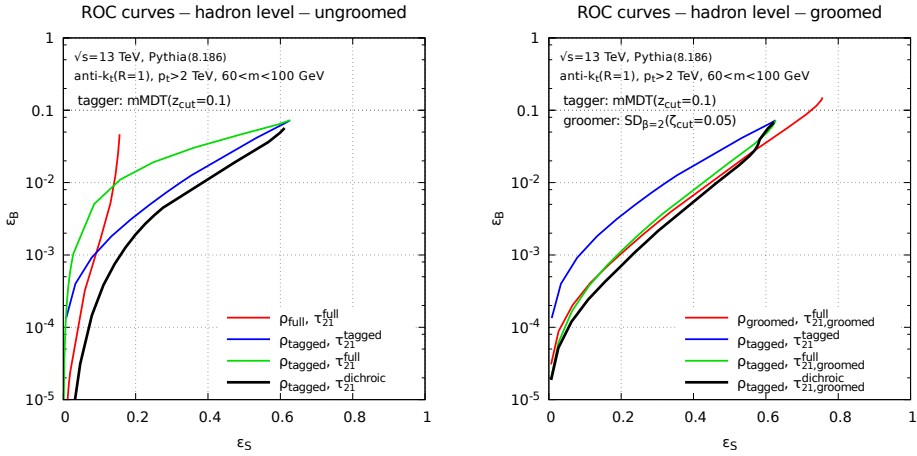


Figure A.2: Using a dichroic tagger has been to increase the signal significance by 25% at a jet p_T of 2 TeV and reduce non-perturbative effects by a factor of 2 to 3 [91].

3329
 3330 of n-subjettiness when used in combination with different versions of softdrop, varying the
 3331 β -parameter. Different values of β results in the algorithm removing more or less radiation. In
 3332 this section we study three groomer definitions: mMDT (softdrop with $\beta = 0$), softdrop with
 3333 $\beta = 2$ and the un-groomed (plain) mass. The mass distribution after applying these algorithms
 3334 is shown in Figure A.3. The current CMS default for V-tagging at the time of this study was
 3335 softdrop $\beta = 0$ and τ_{21} , where τ_{21} was calculated on the un-groomed jet. N-subjettiness can
 3336 be calculated starting from un-groomed jets or jets groomed with different algorithms. Going
 3337 from the most to the least aggressive, the ones studies here are τ_{21} on softdrop $\beta = 0$ jets, τ_{21}
 3338 on softdrop $\beta = 2$ jets, dichroic τ_{21} (τ_2 from softdrop $\beta = 2$ and τ_1 from softdrop $\beta = 0$ jets)
 3339 or τ_{21} calculated on un-groomed jets. The distributions of these are shown in Figure A.4. The
 3340 performance in the signal efficiency versus mistagging rate plane for different versions of τ_{21} , is
 3341 shown in Figure A.5. A cut on the softdrop $\beta = 0$ jet-mass of 65-105 GeV is applied by default

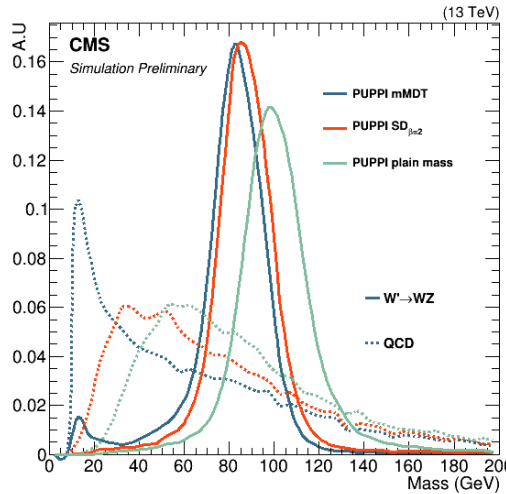


Figure A.3: The bare PUPPI (turquoise), softdrop $\beta = 0$ (blue), and softdrop $\beta = 2$ (red) jet-mass.

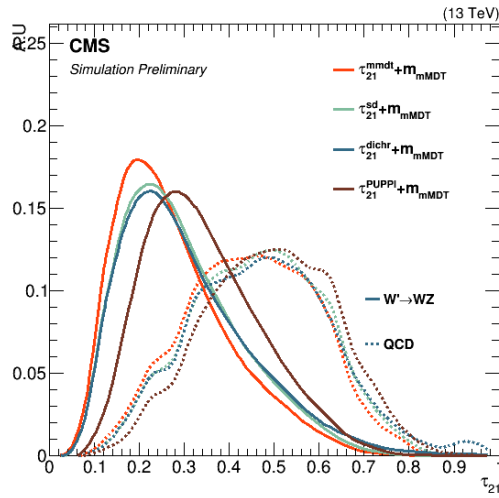


Figure A.4: N-subjettiness distributions after the algorithm has been applied to un-groomed jets (brown, CMS default), or on jets groomed with softdrop $\beta = 0$ (red), softdrop $\beta = 2$ (turquoise) or a mix of both, so-called dichroic (blue), where softdrop $\beta = 0$ is used for τ_1 and softdrop $\beta = 2$ is used for τ_2 .

for all taggers. The CMS default tagger, τ_{21} in combination with softdrop $\beta = 0$ has the lowest signal efficiency for a given mistagging rate. The best performance is achieved when calculating n-subjettiness on softdrop $\beta = 0$ groomed jets. No huge gain in performance is observed when using a dichroic tagger.

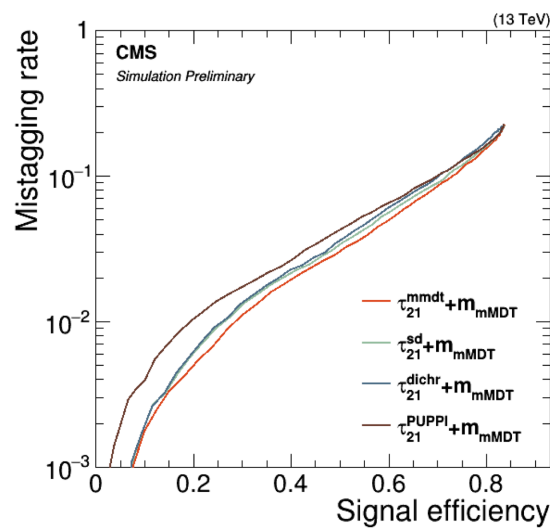


Figure A.5: Performance of a tagger consisting of a selection on the softdrop $\beta = 0$ jet mass of 65-105 GeV and a cut on n-subjettiness computed on groomed or un-groomed jets

3346

APPENDIX B

3347

Search I: Limits per mass category

3348 B.1 Limits per mass category

3349 The asymptotic limits obtained with 2.6 fb^{-1} of 13 TeV CMS data per mass and purity category.

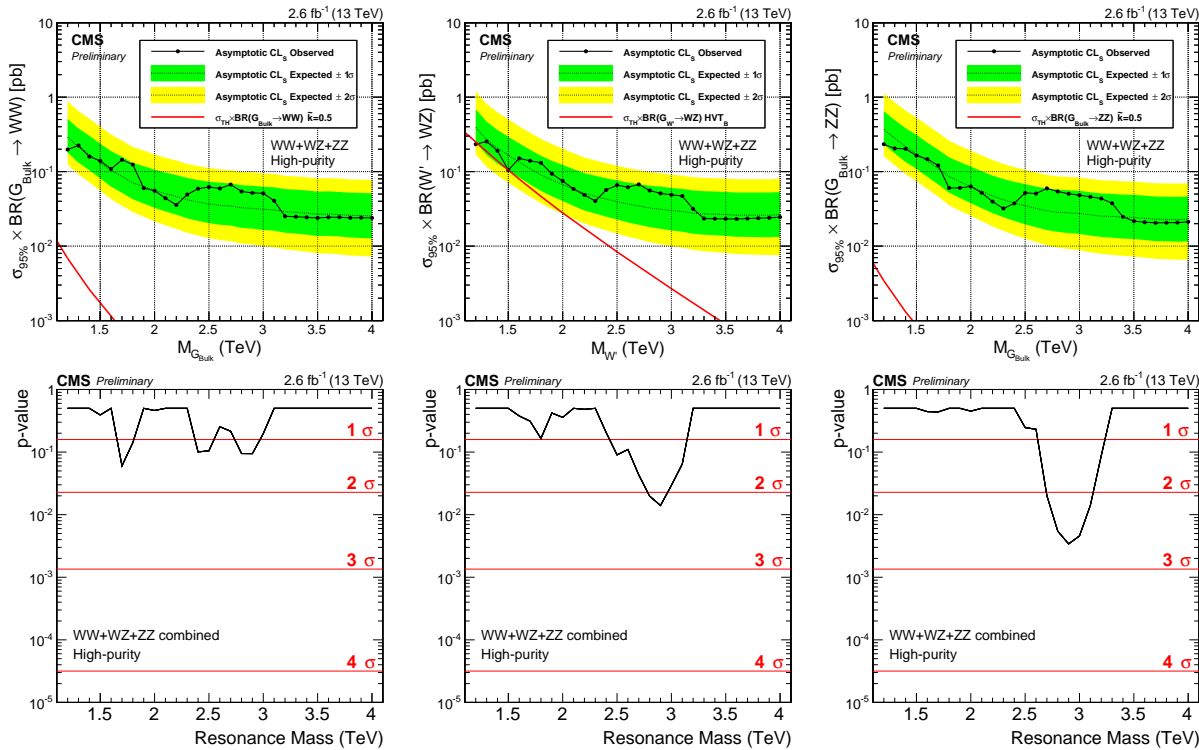


Figure B.1: Expected and observed limits at 95% CL and corresponding p-values obtained in the high purity category using 2.6 fb^{-1} of CMS data. Here for a Bulk $G \rightarrow WW$ (left), $W' \rightarrow WZ$ (middle) and $G \rightarrow ZZ$ (right) signal.

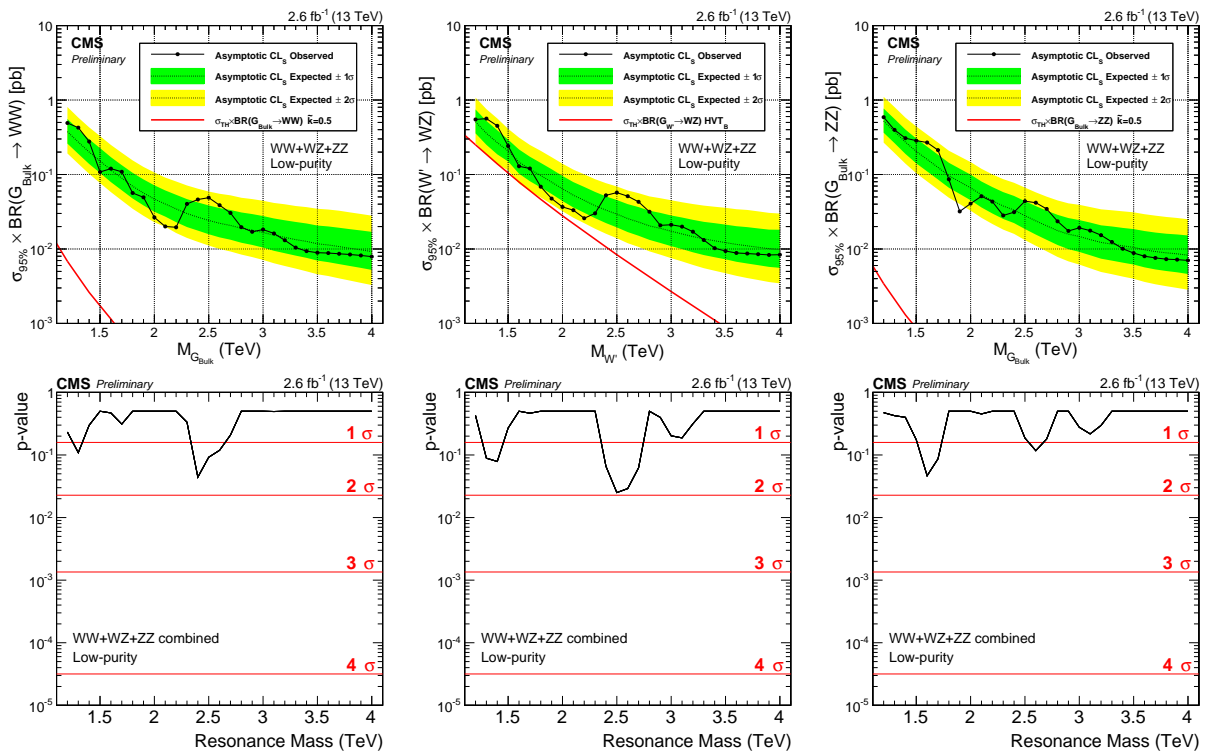


Figure B.2: Expected and observed limits at 95% CL and corresponding p-values obtained in the low purity category using 2.6 fb^{-1} of CMS data. Here for a Bulk $G \rightarrow WW$ (left), $W' \rightarrow WZ$ (middle) and $G \rightarrow ZZ$ (right) signal.

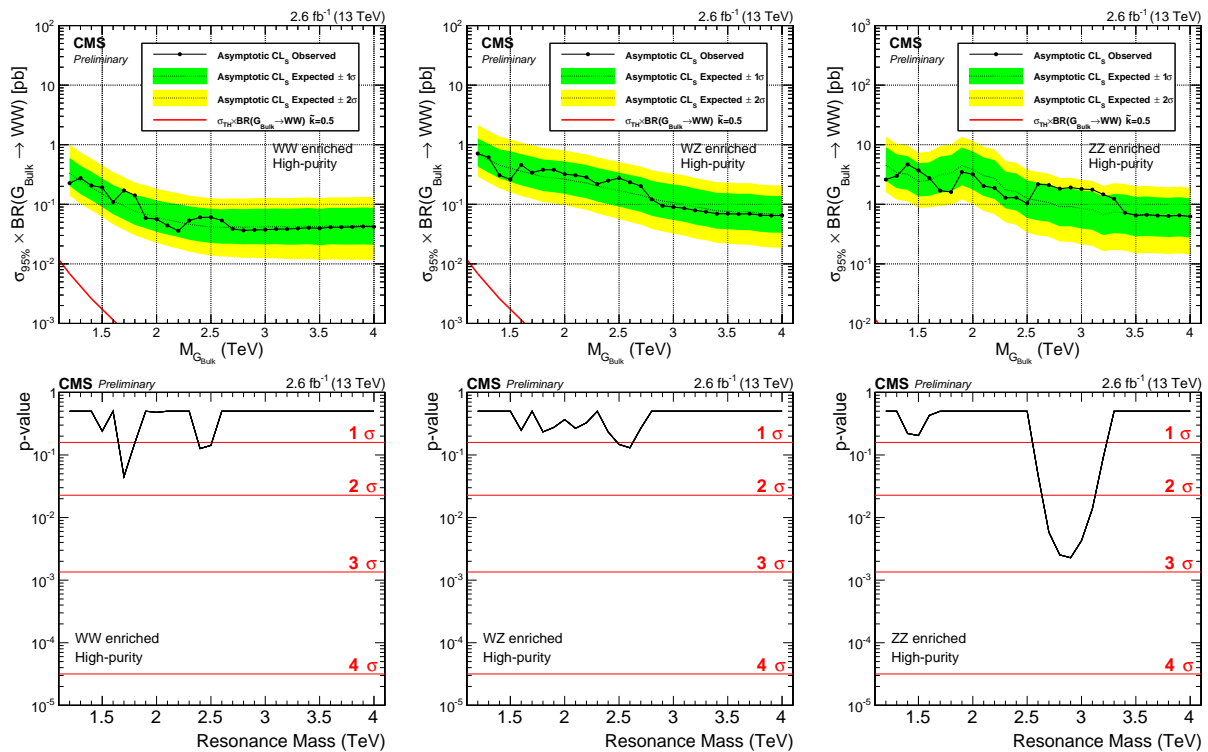


Figure B.3: Expected and observed limits at 95% CL and corresponding p-values obtained for the different mass categories using 2.6 fb^{-1} of CMS data. Here for a Bulk $G \rightarrow WW$ signal in the HP category

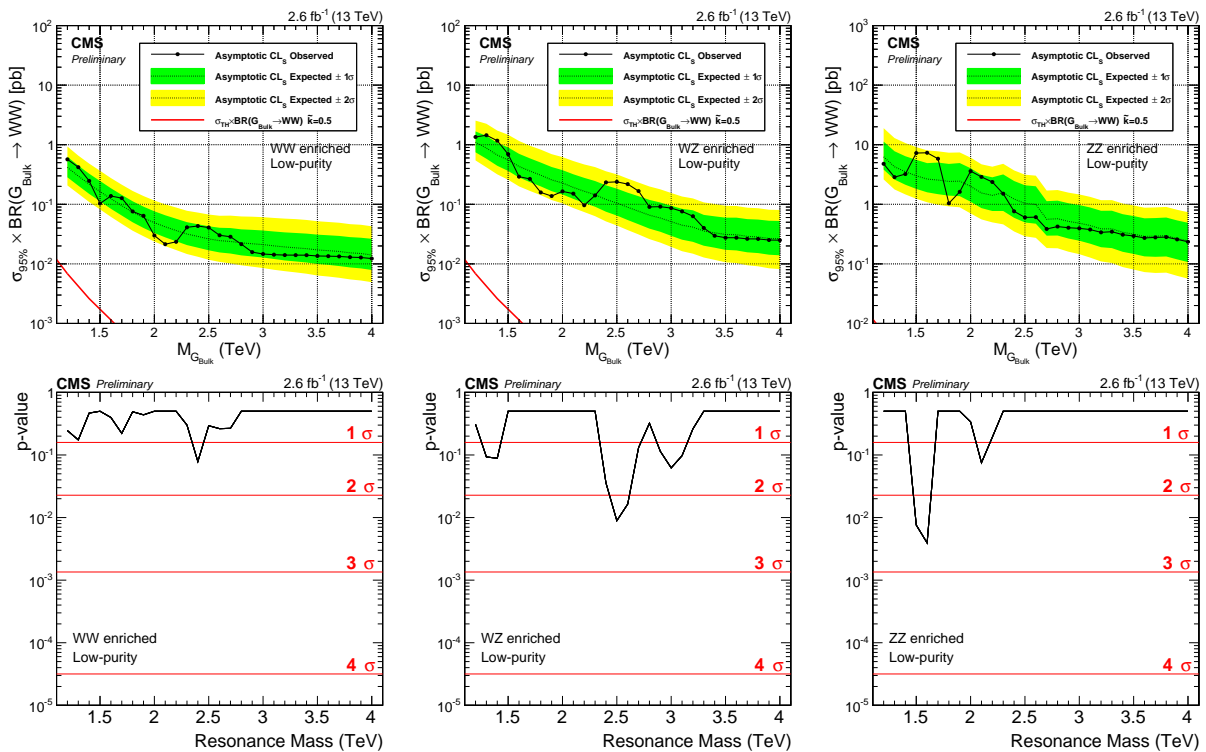


Figure B.4: Expected and observed limits at 95% CL and corresponding p-values obtained in the different mass categories using 2.6 fb^{-1} of CMS data. Here for a Bulk $G \rightarrow WW$ signal in the LP category.

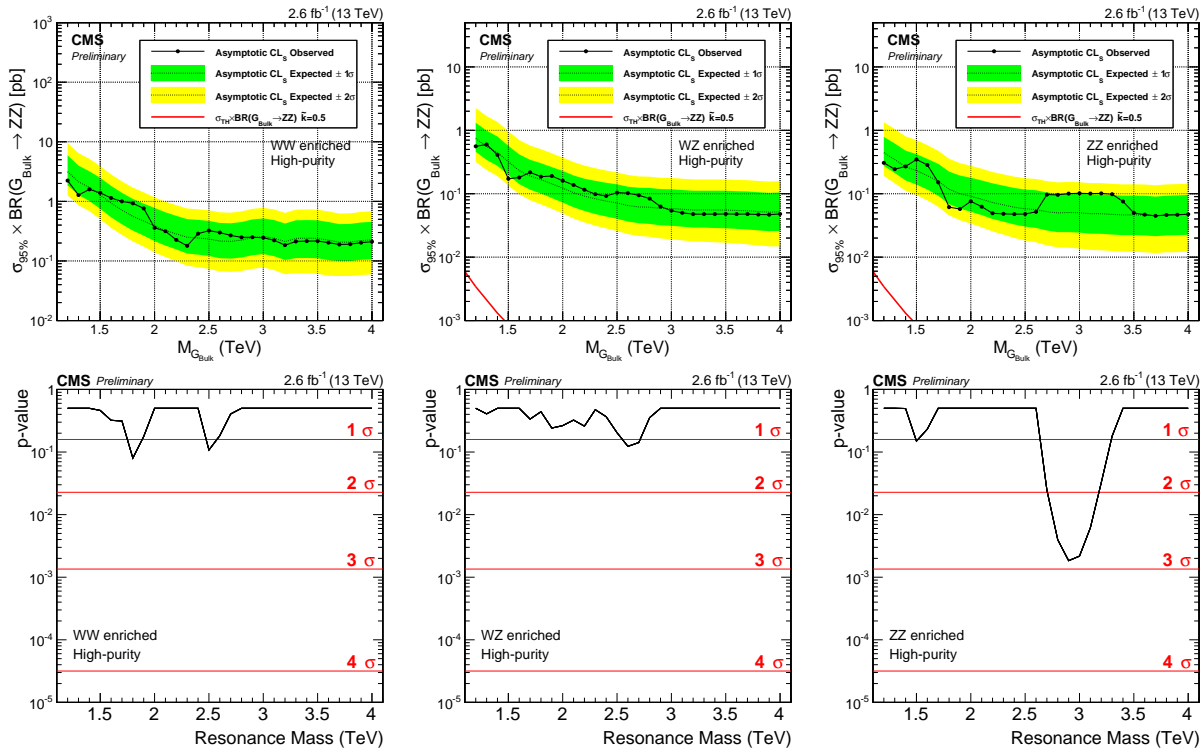


Figure B.5: Expected and observed limits at 95% CL and corresponding p-values obtained in the different mass categories. Here for a $G \rightarrow ZZ$ signal in the HP category.

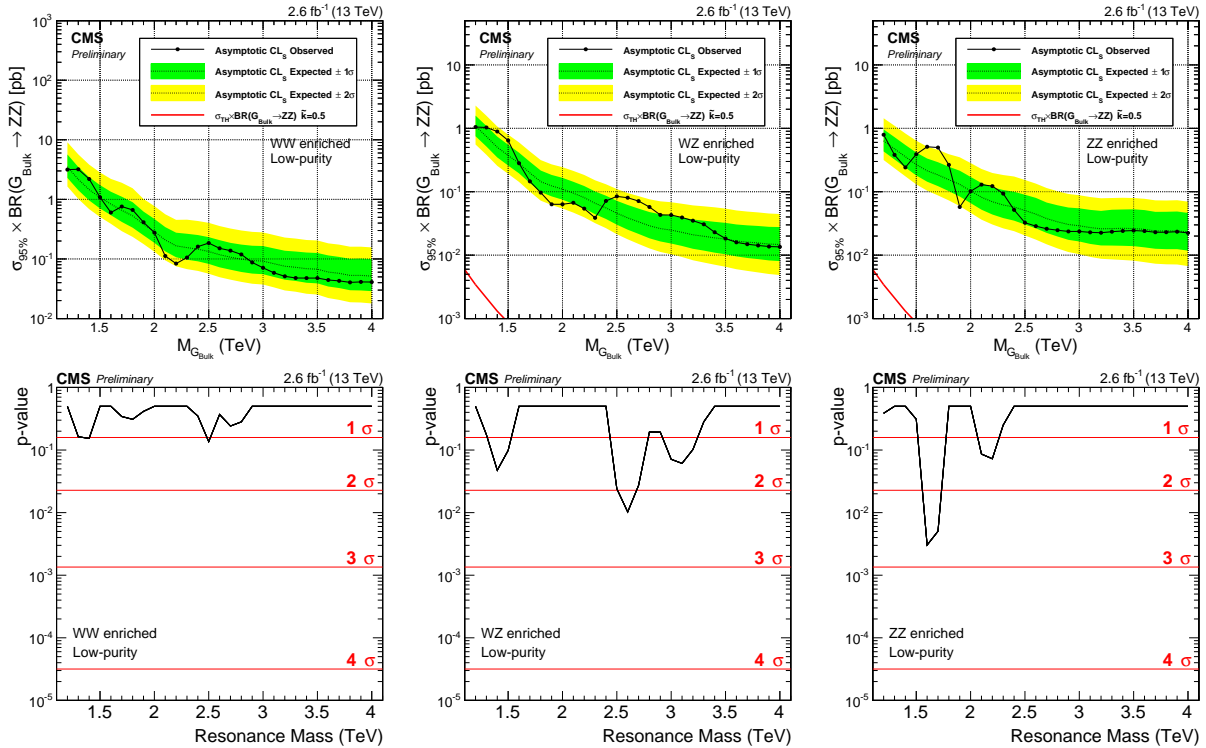


Figure B.6: Expected and observed limits at 95% CL and corresponding p-values obtained in the different mass categories. Here for a $G \rightarrow ZZ$ signal in the LP category.

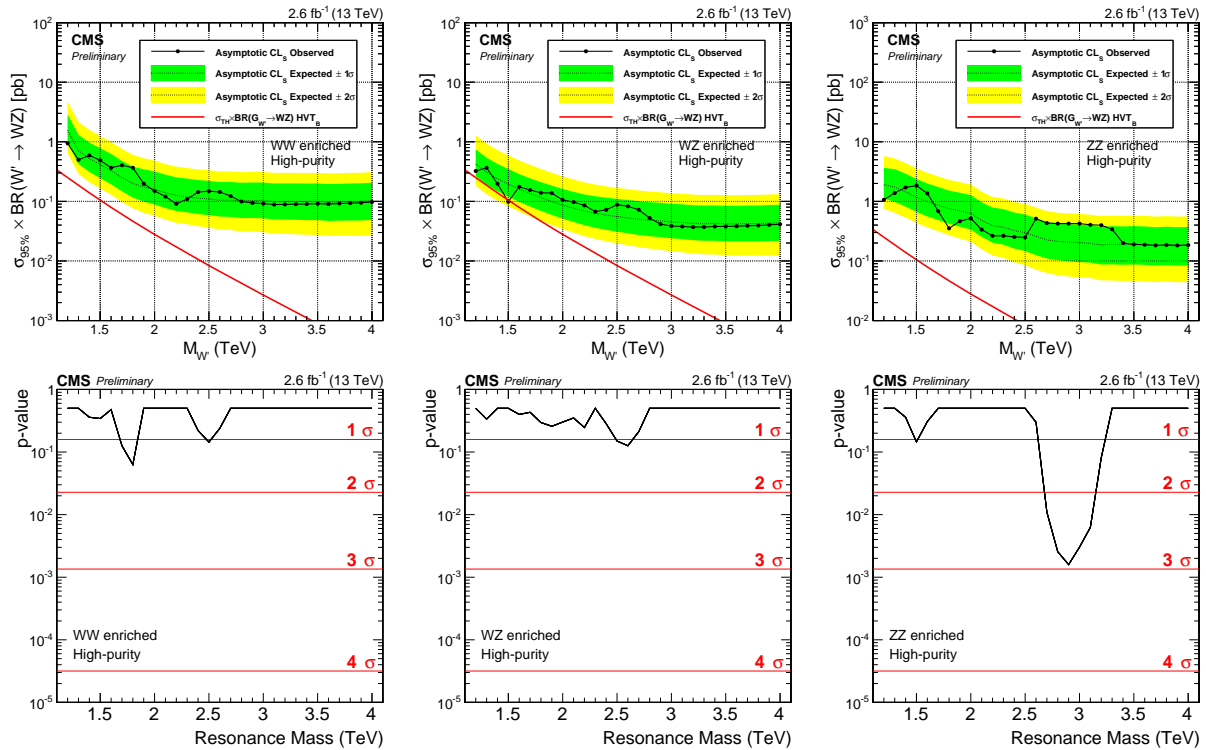


Figure B.7: Expected and observed limits at 95% CL and corresponding p-values obtained in the different mass categories. Here for a $W' \rightarrow WZ$ signal in the high-purity category.

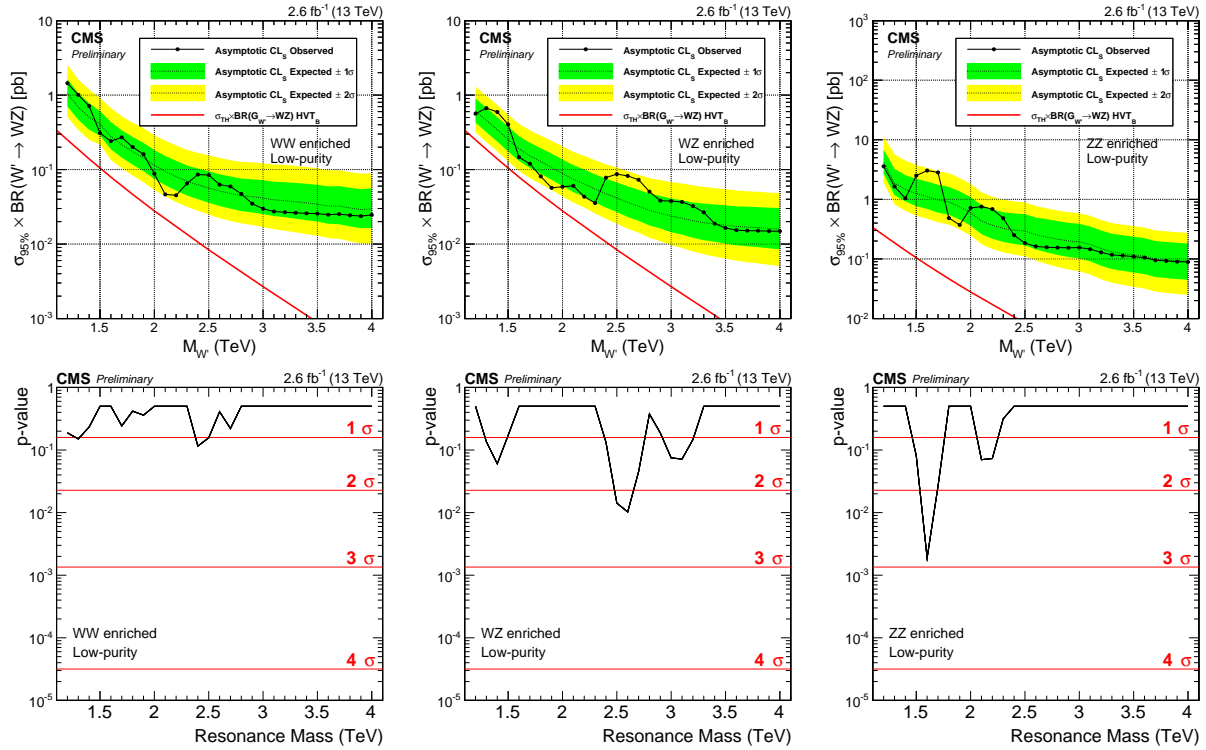


Figure B.8: Expected and observed limits at 95% CL and corresponding p-values obtained in the different mass categories. Here for a $W' \rightarrow WZ$ signal in the low purity category.

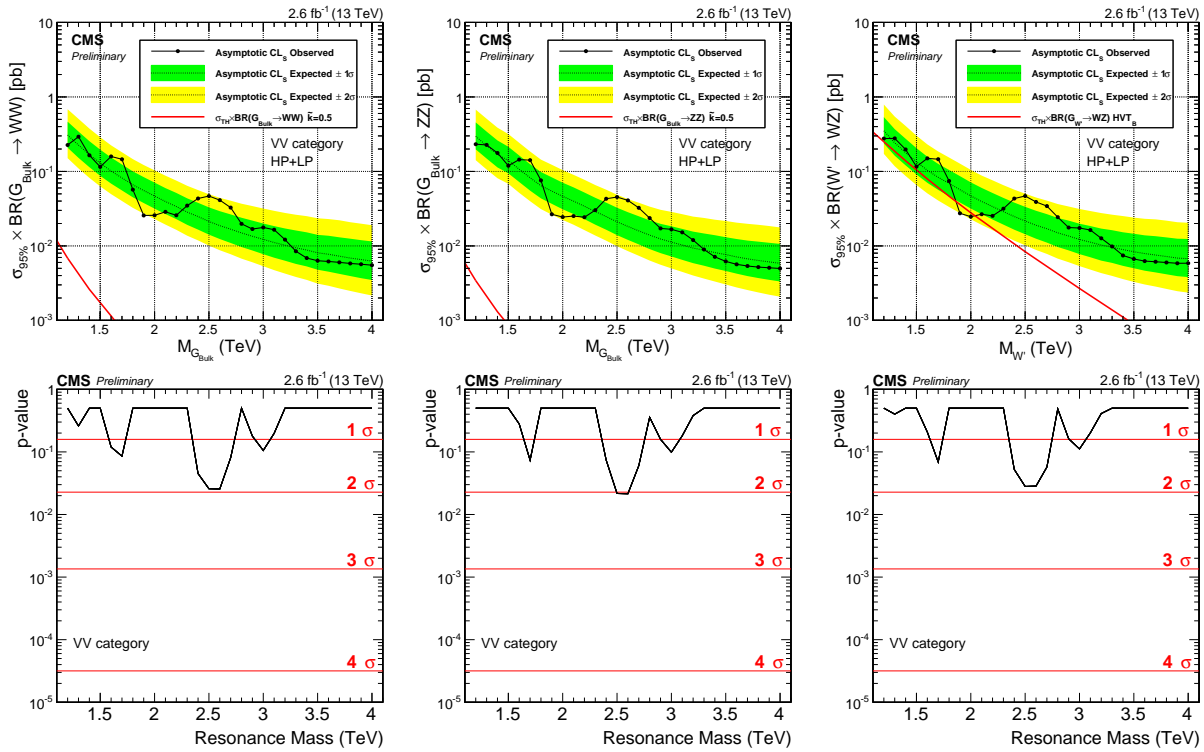


Figure B.9: Expected and observed limits at 95% CL and corresponding obtained without splitting into mass categories. This analysis is performed as a cross check analysis and directly compares with the method used in the corresponding Run 1 analysis. Here for a Bulk $G \rightarrow WW$ (left), $G \rightarrow ZZ$ (middle) and $W' \rightarrow WZ$ signal (right).

3351

APPENDIX C

3352

Search II

3353 C.1 W-tagging scale factor: Additional plots

3354 Figures C.1 shows the $t\bar{t}$ real W (top) and non-W (bottom) PUPPI softdrop jet mass distributions
 3355 for jets that passed (left) and failed (right column) the N-subjettiness selections $\text{PUPPI } \tau_{21} < 0.40$.
 Figures C.2 shows the fitted PUPPI softdrop jet mass distributions for the non-dominant

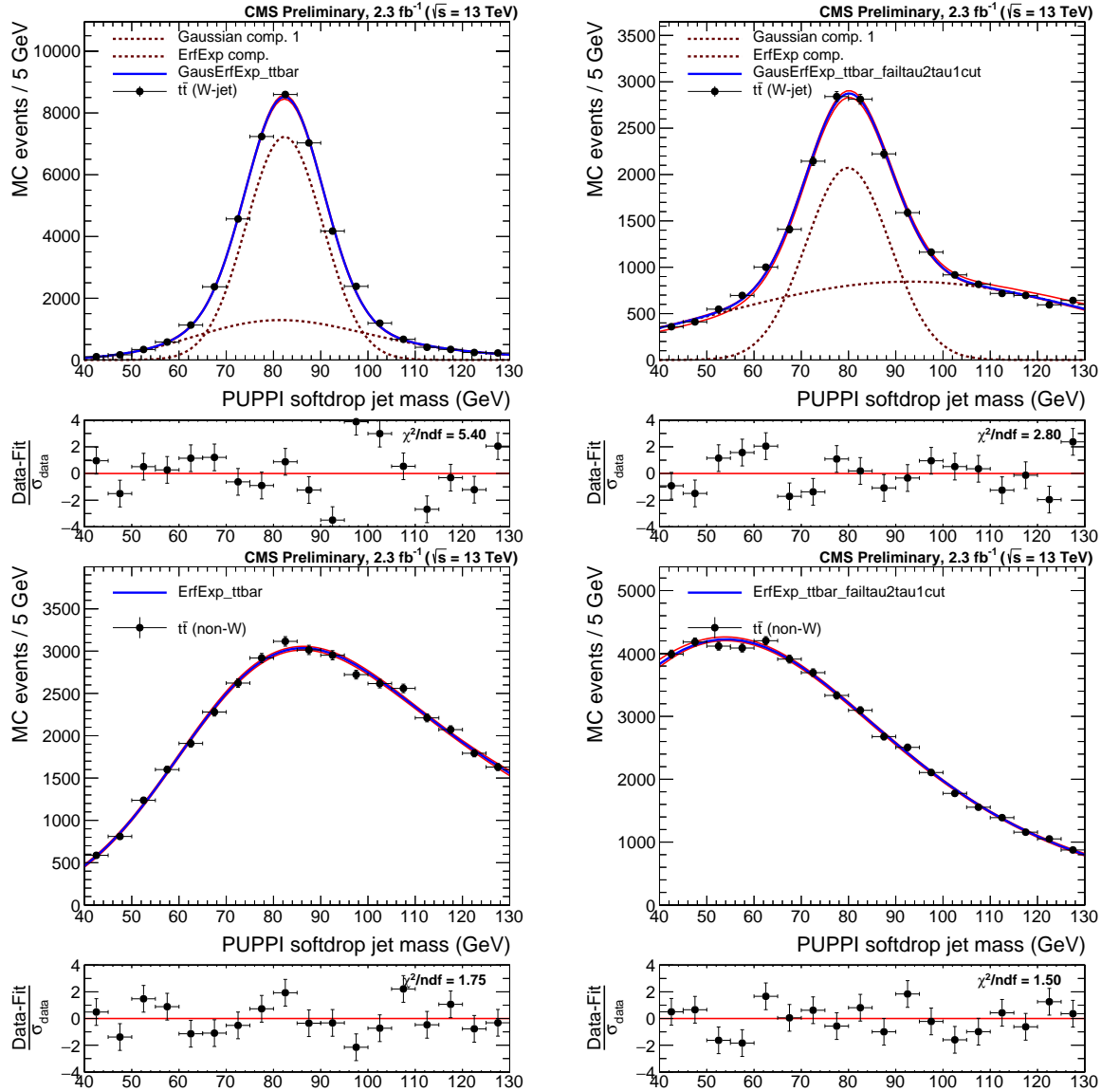


Figure C.1: Fit to the real W (top) and non-W (bottom) softdrop jet mass distribution for jets that pass (left) and fail (right) the cut on $\text{PUPPI } \tau_{21} < 0.4$.

3356

3357 backgrounds in the evaluation of the W-tagging scale factors. Here it is shown for jets that pass

(top) and failed (bottom) the N-subjettiness selections $\text{PUPPI } \tau_{21} < 0.40$.

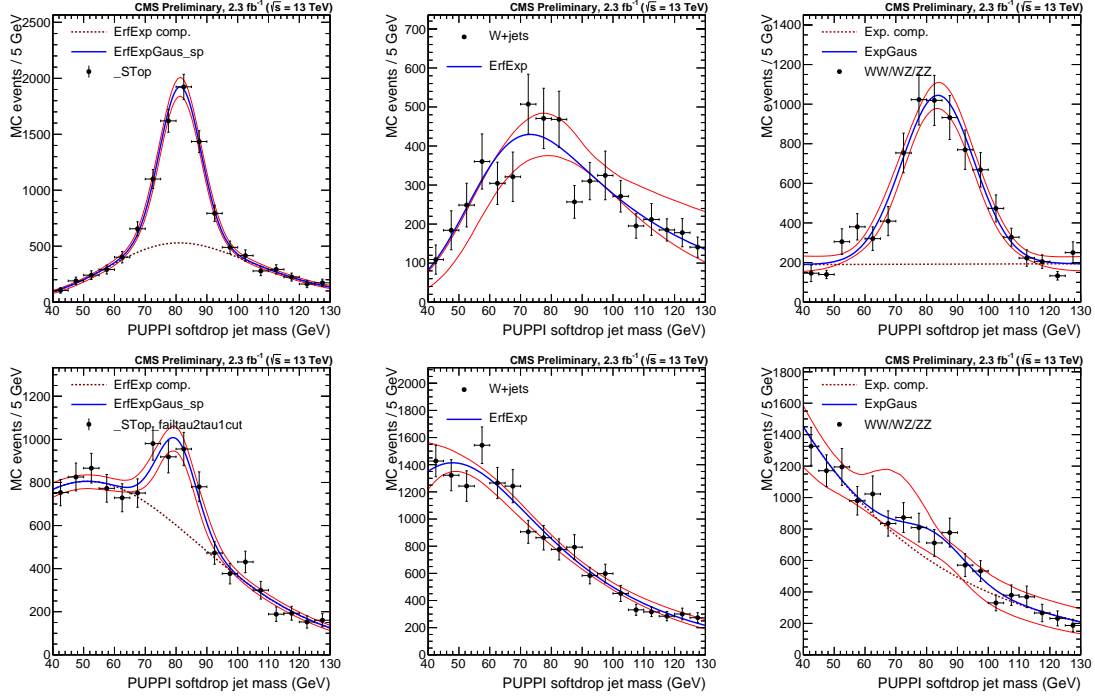


Figure C.2: Fits to the PUPPI softdrop jet mass spectrum for the non-dominant backgrounds (Single top, W+jets and VV respectively) in the pass (top) and fail (bottom) regions.

³³⁵⁹ **C.2 Efficiency scale factors for 2.5 fb^{-1}**

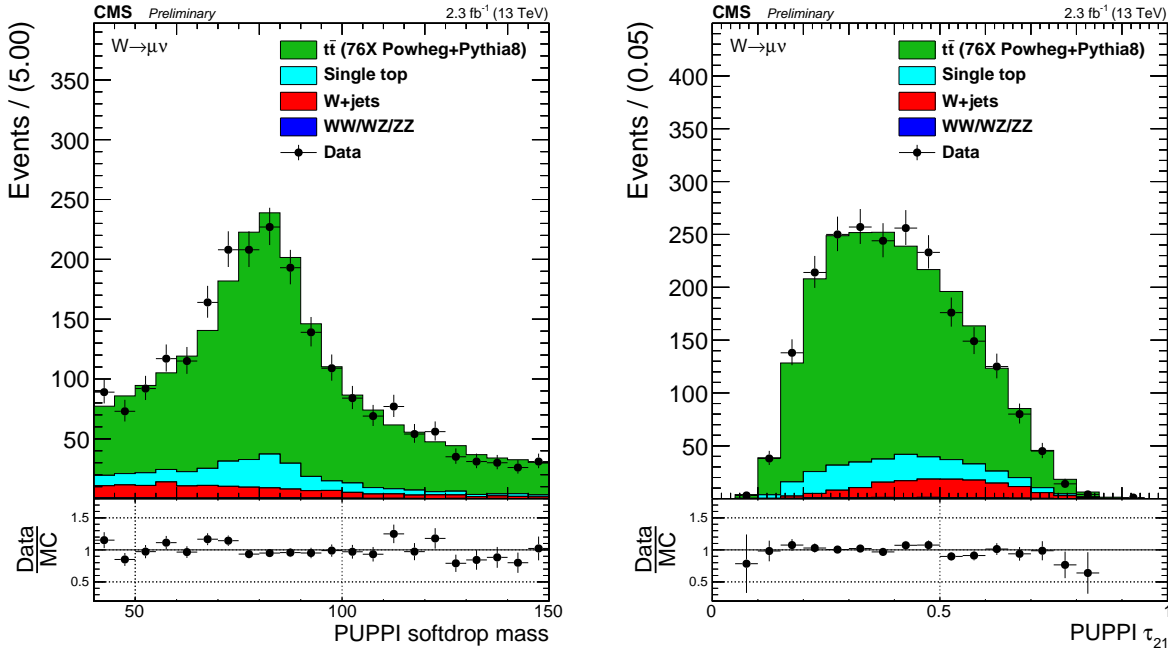


Figure C.3: Distribution of the PUPPI softdrop mass (left) and PUPPI n-subjettiness (right) distribution in the $t\bar{t}$ control sample.

Category	Working point	Eff. data	Eff. simulation	Scale factor
HP	$\tau_2/\tau_1 < 0.4$	0.785 ± 0.045	0.81 ± 0.01	$0.97 \pm 0.06 \text{ (stat)} \pm 0.04 \text{ (sys)} \pm 0.06 \text{ (sys)}$
LP	$0.4 < \tau_2/\tau_1 < 0.75$	0.215 ± 0.057	0.204 ± 0.041	$1.13 \pm 0.24 \text{ (stat)} \pm 0.17 \text{ (sys)} \pm 0.12 \text{ (sys)}$

Table C.1: W-tagging scale factors for high purity and low purity categories for a tagger based on PUPPI softdrop jet mass and τ_{21} .

Parameter	Data	Simulation	Data/Simulation
PUPPI softdrop $\langle m \rangle$	$80.3 \pm 0.8 \text{ GeV}$	$81.9 \pm 0.01 \text{ GeV}$	0.98 ± 0.01
PUPPI softdrop σ	$9.0 \pm 0.9 \text{ GeV}$	$8.5 \pm 0.4 \text{ GeV}$	1.07 ± 0.12

Table C.2: Summary of the fitted W-mass peak fit parameters.

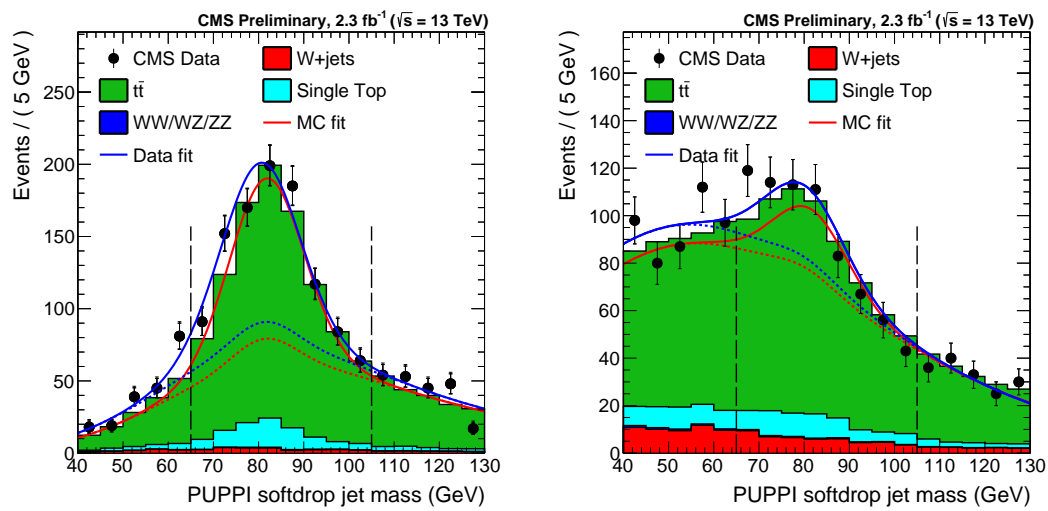


Figure C.4: PUPPI softdrop jet mass distribution for events that pass (left) and fail (right) the PUPPI $\tau_2/\tau_1 < 0.40$ selection. Results of both the fit to data (blue) and simulation (red) are shown and the background components of the fit are shown as short-dashed lines.

3360 C.3 Background fit checks

3361 The background from QCD multijet events is modeled by a smoothly falling distribution in each
 3362 analysis category. The method consists of a smoothness test of the observed data where the
 3363 background is assumed to be described by the following empirical probability density function:

$$\frac{dN}{dm} = \frac{P_0(1 - m/\sqrt{s})^{P_1}}{(m/\sqrt{s})^{P_2}}, \quad (\text{C.1})$$

3364 where m is the dijet invariant mass, \sqrt{s} the centre-of-mass energy, P_0 is a normalization parameter
 3365 for the probability density function, and P_1 and P_2 describe the shape. To ensure that this
 3366 function is sufficient to describe the data in all the different analysis categories, we first perform
 3367 a test to check that no additional parameters are needed and to check the systematic uncertainty
 3368 due to choice of fit function. For these studies we use a data sideband, where one of the two jets
 3369 is required to have a mass between $20 < M_{\text{Softdrop}} < 65$ GeV. In order to quantify how many
 3370 parameters are necessary, a Fishers F-test is performed for the fits to data in the data sideband.
 3371 The critical value that the test statistic must exceed is chosen to be $\alpha > 10\%$. If the returned
 3372 Confidence Level is larger than α , the simpler fit is preferred. The three parameter fit is compared
 3373 with the following 2, 4 and 5 parameter functions:

$$\frac{dN}{dm} = \frac{P_0}{(m/\sqrt{s})^{P_2}}, \quad (\text{C.2})$$

$$\frac{dN}{dm} = \frac{P_0(1 - m/\sqrt{s})^{P_1}}{(m/\sqrt{s})^{P_2 + P_3 \times \log(m/\sqrt{s})}}, \text{ and} \quad (\text{C.3})$$

$$\frac{dN}{dm} = \frac{P_0(1 - m/\sqrt{s})^{P_1}}{(m/\sqrt{s})^{P_2 + P_3 \times \log(m/\sqrt{s}) + P_4 \times \log(m/\sqrt{s})^2}}. \quad (\text{C.4})$$

3374 Additionally, fits with an alternative fit function have also been performed (for the single-tag
 3375 categories we try both 4 and 5 parameter versions):

$$\frac{dN}{dm} = \frac{P_0(1 - m/\sqrt{s} + P_3(m/\sqrt{s})^2)^{P_1}}{(m/\sqrt{s})^{P_2}}, \text{ and} \quad (\text{C.5})$$

$$\frac{dN}{dm} = \frac{P_0(1 - m/\sqrt{s} + P_3(m/\sqrt{s})^2)^{P_1}}{(m/\sqrt{s})^{P_2 + P_4 \times \log(m/\sqrt{s})}} \quad (\text{C.6})$$

3376 C.3.1 Background fit checks in data sideband

3377 We perform a test in a data sideband to make sure the fit functions work on real data and to
3378 exercise the estimation of number of necessary fit parameters via an F-test. The sideband is
3379 constructed by requiring one of the two jets two have a mass in the low softdrop jet mass sideband,
3380 between $20 \text{ GeV} < M_{\text{Softdrop}} < 65 \text{ GeV}$, while the full W/Z-tag selections are applied to the other
3381 jet. The low-mass jet is also required to pass the τ_{21} selection corresponding to the given category.
3382 For the single-tag category, the sideband is constructed by requiring one of the two jets to have a
3383 mass in the low softdrop jet mass sideband, between $20 \text{ GeV} < M_{\text{Softdrop}} < 65 \text{ GeV}$ and the other
3384 in a high-mass sideband, between $105 < M_{\text{Softdrop}} < 200 \text{ GeV}$. One of the jets is also required to
3385 pass the τ_{21} selection corresponding to the given category. We first check whether the sideband
3386 can be used to exercise the F-test by checking whether or not there are features introduced in the
3387 dijet mass spectrum that may be hard to cover with the fit using QCD MC. To do so we look at
3388 the dijet invariant mass spectrum in the signal region divided by the distribution in the sideband.
3389 The obtained distributions are shown in Figure C.5 for three different generators, where the pure
3390 Pythia8 QCD samples (top left) have the highest number of events. The distributions are mostly
3391 smooth, but we do see features introduced in the “WW HP” and “ZZ HP” categories which might
3392 prove difficult to fit, as well as in the tail of the single-tag categories. These kinks shift around
3393 depending on what MC generator is used and do not seem to be a systematic feature caused
3394 by the selection requirements, but rather due to limited statistics. We proceed with exercising
3395 the F-test in a data sideband, with the caveat that there might be features introduced in the
3396 spectrum where statistics are low.

3397 Figure C.6 shows the fit to data in the data sideband for the WW and ZZ mass categories,
3398 both in the HP and in the LP n-subjettiness categories. The corresponding residuals, χ^2 and
3399 F-test results are shown in Table C.7 through C.10. For the double-tag categories, a two or three
3400 parameter function is sufficient to describe the data and we conclude that the function as defined
3401 in C.1 is sufficient for all mass categories. For the single-tag category a five parameter fit seems
3402 to be required in order to describe the data and the fit quality is not optimal. To ensure that the
3403 fit functions with sufficient number of parameters are able to describe the shape in the single-tag
3404 categories, we have additionally looked at the fit quality in QCD MC (see below). Here, the
3405 default dijet function seems sufficient to describe the distributions. The sideband in the single-tag
3406 categories in QCD MC do not show the same features as the data sideband as shown in Figure
3407 C.7.

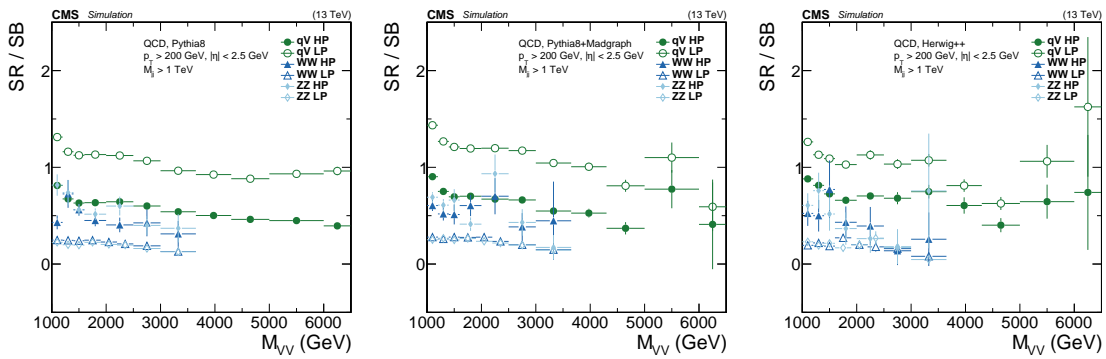


Figure C.5: Dijet mass spectrum in the signal region divided by the dijet mass spectrum in the sidebands using QCD Pythia8 (left), QCD Pythia8+Madgraph (middle) and QCD Herwig++ (right) simulated samples. Here for the double W/Z-tag and the single V-tagged HP and LP categories. Some jumps are observed in the high-mass tail of the dijet invariant mass distribution in the high-purity WW/ZZ categories, but otherwise no strange features seem to be induced by using the sideband.

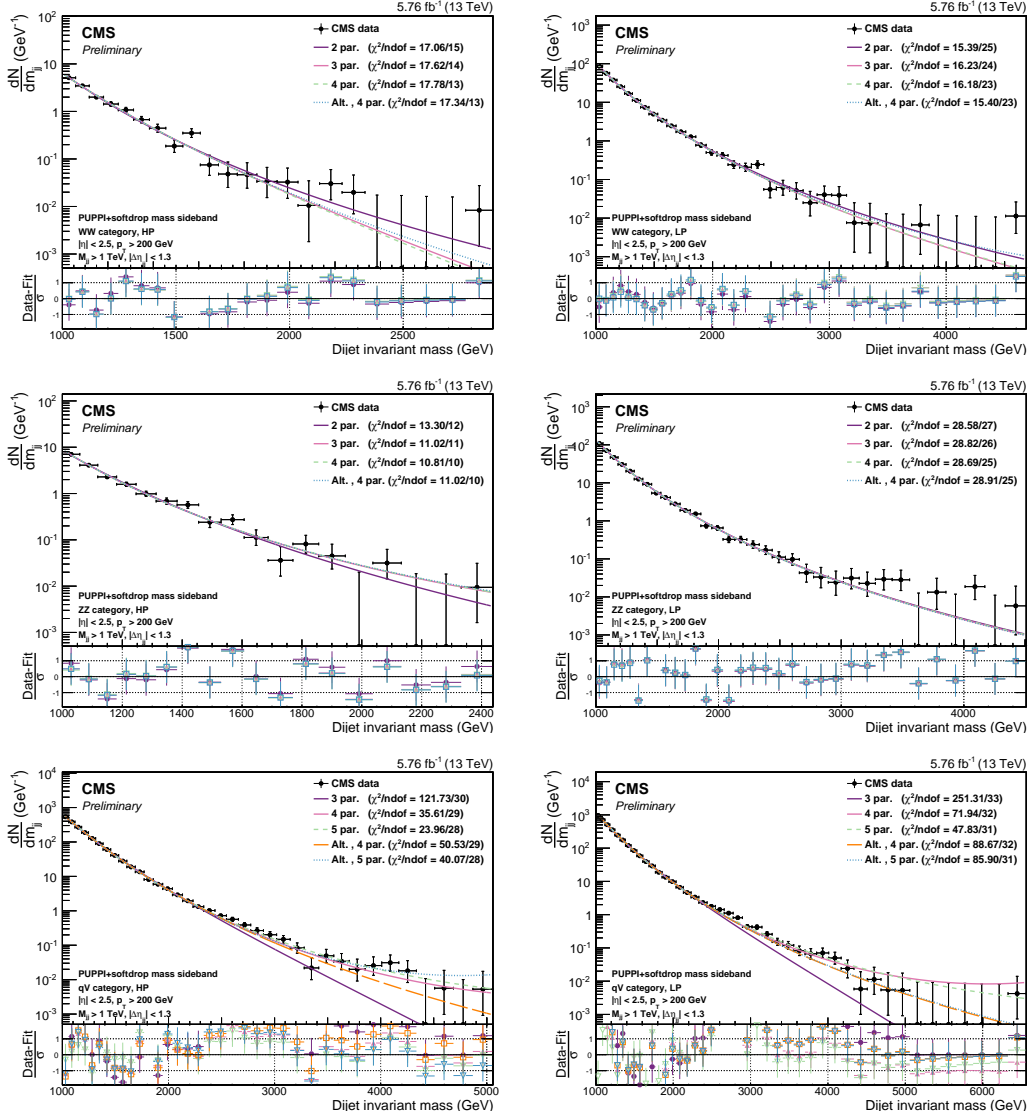


Figure C.6: Fitted dijet mass spectrum in the different mass and purity categories in a data sideband: WW high-purity (top left) and low-purity (top right), ZZ high-purity (middle left) and low-purity (middle right), qV high-purity (bottom left) and low-purity (bottom right).

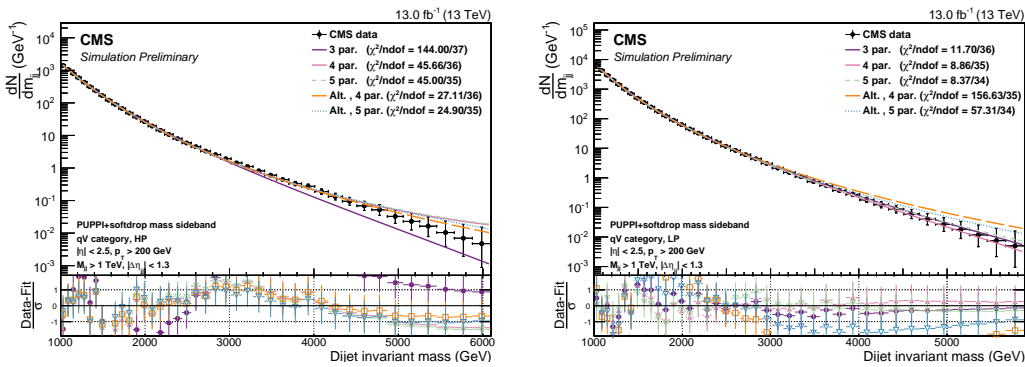


Figure C.7: Fitted dijet mass spectrum in the QCD MC sideband: qV high-purity (left) and low-purity (right).

WW category, HP			
Function	Residuals	χ^2	ndof
2 par	0.129	17.060	15
3 par	0.111	17.623	14
4 par	0.111	17.783	13
Fishers23	2.430	CL	0.140
Fishers34	0.012	CL	0.914

Table C.3: Residuals, χ^2 , and degrees of freedom for the WW category, HP category. A 2-parameter fit is needed to describe these data.

WW category, LP			
Function	Residuals	χ^2	ndof
2 par	0.908	15.388	25
3 par	0.279	16.225	24
4 par	0.263	16.178	23
Fishers23	56.395	CL	0.000
Fishers34	1.406	CL	0.247

Table C.4: Residuals, χ^2 , and degrees of freedom for the WW category, LP category. A 3-parameter fit is needed to describe these data.

ZZ category, HP			
Function	Residuals	χ^2	ndof
2 par	0.215	13.296	12
3 par	0.133	11.022	11
4 par	0.119	10.810	10
Fishers23	7.465	CL	0.018
Fishers34	1.304	CL	0.278

Table C.5: Residuals, χ^2 , and degrees of freedom for the ZZ category, HP category. A 3-parameter fit is needed to describe these data.

ZZ category, LP			
Function	Residuals	χ^2	ndof
2 par	2.459	28.583	27
3 par	2.363	28.817	26
4 par	2.175	28.694	25
Fishers23	1.107	CL	0.302
Fishers34	2.244	CL	0.146

Table C.6: Residuals, χ^2 , and degrees of freedom for the ZZ category, LP category. A 2-parameter fit is needed to describe these data.

qV category, HP			
Function	Residuals	χ^2	ndof
3 par	128.276	121.731	30
4 par	29.113	35.606	29
5 par	7.036	23.962	28
Alt. 4 par	37.232	50.528	29
Alt. 5 par	30.948	40.068	28
Fishers34	102.185	CL	0.000
Fishers45	90.988	CL	0.000
FishersAlt4Alt5	5.888	CL	0.022

Table C.7: Residuals, χ^2 , and degrees of freedom for the qV category, HP category. A 5-parameter fit is needed to describe these data.

qV category, LP			
Function	Residuals	χ^2	ndof
3 par	671.341	251.311	33
4 par	171.593	71.942	32
5 par	80.801	47.830	31
Alt. 4 par	215.431	88.666	32
Alt. 5 par	214.766	85.896	31
Fishers34	96.109	CL	0.000
Fishers45	35.957	CL	0.000
FishersAlt4Alt5	0.099	CL	0.755

Table C.8: Residuals, χ^2 , and degrees of freedom for the qV category, LP category. A 5-parameter fit is needed to describe these data.

3408 C.3.2 Background fit checks in QCD MC

3409 As an additional check, we look at the fit functions in the different signal categories using QCD
3410 MC. This is shown in Figure C.8 for the double and Figure C.9 for the single tag categories. Here
3411 all fit functions and their pull distributions are plotted. The fits are performed in a mass range
3412 corresponding to the expected distribution in the different categories for 13 fb^{-1} of data. We
3413 have adapted the error bars to correspond to the maximum of the expected Poisson error for 13 fb^{-1} of
3414 data and the pure simulation error (accounting for the different weights assigned to the
3415 p_T -binned QCD MC sample). The reason for this choice is to get an estimate of whether the
3416 set of fit functions we plan to use to fit the background distribution in data, and plan to use in
3417 order to understand the systematic uncertainty due to our choice of fit function, are appropriate
3418 and do not produce fake bumps/kinks. As this distribution is the pure MC simulation curve,
3419 whose variation at high masses is much smaller than the expected poisson error for 13 fb^{-1} of
3420 data, we expect the χ^2/ndof to be lower than one. In order to protect against the fact that
3421 the MC simulation at lower dijet masses does not have more statistics than the expected data
3422 for 13 fb^{-1} of data, we use the largest of Poisson and the MC errors. The resulting errors are
3423 therefore a mixture of Poisson and the MC errors and the χ^2/ndof for the QCD MC fits should
3424 not be considered. Fit quality in the form of χ^2/ndof should only be estimated from the fits to
3425 data sideband where pure Poisson errors are used. Overall the fits to QCD MC in the different
3426 categories describe the data well, with a two or three parameter function sufficient to describe the
3427 distributions. However, due to an under fluctuation of the first bin in the “ZZHP” category, the
3428 higher parameter fits are steered by the first bin leading to discrepancies in the tail. This is the
3429 lowest statistics category and the danger for under-fluctuations does exist. We have investigated
3430 the dijet invariant mass distribution down to a dijet invariant mass threshold of 800 GeV to
3431 make sure we are not seeing a turn-on effect. This is shown in Figure C.10. The fits in the data
3432 sideband for the same category (Figure C.6, middle left) do not show the same trend.

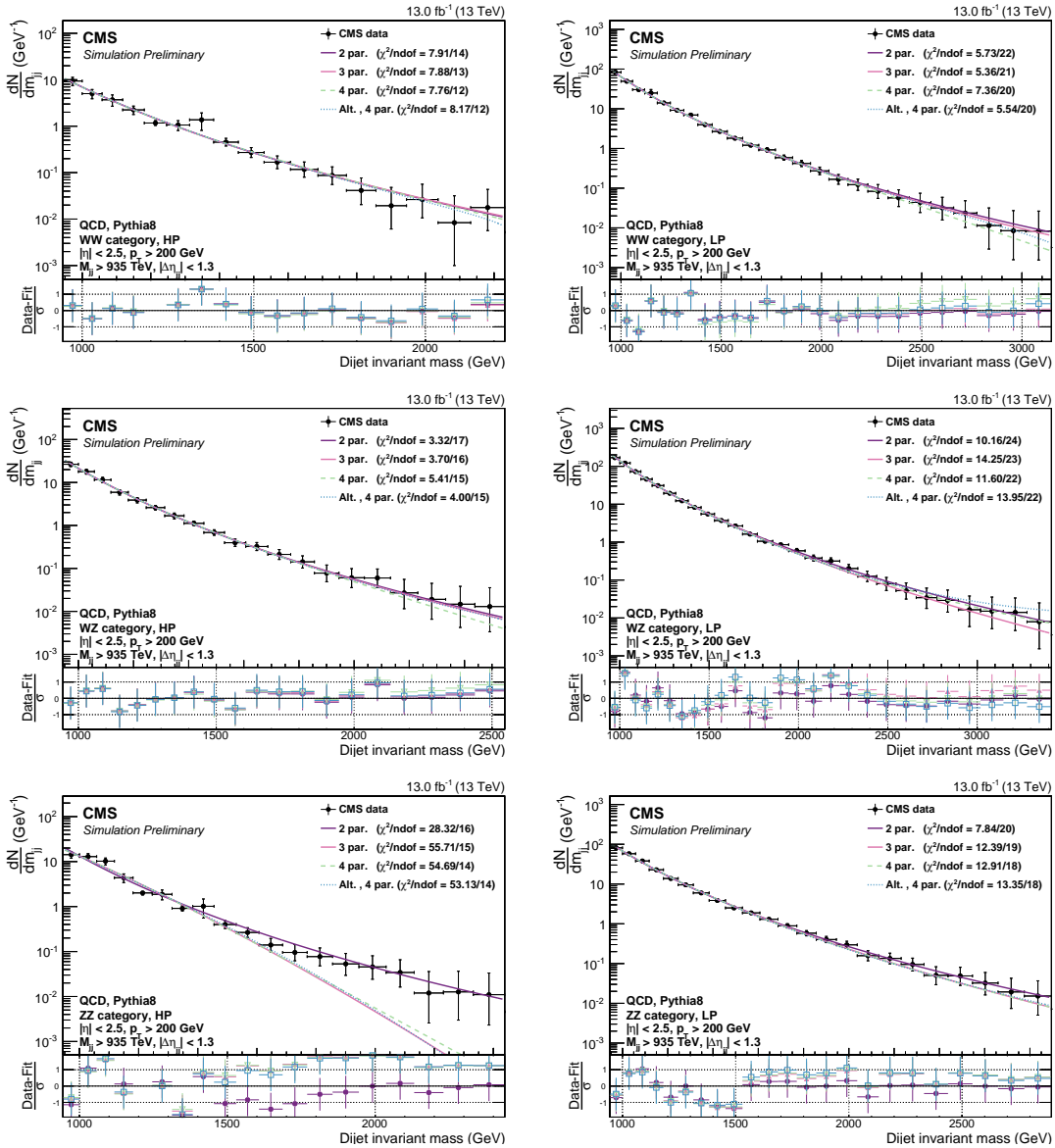


Figure C.8: Background fit for the M_{jj} distribution in QCD MC corresponding to 13 fb^{-1} . Shown here for the high- and low-purity double W/Z-tag category for the three different mass categories: WW category (top), WZ category (middle) and ZZ category (bottom).

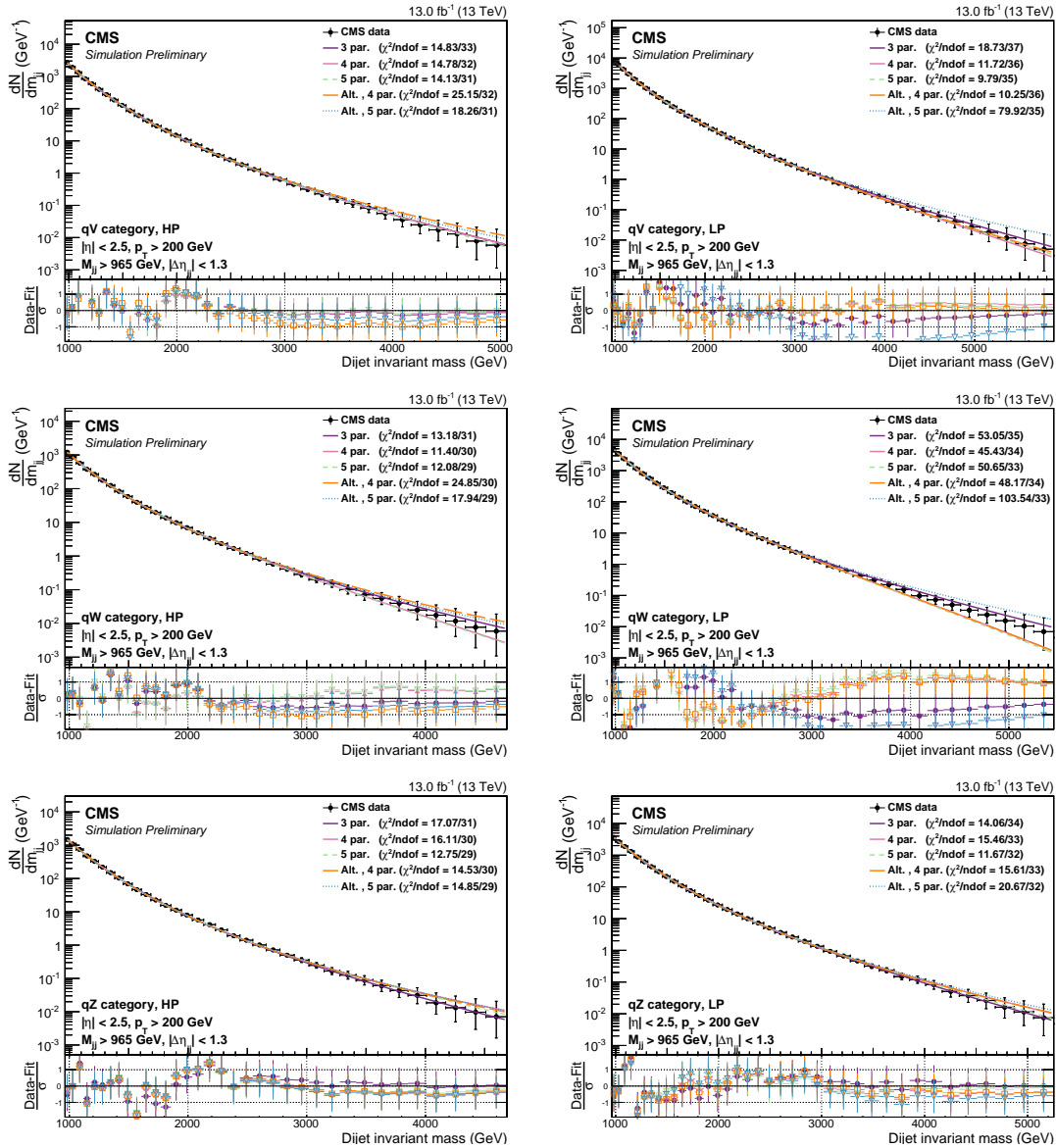


Figure C.9: Background fit for the M_{jj} distribution in QCD MC corresponding to 13 fb^{-1} . Shown here for the high- and low-purity single W/Z-tag category for the two different mass categories: qW category (top) and qZ category (bottom).

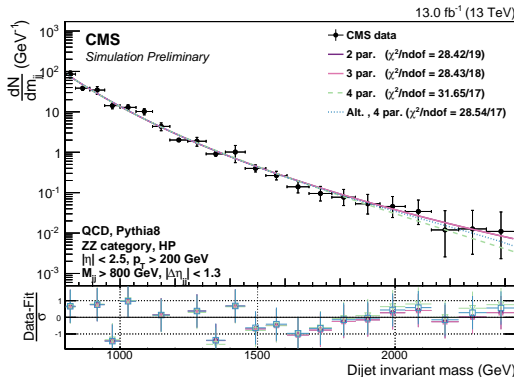


Figure C.10: Background fit for the M_{jj} distribution in QCD MC corresponding to 13 fb^{-1} . Shown here for the high-purity double Z-tag category using a dijet invariant mass threshold of 800 GeV. No turn-on effect at low invariant masses is observed.

³⁴³³ C.4 F-test in signal region

³⁴³⁴ The final F-test performed in order to define the number of fit parameters to be used to fit the
³⁴³⁵ background in each analysis category is performed in the signal region. The resulting fits and
³⁴³⁶ F-test values for the double tag categories are shown in Figure C.11 and Tables C.9 to C.14. The
³⁴³⁷ F-test results for the single-tag category are listed in Tables C.15 to C.18. Here, a three-parameter
³⁴³⁸ fit is sufficient for all categories except the “high-purity” qW category where a 5-parameter fit is
 preferred.

WW category, HP			
Function	Residuals	χ^2	ndof
2 par	0.251	17.673	16
3 par	0.187	14.863	15
4 par	0.183	14.618	14
Fishers23	5.454	CL	0.033
Fishers34	0.391	CL	0.541

Table C.9: Residuals, χ^2 , and degrees of freedom for the WW category, HP category. A 3-parameter fit is needed to describe these data.

WW category, LP			
Function	Residuals	χ^2	ndof
2 par	2.974	13.997	23
3 par	3.082	14.775	22
4 par	3.080	14.768	21
Fishers23	-0.805	CL	1.000
Fishers34	0.015	CL	0.905

Table C.10: Residuals, χ^2 , and degrees of freedom for the WW category, LP category. A 2-parameter fit is needed to describe these data.

WZ category, HP			
Function	Residuals	χ^2	ndof
2 par	2.333	17.562	17
3 par	2.158	16.952	16
4 par	2.114	16.842	15
Fishers23	1.372	CL	0.258
Fishers34	0.338	CL	0.569

Table C.11: Residuals, χ^2 , and degrees of freedom for the WZ category, HP category. A 2-parameter fit is needed to describe these data.

WZ category, LP			
Function	Residuals	χ^2	ndof
2 par	12.301	21.368	25
3 par	6.827	20.715	24
4 par	6.521	20.419	23
Fishers23	20.046	CL	0.000
Fishers34	1.126	CL	0.299

Table C.12: Residuals, χ^2 , and degrees of freedom for the WZ category, LP category. A 3-parameter fit is needed to describe these data.

ZZ category, HP			
Function	Residuals	χ^2	ndof
2 par	0.634	17.919	17
3 par	0.662	17.400	16
4 par	0.716	17.096	15
Fishers23	-0.720	CL	1.000
Fishers34	-1.197	CL	1.000

Table C.13: Residuals, χ^2 , and degrees of freedom for the ZZ category, HP category. A 2-parameter fit is needed to describe these data.

ZZ category, LP			
Function	Residuals	χ^2	ndof
2 par	9.293	19.452	22
3 par	6.884	20.118	21
4 par	6.598	20.076	20
Fishers23	7.701	CL	0.011
Fishers34	0.909	CL	0.351

Table C.14: Residuals, χ^2 , and degrees of freedom for the ZZ category, LP category. A 3-parameter fit is needed to describe these data.

qW category, HP			
Function	Residuals	χ^2	ndof
3 par	69.757	30.375	30
4 par	59.677	28.318	29
5 par	25.298	21.815	28
Alt. 4 par	35.610	22.810	29
Alt. 5 par	25.634	22.687	28
Fishers34	5.067	CL	0.032
Fishers45	39.409	CL	0.000
FishersAlt4Alt5	11.285	CL	0.002

Table C.15: Residuals, χ^2 , and degrees of freedom for the qW category, HP category. A 5-parameter fit is needed to describe these data.

qW category, LP			
Function	Residuals	χ^2	ndof
3 par	153.869	38.713	35
4 par	156.715	38.586	34
5 par	201.767	38.167	33
Alt. 4 par	189.434	39.327	34
Alt. 5 par	192.782	39.170	33
Fishers34	-0.636	CL	1.000
Fishers45	-7.592	CL	1.000
FishersAlt4Alt5	-0.590	CL	1.000

Table C.16: Residuals, χ^2 , and degrees of freedom for the qW category, LP category. A 3-parameter fit is needed to describe these data.

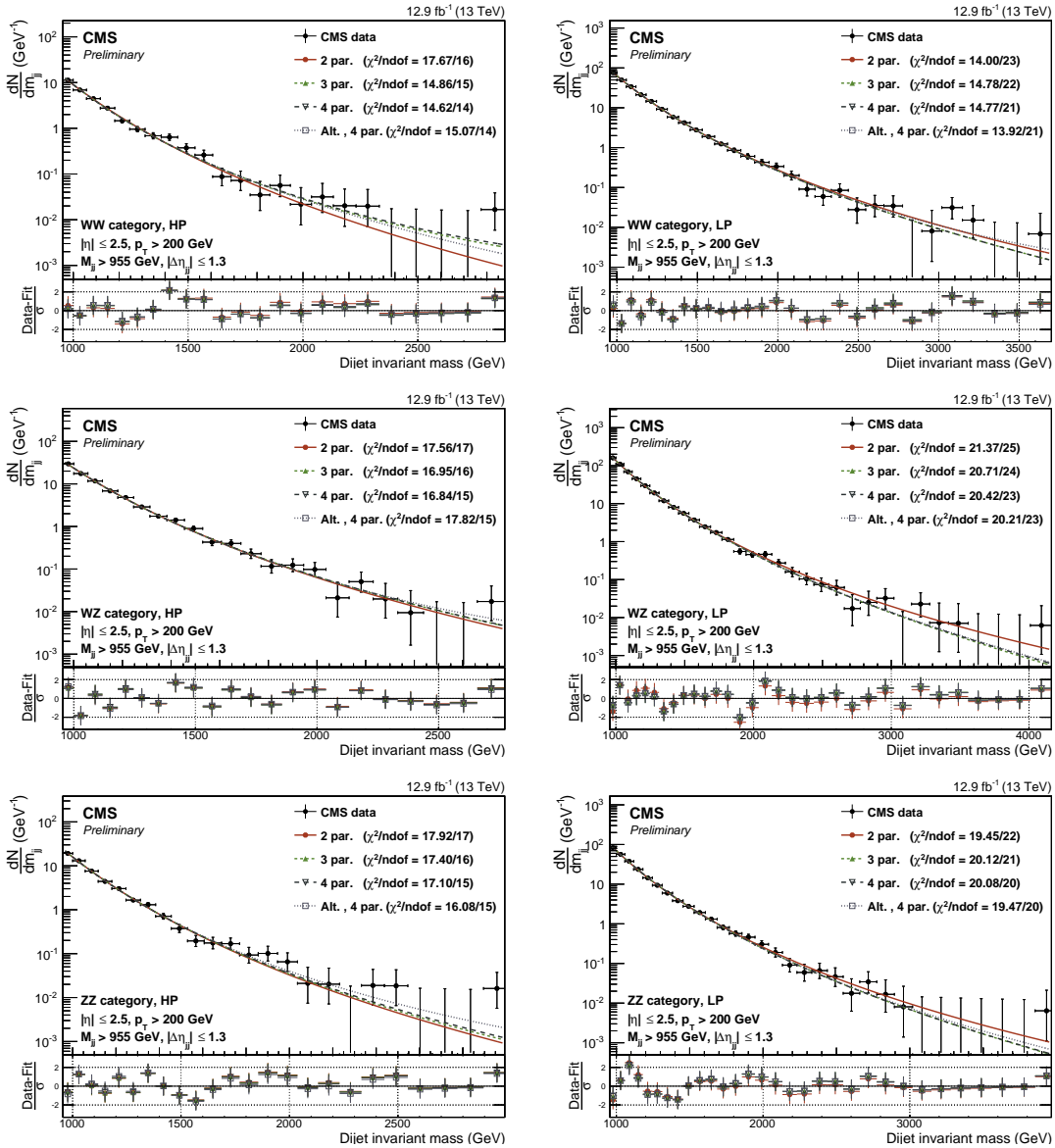


Figure C.11: Background fit for the M_{jj} distribution in the data signal region. Shown here are the high- (left) and low-purity (right) double W/Z-tag categories WW (top), WZ (middle) and ZZ (bottom).

qZ category, HP			
Function	Residuals	χ^2	ndof
3 par	12.963	21.252	30
4 par	12.961	21.252	29
5 par	9.256	19.644	28
Alt. 4 par	13.931	20.977	29
Alt. 5 par	9.739	20.344	28
Fishers34	0.004	CL	0.948
Fishers45	11.609	CL	0.002
FishersAlt4Alt5	12.484	CL	0.001

Table C.17: Residuals, χ^2 , and degrees of freedom for the qZ category, HP category. A 3-parameter fit is needed to describe these data.

qZ category, LP			
Function	Residuals	χ^2	ndof
3 par	369.554	47.426	36
4 par	369.554	47.426	35
5 par	298.358	46.525	34
Alt. 4 par	379.111	47.531	35
Alt. 5 par	379.120	47.531	34
Fishers34	0.000	CL	0.994
Fishers45	8.352	CL	0.007
FishersAlt4Alt5	-0.001	CL	0.000

Table C.18: Residuals, χ^2 , and degrees of freedom for the qZ category, LP category. A 3-parameter fit is needed to describe these data.

3440

APPENDIX D

3441

Search III

3442 D.1 Signal fits

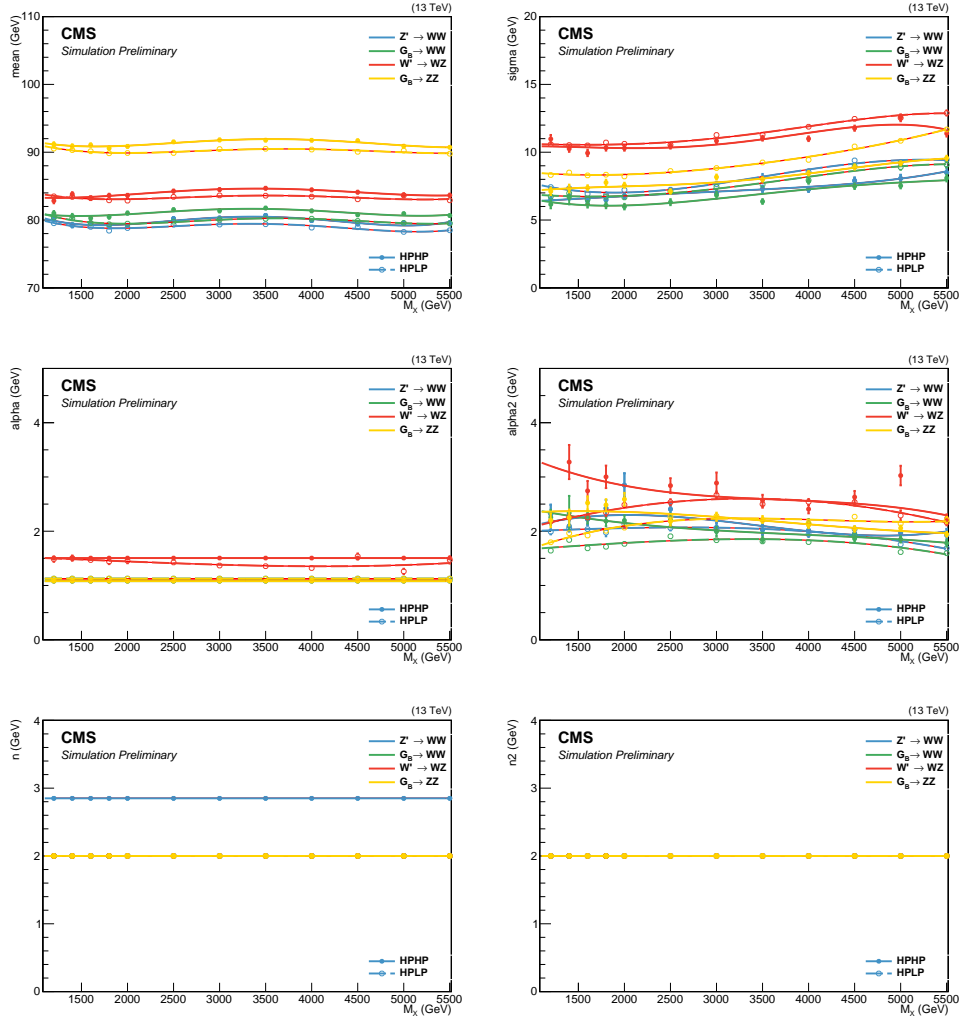


Figure D.1: The interpolated double Crystal-ball parameters for the softdrop jet mass of M_{jet2} as a function of M_X . To improve the stability of the fit some parameters are set constant.

3443 D.2 2016 kernels

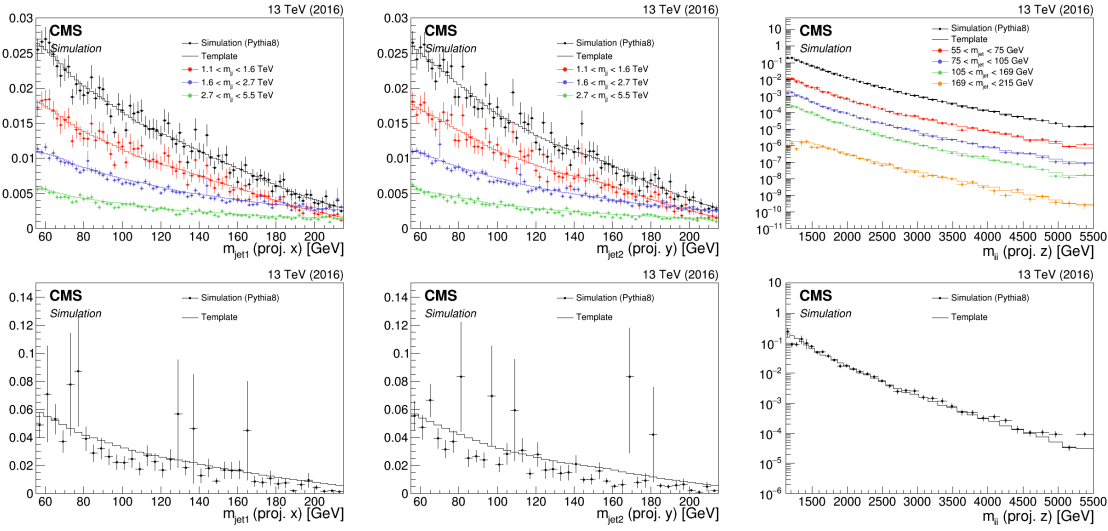


Figure D.2: Comparison between QCD MC simulation (markers) and kernels derived from generator-level quantities (lines) for the HP category (top) and the LP category (bottom) for 2016 MC. The kernels are shown for $M_{\text{jet}1}$ (left), $M_{\text{jet}2}$ (middle) and M_{VV} (right).

3444 D.3 Resonant background

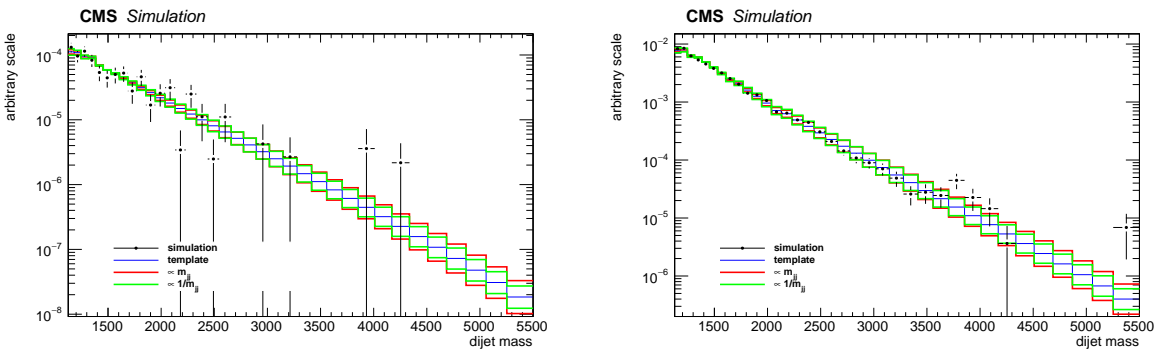


Figure D.3: One-dimensional M_{VV} kernels (solid line) compared to MC (markers) for the Z+jets background in the HP (left) and LP (right) categories. The nominal shape derived from the smoothing procedure can be seen as a blue line, alternative shapes derived from varying the slope of the M_{VV} spectrum are shown in green and red.

3445

Bibliography

- 3446 [1] Particle Data Group Collaboration, “Review of Particle Physics”, *Chin. Phys.* **C40** (2016),
3447 no. 10, 100001, doi:10.1088/1674-1137/40/10/100001.
- 3448 [2] P. Collaboration, “Planck intermediate results - XLVI. Reduction of large-scale systematic
3449 effects in HFI polarization maps and estimation of the reionization optical depth”, *A&A*
3450 **596** (2016) A107, doi:10.1051/0004-6361/201628890.
- 3451 [3] M. Gell-Mann, “Symmetries of Baryons and Mesons”, *Phys. Rev.* **125** (Feb, 1962)
3452 1067–1084, doi:10.1103/PhysRev.125.1067.
- 3453 [4] W. Pauli, “Mathematical contributions to the theory of Dirac’s matrices”, *Ann. Inst. H.
3454 Poincare Phys. Theor.* **6** (1936) 109–136.
- 3455 [5] R. Tumulka, “Pauli Spin Matrices”, pp. 470–472. 07, 2009.
3456 doi:10.1007/978-3-540-70626-7_142.
- 3457 [6] S. Duplij and F. Klinkhamer, “Levi-Civita Symbol”, pp. 227–227. Springer Netherlands,
3458 Dordrecht, 2004. doi:10.1007/1-4020-4522-0_298.
- 3459 [7] S. Weinberg, “Conceptual Foundations of the Unified Theory of Weak and Electromagnetic
3460 Interactions”, *Rev. Mod. Phys.* **52** (1980) 515–523, doi:10.1103/RevModPhys.52.515.
3461 [543(1979)].
- 3462 [8] F. Englert and R. Brout, “Broken Symmetry and the Mass of Gauge Vector Mesons”, *Phys.
3463 Rev. Lett.* **13** (Aug, 1964) 321–323, doi:10.1103/PhysRevLett.13.321.
- 3464 [9] P. W. Higgs, “Broken Symmetries and the Masses of Gauge Bosons”, *Phys. Rev. Lett.* **13**
3465 (Oct, 1964) 508–509, doi:10.1103/PhysRevLett.13.508.
- 3466 [10] G. S. Guralnik, C. R. Hagen, and T. W. B. Kibble, “Global Conservation Laws and Massless
3467 Particles”, *Phys. Rev. Lett.* **13** (Nov, 1964) 585–587, doi:10.1103/PhysRevLett.13.585.

- 3468 [11] P. W. Anderson, “Coherent Excited States in the Theory of Superconductivity: Gauge
 3469 Invariance and the Meissner Effect”, *Phys. Rev.* **110** (May, 1958) 827–835,
 3470 [doi:10.1103/PhysRev.110.827](https://doi.org/10.1103/PhysRev.110.827).
- 3471 [12] J. Goldstone, “Field Theories with Superconductor Solutions”, *Nuovo Cim.* **19** (1961)
 3472 154–164, [doi:10.1007/BF02812722](https://doi.org/10.1007/BF02812722).
- 3473 [13] J. Ellis, “Higgs Physics”, [arXiv:1312.5672](https://arxiv.org/abs/1312.5672).
- 3474 [14] B. Bellazzini, C. Csáki, and J. Serra, “Composite Higgses”, *Eur. Phys. J.* **C74** (2014),
 3475 no. 5, 2766, [doi:10.1140/epjc/s10052-014-2766-x](https://doi.org/10.1140/epjc/s10052-014-2766-x), [arXiv:1401.2457](https://arxiv.org/abs/1401.2457).
- 3476 [15] R. Contino, D. Marzocca, D. Pappadopulo, and R. Rattazzi, “On the effect of resonances in
 3477 composite Higgs phenomenology”, *JHEP* **10** (2011) 081, [doi:10.1007/JHEP10\(2011\)081](https://doi.org/10.1007/JHEP10(2011)081),
 3478 [arXiv:1109.1570](https://arxiv.org/abs/1109.1570).
- 3479 [16] D. Pappadopulo, A. Thamm, R. Torre, and A. Wulzer, “Heavy Vector Triplets: Bridging
 3480 Theory and Data”, *JHEP* **09** (2014) 060, [doi:10.1007/JHEP09\(2014\)060](https://doi.org/10.1007/JHEP09(2014)060),
 3481 [arXiv:1402.4431](https://arxiv.org/abs/1402.4431).
- 3482 [17] L. Randall and R. Sundrum, “Large Mass Hierarchy from a Small Extra Dimension”, *Phys.
 3483 Rev. Lett.* **83** (Oct, 1999) 3370–3373, [doi:10.1103/PhysRevLett.83.3370](https://doi.org/10.1103/PhysRevLett.83.3370).
- 3484 [18] K. Agashe, H. Davoudiasl, G. Perez, and A. Soni, “Warped gravitons at the CERN LHC
 3485 and beyond”, *Phys. Rev. D* **76** (Aug, 2007) 036006, [doi:10.1103/PhysRevD.76.036006](https://doi.org/10.1103/PhysRevD.76.036006).
- 3486 [19] A. L. Fitzpatrick, J. Kaplan, L. Randall, and L.-T. Wang, “Searching for the Kaluza-Klein
 3487 Graviton in Bulk RS Models”, *JHEP* **09** (2007) 013,
 3488 [doi:10.1088/1126-6708/2007/09/013](https://doi.org/10.1088/1126-6708/2007/09/013), [arXiv:hep-ph/0701150](https://arxiv.org/abs/hep-ph/0701150).
- 3489 [20] CERN, “Accelerators and Schedules”, 2018 (accessed November 12, 2018),
 3490 <https://beams.web.cern.ch/content/accelerators-schedules>.
- 3491 [21] CMS, “CMS Detector Design”, 2018 (accessed November 21, 2018),
 3492 <https://cms.cern/news/cms-detector-design>.
- 3493 [22] T. Lenzi, “Development and Study of Different Muon Track Reconstruction Algorithms for
 3494 the Level-1 Trigger for the CMS Muon Upgrade with GEM Detectors”, Master’s thesis, U.
 3495 Brussels (main), 2013.
- 3496 [23] A. Dominguez et al., “CMS Technical Design Report for the Pixel Detector Upgrade”,
 3497 Technical Report CERN-LHCC-2012-016. CMS-TDR-11, CERN, Sep, 2012.

- [24] CMS Collaboration, “The CMS Experiment at the CERN LHC”, *JINST* **3** (2008) S08004, doi:10.1088/1748-0221/3/08/S08004.
- [25] P. Adzic et al., “Energy resolution of the barrel of the CMS electromagnetic calorimeter”, *JINST* **2** (2007) P04004, doi:10.1088/1748-0221/2/04/P04004.
- [26] C. Biino, “The CMS Electromagnetic Calorimeter: overview, lessons learned during Run 1 and future projections”, *Journal of Physics: Conference Series* **587** (2015), no. 1, 012001.
- [27] L. Veillet, “Assembly of the 7th wedge”, (Aug, 2000). CMS Collection.
- [28] S. Sharma, “Understanding the performance of CMS calorimeter”, *Pramana* **69** (Dec, 2007) 1069–1074, doi:10.1007/s12043-007-0229-8.
- [29] CMS Collaboration, “CMS reconstruction improvement for the muon tracking by the RPC chambers”, *PoS RPC2012* (Sep, 2012) 045. 9 p. Presented by Minsuk Kim at the XI workshop on Resistive Plate Chambers and Related Detectors - RPC2012, INFN Laboratori Nazionali di Frascati Italy, February 5-10, 2012.
- [30] CMS, “CMS Luminosity - public results”, 2018 (accessed December 11, 2018), <https://twiki.cern.ch/twiki/bin/view/CMSPublic/LumiPublicResults>.
- [31] P. Billoir, “Progressive track recognition with a Kalman-like fitting procedure”, *Computer Physics Communications* **57** (1989), no. 1, 390 – 394, doi:[https://doi.org/10.1016/0010-4655\(89\)90249-X](https://doi.org/10.1016/0010-4655(89)90249-X).
- [32] A. S. et. Al., “Particle-flow reconstruction and global event description with the CMS detector”, *Journal of Instrumentation* **12** (2017), no. 10, P10003.
- [33] W. Adam, R. Frühwirth, A. Strandlie, and T. Todorov, “Reconstruction of electrons with the Gaussian-sum filter in the CMS tracker at the LHC”, *Journal of Physics G: Nuclear and Particle Physics* **31** (2005), no. 9, N9.
- [34] T. C. collaboration, “Performance of CMS muon reconstruction in pp collision events at s = 7 TeV”, *Journal of Instrumentation* **7** (2012), no. 10, P10002.
- [35] D. Bertolini, P. Harris, M. Low, and N. Tran, “Pileup per particle identification”, *Journal of High Energy Physics* **2014** (2014), no. 10, doi:10.1007/JHEP10(2014)059.
- [36] Y. L. Dokshitzer, G. D. Leder, S. Moretti, and B. R. Webber, “Better jet clustering algorithms”, *JHEP* **08** (1997) 001, doi:10.1088/1126-6708/1997/08/001, arXiv:hep-ph/9707323.

- 3528 [37] S. D. Ellis and D. E. Soper, “Successive combination jet algorithm for hadron collisions”,
 3529 *Phys. Rev.* **D48** (1993) 3160–3166, doi:10.1103/PhysRevD.48.3160,
 3530 arXiv:hep-ph/9305266.
- 3531 [38] M. Cacciari, G. P. Salam, and G. Soyez, “The anti- k_t jet clustering algorithm”, *JHEP* **04**
 3532 (2008) 063, doi:10.1088/1126-6708/2008/04/063, arXiv:0802.1189.
- 3533 [39] J. POG, “Jet Identification: Recommendations for 13TeV data analysis”, 2018 (accessed
 3534 December 18, 2018), <https://twiki.cern.ch/twiki/bin/viewauth/CMS/JetID>.
- 3535 [40] CMS Collaboration, “Determination of Jet Energy Calibration and Transverse Momentum
 3536 Resolution in CMS”, *JINST* **6** (2011) P11002, doi:10.1088/1748-0221/6/11/P11002,
 3537 arXiv:1107.4277.
- 3538 [41] D. Krohn, J. Thaler, and L.-T. Wang, “Jet Trimming”, *JHEP* **02** (2010) 084,
 3539 doi:10.1007/JHEP02(2010)084, arXiv:0912.1342.
- 3540 [42] CMS Collaboration Collaboration, “Pileup Removal Algorithms”, Technical Report
 3541 CMS-PAS-JME-14-001, CERN, Geneva, 2014.
- 3542 [43] J. M. Butterworth, A. R. Davison, M. Rubin, and G. P. Salam, “Jet substructure as a new
 3543 Higgs search channel at the LHC”, *Phys. Rev. Lett.* **100** (2008) 242001,
 3544 doi:10.1103/PhysRevLett.100.242001, arXiv:0802.2470.
- 3545 [44] M. Dasgupta, A. Fregoso, S. Marzani, and G. P. Salam, “Towards an understanding of jet
 3546 substructure”, *JHEP* **09** (2013) 029, doi:10.1007/JHEP09(2013)029, arXiv:1307.0007.
- 3547 [45] A. J. Larkoski, S. Marzani, G. Soyez, and J. Thaler, “Soft Drop”, *JHEP* **05** (2014) 146,
 3548 doi:10.1007/JHEP05(2014)146, arXiv:1402.2657.
- 3549 [46] J. Thaler and K. Van Tilburg, “Identifying Boosted Objects with N-subjettiness”, *JHEP*
 3550 **03** (2011) 015, doi:10.1007/JHEP03(2011)015, arXiv:1011.2268.
- 3551 [47] J. Thaler and K. Van Tilburg, “Maximizing boosted top identification by minimizing
 3552 N-subjettiness”, *Journal of High Energy Physics* **2012** (Feb, 2012) 93,
 3553 doi:10.1007/JHEP02(2012)093.
- 3554 [48] S. Bolognesi et al., “Spin and parity of a single-produced resonance at the LHC”, *Phys.
 3555 Rev. D* **86** (Nov, 2012) 095031, doi:10.1103/PhysRevD.86.095031.
- 3556 [49] CMS Collaboration, “Identification techniques for highly boosted W bosons that decay into
 3557 hadrons”, *JHEP* **12** (2014) 017, doi:10.1007/JHEP12(2014)017, arXiv:1410.4227.

- 3558 [50] M. Bahr et al., “Herwig++ Physics and Manual”, *Eur. Phys. J.* **C58** (2008) 639–707,
3559 [doi:10.1140/epjc/s10052-008-0798-9](https://doi.org/10.1140/epjc/s10052-008-0798-9), arXiv:0803.0883.
- 3560 [51] T. Sjöstrand et al., “An Introduction to PYTHIA 8.2”, *Comput. Phys. Commun.* **191**
3561 (2015) 159–177, [doi:10.1016/j.cpc.2015.01.024](https://doi.org/10.1016/j.cpc.2015.01.024), arXiv:1410.3012.
- 3562 [52] The ATLAS collaboration, “Search for high-mass diboson resonances with boson-tagged jets
3563 in proton-proton collisions at $s=8$ TeV with the ATLAS detector”, *Journal of High Energy*
3564 *Physics* **2015** (Dec, 2015) 1–39, [doi:10.1007/JHEP12\(2015\)055](https://doi.org/10.1007/JHEP12(2015)055).
- 3565 [53] S. Frixione and B. R. Webber, “Matching NLO QCD computations and parton shower
3566 simulations”, *JHEP* **06** (2002) 029, [doi:10.1088/1126-6708/2002/06/029](https://doi.org/10.1088/1126-6708/2002/06/029),
3567 arXiv:hep-ph/0204244.
- 3568 [54] S. Frixione, P. Nason, and B. R. Webber, “Matching NLO QCD and parton showers in
3569 heavy flavor production”, *JHEP* **08** (2003) 007, [doi:10.1088/1126-6708/2003/08/007](https://doi.org/10.1088/1126-6708/2003/08/007),
3570 arXiv:hep-ph/0305252.
- 3571 [55] S. Frixione, P. Nason, and C. Oleari, “Matching NLO QCD computations with Parton
3572 Shower simulations: the POWHEG method”, *JHEP* **11** (2007) 070,
3573 [doi:10.1088/1126-6708/2007/11/070](https://doi.org/10.1088/1126-6708/2007/11/070), arXiv:0709.2092.
- 3574 [56] S. A. et. al., “Geant4—a simulation toolkit”, *Nuclear Instruments and Methods in Physics*
3575 *Research Section A: Accelerators, Spectrometers, Detectors and Associated Equipment* **506**
3576 (2003), no. 3, 250 – 303, [doi:\[https://doi.org/10.1016/S0168-9002\\(03\\)01368-8\]\(https://doi.org/10.1016/S0168-9002\(03\)01368-8\)](https://doi.org/10.1016/S0168-9002(03)01368-8).
- 3577 [57] CMS Collaboration, “Event generator tunes obtained from underlying event and
3578 multiparton scattering measurements”, *Eur. Phys. J. C* **76** (2016) 155,
3579 [doi:10.1140/epjc/s10052-016-3988-x](https://doi.org/10.1140/epjc/s10052-016-3988-x), arXiv:1512.00815.
- 3580 [58] CMS Collaboration, “Search for massive resonances in dijet systems containing jets tagged
3581 as W or Z boson decays in pp collisions at $\sqrt{s}=8$ TeV”, *JHEP* **08** (May, 2014) 173. 37 p.
- 3582 [59] F. Dias et al., “Combination of Run-1 Exotic Searches in Diboson Final States at the LHC”,
3583 *JHEP* **04** (2016) 155, [doi:10.1007/JHEP04\(2016\)155](https://doi.org/10.1007/JHEP04(2016)155), arXiv:1512.03371.
- 3584 [60] CMS Collaboration, “Search for massive WH resonances decaying into the $\ell\nu b\bar{b}$ final state
3585 at $\sqrt{s}=8$ TeV”, *Eur. Phys. J.* **C76** (2016), no. 5, 237,
3586 [doi:10.1140/epjc/s10052-016-4067-z](https://doi.org/10.1140/epjc/s10052-016-4067-z), arXiv:1601.06431.

- 3587 [61] CERN, “Collider Reach”, 2019 (accessed January 12, 2019),
 3588 <http://collider-reach.web.cern.ch/>.
- 3589 [62] J. Alwall et al., “The automated computation of tree-level and next-to-leading order
 3590 differential cross sections, and their matching to parton shower simulations”, *JHEP* **07**
 3591 (2014) 079, doi:[10.1007/JHEP07\(2014\)079](https://doi.org/10.1007/JHEP07(2014)079), arXiv:[1405.0301](https://arxiv.org/abs/1405.0301).
- 3592 [63] T. Sjöstrand, S. Mrenna, and P. Z. Skands, “A brief introduction to PYTHIA 8.1”, *Comput.
 3593 Phys. Commun.* **178** (2008) 852, doi:[10.1016/j.cpc.2008.01.036](https://doi.org/10.1016/j.cpc.2008.01.036), arXiv:[0710.3820](https://arxiv.org/abs/0710.3820).
- 3594 [64] S. C. et al., “Search for resonances in the dijet mass spectrum from 7 TeV pp collisions at
 3595 CMS”, *Physics Letters B* **704** (2011), no. 3, 123 – 142,
 3596 doi:<https://doi.org/10.1016/j.physletb.2011.09.015>.
- 3597 [65] G. Punzi, “Sensitivity of searches for new signals and its optimization”, *eConf* **C030908**
 3598 (2003) MODT002, arXiv:[physics/0308063](https://arxiv.org/abs/physics/0308063). [,79(2003)].
- 3599 [66] CMS Collaboration, “Search for heavy resonances in the W/Z-tagged dijet mass spectrum
 3600 in pp collisions at 7 TeV”, *Phys. Lett.* **B723** (2013) 280–301,
 3601 doi:[10.1016/j.physletb.2013.05.040](https://doi.org/10.1016/j.physletb.2013.05.040), arXiv:[1212.1910](https://arxiv.org/abs/1212.1910).
- 3602 [67] CMS Collaboration Collaboration, “Search for Narrow Resonances using the Dijet Mass
 3603 Spectrum with 19.6fb-1 of pp Collisions at sqrt{s}=8 TeV”, Technical Report
 3604 CMS-PAS-EXO-12-059, CERN, Geneva, 2013.
- 3605 [68] D. J. Hand, “Statistical Concepts: A Second Course, Fourth Edition by Richard G. Lomax,
 3606 Debbie L. Hahs-Vaughn”, *International Statistical Review* **80** (2012), no. 3, 491–491.
- 3607 [69] T. C. collaboration, “Identification of b-quark jets with the CMS experiment”, *Journal of
 3608 Instrumentation* **8** (2013), no. 04, P04013.
- 3609 [70] T. C. collaboration, “Identification of heavy-flavour jets with the CMS detector in pp
 3610 collisions at 13 TeV”, *Journal of Instrumentation* **13** (2018), no. 05, P05011.
- 3611 [71] CMS Collaboration Collaboration, “Search for massive resonances decaying into WW, WZ,
 3612 ZZ, qW and qZ in the dijet final state at $\sqrt{s} = 13$ TeV using 2016 data”, Technical Report
 3613 CMS-PAS-B2G-16-021, CERN, Geneva, 2016.
- 3614 [72] G. Cowan, K. Cranmer, E. Gross, and O. Vitells, “Asymptotic formulae for likelihood-based
 3615 tests of new physics”, *The European Physical Journal C* **71** (Feb, 2011)
 3616 doi:[10.1140/epjc/s10052-011-1554-0](https://doi.org/10.1140/epjc/s10052-011-1554-0), arXiv:[1007.1727](https://arxiv.org/abs/1007.1727).

- [73] M. Dasgupta, A. Powling, and A. Siodmok, “On jet substructure methods for signal jets”, *JHEP* **08** (2015) 079, doi:10.1007/JHEP08(2015)079, arXiv:1503.01088.
- [74] U. Baur, I. Hinchliffe, and D. Zeppenfeld, “Excited quark production at hadron colliders”, *Int. J. Mod. Phys. A* **2** (1987) 1285, doi:10.1142/S0217751X87000661.
- [75] U. Baur, M. Spira, and P. M. Zerwas, “Excited-quark and -lepton production at hadron colliders”, *Phys. Rev. D* **42** (1990) 815, doi:10.1103/PhysRevD.42.815.
- [76] CMS Collaboration Collaboration, “Search for massive resonances decaying into WW , WZ , ZZ , qW , and qZ with dijet final states at $\sqrt{s} = 13$ TeV”, *Phys. Rev. D* **97** (Apr, 2018) 072006, doi:10.1103/PhysRevD.97.072006.
- [77] CMS Collaboration Collaboration, “Jet algorithms performance in 13 TeV data”, Technical Report CMS-PAS-JME-16-003, CERN, Geneva, 2017.
- [78] J. Alwall et al., “Comparative study of various algorithms for the merging of parton showers and matrix elements in hadronic collisions”, *Eur. Phys. J.* **C53** (2008) 473–500, doi:10.1140/epjc/s10052-007-0490-5, arXiv:0706.2569.
- [79] J. Dolen et al., “Thinking outside the ROCs: Designing Decorrelated Taggers (DDT) for jet substructure”, arXiv:1603.00027.
- [80] J. Gallicchio and M. D. Schwartz, “Quark and Gluon Tagging at the LHC”, *Phys. Rev. Lett.* **107** (2011) 172001, doi:10.1103/PhysRevLett.107.172001, arXiv:1106.3076.
- [81] J. A. Aguilar-Saavedra, “Stealth bosons and where to find them”, 2018, <https://indico.cern.ch/event/649482/contributions/2993323/attachments/1688557/2716149/SBAWTFD.pdf>.
- [82] J. A. Aguilar-Saavedra, “Running bumps from stealth bosons”, *Eur. Phys. J.* **C78** (2018), no. 3, 206, doi:10.1140/epjc/s10052-018-5717-0, arXiv:1801.08129.
- [83] ATLAS Collaboration Collaboration, “Search for diboson resonances in hadronic final states in 79.8 fb^{-1} of pp collisions at $\sqrt{s} = 13$ TeV with the ATLAS detector”, Technical Report ATLAS-CONF-2018-016, CERN, Geneva, Jun, 2018.
- [84] T. Heimel, G. Kasieczka, T. Plehn, and J. M. Thompson, “QCD or What?”, arXiv:1808.08979.
- [85] J. A. Aguilar-Saavedra, J. H. Collins, and R. K. Mishra, “A generic anti-QCD jet tagger”, *JHEP* **11** (2017) 163, doi:10.1007/JHEP11(2017)163, arXiv:1709.01087.

- 3647 [86] A. Butter, G. Kasieczka, T. Plehn, and M. Russell, “Deep-learned Top Tagging with a
3648 Lorentz Layer”, *SciPost Phys.* **5** (2018), no. 3, 028,
3649 doi:10.21468/SciPostPhys.5.3.028, arXiv:1707.08966.
- 3650 [87] I. Goodfellow, Y. Bengio, and A. Courville, “Deep Learning”. The MIT Press, 2016.
- 3651 [88] D. P. Kingma and J. Ba, “Adam: A Method for Stochastic Optimization”, *CoRR*
3652 abs/1412.6980 (2014) arXiv:1412.6980.
- 3653 [89] F. Chollet et al., “Keras”. <https://keras.io>, 2015.
- 3654 [90] M. A. et al, “TensorFlow: Large-Scale Machine Learning on Heterogeneous Systems”, 2015.
3655 Software available from tensorflow.org.
- 3656 [91] G. P. Salam, L. Schunk, and G. Soyez, “Dichroic subjettness ratios to distinguish colour
3657 flows in boosted boson tagging”, *JHEP* **03** (2017) 022, doi:10.1007/JHEP03(2017)022,
3658 arXiv:1612.03917.